



UNIVERSITY OF
BIRMINGHAM

BLENDING OF NON-NEWTONIAN FLUIDS IN STATIC MIXERS: ASSESSMENT VIA OPTICAL METHODS.

by

Federico Alberini

A thesis submitted to
The University of Birmingham
for the degree of
DOCTOR OF PHILOSOPHY

School of Chemical Engineering
College of Engineering and Physical Sciences
The University of Birmingham
October 2013

UNIVERSITY OF
BIRMINGHAM

University of Birmingham Research Archive

e-theses repository

This unpublished thesis/dissertation is copyright of the author and/or third parties. The intellectual property rights of the author or third parties in respect of this work are as defined by The Copyright Designs and Patents Act 1988 or as modified by any successor legislation.

Any use made of information contained in this thesis/dissertation must be in accordance with that legislation and must be properly acknowledged. Further distribution or reproduction in any format is prohibited without the permission of the copyright holder.

Abstract

The performance of KM static mixers has been assessed for the blending of Newtonian and time-independent non-Newtonian fluids using planar laser induced fluorescence (PLIF). A stream of dye is injected at the mixer inlet and the distribution of dye at the mixer outlet is analyzed from images obtained across the pipe cross section. The effect of superficial velocity, scale of static mixer, flow ratio between a primary and a secondary injected flow and finally the injection position, are investigated to determine the consequences on mixing performance. Different methods are discussed to characterize mixing performance, comparing CoV and maximum striation thickness. Conflicting trends are revealed in some experiments results, leading to the development of an areal based distribution of mixing intensity and a distribution of striation with high mixing intensity. For two-fluids blending, the addition of a high viscosity stream into the lower viscosity main flow causes very poor mixing performance, with unmixed spots of more viscous component observable in the PLIF image. The final part of the work is focused on a preliminary understanding of advective mechanisms such as shearing of non-Newtonian fluid drops and stretching of a non-Newtonian fluid filaments.

*Come una fenice
risorgero' dalle mie ceneri,
tutto cio' che mi colpisce,
un giorno mi fortifichera'.*

*Like a Phoenix
I will rise from my ashes,
Everything that hits me now
will one day make me stronger.*

“Chi poco pensa molto erra.”
“He who thinks little errs much.”

Leonardo da Vinci

ACKNOWLEDGMENTS

First and foremost, I would like to express my gratitude towards my supervisor Prof. Mark J.H. Simmons who gave me the opportunity to start this adventure. It has been a privilege and great pleasure to work with him and Dr. Andrew Ingram not only for their constant guidance and valuable input throughout the course of this research, but also for their friendship. I would also like to thank all people from Chemical Engineering who helped me during these 3 years. A special thank goes to Lynn Draper which helped me several times to solve many administrative issues and to joined me for several cups of proper coffee. Financial support was provided by the Engineering and Physical Sciences Research Council (UK) and Johnson Matthey (JM) sponsorship. I am also grateful to my industrial supervisor Prof. Hugh Stitt for his interest and encouragement.

Dulcis in fundo, I would like to thank my family for their encouragement and understanding over the years and Giulia for always being with me along this journey and her infinite patience and help during my writing up stage.

TABLE OF CONTENTS

<i>Abstract</i>	<i>i</i>
<i>Acknowledgments</i>	<i>iii</i>
<i>Table of contents</i>	<i>iv</i>
<i>List of figures</i>	<i>ix</i>
<i>List of tables</i>	<i>xv</i>
<i>List of abbreviations</i>	<i>xvii</i>
1. INTRODUCTION	1
1.1. Background	1
1.2. Objectives of the thesis	4
1.3. Thesis layout	5
2. LITERATURE REVIEW	7
2.1. Fluid mechanics fundamentals	8
2.1.1. Newtonian fluids.....	8
2.1.2. Non-Newtonian fluids	10
2.1.3. Rheological measurements.....	16
2.1.3.2.Extensional viscosity measurement.....	19
2.2. Mixing Fundamentals	22
2.2.1. Laminar flow	23
2.2.2. Chaotic flow	24
2.2.3. Turbulent flow	26
2.3. Mixing equipment	27
2.3.1. Mixing of non- Newtonian fluids in batch processes – stirred vessels	28
2.3.2. Mixing Of Non- Newtonian Fluids In Continuous Processes- Static Mixers	30

2.4. Measures of mixing performance	34
2.4.1. Measures to quantify scale	34
2.4.2. Measures to quantify intensity.....	35
2.4.3. Techniques used to obtain measures of mixedness	41
2.5. Mixing performance of static mixers	49
2.5.1. Industrial applications and commercial static mixers.....	50
2.6. Conclusions	55
3. MATERIALS AND METHODS	58
3.1. Introduction.....	58
3.2. Rheological measurements.....	60
3.2.1. Rheology of model fluids using TA AR 1000 rheometer.	60
3.2.2. The Bohlin Gemini II Opto-rheometer.....	63
3.3. Flow Visualisation	64
3.3.1. Planar Laser Induced Fluorescence (PLIF)	64
3.3.1.1.Intensity of segregation (CoV and log-variance).....	66
3.3.1.2.Scale of segregation (striation characterisation).....	68
3.3.2. High speed imaging.....	69
3.4. Static Mixer Rig	70
3.4.1. Static mixer rig for PLIF	70
4. USE OF AN AREAL DISTRIBUTION OF MIXING INTENSITY TO DESCRIBE BLENDING OF NON-NEWTONIAN FLUIDS IN A KENICS KM STATIC MIXER USING PLIF.....	74
4.1. Introduction	74
4.2. Material and Methods	76
4.2.1.Fluids and Flow Conditions	76
4.2.2.Characterisation of mixing performance from the PLIF images.....	79
4.3. Results and Discussion.....	81
4.3.1.Pressure Drop	81
4.3.2.Images obtained from PLIF technique	83

4.3.3. Analysis of Mixing Performance from PLIF Images	85
4.3.4. Areal Distribution of Mixing Intensity	89
4.4. Conclusions	94
5. USE OF PLIF TO DETERMINE THE EFFECT OF SYSTEM AND FLUID PARAMETERS UPON THE BLENDING OF SHEAR-THINNING FLUIDS IN KM STATIC MIXERS.	96
5.1. Introduction	96
5.2. Material and Methods	99
5.2.1. Fluids and Flow Conditions	99
5.2.2. Characterisation of mixing performance from the PLIF images	101
5.3. Results and Discussion	103
5.3.1. Effect of velocity for different scales at constant flow ratio	106
5.3.2. Effect of flow ratio and injection position at constant velocity and scale	126
5.4. Conclusion	132
6. EFFECT OF SYSTEM AND FLUID PARAMETERS UPON THE BLENDING OF NON-NEWTONIAN FLUIDS: COMPARISON BETWEEN SMX PLUS AND KM STATIC MIXER	134
6.1 Introduction	134
6.2 Material and Methods	137
6.2.1. Fluids and Flow Conditions	137
6.3. Results and discussion	139
6.3.1. Pressure drops comparison between KM and SMX Plus static mixer	143
6.3.2. Effect of velocity for different scales at constant flow ratio	145
6.3.3. Effect of flow ratio and injection position at constant velocity and scale	166
6.3.4. Time independency	173
6.3.5. Energy consumed in KM and SMX Plus static mixers	175
6.4. Conclusions	180

7. UNDERSTANDING OF NON-NEWTONIAN BLENDING: FOCUSING ON FILAMENT STRETCHING AND DROP STRETCHING	182
7.1. Introduction.....	182
7.2. Experimental methods.....	184
7.2.1. Shear drop stretching.....	184
7.2.2. Filament stretching	187
7.3. Results.....	190
7.3.1. Drop stretching under a continuous shear field	190
7.3.2. Filament stretching	194
7.4. Conclusions.....	206
8. CONCLUSIONS AND FUTURE RECOMMENDATIONS	208
8.1. Conclusions.....	208
8.2. Future recommendations	212
APPENDIX.....	214
APPENDIX A: Equipment specification.....	214
A1. Cone and plate geometries.....	214
A2. Force transducer.....	215
A3. Photron SA3 FASTCAM.....	217
APPENDIX B: V3V apparatus.....	219
B1. Volumetric 3-Component Velocimetry (V3V)	219
APPENDIX C: Minor experiments.....	224
C1: Fluid dynamic of a Kenics KM static mixer.....	224
C2: V3V experiment.....	225

C2.2 Experimental setup.....	227
C2.3 Results.....	229
C2.4 Conclusions.....	235
C.3 Injection position effects.....	236
C3.1 Introduction.....	236
C3.2 Experimental setup.....	237
C3.3 Results.....	238
C3.4 Conclusions.....	243
APPENDIX D: MATLAB scripts.....	245
D1: Script of intensity of segregation: Coefficient of variation and LogVa.....	245
D2: Script for scale of segregation: Striation thickness.....	247
D3: Script for scale and intensity of segregation: Area fraction and striation area distribution.....	251
REFERENCES.....	255

List of figures

Figure 2.1 Schematic representation of unidirectional shearing flow (Non-Newtonian Flow and Applied Rheology).....	9
Figure 2.2. Schematic of shear stress shear rate behaviour for time-dependent fluids (Non-Newtonian Flow and Applied Rheology).	12
Figure 2.3 Schematic shear stress shear rate behaviour for shear thinning fluid (Chhabra and Richardson).....	14
Figure 2.4 Selected rheometer geometries: a) Cone and plate (AR 1000 manual), b) parallel plate. Parameters defined in this Figure are used in Table 2.2 below.....	17
Figure 2.5 Flow of a Herschel-Bulkley fluid down a cylindrical pipe of constant diameter ..	19
Figure 2.6 Schematic of turbulent and laminar flow in a pipe.....	24
Figure 2.7 Stretching field and Lyapunov exponent (Handbook of industrial mixing).	27
Figure 2.9 Example of Poincare plot (Schlutt et al., 2012).....	37
Figure 2.10 Three dimension of mixing: intensity of segregation, scale of segregation, and exposure ((Kukukova et al., 2009))......	40
Figure 2.11 Laser Doppler Anemometry (LDA) (Dantec dynamics web site)	43
Figure 2.12 Magnetic resonance imaging (MRI).....	44
Figure 2.13 Schematic view of positron emission particle tracking functioning: on the sides the detectors which detect and localise the particle from the radioactivity signal of the particles.....	46
Figure 2.14 Geometries of: a) KM static mixer elements and b) SMX PLUS static mixer elements.....	52
Figure 2.15 Classification of unit operation using static mixer (Thakur et al., 2003)	56
Figure 3.1 ARI1000 rheometer.	60
Figure 3.2 Rheology of the non-Newtonian fluids used fitted to the Herschel-Bulkley model.	61
Figure 3.3 Gemini II rheometer: (a) Opto-rheometer; (b) opto-sample platform; (c) opto-geometry.....	63
Figure 3.4 Concentration of Rhodamine 6G versus gray scale value for the two solution of Carbopol 940.....	65
Figure 3.5: Explanation of algorithm of intensity of segregation	66
Figure 3.6 Photron FASTCAM SA3.....	69

<i>Figure 3.7 Schematics of the static mixer test rig. (a) overall schematic; (b) dimensions of static mixer test section showing location of pressure transducers; (c) picture of the PLIF rig.....</i>	<i>71</i>
<i>Figure 3.8 Pattern flow using peristaltic and gear pump for selected experiments for KM and SMX+ static mixers.....</i>	<i>73</i>
<i>Figure 4.1 Injection positions.....</i>	<i>78</i>
<i>Figure 4.2 Development of areal analysis method. (a) Identification of regions in the grayscale distribution with a given mixing intensity; (b) raw image; (c) example of image processing for the experiment #1 12 elements with regions of mixing intensity > 60% in white.....</i>	<i>79</i>
<i>Figure 4.3 Pressure drop measurements made for both continuous phase fluids in the empty pipe and comparison with theoretical predictions.....</i>	<i>81</i>
<i>Figure 4.4: Raw PLIF Images. (a) and (b) show #1_n for 6 and 12 elements; (c) and (d) show #1_m for 6 and 12 elements and (e) and (f) show #2 for 6 and 12 elements respectively.....</i>	<i>83</i>
<i>Figure 4.5: Coef?cient of variation (CoV) data from Alloca and Streiff compared with the present study.</i>	<i>86</i>
<i>Figure 4.6: CoV versus $\Delta P/p$ for all the experiments developed for this work compared with eq. (2.31) (x in the plot).</i>	<i>87</i>
<i>Figure 4.7: Comparison of (a) intensity (log-variance) and (b) scale of segregation (maximum striation thickness) obtained from the PLIF analysis.</i>	<i>88</i>
<i>Figure 4.8. Application of the areal mixing analysis to the PLIF images obtained for 12 KM mixing elements. Discrete distributions are shown for (a) experiment #1_n, (b) experiment #1_m and (c) experiment #2 respectively. Areas in white are within the range of interest....</i>	<i>89</i>
<i>Figure 4.9: Bar graph showing discrete areal intensity distributions for each experiment.</i>	<i>91</i>
<i>Figure 4.10: Cumulative areal intensity distributions as a means of determining relative mixing performance between experiments.....</i>	<i>92</i>
<i>Figure 4.11: Gray scale distributions for (a) experiment #1_n and (b) experiment #1_m and (c) experiment #2, all carried out with 12 KM elements. Sub figures (d), (e) and (f) show the breakdown of area fraction due to G_{X-} and G_{X+} for experiments #1_n, #1_m and #2 respectively.....</i>	<i>93</i>

<i>Figure 5.1 Injection position and static mixer dimension used for the experiments of Chapter :</i>	101
<i>Figure 5.2 Three different zones that describe the size of striation with high mixer intensity in terms of no dimensional area and perimeter.</i>	102
<i>Figure 5.3 Raw images of all experiments: (a) Experiment 1a at different superficial velocities, (b) Experiment 1b at different superficial velocities, (c) Experiment 2a at different superficial velocities, (d) Experiment 2b at different superficial velocities, (e) Experiment 3a,b and 4a,b at the design velocity of 0.3 [ms⁻¹].</i>	105
<i>Figure 5.4 Effect of velocity for different scales at constant flow ratio: a) CoV (intensity of segregation) versus $\Delta P/\rho$ and b) max striation area (scale of segregation) versus $\Delta P/\rho$, for #1a&b and #2a &b at selected velocities.</i>	108
<i>Figure 5.5 Bar graph showing discrete areal intensity distributions (a) for #1a&b and (b) #2a&b at selected velocities.</i>	111
<i>Figure 5.6 Fraction of mixing better than 80% ($X>80\%$) versus $\Delta P/\rho$ for experiment #1a&b and #2a&b.</i>	112
<i>Figure 5.7 Effect of velocity and different injection for ½” device: a) striation areas for selected ranges (injection fluid 1); b) striation areas for selected ranges (injection fluid 2); c) distribution of striation sizes for injection fluid 1 and for injection fluid 2.</i>	118
<i>Figure 5.8 Effect of velocity and different injection for 1” device: a) striation areas for selected ranges (injection fluid 1) (#2a); b) striation areas for selected ranges (injection fluid 2) (#2b); c) distribution of striation sizes for injection fluid 1 and for injection fluid 2.</i>	124
<i>Figure 5.9 Total “interfacial length” over the static mixer perimeter for mixing intensity better than 80% ($X>80\%$) versus $\Delta P/\rho$ for experiment #1a,b and #2a,b.</i>	125
<i>Figure 5.10 Effect of flow ratio and injection position at constant velocity and scale: a) CoV (intensity of segregation) and max striation area at constant $\Delta P/\rho$, b) bar graph showing discrete areal intensity distributions for #2a, #2b,#3a, #3b, #4a and #4b at $v=0.3 \text{ ms}^{-1}$.</i>	127
<i>Figure 5.11 Effect of flow ratio and different injection for 1” device: a) striations area for selected ranges (injection fluid 1) (#3a) b) striations area for selected ranges (injection fluid 2) (#3b), c) distribution of striation size for injection fluid 1 and for injection fluid 2.</i>	129
<i>Figure 5.12 Effect of injection position and different injection for 1” device: a) striations area for selected ranges (injection fluid 1) (#4a) b) striations area for selected ranges (injection fluid 2) (#4b), c) distribution of striation size for the injection of fluid 1 and injection of fluid 2.</i>	131

<i>Figure 6.1 All the specifics of static mixer dimensions including secondary flow inlet dimensions and injection position.....</i>	<i>139</i>
<i>Figure 6.2. Pattern flow using gear pump for selected experiments for KM and SMX Plus static mixers.</i>	<i>139</i>
<i>Figure 6.3 Raw images of all SMX experiments: (a) Experiment 5a at different superficial velocities, (b) Experiment 5b at different superficial velocities, (c) Experiment 6a at different superficial velocities, (d) Experiment 6b at different superficial velocities, (e) Experiment 7a,b and 8a,b at the design velocity of 0.3 [ms⁻¹].....</i>	<i>142</i>
<i>Figure 6.4 Fraction of mixing better than 80% (X>80%) versus $\Delta P/\rho$ for experiments with different geometries using 1/2" device.</i>	<i>144</i>
<i>Figure 6.5 Effect of velocity for different scales at constant flow ratio: a) CoV (intensity of segregation) versus $\Delta P/\rho$ and b) max striation area (scale of segregation) versus $\Delta P/\rho$, for #5a, b and #6a,b at selected velocities.</i>	<i>146</i>
<i>Figure 6.6. Bar graph showing discrete areal intensity distributions (a) for #1a,b and (b) #2a,b at selected velocities.</i>	<i>148</i>
<i>Figure 6.7 Fraction of mixing better than 80% (X>80%) versus $\Delta P/\rho$ for experiment #5a&b and #6a&b.</i>	<i>149</i>
<i>Figure 6.8. Effect of velocity and different injection for 1/2" device: a) striation areas for selected ranges (injection fluid 1); b) striation areas for selected ranges (injection fluid 2); c) distribution of striation sizes (injection fluid 1 vs injection fluid 2).....</i>	<i>154</i>
<i>Figure 6.9 Effect of velocity and different injection for 1" device: a) striation areas for selected ranges (injection fluid 1); b) striation areas for selected ranges (injection fluid 2); c) distribution of striation sizes (injection fluid 1vs injection fluid 2).....</i>	<i>162</i>
<i>Figure 6.10 Total "interfacial length" over the static mixer perimeter for mixing intensity better than 80% (X>80%) versus $\Delta P/\rho$ for experiment #5a&b and #6a&b.....</i>	<i>165</i>
<i>Figure 6.11 Effect of flow ratio and injection position at constant velocity and scale: a) CoV (intensity of segregation) and max striation area at constant $\Delta P/\rho$, b) bar graph showing discrete areal intensity distributions for #6a, #6b,#7a, #7b, #8a and #8b at v=0.3 ms⁻¹.....</i>	<i>167</i>
<i>Figure 6.12 Effect of flow ratio 25 and different injection for 1" device: a) striations area for selected ranges (injection fluid 1) b) striations area for selected ranges (injection fluid 2), c) distribution of striation size (injection fluid 1vs injection fluid 2).....</i>	<i>170</i>

<i>Figure 6.13 Effect of injection position and different injection for 1" device at constant flow ratio of 25: a) striations area for selected ranges (injection fluid 1) b) striations area for selected ranges (injection fluid 2), c) distribution of striation size for the injection of fluid 1 and injection of fluid 2.</i>	<i>172</i>
<i>Figure 6.14 Flow pattern for selected experiments at different detection time for KM and SMX Plus static mixers.</i>	<i>174</i>
<i>Figure 6.15 Fraction of mixing better than 80% ($X > 80\%$) versus $\Delta P/\rho$ for experiments with different geometries using 1/2" device.</i>	<i>175</i>
<i>Figure 6.16 Fraction of mixing better than 80% ($X > 80\%$) versus $\Delta P/\rho$ for experiments with different geometries using 1" device.</i>	<i>176</i>
<i>Figure 7.1 Drop stretching experiments.....</i>	<i>185</i>
<i>Figure 7.2. a) Location of the drop in each experiment and b) example of measurement of drop perimeter.</i>	<i>186</i>
<i>Figure 7.3 Filament stretching rig.....</i>	<i>187</i>
<i>Figure 7.4 Selected images for D just before the breakage and D_0 using fluid 1 at the velocity of 1.25 mm s^{-1}.....</i>	<i>188</i>
<i>Figure 7.5 Example of force measurement and explanation of how the energy spent for the stretching has been calculated.....</i>	<i>190</i>
<i>Figure 7.6 P/P_0 versus the energy applied by the rheometer for fluid 1.</i>	<i>191</i>
<i>Figure 7.7 P/P_0 versus the energy applied by the rheometer for fluid 2.</i>	<i>192</i>
<i>Figure 7.8 Images at maximum time for all the runs for fluid 1(a) and 2 (b).</i>	<i>193</i>
<i>Figure 7.9 P/P_0 at maximum selected time versus power spent for both fluids.....</i>	<i>194</i>
<i>Figure 7.10 Force measurement at different speeds for filaments of fluid 1 at constant volume.....</i>	<i>195</i>
<i>Figure 7.11 Force measurement at different speeds for filaments of fluid 2 at constant volume.....</i>	<i>196</i>
<i>Figure 7.12 Filament of fluid at t_0 with highlighted contact angle (θ) for both fluids.</i>	<i>197</i>
<i>Figure 7.13 Variation of filament diameter versus time: a) filament of fluid 1, b) filament of fluid 2.</i>	<i>199</i>
<i>Figure 7.14 Extensional viscosity versus Hencky strain at different stretching rates for Fluid 1 a) and 2 b).....</i>	<i>200</i>
<i>Figure 7.15 Variation of filament diameter versus energy: a) filament of fluid 1 and b) filament of fluid 2.....</i>	<i>202</i>

<i>Figure 7.17 Comparison of energy spent values for the stretching of the two fluids at different velocities and range of D/D_0.</i>	205
<i>Figure 7.18 Selected images of striations areas for a selected range of mixing intensity for two experiment run at same conditions but using different injection.</i>	205
<i>Figure B1.1. Probe and cameras of V3V (TSI V3V brochure).</i>	219
<i>Figure B1.2 Measurement volume of V3V (TSI V3V brochure).</i>	221
<i>Figure B1.3 Principle of triplets for the V3V (TSI V3V brochure).</i>	222
<i>Figure B1.4. Calibration procedure for V3V: a) automated multi-plane calibration and (b) triplet size at each calibration plane (TSI V3V brochure).</i>	223
<i>Figure C1.1 Different positions of injection</i>	224
<i>Figure C2.1 a) 6 elements of KM static mixer made by transparent material, b) enclosure box and static mixer used for V3V experiment.</i>	227
<i>Figure C2.2 V3V rig.</i>	228
<i>Figure C2.3 Raw images of the three views of V3V cameras.</i>	229
<i>Figure C.2.4 Vector scatter of static mixer system using 80% w/w glycerol solution.</i>	230
<i>Figure C2.5 Flow field of different YX cross sections of static mixer.</i>	231
<i>Figure C2.6 a) Sections of static mixer; b)Flow field of different YX cross sections of static mixer element.</i>	232
<i>Figure C2.7. Reynolds number distribution inside the static mixer volume.</i>	233
<i>Figure C2.8 a) Vorticity distribution in the static mixer;b) Magnitude vorticity distribution in the static mixer.</i>	235
<i>Figure C3.1 a) Positions where the camera was pointed; first element and at the bottom of static mixer. b) Different position of injection investigated.</i>	237
<i>Figure C3.2. View of the central injection in an empty pipe (a and f), the view of 2nd and 3rd element of KM where the injection of the secondary flow is attached to the first element (b and g), the raw PLIF images at the end of 6 element of KM static are presented (e and l), PIV analysis (axial section) for central injection in an empty pipe (c and h) and gray scale values distribution of static mixer section (d and i).</i>	240
<i>Figure C3.3 Visualisation of injection in the two selected position, FAR and CLOSE at superficial velocity of 0.3 m s^{-1}. Raw PLIF images for selected experiment using 6 elements KM static mixer.</i>	242

Figure C3.4 Visualisation of injection in the two selected position, central and wall at superficial velocity of 0.3 m s^{-1} . Raw PLIF images for selected experiment using 6 elements KM static mixer.....243

List of Tables

<i>Table 2.1 constitutive equations to describe shear thinning fluids.....</i>	<i>15</i>
<i>Table 2.2 Shear rate and stress factors.</i>	<i>18</i>
<i>Table 2.3. Comparison between features of static mixer and stirred tank.</i>	<i>33</i>
<i>Table 2.4 Summary of different approaches to quantify the scale and intensity</i>	<i>39</i>
<i>Table 2.5 Commercially available static mixer (Thakur et al., 2003).....</i>	<i>52</i>
<i>Table 2.6 Industrial applications of commercial static mixers.....</i>	<i>54</i>
<i>Table 3.1 Tabulated Herschel-Bulkley model parameters obtained from rheological data and physical properties of the glycerol solution used in the experiments.....</i>	<i>62</i>
<i>Table 4.1: Summary of experimental conditions.</i>	<i>77</i>
<i>Table 4.2: Pressure drops over empty pipe (0.53 m) and 12 KM mixer elements (0.53 m) for the continuous phase fluids (Fluid I_n and Fluid I_m)......</i>	<i>82</i>
<i>Table 4.3: CoV_r from experimental data and eq. (2.31).....</i>	<i>85</i>
<i>Table 5.1 Experimental conditions for all experiments.....</i>	<i>100</i>
<i>Table 6.1. Experimental conditions for all experiments.....</i>	<i>138</i>
<i>Table 6.2 K values for KM and SMX Plus static mixer at different superficial velocity.....</i>	<i>144</i>
<i>Table 6.3 KM element geometry dimensions.....</i>	<i>177</i>
<i>Table 6.4 SMX Plus element geometry dimensions</i>	<i>178</i>
<i>Table 6.5 Values of energy per unit mass and power per unit mass for KM and SMX Plus at three different superficial velocities.....</i>	<i>180</i>
<i>Table 7.1 Values of capillary force and the physical quantities for the evaluation of them.</i>	<i>197</i>
<i>Table 7.2 Final dimensions of filament before the breakage.....</i>	<i>204</i>

Table 7.1 Values of capillary force and the physical quantities for the evaluation of them. 197
Table 7.2 Final dimensions of filament before the breakage.....204

Table.A1 Cone and plates features (AR100 Manual).....214

Abbreviations in alphabetical order

<i>C</i>	<i>Clearance</i>
<i>CoV</i>	<i>Coefficient of Variance</i>
<i>D</i>	<i>Diameter</i>
<i>D_{sm}</i>	<i>Diameter static mixer</i>
<i>F</i>	<i>Stretching force</i>
<i>h</i>	<i>Distance lower and upper plate</i>
<i>H</i>	<i>Fluid Filled Height</i>
<i>HEV</i>	<i>High Efficiency Vortex static mixer</i>
<i>K</i>	<i>Consistency index</i>
<i>KAM</i>	<i>Kolmogorov Arnold Moser</i>
<i>KM</i>	<i>Kenics Mixer</i>
<i>L</i>	<i>Length</i>
<i>LDA</i>	<i>Laser Doppler Anenometry</i>
<i>L_e</i>	<i>Long Length element</i>
<i>l_e</i>	<i>Short length element</i>
<i>MRI</i>	<i>Magnetic resonance imaging</i>
<i>n</i>	<i>Power index</i>
<i>P</i>	<i>Perimeter</i>
<i>PEPT</i>	<i>Particle Emission Positron Tracking</i>
<i>PIV</i>	<i>Particle Image Velocimetry</i>
<i>PLIF</i>	<i>Planar Laser Induced Fluorescence</i>
<i>P_w</i>	<i>Power</i>
<i>Q</i>	<i>Flow rate</i>
<i>R</i>	<i>Radius</i>

r	<i>Radius filament</i>
Re	<i>Reynolds number</i>
Sc	<i>Schmidt number</i>
SMV	<i>Sulzer Static Mixer Vortex</i>
SMX	<i>Sulzer Static Mixer</i>
T	<i>Tank diameter</i>
t	<i>Time</i>
t_e	<i>Thickness static element</i>
v	<i>Velocity</i>
$V3V$	<i>Voumetric 3 components velocimetry</i>
x_e	<i>Width of sticks of static mixer</i>
γ_w	<i>Shear rate at wall</i>
ΔP	<i>Pressure Drop</i>
ε	<i>Stretching rate</i>
η_e	<i>Extensional viscosity</i>
Λ	<i>Lyapunov exponent</i>
λ	<i>Stretching</i>
μ	<i>Shear viscosity</i>
ρ	<i>Density</i>
σ_a	<i>Axial stress</i>
σ_e	<i>Extensional stress</i>
σ_r	<i>Radial stress</i>
τ_0	<i>Yield stress</i>
τ_w	<i>Shear stress at wall</i>
ω	<i>Angular velocity</i>
Γ	<i>Torque</i>

1. INTRODUCTION

1.1. Background

Laminar mixing using static mixers has been the subject of much interest in the last few decades. From an industrial perspective, static mixers provide the opportunity to progress towards reductions in inventory and plant footprint, whilst for academia, the research field is ongoing, particularly for the blending of fluids with complex rheology. From a practical point of view, the development of knowledge of laminar mixing in such devices is essential in order to ensure a similar or an improved process performance compared with traditional batch processes (e.g. stirred vessels).

Additional advantages of continuous processes include the reduction of utility costs and improved process flexibility allowing rapid product changeover, with the caveat that improved process control measures will be required to ensure consistent product quality. Many studies have been carried out on this subject with particular emphasis on heat and mass

transfer characteristics. For example, Joshi et al. (1995) compared the performance of static mixers with open tube designs in order to verify performance improvements in terms of heat transfer enhancement in laminar flow.

The choice of static mixer design for a given process duty is a moot point; the optimisation of geometry is a major challenge in pipe mixing with laminar flows, due to the absence of an advective radial mixing mechanism since all fluid streamlines are in the axial direction. Many works in the literature deal with the comparison of different commercial static mixers in the laminar flow regime, such as the Kenics (KM) and SMX mixer designs which are the focus of this thesis. In the work of Rauline *et al.* (2000) the performances of these different geometries of static mixer are compared using 3D numerical simulations. Several criteria are chosen as the basis for the performance evaluation, namely, pressure drop per unit length, the number of mixer elements, the Lyapunov exponent, the mean shear rate and the intensity of segregation. The main purpose of laminar mixing studies is to gain understanding of the physical principles in order to develop meaningful theory. This topic has evolved mainly from empiricism to a semi qualitative level, via experimental and modelling methodologies. Laminar mixing is applicable in many different industrial applications including food (Talansier *et al.*, 2013), personal care, household products, slurries, polymer manufacture and, finally, catalyst washcoats. All of these products have a non-Newtonian rheology, as indeed do most fluids processed by industry; this entails an additional complication in understanding mixing performance. The literature on static mixers has generally concentrated on the blending of Newtonian fluids (Zalc *et al.*, 2002) or on providing performance for the blending of non-Newtonian fluids based upon bulk fluid flow or pressure drop measurements (Meijer et al., 2012, Kumar *et al.*, 2008, Chandra *et al.*, 1992, Ishikawa *et al.*, 1996). No literature exists on the local mixing conditions as a function of the blending of single, or multiple fluids with non-Newtonian rheology, yet in the context of foods and

polymers, this is key data. Liquid mixing applications are frequently carried out at low velocities or involve high viscosity substances or liquids with complex rheology which drastically increase the pressure drop of the system.

However, in most of the works where mixing performance is discussed, the characterisation is usually based upon statistical approaches such as the coefficient of variation or maximum striation size. These two methods have been discussed at length and sometimes criticised in the literature (Kukukova *et al.*, 2009) in particular when a complex mixing pattern has to be characterised. These methods, if used in isolation, can create misleading results. The need for a combined method which allows the characterisation of scale and intensity of mixing leads to the main objective of this thesis. Mixing performances for the blending of non-Newtonian fluids using static mixers will be presented showing the characterisation of mixing following the previous methods (coefficient of variation and maximum striation thickness) and the proposed combined method.

1.2. Objectives of the thesis

The overall aim of this thesis is the development of a new approach to define mixing performance for inline mixing using mainly non-Newtonian fluids. The methods developed are generic in nature and can be applied to a wide range of mixing processes where information about mixing pattern is required, nevertheless the focus of this thesis is on blending in static mixers which provide a mechanism to benchmark the approaches developed. The core of this new method is the analysis of mixing patterns obtained using the Planar Laser Induced Fluorescence (PLIF) technique. PLIF analyses are carried out in the laminar mixing regime with the use of Non-Newtonian fluids.

The methods have been developed according to the specific objectives of the study which are given below:

- Development of a new method to characterise mixing performance using an areal distribution of mixing intensity to describe blending of non-Newtonian fluids in Kenics static mixer. (Chapter 4)
- Comparison of the new analysis methods with conventional mixing parameters which represent the scale and intensity of segregation. (Chapter 4)
- Development of a new analysis to characterise scale of segregation more deeply based on previous developed method. (Chapter 5)
- Study of the effect of system and fluid parameters as flow rate, flow ratio, size of static mixer, different injection and different injection position upon the blending of Non-Newtonian fluids in a KM static mixer. Different experiments are carried out and compared for the understanding of the behaviour of shear thinning fluids upon different conditions. (Chapter 5)

- Comparison of the behaviour of different static mixers at the same inlet conditions, in terms of performance and energy consumed, focussing on KM and SMX Plus designs (Chapter 6).

These analyses presented enable the efficiency of different static mixers to be determined: how the behaviour of Non-Newtonian fluids affects the mixing performance is a key objective of this thesis to enable determination of the optimal mixing conditions for a given duty. The final aim of the thesis is to obtain understanding of the individual phenomena causing mixing by advection within static mixers. Preliminary studies have been made which aim to obtain understanding of how the disruption of single fluid filaments under the action of shear or elongational stresses leads to an increase in interfacial area (Chapter 7). This part of work has been focussed on filament stretching and drop stretching of non-Newtonian fluids. These simplified systems have been investigated to obtain new information about the advective mechanisms for the blending of non-Newtonian fluids.

1.3. Thesis layout

Chapter 2 contains a review of the literature on the fundamentals of mixing in terms of rheology of fluids and types of process used for the mixing. Particular attention is paid to the determination of mixing performance describing the different approaches which have been used. Relevant batch and continuous mixing equipment are reviewed focussing on laminar flow and on the blending of non-Newtonian fluids.

In Chapter 3 the materials and methods used in this thesis work are described. A detailed description of rig and apparatus for the different experiments is given focusing on Planar

Laser Induced Fluorescence (PLIF) experiments, which are the core of this thesis work. The characterization of all the fluids used is presented including their rheology.

Chapter 4 is the first results chapter which concentrates on the explanation of the new developed areal based method to characterise mixing performance from PLIF images. The work focusses on the blending of non-Newtonian fluids in a KM static mixer¹.

Chapter 5 deals with the effect of fluid parameters on the blending of non-Newtonian fluids focusing on injection of fluid with different rheology from the ‘continuous’ phase in a KM static mixer. The mixing performance is assessed using both the new method and traditional approaches, with similarities and differences highlighted².

Chapter 6 follows the structure of Chapter 5 but instead of using the KM static mixer, the SMX Plus static mixer is investigated. A comparison in terms of mixing performances and energy consumed is described.

Chapter 7 is the last results chapter, which consists of a preliminary study of simplified systems that represents specific aspects of the mixing mechanism. Investigations on the shearing of drops and stretching of filament of different non-Newtonian fluids are presented.

Finally in the last chapter a summary of all the conclusion of this work is proposed.

Publications arising from this thesis

The following articles have been published or presented as part of this research

Conferences

¹ This chapter has been published (in part) as ALBERINI F., M.J.H. SIMMONS, A. INGRAM, E.H. STITT. Use of an areal distribution of mixing intensity to describe blending of non-Newtonian fluids in a Kenics KM static mixer using PLIF. AIChE journal (accepted) (2013).

² This chapter has been submitted (in part) for publication in Chemical Engineering Science as ALBERINI F., M.J.H. SIMMONS, A. INGRAM, E.H. STITT. Effect of system and fluid parameters upon the blending of shear-thinning fluids in a KM static mixer. Chemical Engineering Science journal (submitted) (2013).

ALBERINI F., M.J.H. SIMMONS, A. INGRAM, E.H. STITT. Mixing of time-independent non-Newtonian fluids in a Kenics static mixer using an optical method for intensity and scale of segregation. Oral presentation at International Symposium on Mixing in Industrial Processes VII (BEIJING 2011).

ALBERINI F., M.J.H. SIMMONS, A. INGRAM, E.H. STITT. A single mixing criterion to identify mixing performance based on a combination of scale and intensity segregation in static mixers using non-Newtonian fluids. Oral presentation IChemE student competition mixing subject (LONDON 2012).

ALBERINI F., M.J.H. SIMMONS, A. INGRAM, E.H. STITT. A combined criterion to identify mixing performance for the blending of non-Newtonian fluids using a km static mixer. Oral presentation at NAMF mixing 23 (MAYAN RIVIERA, MEXICO 2012).

ALBERINI F., M.J.H. SIMMONS, A. INGRAM, E.H. STITT. Use of an areal distribution of mixing intensity to describe blending of non-Newtonian fluids in a Kenics KM static mixer using PLIF. Poster presentation at 14th European conference on mixing (WARSAW, POLAND 2012).

Journal papers

ALBERINI F., M.J.H. SIMMONS, A. INGRAM, E.H. STITT. Use of an areal distribution of mixing intensity to describe blending of non-Newtonian fluids in a Kenics KM static mixer using PLIF. AIChE journal (accepted) (2014)

ALBERINI F., M.J.H. SIMMONS, A. INGRAM, E.H. STITT. Effect of system and fluid parameters upon the blending of shear-thinning fluids in a KM static mixer. Chemical Engineering Science journal (submitted) (2014)

CHAPTER 2

2. LITERATURE REVIEW

2.1. Introduction

This chapter contains a review of the current literature on the fundamentals of mixing of non-Newtonian fluids and on the various methodologies which can be applied to characterise mixing in equipment relevant to this thesis. In the first section of this chapter, a review of the rheological behaviour of different fluids is presented focusing on non-Newtonian fluids. After, a detailed description is given of mixing mechanisms which occur as a function of flow regime. The literature on batch and continuous mixing processes are compared and different approaches to the measurement of mixing performance are presented. Methods to quantify mixing performance are reviewed focusing on alternative methods to determine scale and intensity in addition to the different measurement techniques which can be used. Finally an

overall summary of the available literature on the operation and performance of static mixers for different applications is given.

2.2. Fluid mechanics fundamentals

2.2.1. Newtonian fluids

In continuum mechanics, a fluid is deformed as it flows due to applied external forces. Frictional effects are exhibited by the motion of molecules relative to each other, this friction exhibits itself through the fluid's dynamic viscosity which is a bulk fluid property (Chemical Engineering Volume 1). A Newtonian fluid is defined as a fluid whose dynamic viscosity (μ) is constant, which implies a linear relationship between the applied shear stress (τ) and the observed shear rate ($\dot{\gamma}$). It can be shown that at the limit of small angular deformations, the shear rate is equivalent to the velocity gradient in the flow (Chemical Engineering Volume 1) this leads to Newton's law of viscosity, written below for 1-D flow in the x direction shown in Figure 2.1. :

$$\frac{F}{A} = \tau = \mu \left(-\frac{dV_x}{dy} \right) = \mu \dot{\gamma} \quad (2.1)$$

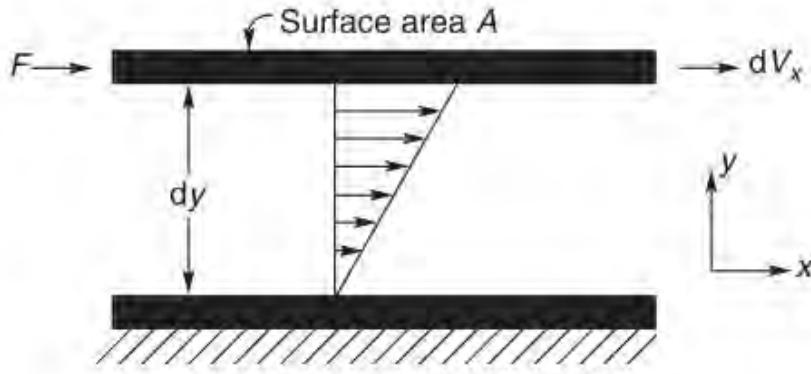


Figure 2.1 Schematic representation of unidirectional shearing flow (Chhabra et al., 2008).

More precisely, a fluid is Newtonian if, and only if, the tensors that describe the viscous stress and the strain rate are related by a constant viscosity tensor that does not depend on the stress state and velocity of the flow (Rheology - Principles, Measurements and Applications).

$$\tau = -p \begin{bmatrix} 1 & 0 & 0 \\ 0 & 1 & 0 \\ 0 & 0 & 1 \end{bmatrix} + \mu \begin{bmatrix} 0 & \dot{\gamma} & 0 \\ \dot{\gamma} & 0 & 0 \\ 0 & 0 & 0 \end{bmatrix} \quad (2.2)$$

If the fluid is not compressible the tensor of the stress is simplified as in (2.1) and the viscosity tensor reduces to two real coefficients, describing the fluid's resistance to continuous shear deformation and continuous compression or expansion, respectively. Newtonian fluids are the simplest mathematical models of fluids that account for viscosity. Although no real fluid fits perfectly with the definition, many common fluids, such as water, glycerol and glucose syrup can be assumed to be Newtonian for practical calculations under ordinary conditions.

2.2.2. Non-Newtonian fluids

Unfortunately, many important fluids in the chemical industry display non-Newtonian behaviour at moderate rates of strain. The range of fluids is wide and includes polymer solutions, which have very large molecular weights and form long chains that give a shear thinning or thickening behaviour, as well as emulsions and slurries containing suspended particles which may or may not be deformable. These liquids do not respect Newtonian behaviour in several ways but the most easily quantified is the nonlinear function of shear stress with shear rate. In polymer solutions this effect depends upon the history of the local strain rate experienced by the fluid due to elastic properties leading to a time-dependent effect; this manifests itself more strongly with increasing polymer concentration and lengthens the relaxation times of the polymer chains within the fluid. However, some fluids do not experience time-dependent behaviour and thus their flow rheology can be expressed simply in terms of constitutive laws or equations which are non-linear relationships between the shear stress and shear rate. Thus non-Newtonian fluids can be classified as either time-dependent or time-independent.

2.2.2.1. Time dependent

When the flow behaviour of a non-Newtonian fluid is dependent not only upon the shear rate but also on the time, a simple constitutive equation cannot be used. Examples of these materials are pastes (high solids fraction suspensions of solids in liquid), crude oils and certain foodstuffs where their apparent viscosities gradually change with the time due to changes in the internal microstructures of the material. Time-dependent fluid behaviour may be further sub-divided into two categories: thixotropy and rheopexy or negative thixotropy shown in Figure 2.2.

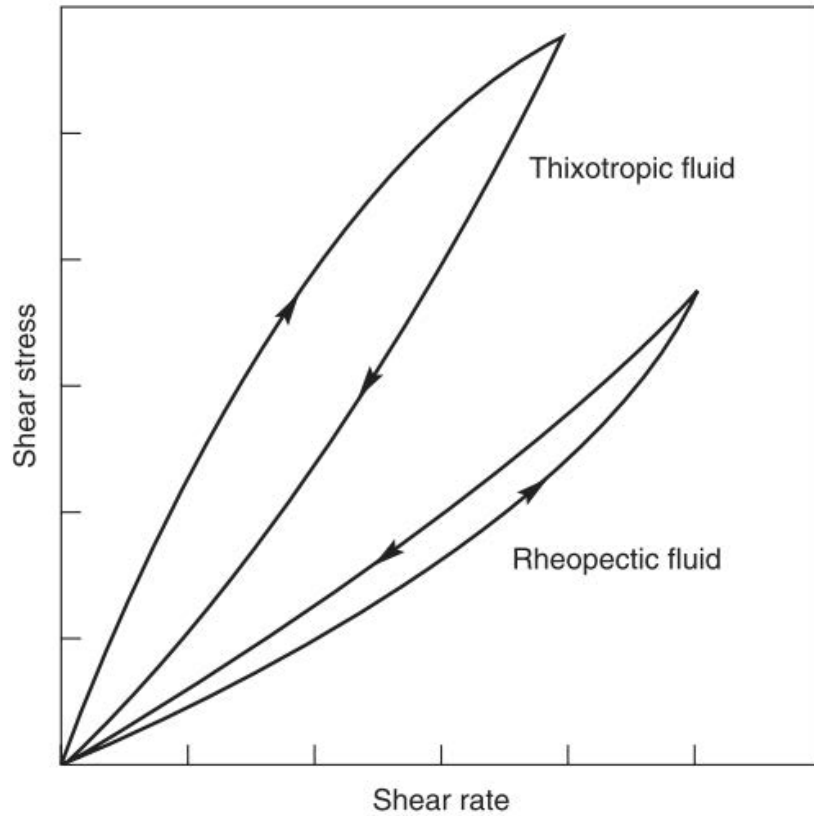


Figure 2.2. Schematic of shear stress shear rate behaviour for time-dependent fluids (Chhabra et al., 2008).

A material shows a thixotropic behaviour if, when it is sheared at a constant rate, its apparent viscosity (or the corresponding shear stress) decreases with the time. However, when the apparent viscosity increases with time of shearing, these fluids are said to display rheopexy or negative thixotropy (Keller *et al.*, 1990) (Pradipasena *et al.*, 1977). Fluids which show rheopexic behaviour can be found in different applications from printer inks to drilling muds in geothermal applications.

2.2.2.2. Time independent

Non-Newtonian fluids present a time independent behaviour, where the apparent viscosity is not related to time and changes only as a function of the applied shear rate. Generally the group is sub-divided in three categories: shear thinning, shear thickening and viscoplastic fluids.

- Shear thinning fluids

Shear thinning or pseudo-plastic fluids represent the most common type of time-independent non-Newtonian fluid behaviour. Their characteristic behaviour is described by the decrease of the apparent viscosity with the increasing of shear rate (Boger *et al.*, 1977). The most common constitutive equation used to describe the behaviour of a shear thinning fluid is the power law, which relates the shear stress to the shear rate as:

$$\tau = K\dot{\gamma}^n \quad (2.3)$$

where K and n are the consistency and flow indices, respectively ($n < 1$ for a shear-thinning fluid)(see Figure 2.3).

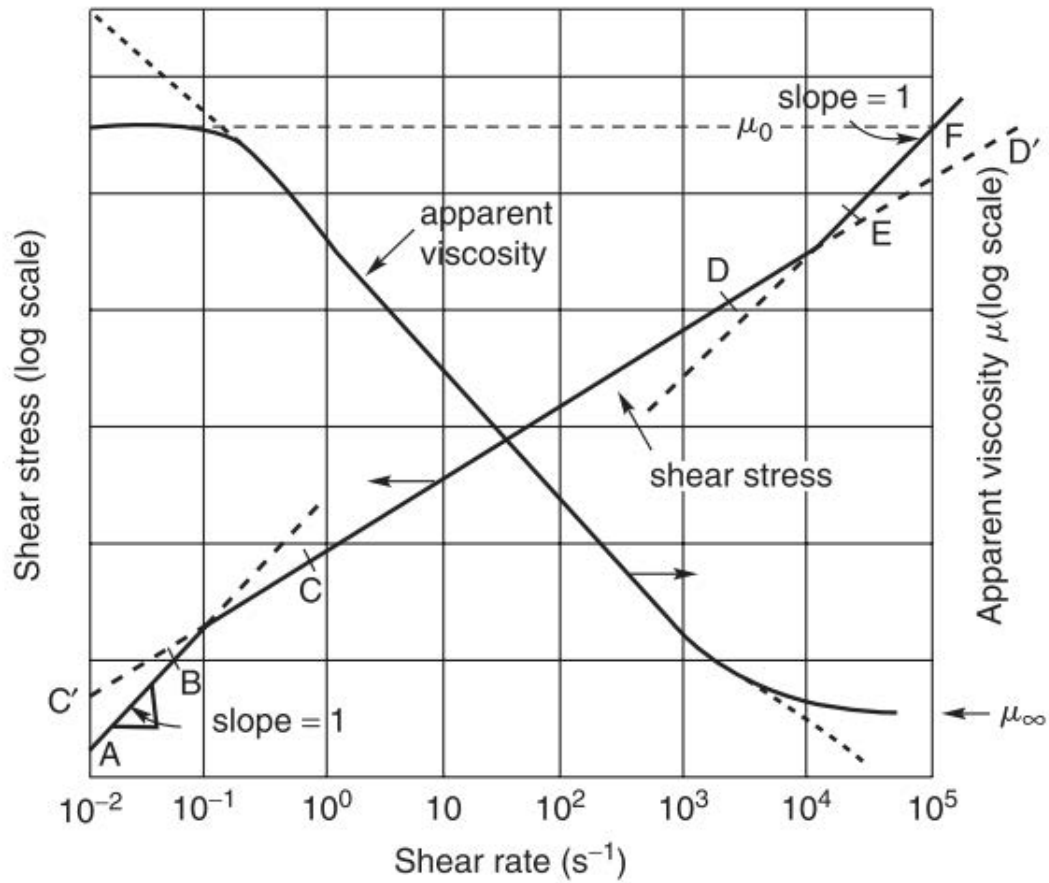


Figure 2.3 Schematic shear stress shear rate behaviour for shear thinning fluid (Chhabra et al., 2008).

A large number of alternative constitutive equations can be used and are reported in the literature; examples of the most common ones are reported in table 2.1 below.

Table 2.1 constitutive equations to describe shear thinning fluids

Name	Equation	Description
Carreau	$\frac{\mu - \mu_\infty}{\mu_0 - \mu_\infty} = \left[1 + \left(\lambda \dot{\gamma} \right)^2 \right]^{\frac{n-1}{2}}$	This model can describe shear thinning behaviour over wide ranges of shear rates based on four parameters. Newtonian fluid behaviour can be also described when $\mu = \mu_0$, $n=1$ or $\lambda = 0$ or both. (generally $n < 1$ and λ is a fitting parameter)
Ellis	$\mu = \frac{\mu_0}{1 + \left(\frac{\tau}{\tau_{1/2}} \right)^{\alpha-1}}$	μ_0 is the zero shear viscosity the index α is a measure of the degree of shear thinning behaviour (the greater the value of α , greater is the extent of shear-thinning), $\tau_{1/2}$ represents the value of shear stress at which the apparent viscosity has dropped to half its zero shear value
Cross	$\frac{\mu - \mu_\infty}{\mu_0 - \mu_\infty} = \frac{1}{1 + k \left(\dot{\gamma} \right)^n}$	$n < 1$ and k are the fitting parameters. This model reduces to the Newtonian fluid behaviour when $k = 0$ and when $\mu = \mu_0$, it reduces to power-law model.

- Shear thickening fluids

When the apparent viscosity increases with increasing shear rate, the fluid is called shear thickening or dilatant. Their properties can often be approximated by a power law equation (2.1), as for pseudo plastic fluids, but with values of power law index, $n > 1$. The term “dilatant” has also been used for suspensions where the particles and the liquid of the suspension play a critical role on the overall rheology.

- Visco-plastic fluids

In this thesis, the fluids used are represented by this group of time independent non-Newtonian fluids. The most common fluid model for visco-plastic behaviour is the Bingham model.

A Bingham fluid model is a visco-plastic material with a plug region in which the shear stress is less than the yield stress. The Bingham fluid model is the simplest constitutive equation in common use that describes a material that possesses a “yield stress”. The Bingham fluid is usually defined in a fully-developed one-dimensional flow in which there is only one velocity

component, v_x that is a function only of the transverse direction y (Lipscomb *et al.*, 1984)

where :

$$\dot{\gamma} = \frac{dv_x}{dy} \quad (2.4)$$

The shear stress tensor is described as:

$$\tau = \tau_0 \dot{\gamma} + \eta_0 \dot{\gamma} \quad \text{for } \tau > \tau_0 \quad (2.5)$$

$$\dot{\gamma} = 0 \quad \text{for } \tau < \tau_0 \quad (2.6)$$

Where τ_0 is the yield stress and η_0 is the slope of shear stress and shear rate curve. Another common model used to describe the rheological behaviour of shear thinning and visco-plastic fluids (due to the presence of yield stress) is the Herschel Bulkley model. It is a simple generalization of the Bingham plastic model, where the non-linear flow curve is defined by an equation containing three constants:

$$\tau = \tau_0 + K \dot{\gamma}^n, \quad (2.7)$$

K and n are the consistency and flow indices, respectively and τ_0 is the yield stress.

2.2.3. Rheological measurements

2.2.3.1. Shear viscosity measurement

A rheometer is the most common laboratory device which is used to measure the rheology behaviour of fluids. Different geometries can be used for the characterisation of different types of fluid. Cone and plate (Figure 2.4a) and parallel plate (Figure 2.4b) are the geometries used in this work which generally involve the use of single phase homogeneous samples. The main difference between these two geometries is the gap between the plate and the sample platform. When the analysed fluid presents a non-Newtonian rheological behaviour the cone and plate geometry has to be used because the gap changes as a function of the angle α which allows a constant shear along the whole sample (see Figure 2.4a).

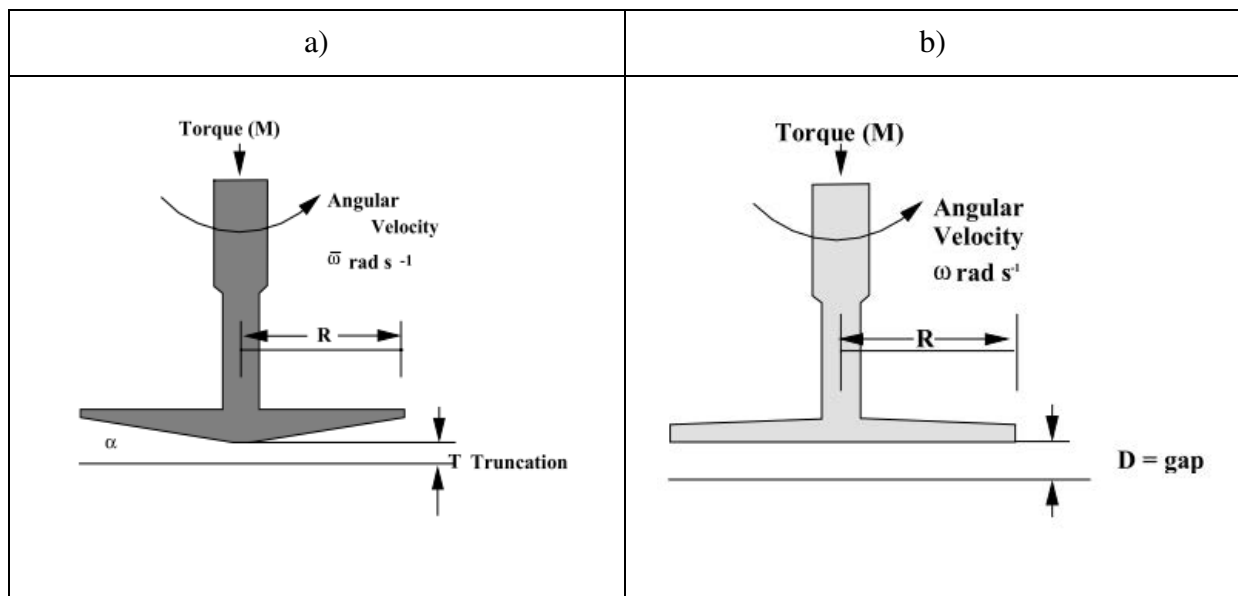


Figure 2.4 Selected rheometer geometries: a) Cone and plate (AR 1000 manual), b) parallel plate. Parameters defined in this Figure are used in Table 2.2 below

To analyse the sample; either a controlled shear stress or shear rate can be applied to obtain the behaviour under shear whereas some rheometers apply an extensional stress to determine

the extensional viscosity of the fluid. In Table 2.2 the shear rate and stress factors are presented for both selected geometries.

Table 2.2 Shear rate and stress factors.

Cone and plate	Shear rate = $F_y \omega$; where $F_y = 1/\tan(\alpha)$
	Shear stress = $F_\sigma M$; where $F_\sigma = 3/(2\pi R^3)$
Parallel plate	Shear rate = $F_y \omega$; where $F_y = R/\text{gap}$
	Shear stress = $F_\sigma M$; where $F_\sigma = 2/(\pi R^3)$

Another apparatus used for the determination of rheology is the capillary rheometer which is based on controlled extrusion of a test material. From material flow and deformation properties the rheology is characterized under conditions of high force (or pressure), high shear rate and at elevated temperature. Different capillary dies are mounted with precise dimensions and allow simultaneous determination of shear and extensional viscosity. The basics of this measurement can be linked to knowledge of the capillary die dimensions, piston speed and pressure. As Hanks (1979) has shown, it is possible to develop a series of graphical charts which can be used to carry out process design calculations such as to predict the pressure drop (ΔP) for a given flow system or, conversely to estimate the volumetric flow rate (Q) for a given pipe-pump combination, for the laminar flow of Herschel-Bulkley fluids in a concentric annulus.

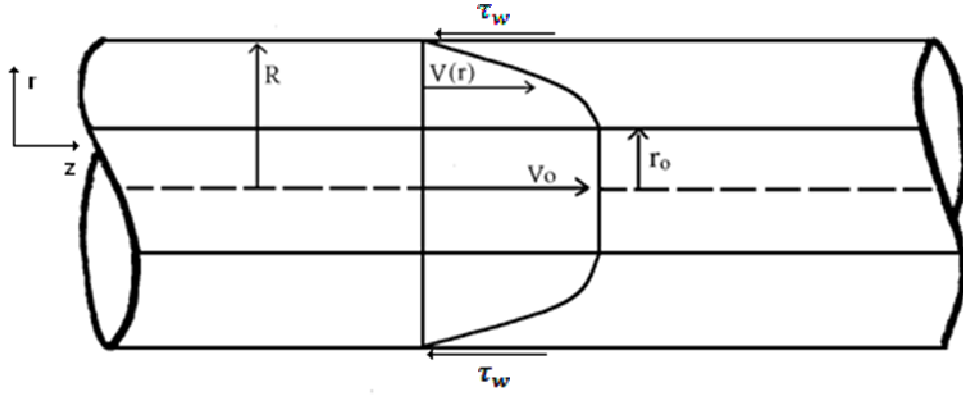


Figure 2.5 Flow of a Herschel-Bulkley fluid down a cylindrical pipe of constant diameter

For flow down a pipe, performing a force balance enables calculation of wall shear rate,

$$\gamma_w = \left(\frac{dV_z}{dr} \right) \text{ (2.8) and wall shear stress, } \tau_w = k \left(\frac{dV_z}{dr} \right)_w^n \text{ as:} \quad (2.9)$$

$$\tau_w = \frac{\Delta P}{L} \times \frac{d}{4} \quad (2.10)$$

$$\gamma_w = \left(\frac{3n+1}{4n} \right) \times \frac{32Q}{\pi d^3} \quad (2.11)$$

From eq. (2.10) and eq. (2.11) an apparent viscosity has been obtained (2.12) that allows to characterize the fluid with a Reynolds number.

$$\mu = \frac{\tau_w}{\gamma_w} \quad (2.12)$$

Finally the eq. is how the Q , flow rate, is correlated to the pressure drop, yield stress, consistency Index and power law index.

$$Q = \frac{8\pi L^3}{\Delta P} \times \frac{1}{k^{1/n}} \times \left[\frac{n}{3n+1} \times \left(\left(\frac{\Delta P}{L} \times \frac{R}{2} \right) - \tau_0 \right)^{\frac{3n+1}{n}} + \frac{2\tau_0 n}{2n+1} \times \left(\left(\frac{\Delta P}{L} \times \frac{R}{2} \right) - \tau_0 \right)^{\frac{2n+1}{n}} + \frac{\tau_0^2 n}{n+1} \times \left(\left(\frac{\Delta P}{L} \times \frac{R}{2} \right) - \tau_0 \right)^{\frac{n+1}{n}} \right] \quad (2.13)$$

2.2.3.2. Extensional viscosity measurement

In addition to the shear viscosity, extensional viscosity is another important parameter. Whilst in shear flow the liquid elements move over each other, for extensional flow the liquid elements flow away from the other. The extensional viscosity rheometer is based on the analysis of the stretching of a liquid filament. Most of common rheometers which measure extensional viscosity are equipped with a camera synchronized with a force transducer in order to measure the filament diameter with time and determine the corresponding stress applied to the fluid. The extension of a filament is not easy to induce in some liquids because it is difficult to maintain the shape of a stream of low viscosity liquid and stretch it in a normal operational condition. Extensional flow can be easily observed for substances having high viscosity. However, the most popular and important materials for studying extensional flows are polymer melts or concentrated solutions. The ability to stretch and to form fine filaments or thin films is a very special rheological property of polymers due to the viscoelastic properties of the material (Rheology Concepts, Methods, and Applications). It is easy to imagine why polymeric substances can be stretched: the extension of polymeric filament leads to alignment of macromolecules and creates a dominating orientation of matter. It results in increasing resistance to further deformation of this stress-induced macromolecular structure. The extensional viscosity is the net tensile stress, σ_E , divided by the rate of deformation, $\dot{\epsilon}$. As for the shear viscosity, the extensional viscosity is not constant for non-Newtonian fluids. Although the shear viscosity changes with the shear rate, the extensional viscosity is modified by variation of stress, due to decreasing of the diameter of the filament at constant deformation rate. For uniaxial extensional flow (Sridhar *et al.*, 1991) when a filament is stretched at constant deformation rate the fluid velocity in the direction of the flow it is proportional to the deformation rate.

$$v = \varepsilon x \quad (2.14)$$

where the x is the direction of the flow. Furthermore, the velocity of the motorized stage is equal to dl/dt which is the variation of the filament length versus time. Rewriting the previous equation the correlation between the filament length and the deformation rate is described by:

$$\frac{dl}{dt} = \varepsilon \times l \quad (2.15)$$

By integrating the eq.(2.13), it is found that the length has an exponential increase with time.

$$l = l_0 \exp\left(\frac{\varepsilon \times t}{2}\right) \quad (2.16)$$

As expected, the radius of the filament decreases exponentially with time.

$$r = r_0 \exp\left(-\frac{\varepsilon \times t}{2}\right) \quad (2.17)$$

When a filament it is stretched in axial direction and a force transducer is used to measure the instantaneous force, experimental values of extensional viscosity can be calculated.

In order to measure experimentally the total stress applied on the filament, a force balance has to be considered in axial and in radial direction.

$$\sigma_a = \frac{F_0}{A} - \rho g z - \frac{2\gamma}{r} \quad (2.18)$$

$$\sigma_r = \frac{\gamma}{r} \quad (2.19)$$

where F_0 is the force measured at time t , ρ is the density of the liquid, g gravitational acceleration, z is $l/2$ and γ is the surface tension.

The extensional viscosity is defined as:

$$\eta_e = \frac{(\sigma_a - \sigma_r)}{\dot{\epsilon}} \quad (2.20)$$

$$\eta_e = \left(\frac{F_0}{A} - \rho g z - \frac{\gamma}{r} \right) \times \frac{1}{\dot{\epsilon}} \quad (2.21)$$

Usually the variation of the extensional viscosity in function of rate of deformation is analysed to identify the viscous-elastic nature of the material. Other important feature of this analysis is the possibility of determination of the energy spent for the stretching and breakage of the filament. Using the data obtained from the force transducer, and knowing the velocity with which the filament is stretched the power is calculated as:

$$P = \frac{(\sigma_a - \sigma_r)}{v} \quad (2.22)$$

The study of the features of the extensional flow is subject of interest in many recent works in order to understand the complex nature of non-Newtonian fluids. An example is the effect on the mass transfer diffusion for a unsteady extensional creeping flow where the deformation of a drop was the cause of increase of mass transfer (Favelukis *et al.*, 2013). The understanding of this mechanism applies to many processes; indeed it is relevant for the operation of inkjet printing, coating processes and drug delivery systems, as well as the generation of micro droplets (Galindo-Rosales *et al.*, 2013).

2.3. Mixing Fundamentals

Two basic mechanisms are responsible for fluid mixing: diffusion and advection. Advection, that is the transport of matter by a flow, is required for mixing. The quality of the mixing is in function of the energy input in the system which, in flow, increases with the gradient of pressure between two different points in the system. The pressure gradient has a direct consequence on the bulk flow promoting the mixing of the fluids. In fluid mechanics to identify which of the two mechanisms is predominant a non dimensional number called Schmidt number (Sc) is used. It was named after the German engineer Ernst Heinrich Wilhelm Schmidt (1892-1975). Schmidt number is a dimensionless number defined as the ratio of advection (kinematic viscosity) to diffusion (molecular diffusion), and it is used to characterize fluid flows in which there are simultaneous momentum (advection) and mass diffusion convection processes. The higher the Schmidt number's, is the higher is the contribution of advection compared to the molecular diffusion. In liquids, molecular diffusion alone is not efficient for mixing since they possess comparatively low diffusivity values, thus for liquid mixing $Sc \gg 1$. The mixing of fluids is dependent upon the flow regime, i.e. whether the flow is laminar or turbulent, which can be determined according to the value of the Reynolds number, which is the ratio of inertial to viscous forces.

$$Re = \frac{\rho u D}{\mu} \quad (2.23)$$

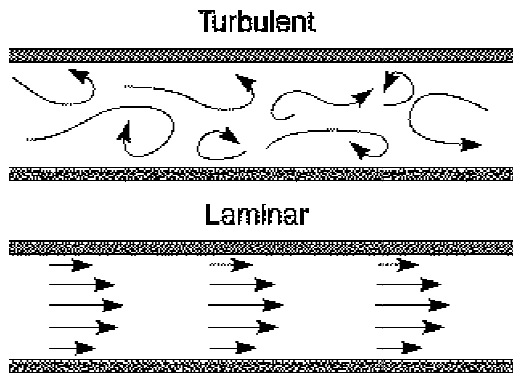


Figure 2.6 Schematic of turbulent and laminar flow in a pipe

2.3.1. Laminar flow

The laminar regime prevails at low flow velocities where the pressure-velocity relationship is a function of the viscous properties of the fluid. Laminar flow is also referred to as streamline or viscous flow. In laminar flow, layers of fluid flow over one another at different speeds with virtually no mixing between layers (Figure 2.6). This mixing mechanism generates a poor mixing environment, because fluid motion is dominated by linear, viscous forces instead of non-linear inertial forces. If the forcing is time-independent, fluid particles can follow concentric, closed streamlines, and that can mean it is possible to characterise and predict the fluid dynamic properties of the mixing equipment more easily than in turbulent flow. In the past the main problem of using laminar mixing was very poor efficiency of mixing, but static mixers enable this limitation to be overcome by employing chaotic mixing mechanisms (see § 2.2.2 below). The flow in a straight pipe is a typical example of steady, non-chaotic flows. This problem is two dimensional, since the geometry possesses complete angular symmetry. The velocity v is a function of the radius of the pipe r and when:

$$v(r)=v(R), \quad (2.24)$$

velocity is zero due to the no-slip condition. It is well established that laminar flow of a Newtonian fluid produces a steady parabolic velocity profile within the pipe. If two different

fluids have to be mixed and they are injected from two different inlets inside a pipe without diffusion, the streamlines of the fluids remain confined because they flow parallel along the pipe. Due to diffusion, mass transfer takes place on the interface between the two different fluids, but for viscous flows this effect is confined to very small length scales for typical processing times.

2.3.2. Chaotic flow

Chaotic flow involves the stretching and folding of fluid elements in laminar flow which enables the interfacial area between elements to grow at an exponential rate, as opposed to the linear growth rate which would normally be expected in laminar (shear) flow. Numerous experimental and computational examples have shown that real fluid flows can produce the type of stretching and folding that leads to chaos (Ottino, 1990). Chaos is impossible in steady flow because it is completely characterised by time-invariant streamlines that coincide with path lines, and fluid elements lie within the same streamlines at all times. In fluid flows, a necessary but not sufficient condition for chaos is "streamline crossing" of two streamline portraits taken at arbitrary times. The crossings can create a special type of folding which is the preliminary step for mixing using a chaotic mechanism. The other condition created by the chaos is the stretching which can generate results in effective mixing within chaotic regions if it is accompanied by folding. Ottino (1992) stated that mixing can be described in geometrical terms which is an idea proposed in a lecture-demonstration by Osborne Reynolds in 1894. However, the mixing needs not to be widespread. In general, poorly mixed regions known as Kolmogorov-Arnold-Moser (KAM) islands, coexist with well-mixed chaotic regions. The Poincare maps were largely used to characterize the chaotic mixing (Ling, 1993). This theory is based on one of the best-known findings in chaos theory which is the

periodic windows of one-dimensional maps. Other two important properties of chaotic systems make them excellent for mixing: these are the exponential divergence of nearby particle trajectories and the irregular frequency distribution of stretching.

Considering the Lyapunov theory (Eden *et al.*, 1991), in a chaotic system the distance separating two fluid particles initially located very close to one another will diverge exponentially with time. Considering that the objective of any mixing operation is to disperse clusters of material, exponential divergence of clusters of material that are initially close to each other is extremely desirable for mixing applications. As Gelaro *et al.* (2002) report in their work, the traditional linear stability analysis focuses the attention on the asymptotic growth of infinitesimally small perturbations as a fundamental measure of the instability. In the mixing field, the perturbations may be regarded as a measure of diffusion or advective mixing that changes from the initial conditions to the point where it is analysed. If one considers perturbations growing on a time-dependent basic state, as in a realistic model of the atmosphere, then the leading Lyapunov exponent is the relevant measure of asymptotic mixing growth. To summarise all in an equation, if the initial distance between two particles is represented by an infinitesimal vector of length l_0 and l_n is the length at a later time t_n the stretching of a fluid element, denoted by λ grows as:

$$\lambda = \frac{l_n}{l_0} = e^{\Lambda t} \quad (2.25)$$

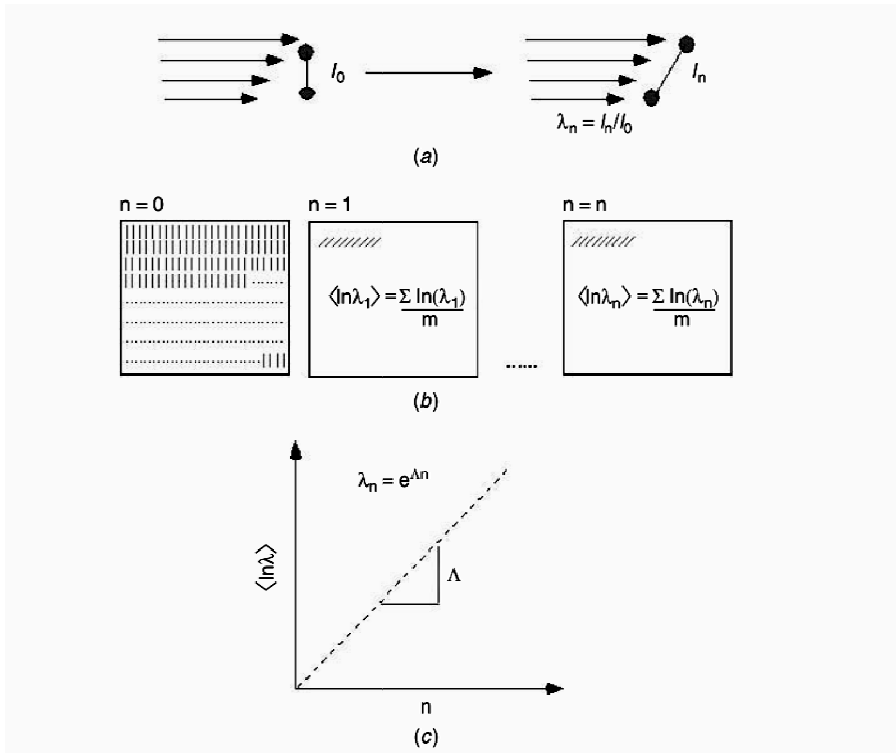


Figure 2.7 Stretching field and Lyapunov exponent (Paul et al., 2004).

In figure 2.7 (a) a small material filament, represented by a vector l_0 , is convected by a flow. As a consequence, its length increases from the initial l_0 to l_n . The stretching (λ) experienced by the material after each period n is the ratio l_0/l_n . In figure 2.7 (b) an array of small vectors is placed in the flow, and the stretching of each is measured and an average λ can be calculated. In fig.2.7 (c) chaotic flow, λ grows exponentially, and the exponent characterising the growth rate (the Lyapunov exponent) can be calculated from the slope of the curve $\ln(\lambda)$ versus n .

2.3.3. Turbulent flow

The turbulent flow regime prevails at high value of Reynolds number. Turbulent flow is characterized by irregular movement with a non-deterministic path which is intrinsically

time-dependent. The fluid travels in irregular paths with non-observable patterns and no definite layers. The velocity field is non-steady, which implies a continuous reorientation of fluid particles along Lagrangian trajectories. Below a critical velocity, oscillations in the flow are unstable and any disturbance quickly disappears and the flow follows straight stream lines (Figure 2.6).

Flow is governed primarily by the inertial properties of the fluid in motion. A fluid in turbulent flow is subject to random fluctuations in terms of velocity and direction. Turbulent flow commences only when local Reynolds number exceed a critical value, creating in the system the coexistence of different regimes. Considering an empty pipe, there are three separate flow regimes across the diameter of the pipe: laminar flow next to the wall, where the velocity is below the critical value; a central core of turbulent flow, and a transitional zone between the two.

Most of the flow equations are empirical but they are currently used for the understanding and characterisation of such complex phenomenon. The most common is the Fanning friction factor which is proportional to the ratio of shear stress at the wall divided by the density and the square of the velocity. This parameter is commonly used to determine pressure drop in pipes and also static mixers, by use of adjustable empirical constants.

2.4. Mixing equipment

The mixing of liquids is a key operation in which two or more miscible liquids are mixed together to reach a certain degree of homogeneity (Paul et al., 2004). Mixing is ubiquitous for the manufacture of a wide range of products starting from food, personal care, home care and expanding to the production of catalysts. Blending may take place between high or low viscosity liquids, miscible and immiscible fluids (e.g. emulsions, foams). The mixing of fluids is generally achieved using either batch or continuous processes. In batch processes,

stirred tanks and similar devices are used to blend fluids where the impeller generates the fluid motion. The amount of time required to reach the degree of homogeneity desired is known as the blend time or residence time which is the time spent by the fluids inside the tank before being mixed. Static mixer or similar devices are used for continuous processes where fluids are pumped through mixing elements installed inside pipes. Whilst the flow regime of the system can be determined using the Reynolds number, this approach is more complicated when non-Newtonian fluids are used since the viscosity is not constant. Liquids with low viscosities are generally mixed in the turbulent flow regime (Nienow, 1997) (Kumar *et al.*, 2008). In comparison, for highly viscous fluids a certain shear force may be needed in order for uniformity to be reached. Mixing of viscous liquids typically occurs in the laminar flow (Alvarez *et al.*, 2002b) regime and stagnation points, known as islands of unmixedness, may form (Perry *et al.*, 1997). Due to the complexity of the geometry usually the range of Reynolds numbers which determine different regimes are different between static mixer and stirred tank (Chandra *et al.*, 1992).

2.4.1. Mixing of non-Newtonian fluids in batch processes – stirred vessels

Most of the chemical production involves the use of mechanically agitated stirred vessels for manufacturing. Understanding of the behaviour of stirred tanks has received considerable research effort over the last few decades. Unfortunately, most of the fluids used in industry have a non-Newtonian behaviour; research has generally focused (although not exclusively) on the blending of single and multiphase low viscosity fluids in the turbulent flow regime. This area is not the focus of this study and hence this review will focus on the relatively limited number of works performed for viscous mixing of non-Newtonian fluids. As mentioned several times previously in this thesis, the rheology of non-Newtonian fluids complicates the study of fluid dynamics or the mixing performance of any system where they

are applied. The fundamental mixing mechanism for these vessels is via the transfer of momentum to the material within the vessel via the physical movement of rotating impeller blades. Stirred tanks containing non-Newtonian fluids have been studied in gas liquid systems (Tecante *et al.*, 1993) or even in three phases (gas-liquid-solid) (Kawase *et al.*, 1997). The huge variety of processes carried out in stirred vessels span a wide range of vessel sizes and geometries for optimal process efficiency. A standard nomenclature exists to describe the dimensions of a vertical cylindrical tank. The height where fluid is filled, H, tank diameter (T), impeller diameter (D) and the clearance from the tank bottom (C), are the parameters used for standard configurations in terms of geometric ratios such as D/T, C/T etc. In the last few years more studies have been devoted to the fluid dynamics of non-Newtonian fluids. Different impeller types have been investigated to understand which one is more suitable for high mixing performance. Usually the behaviour of Newtonian fluids is compared to non-Newtonian ones (Aubin *et al.*, 2000) in order to elucidate the difference between the two systems. For fluids which present a non-Newtonian behaviour, research has been performed to obtain the shape of stagnant and moving regions within the vessels (due to the formation of caverns) which can occur in the blending of viscoplastic and also pseudoplastic fluids. (Hirata *et al.*, 1994) (Galindo *et al.*, 1992). A further study investigates the cavern size using both experimental and computational approaches (Adams *et al.*, 2007). The technique of particle image velocimetry (PIV, see later §3.3.1) is largely used to investigate the fluid dynamic of stirred tank but also alternative techniques are applied in particular when the used fluids are opaque (Fangary *et al.*, 1999) (Simmons *et al.*, 2007).

2.4.2. Mixing Of Non- Newtonian Fluids In Continuous Processes- Static Mixers

Since in liquids the mixing obtained by diffusion is poor, it is necessary to design mixers which introduce chaos to the flow if the regime is laminar. This is the basis of operation of static mixers which are the focus of this thesis. The mechanism in all static mixers is quite similar where a periodic forcing of the fluid stretches and folds the fluid streamlines. The most common application is the mixing of shear sensitive fluids such as polymers, where the fluids are mixed under very gentle process conditions. The dispersion of gases and liquids in highly viscous fluids is also another characteristic application of this device. The flow inside the static mixer is characterised by an exponential rate of stretching and also reorientation due to repeated changes in flow direction (hence for this reason it is called chaotic mixing, see §2.2.2). In the literature the actual first patent on a static mixer dates from 1874 where Sutherland describes a single element, multilayer, motionless mixer, used to mix air with a gaseous fuel (Meijer *et al.*, 2012). A static mixer is a device with no moving parts and it relies on the motion of the fluid, due to external pumping, to move fluids through it. The structures placed within the pipe and the static mixer elements divide, recombine, spread and rotate the fluids as they flow through the pipe. Process factors considered in static mixer design and configuration are pressure drop, heating or cooling requirements, length of piping, flow rates, fluid viscosities and densities. There are several advantages in the use of static mixers compared to motorized mixer systems. The required energy for the blending in static mixers comes from the pumping power necessary to move fluids. Residence times are typically short in a static mixer, making it ideal for fast blending requirements. Static mixers are installed as easily as a typical segment of pipe and maintenance and space requirements are minimal. In many cases, mixing in pipelines is better and more economical than in

vessels. In particular, continuous large-scale mixing of multiple process streams is easily accomplished using a static mixer arrangement.

The first applications of static mixers in industry began in the 1970s. Before that investigations of continuous processes were mostly restricted to academic research. During the last 10-15 years, many industries have moved from batch to continuous processes to reduce cost of utilities and space requirements for production. The flexibility of production is also another important factor which addresses the development of inline mixing. Static mixers for process industry applications were initially developed for blending of fluids in laminar flow (Grace, 1982) and applications in heat transfer; turbulence and multiphase systems were implemented much later (Baladyga, 2001). The operation and design of static mixers are discussed in key texts, for example “Mixing In The Process Industries” by Nienow *et al.* and the “Handbook of Industrial Mixing” by Paul *et al.*; unfortunately most of the correlations are described only for the mixing of Newtonian fluids.

Two different criteria are used to judge the efficiency of static mixer: the first is energy consumption (measured in terms of the dimensionless pressure drop per unit length) and the second is its dimensions (measured in terms of length or number of elements). Most of the works, where the comparison of performance of static mixer has been reported, are concentrated on Newtonian fluids (Pahl *et al.*, 1980) (Rauline *et al.*, 2000) (Rauline *et al.*, 1998) (Meijer *et al.*, 2012). Extensive blending data have been collected by Wadley *et al.* (2005) for the Sulzer SMV, KM and HEV mixers in the transitional and turbulent flow regimes, using a laser-induced fluorescence (LIF) technique.

In the following Table 2.3 the main characteristics of static mixer versus stirred tanks are reported (showing the advantages of a continuous process).

Table 2.3. Comparison between features of static mixer and stirred tank for non-Newtonian fluids in laminar flow.

Static mixer	Stirred tank
Small space requirement	Large space requirement
lower power required for non-Newtonian fluids	High power consumption
Low equipment cost	High equipment cost
No moving parts except pump	Agitator drive and seals
Short residence times	Long residence times
Good mixing at low shear rates	Locally different ranges of shear rates



SMV



SMX



SMXL



SMF



HEV



HEV (turbulent mixer)



KM (laminar mixer)



KM (turbulent mixer)



KM (gas-liquid)



KM (liquid-liquid)

Lightnin static mixer

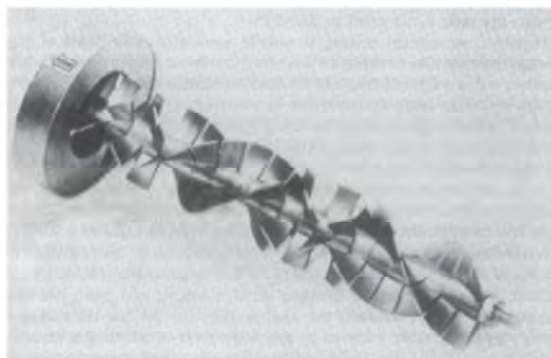


Figure 2.8 Selection of commercially available static mixers. (Arranged from Chhabra et al., 2008)

A selection of commercially available static mixer designs is shown in Figure 2.8 above. In the last few years many different companies and research groups have developed their own designs or investigated the possibility of modifications to existing geometries (Meijer *et al.*, 2012) (Anderson *et al.*, 2000) which has drastically increased the number of static mixer types available.

2.5. Measures of mixing performance

2.5.1. Measures to quantify scale

The scale of segregation measures the thickness or dimension of the fluid striations in the lamellar structure generated by chaotic flow. Different approaches can be found in the literature to characterise these patterns:

- Distribution of striation thicknesses;

For the characterisation of mixing performance for incompressible 2D chaotic flows, the distribution of striation thickness can be computed from the stretching distribution (Zalc *et al.*, 2002b) assuming that material filaments are stretched in one direction and simultaneously compressed in another direction at the same rate. Often the local micro-mixing intensity in chaotic flows is usually characterized by the distribution of striation thicknesses.

- Determination of stretching field;

Another approach is the determination of stretching field which characterise the elongation of fluid filaments in each region of a flow. As previously introduced in § 2.2.2, the Lyapunov exponent measures the average stretching of fluid filaments after an infinite amount of time. The larger the Lyapunov exponent is, the more efficient a mixing process is. Topological entropy follows a similar approach to the Lyapunov exponent measuring the average

stretching of fluid filaments but in a finite amount of time. The larger the topological entropy is, the more efficient a mixing process is.

- Determination of inter-material area density ;

An alternative approach is the inter-material area density which measures the amount of contact area between mixture components in each region of a flow.

2.5.2. Measures to quantify intensity

Generally the more commonly used approach for the classification of mixing is the study of intensity of segregation. Danckwerts (1952) suggested that the effect of incomplete mixing could be described by using statistical concepts which is the most common approach to define the intensity of segregation. The idea of representing mixing performance using statistical concepts was enhanced by Larosa *et al.* (1964) in the 1960s where in his experimental study he presents one of the first correlation based on Danckwerts' postulation. In the following decades many works have been developed with the aim of understanding and classifying the behaviour of chaotic mixing (Ottino, 1990) (Ottino *et al.*, 1992). In the literature there are many approaches for the calculation of the intensity of segregation (Paul *et al.*, 2004).

- Coefficient of variation and Log-variance;

The most popular method to describe the intensity of segregation is the coefficient of variation, CoV,. The CoV is defined as

$$CoV = \frac{\sigma}{\bar{C}} \quad (2.26)$$

where σ is the standard deviation and \bar{C} is the average of the property (e.g. concentration) used to characterise the mixing through the device. A similarly derived quantity is the Log-variance which is defined as:

$$\log Va = \log \sigma^2 = \log \left[\frac{1}{N-1} \sum_{i=1}^N [C-1]^2 \right] \quad (2.27)$$

where C is the normalised mixing quantity and N is the number of instantaneous measurements made on the mixing system.

- Segregation index;

Alternative approach to the CoV is the segregation index (Asmar *et al.*, 2002) which relates the degree of mixing to the standard deviation of mixing measure for different sample points. as:

$$I_s = \frac{\sigma^2}{\sigma_{MAX}^2} \quad (2.28)$$

where σ_{max}^2 is the variance for a completely segregated mixture and σ^2 is the variance of the system. In practical cases this is measured by taking a sufficient number of random samples of a specific size and calculating their variance e.g. by measurement of the spatial distribution of the concentration of a dye. This index has been widely discussed and used by several researchers (Aubin *et al.*, 2003) (Men *et al.*, 2007).

- Poincare plot;

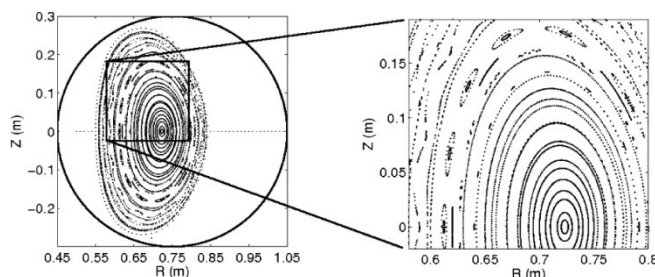


Figure 2.8 Example of Poincare plot (Schlutt *et al.*, 2012)

Another approach to determine the efficiency of the blending is the determination of mixing patterns by particle tracking (Poincare plots see Figure 2.13). This method applies the use of fluid tracer particles which are injected in the flow and their location is tracked during the mixing process by computational or experimental visualization methods. The efficiency of the mixing process is described by how rapidly the particles become dispersed in the system. The equations and methods which are commonly used to characterise the scale and intensity of segregation are summarised in Table 2.4 below.

Table 2.4 Summary of different approaches to quantify the scale and intensity

MEASURES OF SCALE OF SEGREGATION	
Striation thickness method	Measures of striation dimensions from image analysis or CFD data.
Lyapunov exponent method	Measure of stretching factor as: $\lambda = \frac{l_n}{l_0} = e^{\Lambda t}$ CFD data and turbulent experimental data.
Topological entropy method	Measure of an average stretching factor of in a finite amount of time. (Only CFD)
Inter-material area method	This measure is the amount of contact area between mixture components in each region of flow. Mostly applied using CFD but 2D images can also be used.
MEASURES OF INTENSITY OF SEGREGATION	
Coefficient of variation	$CoV = \frac{\sigma}{C}$
Log-variance	$\log Va = \log \sigma^2 = \log \left[\frac{1}{N-1} \sum_{i=1}^N [C-1]^2 \right]$
Segregation index	$I_s = \frac{\sigma^2}{\sigma_{MAX}^2}$
Poincare plots	Describe mixing patterns by particle tracking

Within the literature, these different approaches for the measurement of mixing performance have been discussed since the early 1950s. Most recently Kukukova *et al.* (2009) suggested in their work a new model to characterise mixing performance based on three key concepts: intensity of segregation, scale of segregation, and exposure. The main concern of this work is the need to provide not only one of measurements of the mixing performance (scale or intensity) but at least both. If only a single variable is considered, the analysis of mixing performance can give misleading conclusions. This issue is illustrated in Figure 2.10.

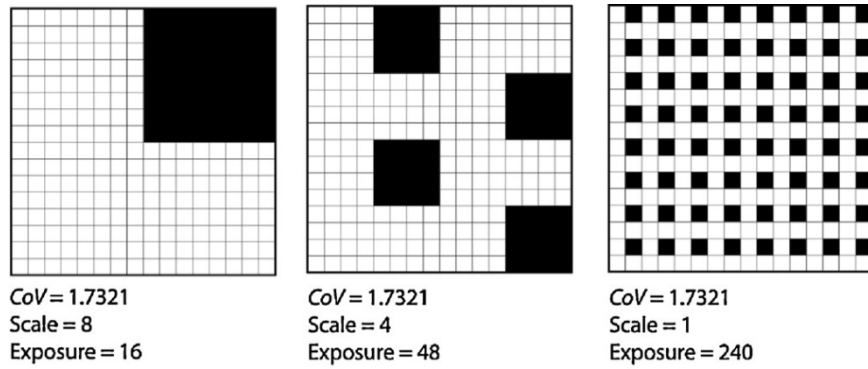


Figure 2.9 Three dimension of mixing: intensity of segregation, scale of segregation, and exposure (Kukukova et al., 2009).

Figure 2.10 shows checkerboard patterns, which are organised from left to right by scale of the pattern which is equal to the number of the neighbouring cells on one side of each black square. In the three checkerboards the intensity described with the coefficient of variation is constant. Other parameter is also defined, called exposure, which is the rate of reduction in segregation as:

$$E \cong \sum_{i=1}^{N_t} \sum_{j=1}^{N_b} \frac{1}{2} k' a_{ij} (C_i - C_j) \quad (2.29)$$

where N_t is the number of squares in check board, N_b is the number of the neighbouring squares, $k' = 1$ is the strength of the interaction, $a_{ij} = 1$ is the contact area per side, and $(C_i - C_j)$ is the concentration difference between two consecutive neighbours. A simple system was considered in this work: the concentration of the black squares is defined as $C_i = 1$, and for white squares as $C_i = 0$.

This figure 2.10 explains how the scale and the intensity are different in terms of what they are suitable to measure. Considering only the scale moving toward right of the figure, the mixing seems to improve; however considering only the intensity, the mixing performance does not change. Clearly, in this work it was suggested that all variables (intensity and scale)

play important roles in industrial mixing problems, and therefore they should all be considered to characterise different aspects of mixing performance. Kresta and her research group have carried out deep investigations to find an efficient and global method for the evaluation of mixing performance taking into account scale and intensity. One paper from her group (Kukuková *et al.*, 2008) investigates the application of spatial statistics methods in order to determine the effect of the sampling scale on the mixing performance. Two measures of mixing were used: the coefficient of variation CoV and the maximum striation thickness. For the evaluation of these parameters three sampling methods were tested, quadrats, probes and transects. In that work two CFD data sets were used as test cases: dispersion of floating particles in a turbulent stirred tank and laminar mixing of tracer particles in a micro-mixer. The objectives of the investigation were to explore the data resolution and sampling protocols needed to get accurate measures of CoV and striation thickness for ideal data sets, one turbulent and one laminar. Unsurprisingly, the information collected from the results of data sets gave, sometimes conflicting answers in term of which was the better method. In the turbulent regime, the dominant mechanism of advection is also called macro-mixing, which is better identified by the intensity of segregation (CoV). In laminar flow, micro-mixing is better identified by the scale of segregation which can be evaluated using the analysis of striation thickness. These works have been studied and the presented concepts have been used and elaborated in this thesis for the development of methodology which allows the classification of mixing in terms of scale and intensity.

2.5.3. Techniques used to obtain measures of mixedness

The understanding of blending for non-Newtonian fluids in static mixers has been developed more on the fluid dynamic aspects. Measured pressure drops as a function of rheology is a subject of research which has been developed in the last few decades thanks to the progress of rheometric measurements and pressure drop transducers. Another aspect of the research for the blending of non-Newtonian fluids in inline mixing is the study of mixing performance from the velocity field. The approach taken in general is to understand mixing as a function of the observed flow field rather than calculation of parameters which relate to mixing quality. The data generated has also been used to validate computer based simulations, for example using Computational Fluid Dynamics (CFD) (Adams *et al.*, 2007) (Peryt-Stawiarska, 2011). However there is not yet a clear idea how all this information can be related to the design of a rig for the blending of non-Newtonian fluids. In the following sections, the application of different flow visualisation methods used in mixing research are outlined. Not all of these are used in this thesis but they are included for completeness. The methods discussed include optical visualisation methods (Laser Doppler Anemometry (LDA), Particle Image Velocimetry (PIV), Planar Laser Induced Fluorescence (PLIF)) as well as nucleonic and spectroscopic methods (Positron Emission Particle Tracking (PEPT), Magnetic Resonance Imaging (MRI)).

2.5.3.1. Laser Doppler Anemometry (LDA)

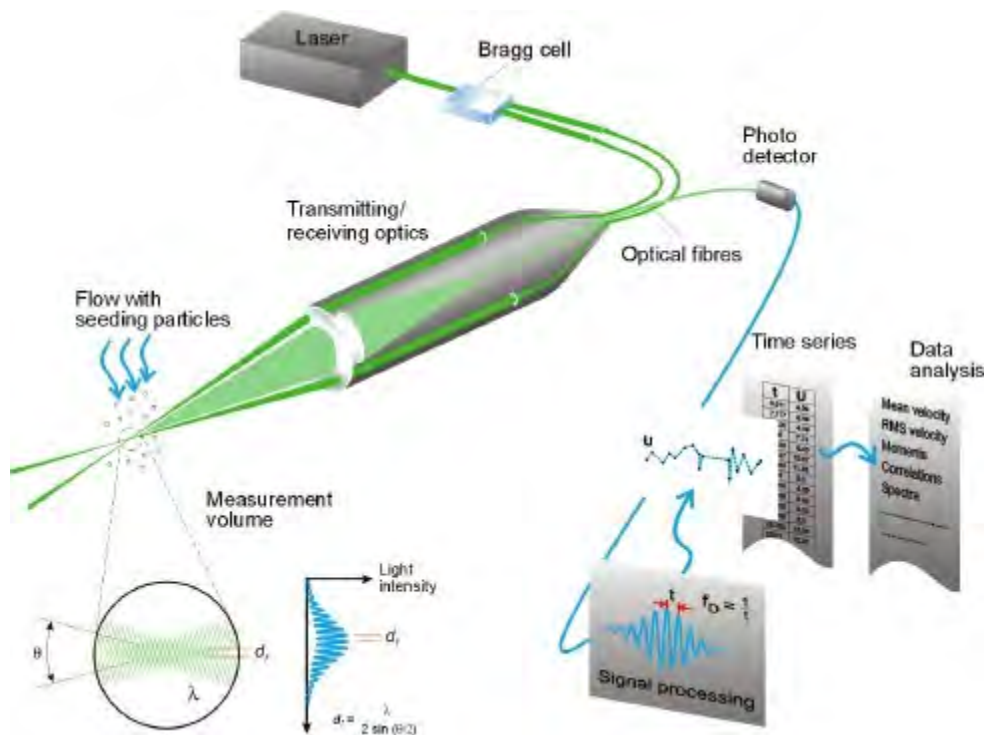


Figure 2.10 Laser Doppler Anemometry (LDA) (Dantec dynamics web site)

Laser Doppler Anemometry (LDA), uses the Doppler frequency shift caused by particles moving in a laser beam to obtain flow velocities in transparent or semi-transparent fluid flows. For this technique lasers with wavelengths in the visible spectrum are commonly used; these are typically He-Ne, Argon ion, or laser diode, allowing the beam path to be observed. The probe volume is typically in the order of millimetres long. The light intensity is modulated due to interference between the laser beams. This produces parallel planes of high light intensity called fringes. The fringe distance is defined by the wavelength of the laser light and the angle between the beams. As particles (either naturally occurring or induced) entrained in the fluid pass through the fringes, they reflect light that is collected by a photo detector. The photo-detector converts the fluctuating light intensity to an electrical signal, the Doppler burst, which is sinusoidal with a Gaussian envelope due to the intensity profile of the

laser beams. By combining three devices (e.g.; He-Ne, Argon ion, and laser diode) with different wavelengths, all three flow velocity components can be simultaneously measured. This technique was largely used in the 1980's in particular for the study of system in turbulence regime (Allan *et al.*, 1984) (Ku *et al.*, 1986) investigated the flow field of non-Newtonian fluids in the arteries determining the viscous-elastic effects on the flow using LDA. More recent works are concentrated on the study of the behaviour of non-Newtonian fluids in a conduit; starting from an empty pipe, which is the simplest geometry (Poole *et al.*, 2005), and arriving to the study of static mixer (Peryt-Stawiarska *et al.*, 2008) which is more relevant to the work presented in this thesis.

2.5.3.2. Magnetic resonance imaging (MRI)

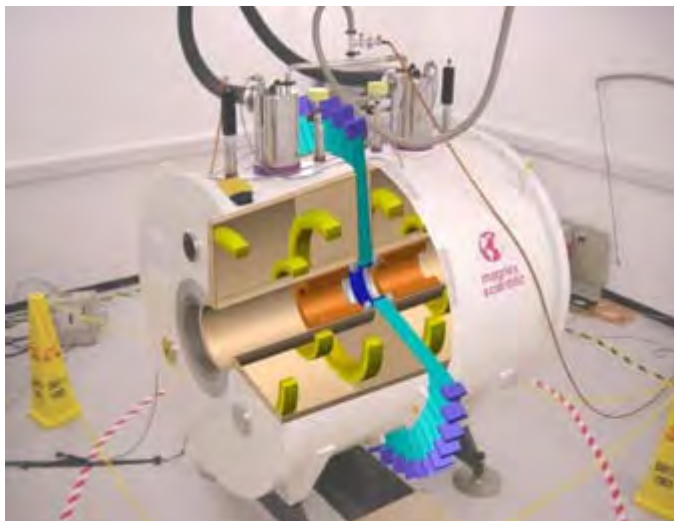


Figure 2.11 Magnetic resonance imaging (MRI)

Magnetic resonance imaging (MRI) is a medical imaging technique used in radiology to visualize internal structures of the body in detail. Many research groups use this technique for the flow visualisation in different geometries. MRI makes use of the property of nuclear magnetic resonance (NMR) to image nuclei of atoms inside the analysed system. An MRI scanner is a device in which the patient lies within a large, powerful magnet (Figure 2.12)

where the magnetic field is used to align the magnetization of some protons of the fluid, and radio frequency magnetic fields are applied to systematically alter the alignment of this magnetization. This causes the nuclei to produce a rotating magnetic field detectable by the scanner and this information is recorded to construct an image of the scanned area of the body. Magnetic field gradients cause nuclei at different locations to precess at different rates, which allows spatial information to be recovered using Fourier analysis of the measured signal. By using gradients in different directions, 2D images or 3D volumes can be obtained in any arbitrary orientation.

Tozzi *et al.* (2012) characterised the mixing performance of two viscous liquid streams in an in-line static mixer. The mixer is a split-and-recombine design that employs shear and extensional flow to increase the interfacial contact between the components. Using a non-Newtonian test fluid of 0.2% w/w Carbopol and a doped tracer fluid of similar composition, mixing in the unit is visualized using MRI. It is a very powerful experimental probe of molecular chemical and physical environment as well as sample structure on the length scales from microns to centimetres. Traditionally MRI has utilized super conducting magnets which are not suitable for industrial environments and not portable within a laboratory. Recent advances in magnet technology have permitted the construction of large volume industrially compatible magnets suitable for imaging process flows. The range of application of this technique is wide without any limitation on the complexity of the geometry of the system, other than the dimensions of the equipment being able to fit into the scanner which is a significant limitation.

2.5.3.3. Positron emission particle tracking (PEPT)

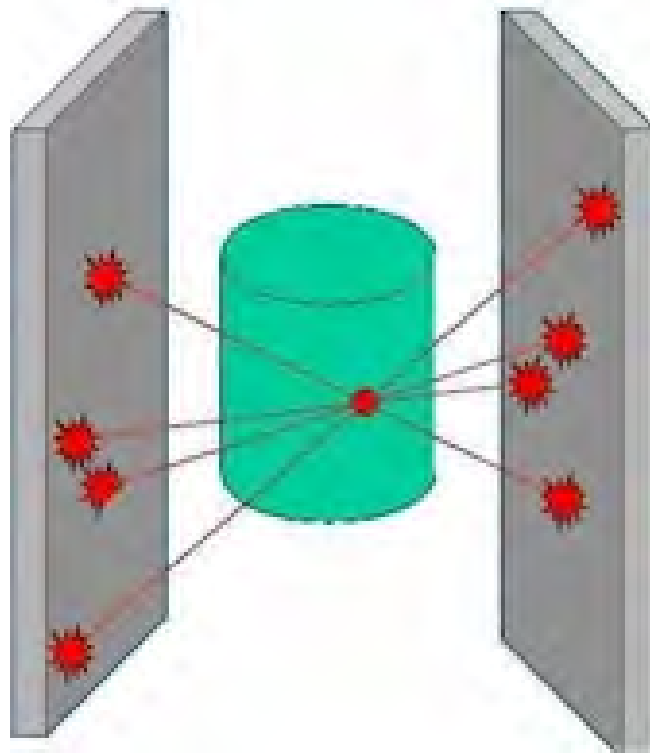


Figure 2.12 Schematic view of positron emission particle tracking functioning: on the sides the detectors which detect and localise the particle from the radioactivity signal of the particles.

Positron emission particle tracking (PEPT) is a Lagrangian flow visualisation technique, which makes it possible to measure flow patterns in three dimensions in enclosed and opaque systems (Fangary *et al.*, 1999). This technique is based on the use of a radioactively labelled particle, selected in this case on the basis of size and density to follow the flow of the fluid. The radiotracer decays by positron emission, which after annihilation with an electron nearby results in the release of two back-to-back gamma photons that are each detected by sensitive gamma scintillation detectors, located either side of the equipment under study (Parker *et al.*, 1993). According to the tracer activity, many thousands photon pairs are emitted every second. Each pair provides a “line of response” along which the decay must have happened. Triangulation of successive lines gives the location of the particle. A computer algorithm

corrects for random error such as scattering and invalid pairing. Rafiee *et al.* (2013) in her work showed how PEPT can be used to study laminar flow of a high viscosity Newtonian and non-Newtonian fluid in a Kenics static mixer (KM). Her work shows data from PEPT experiments which are determined from Cartesian coordinates of a single tracer moving within a system (static mixer). The change in velocity indicates a change in particle location relative to the solid boundaries of the geometry (i.e. the blade or the wall). The distance taken for the particle to reach a steady speed following such a step change could be a measure of the flow development. Through analysis of the trajectories of many hundreds of passes of the tracer particle through the mixer, it is possible to compute the overall flow field and to visualise how the fluid twists and folds as it passes along the mixer. Velocity maps in three dimensions can be created and striation formation can be observed from these data.

2.5.3.4. PIV/PLIF

Planar Laser Induced Fluorescence (PLIF) is an optical technique which tracks the spatial concentration distribution of an added fluorescent dye at fixed intervals of time. A laser sheet is used to illuminate a plane in the flow and images are captured using an orthogonally mounted digital camera. The cameras used contain either charge-coupled device (CCD) or complementary metal-oxide-semiconductor (CMOS) based sensors; the latter are becoming increasingly common due to reduced manufacturing cost and they are approaching parity with CCD sensors in terms of their quantum efficiency (sensitivity). The fluorescent dye illuminated by the laser sheet is excited by the laser light; it absorbs photons of laser light and re-emits photons of light at a lower frequency. For example a common set-up involves use of Nd-YAG or diode lasers which emit at 532 nm (green) with Rhodamine 6G dye which produces fluorescent light at 550-560 nm (yellow). Cut off filters can be used on the camera to prevent extraneous laser light from appearing in the image.

This technique is able to detect the concentration maps of the system at different times of capture and has been used widely in stirred tanks investigating laminar flow, visualizing the mixing patterns, studying the stretching of the fluid elements, and also characterising mixing by means of the gradient of concentration (CoV) and segregation (striation thickness) in many different works ((Alvarez *et al.*, 2002a), (Szalai *et al.*, 2004), (Zalc *et al.*, 2002a), (Ottino, 2000), (Arratia *et al.*, 2006) , (Zalc *et al.*, 2001), (Arratia *et al.*, 2004)). PLIF has also been demonstrated as a valuable method to quantify mixing times in agitated vessels both in the laminar and turbulent regime, by determination of the time required for the concentration of the dye to become uniform within a given confidence interval (Simmons *et al.*, 2007), (Hall *et al.*, 2004)). Ventresca *et al.* (2002) performed an investigation of dependence of laminar mixing efficiency of a motionless mixer upon viscosity ratio at low Reynolds number. The fluids used were aqueous solutions of CMC which are transparent liquids with a non-Newtonian rheology. The device used for the experiments consists of five elements of SMX static mixer. The mixing performance was evaluated using imaging analysis of the cross section of the pipe, detected at bottom of the static mixer. The images were detected using PLIF technique where resolved spatial variations of fluorescence intensity were recorded using a CCD camera. Ventresca in his work evaluated mixing performance considering both scale and intensity of segregation; for the first using correlograms and for the second CoV and intensity histograms are presented. The conclusion of this work underlined the role of the viscosity ratio between the main flow and the injection on the mixing performance. For low viscosity ratio, statistical descriptions (CoV) were important indicators of mixing effectiveness (Ventresca *et al.*, 2002). The scale described with correlograms is a viable statistic for indication of goodness of mixing , but following Ventresca's work the information of the scale of segregation analysis can be misleading when

diffusion occurs. However the main conclusion of this work was that the intensity of segregation was the most valuable tool for the detection of level of mixing. In another recent work Lehwald (2012) investigated the mixing in static mixer using a previously established method for the characterization of micro-mixing and macro-mixing based on Two-Tracer-PLIF (Lehwald *et al.*, 2010) carried out simultaneously with PIV for measuring the velocity and mixing fields induced by a static mixer element. Using the velocity map and an analysis of the segregation index the mixing performance was determined (refer to § 2.4.2).

2.5.3.5. Other optical techniques to determine mixing performance

Qualitative characterization techniques are mostly based on optical apparatus which necessitate transparent devices or at least devices with transparent viewing windows. The information obtained on mixing performance can give an approximation of mixing time in terms of residence time in batch system or in terms of number of elements for static mixer (Ghanem *et al.*, 2013). The acid–base or pH indicator reactions is one of the alternative used optical technique. The generation of colour change in acid-base reactions relies on the presence of a pH indicator in the basic or acidic solution. A number of different pH indicators have been used for characterizing mixing in particular for the detection of micromixing. A wide range of pH indicators are available in the market. Ghanem in his review work described the works of Branebjerg and Kockmann (1995) and Cabaret *et al* (2007) where the former estimated a mixing time by recording the time of colour change: the latter considered a mixing length defined as the downstream length in the mixer where colour change was no longer visible. A limitation of this technique, as most of 2D techniques, is the need of multi projections to get the pattern of full volume of the system. Another limitation of this technique is the resolution of images. Generally the colour images have a lower resolution

than grey scale images. For a statistical analysis (calculation of the coefficient of variation) this aspect can drastically influence the results. Other technique used for the detection of mixing performance is the dilution of coloured dyes. Using this method, concentrated solutions of coloured dye are contacted with colourless solutions or simply pure water in the studied system. Mixing quality and flow structures can be clearly observed at different positions along the mixer. Flow instabilities and vortices can also be visually spotted giving the possibility of a qualitative analysis without the possibility of a quantitative approach due to the resolution of the image that can be obtained.

2.6. Mixing performance of static mixers

Mixing quality relationships for static mixers are expressed in terms of a wall shear rate, $\dot{\gamma}$, which for the flow of a Newtonian fluid can be determined as

$$\dot{\gamma} = \frac{KV}{D} \quad (2.30)$$

where K is a constant (equal to 8 for a plain pipe and 28 for a KM static mixer used later in this study), V is the superficial pipe velocity and D is the pipe diameter. For different types of static mixer, equivalent values of K are quoted which compensate for the increased wetted perimeter due to the mixer internals; increased dissipation due to changes in flow pattern (fluid deformation, stretching and folding) and changes in fluid drag forces cause increased pressure drop over a plain pipe (Shah *et al.*, 1991). This shear rate is thus related to the pressure drop per unit length, a measure of the energy input to the fluid to obtain the required mixing and L/D , where L is the length of static mixer and D the diameter. Clearly, this correlation is fundamentally flawed for non-Newtonian systems since eq. (2.30) is no longer valid and any extrapolation must be carefully checked.

Literature correlations may be found which relate CoV to the length of static mixer required:

$$CoV_r = \frac{CoV}{CoV_0} = K_i^{\frac{L}{D}} \quad (2.31)$$

where CoV_0 is initial coefficient of variation in the unmixed material and CoV is the coefficient of variation required by the mixing duty. CoV_r is the ratio of these two quantities, thus expressing the reduction in CoV required by the process. K_i is the fit to the slope of the CoV decay line.

Other correlation are concerned with the number of striations per element;

$$N=2^n \quad (2.32)$$

Where N is the number of striation and n is the number of static mixer element which is for this correlation a KM static mixer. Similar correlation regarding the striation number can be found in the literature for ISG (4^N), Inliner ($3(2)^{N-1}$) and SMV ($n_c(2n_c)^{N-1}$ where n_c is the number of the channel). Clearly, these correlations are fundamentally flawed for non-Newtonian systems since the rheological fluid behaviour may change the performance and any extrapolation must be carefully checked.

2.6.1. Industrial applications and commercial static mixers.

In the following Tables 2.5 and 2.6 are presented most of the commercial static mixers and the industrial applications in function of geometry and flow regime.

Table 2.5 Commercially available static mixer (Thakur et al., 2003).

Company	Static mixer
Chemineer-Kenics	Kenics mixer (KM), HEV (high efficiency vortex mixer)
Koch-Sulzer	Sulzer mixer SMF, SMN, SMR, SMRX, SMV, SMX, SMXL
Charles Ross & Son	ISG (interfacial surface generator), LPD (low pressure drop), LLPD
Wymbs Engineering Lightnin	HV (high viscosity), LV (low viscosity) Inliner Series 45, Inliner Series 50
EMI	Cleveland

Komax

Komax

Brann and Lubbe

N-form

Toray

Hi-Toray Mixer

Prematechnik

PMR (pulsating mixer reactor)

UET

Heliflo (Series, I, II and III)

In this thesis work two specific geometries are used for the experiments: SMX PLUS and KM static mixer which are shown in Figure 2.18.



Figure 2.13 Geometries of: a) 4 KM static mixer elements and b) 4 SMX PLUS static mixer elements.

Kenics KM static mixers are equipped with helical mixing elements which direct the flow of material radially toward the pipe walls and back to the centre. Additional velocity reversal and flow division results from combining alternating right- and left-hand elements, thus increasing mixing efficiency (Chemineer (KM) web site).

The SMX PLUS static mixer is an evolution of the SMX design featuring lower pressure drop with similar mixing performance. The use of a reduced number of bars and gaps between the bars, allows a reduction of the pressure drop of the mixer to less than 50% while the mixing quality after a given number of elements remains nearly equivalent with the original SMX. As a result, significant cost savings can be achieved through reduced mixer and pipe diameters, or by using smaller pumps (Sulzer(SMX+) web site). Other important feature of this device is the capability of excellent mixing and dispersing even with widely differing fluid viscosities. The compact design and the short residence time sometimes can reduce the degradation of the product.

Table 2.6 Industrial applications of commercial static mixers.

Mixer	Flow regime	Area of application
Kenics	Laminar/turbulent	Thermal homogenization of polymer melt. Gas-liquid dispersion. Dilution of feed to reactor.
	Turbulent	Dispersion of viscous liquids
SMX PLUS	Laminar	Mixing of high viscosity liquids and liquids with extremely diverse viscosity, homogenization of melts in polymer processing
SMV	Turbulent	Low viscosity mixing and mass transfer in gas-liquid systems. Liquid-liquid extraction. Homogeneous dispersion and emulsions.
SMXL	Laminar	Heat transfer enhancement for viscous fluids
SMF	Laminar	Sludge conditioning, pulp stock blending, bleaching and dilution, bleaching of suspension and slurries
SMR	Laminar	Polystyrene polymerization and devolatilization
HEV	Turbulent	Low viscosity liquid-liquid blending, gas-gas mixing
LPD	Laminar	Blend two resins to form a homogeneous mixture

	Turbulent	Blending grades of oil or gasoline
LLPD	Turbulent	Blending grades of oil or gasoline
	Laminar	Blend out thermal gradient in viscous streams
ISG	Laminar	Blending catalyst, dye or additive into viscous fluid Homogenization of polymer dope. Pipeline reactor to provide selectivity of product.
	Turbulent	Waste water neutralization
Inliner mixer series 45	Turbulent	Fast reaction and blending application including widely differing viscosity, densities and fluid with unusual properties, such as polymer
Inliner mixer series 50	Turbulent	Chemical and petrochemical systems, hydrocarbon refining, caustics, pulp and fast reactions
SMV-4	Turbulent	Fine liquid–liquid dispersions (water–kerosene). Dispersion of immiscible fluids. e.g. water–kerosene.
Static-mixer woven screen	Turbulent	Dispersion of kerosene in water.
Komax SM	Turbulent	Mixing food products such as margarine and tomato pastes, viscous liquids like syrups and light fluids like juices.

As shown in the Table 2.6, static mixer devices are used in a wide range of industry. However the applications of all designs can be classified in four main groups (Figure 2.14) which increase the rate of mixing and uniformity for competing rate processes (Thakur et al., 2003):

- Mixing of miscible fluids;
- Interface generation between non-miscible phases;
- Heat transfer operation and thermal homogenization;
- Axial mixing

The mixing of miscible fluids can be divided into two subgroups, depending on whether the flow regime is laminar or turbulent. Most of previous cited works are included in this group including homogeneous reactions. The second group can be divided in function of the nature of the phases: gas–liquid, immiscible liquid–liquid, liquid–solid and solid–solid operations can be distinguished (Theron *et al.*, 2011) (Lobry *et al.*, 2011) (Fradette *et al.*, 2007) (Talansier *et al.*, 2013) (Jaworski *et al.*, 2007) (Das *et al.*, 2005) (Pacek *et al.*, 1997). The range of this group can cover multiphase reactions, separation processes, such as reactive absorption, or distillation. Thermal homogenization and heat transfer in heat exchangers involving viscous fluids in the laminar regime, such as polymer solutions are the typical process classified in the third group (Li *et al.*, 1996) (Li *et al.*, 1998) (Kalbitz *et al.*, 1991) (Vandermeer *et al.*, 1978) (Fan *et al.*, 1977). Static mixing elements are used in turbulent flow to reduce the exchanger size. Other applications which are included in this group are the reactions which imply heat transfer. Finally in the axial mixing group are included all the processes where solids are involve in the process. An example of application can be the waste treatment of organic material or general waste which can be mixed before enter in the oven for the gasification, after a previous milling.

STATIC MIXERS IN THE PROCESS INDUSTRIES

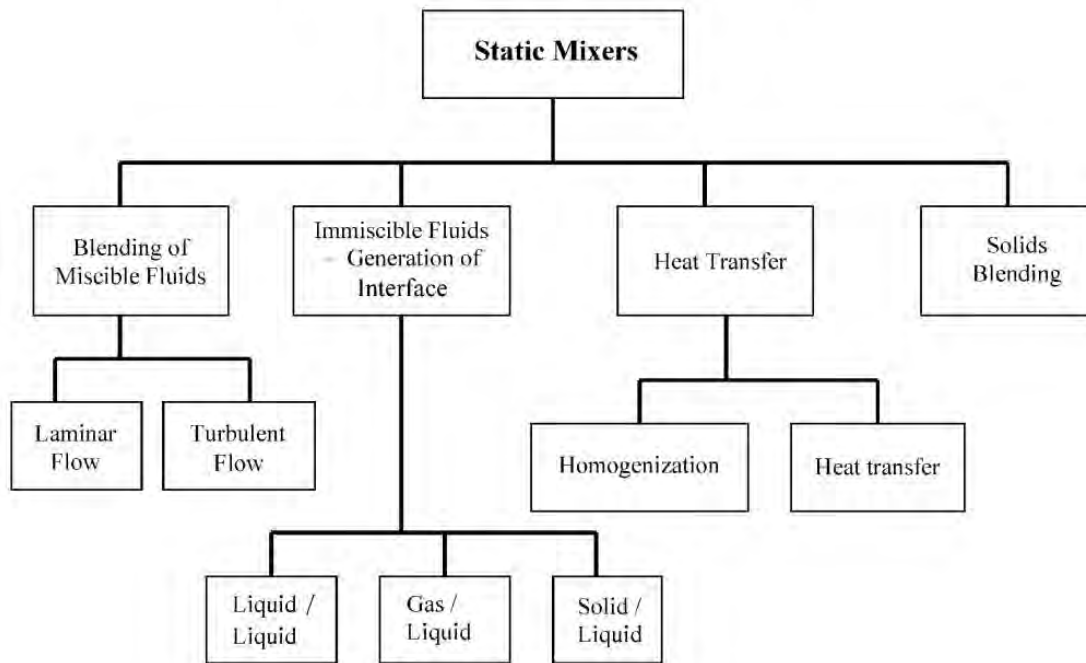


Figure 2.14 Classification of unit operation using static mixer (Thakur *et al.*, 2003)

2.7. Conclusions

This literature review is presented in order to give an overall view of the problem of mixing in static mixers. Different aspects of mixing have been discussed starting from fundamentals of mixing which give a background and allow a better understanding of the work. The physical characteristics of the system and how they are measured are explained. Although a general overview of various methodologies to determine mixing performance is proposed, the focus of this work is on the blending of non-Newtonian in laminar regime. A specific importance is given to the concentration distribution as a source of information for the blending performance which is the core of this work where image analysis of PLIF raw images has been used. Clearly the concentration distribution is not the only important aspect for the understanding of the blending of non-Newtonian fluids. The flow field of the system has to be equally considered for a full characterization of mixing performance. However, as it

is complicated to determine the concentration distribution from the flow field, it is even more challenging to verify the flow field from the concentration distribution. In this work these two aspects are investigated: the focus is on the explanation of effects (concentration distribution and mixing pattern) and some basic preliminary studies of causes (flow field, shear rate, stress, etc.) are also presented. Both are critical steps to gain deep understanding of the mixing performance of non-Newtonian fluids undergoing laminar flow in static mixers.

3. MATERIALS AND METHODS

3.1. Introduction

In this thesis different aspects of the mixing and characterisation of non-Newtonian fluids are investigated and various experimental techniques have been used. These may be characterised according to:

- Rheological Measurements

The first step to characterise the behaviour of a non-Newtonian fluid is the study of its rheology which is carried out in this work using various rheometers including standard equipment (TA Instruments AR1000) as well as a Bespoke optical rheometer where replacement of the bottom plate with optical glass enables visualisation of the flow of the material under shear. These are described in §3.2. The extensional behaviour of the fluid has also been examined using a flow rig which allows the measurement of the force applied for the stretching and breakage of a filament of non-Newtonian fluid, together with imaging, description of this bespoke equipment is given in Chapter 7.

- Flow visualisation

The core technique used for most of this work is the planar laser induced fluorescence (PLIF) which is described in §3.3.1. In addition, a modification of the Particle Image Velocimetry technique has been applied to obtain 3-D flow information inside a transparent KM model static mixer. High speed imaging has also been carried out on a longitudinal section of the static mixer to visualize the effect of different injection positions, inside and at the bottom (see §3.3.2)

Following the description of the experimental methods used, an overview of the static mixer rig used in this work for the PLIF experiments is given in §3.4.

3.2. Rheological measurements.

3.2.1. Rheology of model fluids using TA AR 1000 rheometer.

The non-Newtonian behaviour of the model fluids has been characterized using the AR1000 rheometer.



Figure 3.1 AR1000 rheometer.

The TA Instruments AR rheometers have controlled stress or rate capability and can handle a wide range of geometries and fluid types. The rheometer consists of 4 main parts: the rheometer head, draw rod, geometry and sample platform. The rheometer head is the motorized part where the drag-cup motor is located. In addition an air bearing allows virtually friction free application of torque. The design of this air bearing is a compromise among consumption, friction, stiffness and tolerance to contamination. The geometry is another fundamental part of a rheometer which is changed to suit the measurement being performed. The geometry is connected to a draw rod which is controlled by the motor.

The working fluids are aqueous solutions of glycerol or Carbopol 940 (Lubrizol Corp, Ohio, USA), a cross-linked polyacrylate polymer. The solutions of Carbopol 940 were chosen to mimic specific JM process fluids. The rheology of fluids was obtained by equipping the TA AR 1000 with a 40 mm diameter 2° steel cone. In Figure 3.2, both non-Newtonian fluids were found to be well represented by the Herschel-Bulkley(eq. 3.1) model over a range of shear rates, from 0.1 – 1000 s⁻¹.

$$\tau = \tau_0 + K\dot{\gamma}^n, \quad (3.1)$$

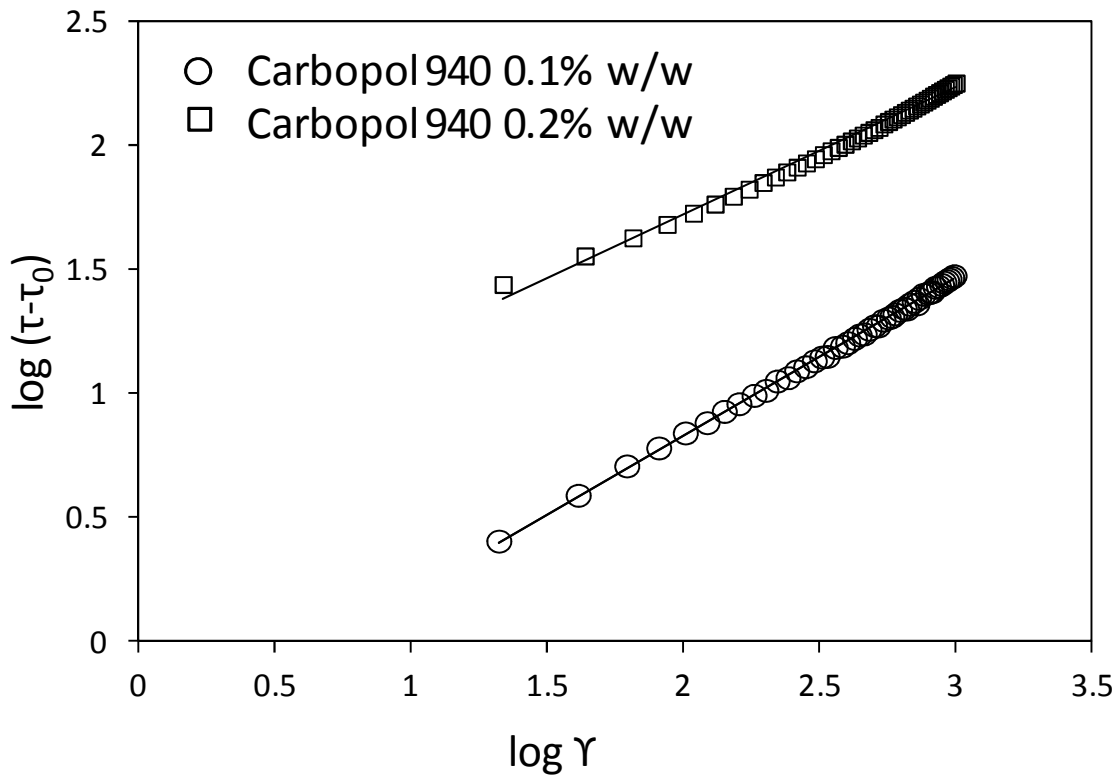


Figure 3.2 Rheology of the non-Newtonian fluids used fitted to the Herschel-Bulkley model.

The calculated rheological parameters are given for both solutions, together with their polymer concentration and pH in Table 3.1. The two fluids were chosen so that the effect of injection of a more viscous secondary flow could be studied, which is the core focus of this

work. The less viscous fluid (Carbopol 940 0.1% w/w) (fluid 1) was always used as the primary flow, whilst either fluid 1 or the more viscous fluid 2 (Carbopol 940 0.2% w/w) were used as the secondary flow.

Table 3.1 Tabulated Herschel-Bulkley model parameters obtained from rheological data and physical properties of the glycerol solution and Carbopol solutions used in the experiments at constant temperature of 22°C.

	Density	Yield stress	Power law exp.	Consistency Index	pH
	ρ (kg m ⁻³)	τ_0 (Pa)	n (-)	k (Pa s ⁿ⁻¹)	(-)
Fluid 1: 0.1% wt Carbopol 940	1000	3.2	0.7	0.26	4.5
Fluid 2: 0.2% wt Carbopol 940	1000	25.2	0.42	6.74	5
Fluid n: 80% wt Glycerol	1200	-	-	-	-

However in some experiments also a solution of glycerol is used in order to compare the results with Newtonian fluid data found in the literature.

3.2.2. The Bohlin Gemini II Opto-rheometer.

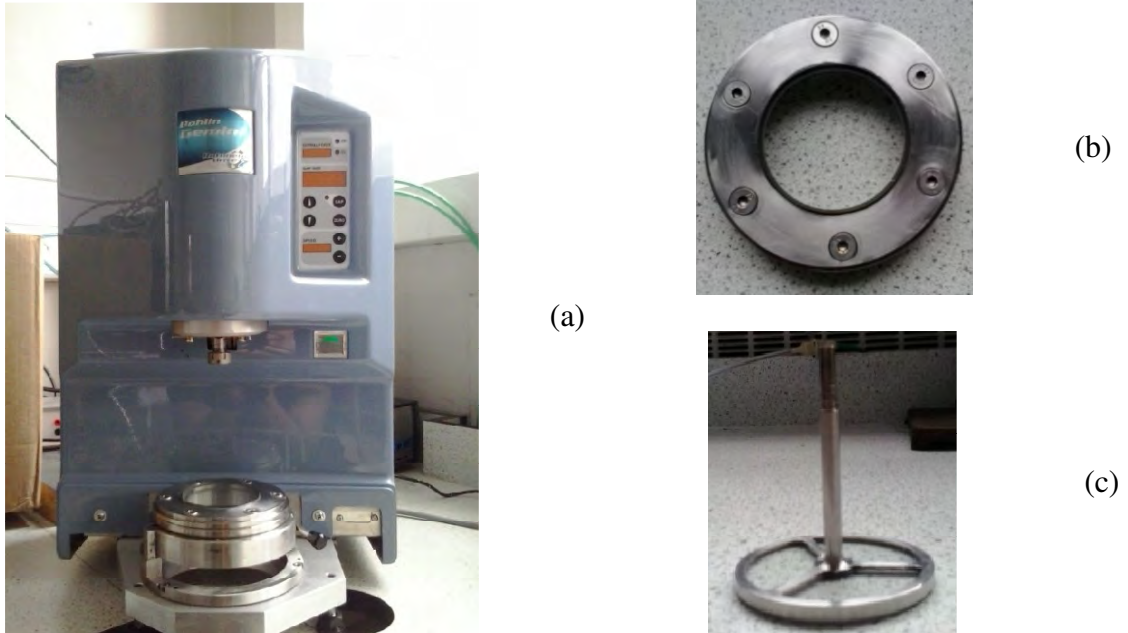


Figure 3.3 Gemini II rheometer: (a) Opto-rheometer; (b) opto-sample platform; (c) opto-geometry.

The Bohlin Gemini II is also a rotational rheometer system. The experiments carried out with this rheometer were concentrated on the effect of different shear rates on mixtures of the selected non-Newtonian fluids and the drop stretching at fixed shear. This rheometer is equipped with a sample platform (Figure 3.3b) and geometries (Figure 3.3c) made from optical glass which allows the fluid being sheared to be visualised.

3.3. Flow Visualisation

3.3.1. Planar Laser Induced Fluorescence (PLIF)

The 2-D PLIF measurements were performed using a TSI PIV system (TSI Inc, USA). The system comprises a 532 nm (green) Nd-Yag laser (New Wave Solo III) pulsing at 7 Hz, synchronized to a single TSI Powerview 4MP (2048 × 2048 pixels) 12 bit CCD camera using a synchronizer (TSI 610035) attached to a personal computer. The PIV system was controlled using TSI Insight 4G software. The camera is equipped with a 545 nm cut-off filter to eliminate reflected laser light so that only the fluorescent light emitted by the Rhodamine 6G dye ($\lambda = 560$ nm, yellow) excited in the measurement plane is captured on the image. The spatial resolution of the measurements was $10 \mu\text{m pixel}^{-1}$ and $20 \mu\text{m pixel}^{-1}$ for the $\frac{1}{2}$ " and 1" scale mixers respectively. A method for pixel-by pixel calibration of the measurements, to ensure linearity between the measured gray scale values and the dye concentrations was used and is described in § 3.3.1.1 . This enabled selection of the concentration of the dye in the secondary flow as 0.5 mg L^{-1} in order to ensure all measurable concentrations in the mixing section were within the linear range. The following chart shows the linear relationship between gray scale values and concentration of Rhodamine 6G between 0.1 to 2 mg L^{-1} for the two Carbopol solutions.

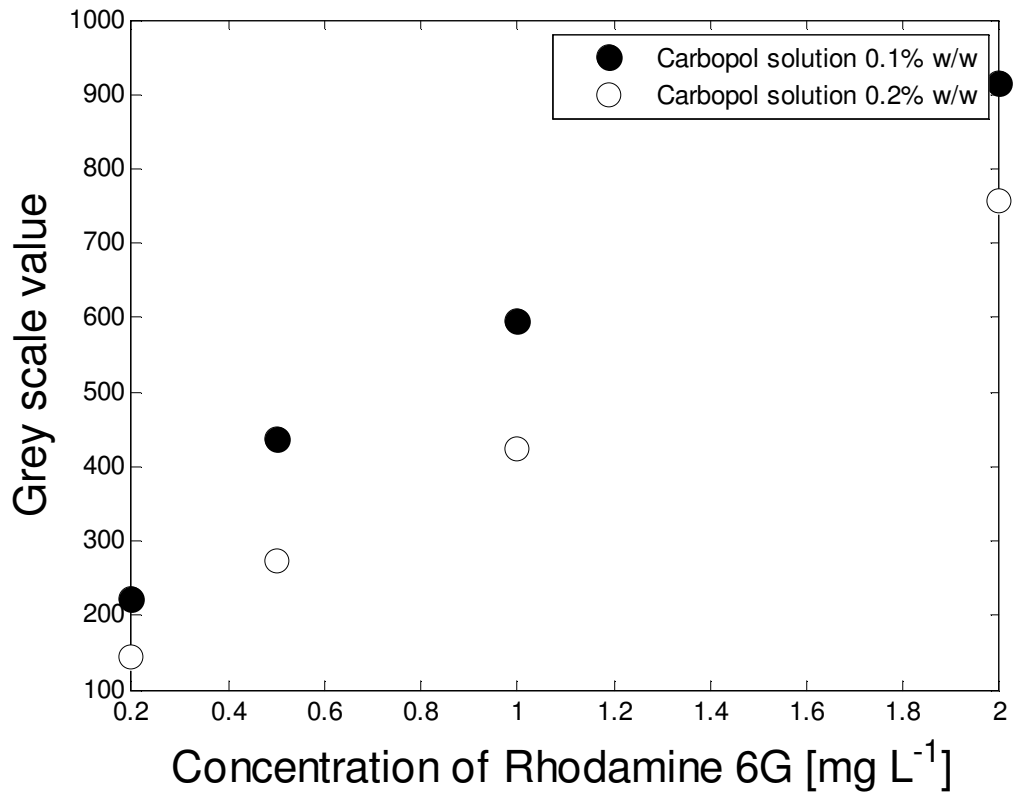


Figure 3.4 Concentration of Rhodamine 6G versus gray scale value for the two solution of Carbopol 940

The generation of MATLAB algorithms for intensity and scale of segregation were at first developed only for the calculation of CoV and striation thickness. As discussed in the literature review, most of the published works use CoV or log-variance) (LogVa) as the parameter to describe the mixing performance, where

$$CoV = \frac{\sigma}{\bar{C}}; \quad (3.2)$$

$$\bar{C} = \frac{C_i - C_0}{C_\infty - C_0}; \quad (3.3)$$

and LogVa is defined as:

$$\log Va = \log \sigma^2 = \log \left[\frac{1}{N-1} \sum_{i=1}^N [\bar{C} - 1]^2 \right]; \quad (3.4)$$

Where C_0 is the background value obtained from the calibration ($C_0 \rightarrow 0$), C_i is the measured concentration in element i and C_∞ is the fully mixed concentration assuming perfect blending of the dye, which corresponds to the average concentration in the image.

An important value to enable evaluation of the CoV is the C_∞ which is calculated using the information from a previous calibration of different solutions of the dye (Figure 3.4). The calibration values are essential to determine the instantaneous concentration in each pixel of the raw image determined from the known gray scale value.

In the following paragraphs all the algorithms used in this thesis work are explained: CoV, striation thickness, area fraction method and striation area distribution method are presented.

3.3.1.1. Intensity of segregation (CoV and log-variance)



Figure 3.5: Explanation of algorithm of intensity of segregation

In other works, the scale of segregation is evaluated to characterize the mixing performance using the striation thickness so this is an important parameter to obtain. The image is divided in 'nxn' number of boxes (Figure 3.5) where each box is a pixel and it has a value of grey scale which correlates to the concentration of present dye. As mentioned before, the C_{∞} is calculated assuming an ideal equilibrium state where the concentration is constant at each point. The identification of the background, C_o , (in this case only Carbopol solutions without the injection of dye) is an important parameter to evaluate in order to calculate the CoV or LogVa. Once the linear relationship between the gray scale values and concentration of the dye in a specific range has been proven, an array of real values of concentration of dye and an array with the correspondent grey scale values are determined using a simple quadratic regression, the terms 'M' and 'Q' are evaluated to define the equation which correlates gray scale and concentration as:

$$Y = Mx + Q \quad (3.5)$$

Y is the grey scale value, x is the concentration, M is the gradient and Q is the coefficient of the line. From the equation (3.4) the instantaneous concentration (C_i) is evaluated for each pixel of the raw image which allows the evaluation of the CoV or LogVa.

CoV and LogVa were calculated by analysis of the PLIF images using an algorithm developed in MATLAB. The images were imported into MATLAB and converted into a 2048×2048 matrix with each element in the matrix corresponding to a pixel in the image. With the 12 bit camera used, each element contains an integer number between 0 (black) and 4095 (white). The region within the matrix corresponding to the pipe cross section was isolated and the number of elements in this region N , was counted. CoV and LogVa were then determined using eqns (3.1) and (3.3) respectively, defining the mixing property, \bar{C} , as the dimensionless concentration.

3.3.1.2. Scale of segregation (striation characterisation)

The striation thickness distribution was determined using a MATLAB algorithm which performed a row by row (or column by column) analysis of the imported image matrix. The number of contiguous pixels with the same gray scale value (within a pre-defined tolerance) and thus within the same striation were counted and converted to a length via calibration ($10 \mu\text{m pixel}^{-1}$ for $\frac{1}{2}$ " diameter and $20 \mu\text{m pixel}^{-1}$ for 1" diameter). This automated method was used due to the difficulty of manual analysis of the data. A limitation of the method is that it does not identify if individual striations in adjacent rows or columns are within the same striation. Other important limitation is the arbitrary choice of the tolerance which identifies the different striations in terms of gray scale value. In this work it was used a 5% difference in terms of gray scale value to identify a border between different striations. This weights the distribution in favour of the larger striations, since they occupy a larger cross sectional area. Although these data are not therefore absolute, the method does allow relative comparisons between the different experiments.

3.3.2. High speed imaging

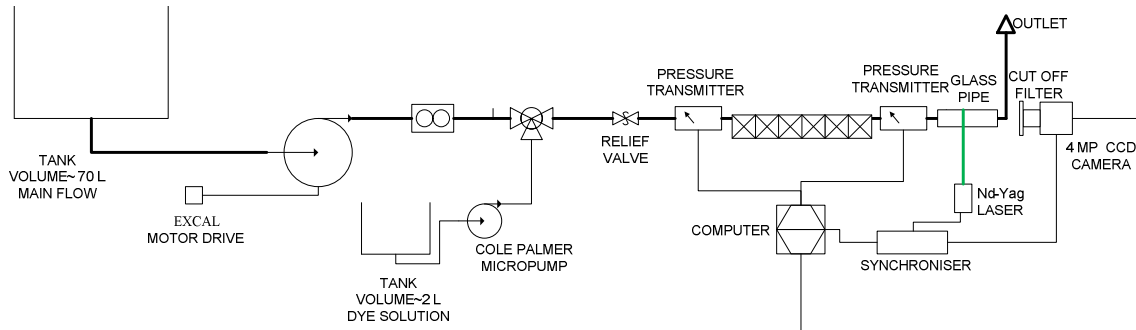


Figure 3.6 Photron FASTCAM SA3

For this thesis work a Photron FASTCAM SA3 has been used. This camera has a CMOS sensor which provides mega pixel resolution (1K by 1K pixels) up to 2,000 frames per second (fps). The sensor provides 12-bit dynamic range from its large seventeen micron square pixels which allows an excellent resolution shout. A two microsecond global electronic shutter ensures a blur free regardless of speed. FASTCAM SA3 60K provides 2,000 fps at 1,024 by 1,024 pixel resolution, and reduced resolution operations as fast as 60,000 fps.

3.4. Static Mixer Rig

3.4.1. Static mixer rig for PLIF(a)



(b)

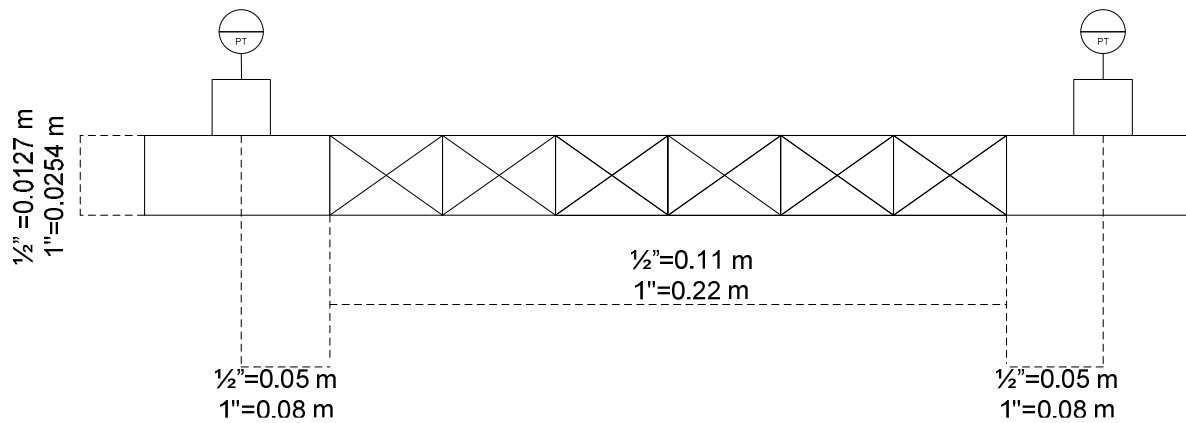
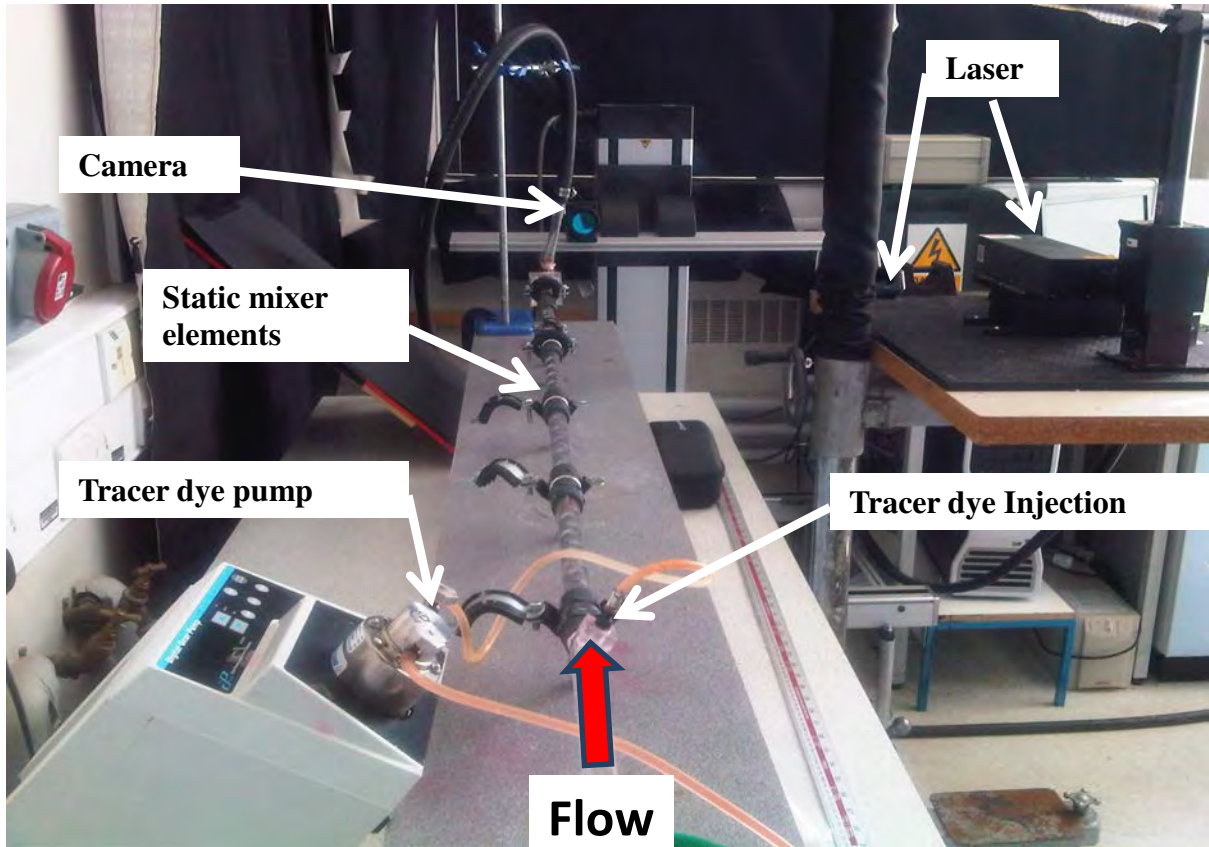


Figure 3.7 Schematics of the static mixer test rig. (a) overall schematic; (b) dimensions of static mixer test section showing location of pressure transducers;

(c)



(d)



Figure 3.7 (c) picture of the PLIF rig;(d) window used to capture the cross section of glass pipe.

Figure 3.7a shows an overall schematic of the experimental rig with Figure 3.7b giving a picture of the static mixer test section. KM and SMX static mixers of internal diameter (ID) 12.7 mm (1/2") and 25.4 mm (1"), with lengths of 0.11 m ($L/D = 9$) and 0.22 m ($L/D = 9$) respectively have been used. For the 1/2" ID mixer, the primary flow is delivered by a Liquiflo gear pump controlled using a motor drive (Excal Meliamex Ltd) and monitored

using an electromagnetic flow meter (Krohne). Flow to the 1" ID mixer is delivered by an Albany rotary gear pump controlled using an inverter control WEG (model CF208). For both mixer scales, the secondary flow is introduced using a Cole-Parmer Micropump (GB-P35) and is doped with fluorescent dye (Rhodamine 6G). In the first results chapter (Chapter 4) the injection of doped fluid is in the centre of the pipe and placed at a distance of one pipe diameter from the first static mixer element in all experiments. For the other result chapters where the PLIF technique is used the injection of doped fluid is in the centre and placed as close as possible to the first mixer element. A Tee piece is placed at the end of the mixer section which has a glass window inserted on the corner of the Tee, normal to the axis of the main pipe, in order to enable flow measurements using PLIF, that requires optically transparent materials. A glass pipe section upstream of the Tee at the mixer section outlet provides optical access for the laser sheet to illuminate the transverse section. Two pressure transmitters were located both upstream (PR-35X / 10 bar, Keller UK) and downstream (Figure 3.7b) (PR-35X / 1 bar, Keller UK) of the static mixer section, enabling measurement of the pressure drop at a sampling rate of 5 Hz. The transducers were placed as close as possible to the mixer section, being mounted 4 pipe diameters before and after the section respectively (Figure 3.7b). The pressure transmitters also incorporated PT100 thermocouples enabling fluid temperature to be monitored throughout the experiments. The temperature of the fluids was maintained at 22°C to ensure fluid rheology remained constant. Pressure drop data was obtained for the continuous phase fluids over a range of superficial velocities from $0.1 < V < 0.6 \text{ m s}^{-1}$ ($60 < Q < 300 \text{ L hr}^{-1}$ for the 1/2" scale mixer and $180 < Q < 1080 \text{ L hr}^{-1}$ for the 1" scale mixer). The choice of injection pump proved important to obtain reliable results. Figure 3.8 shows the pattern for selected runs for KM and SMX+ static mixer using a gear and a peristaltic pump for the injection. The latter was found to generate a pulsed flow which creates an extra perturbation in the system; hence the measurements obtained were time-dependent (see Figure 3.8 below). Therefore the gear pump was used where successive images were found to be identical.









Pump	Peristaltic (PP)		Gear (GP)	
	t_1	t_2	t_3	
KM 6 elements $v=0.1 \text{ m s}^{-1}$ Injection fluid 1 FR=1/25				
SMX+ 6 elements $v=0.1 \text{ m s}^{-1}$ Injection fluid 1 FR=1/25				

Figure 3.8 Pattern flow using peristaltic and gear pump for selected experiments for KM and SMX+ static mixers.

4. USE OF AN AREAL DISTRIBUTION OF MIXING INTENSITY TO DESCRIBE BLENDING OF NON-NEWTONIAN FLUIDS IN A KENICS KM STATIC MIXER USING PLIF.

4.1. Introduction

Many process industry sectors, including food, home and personal care, catalyst and plastic manufacture, are tasked with the blending of highly viscous or non-Newtonian materials, often incorporating multiple immiscible phases. Applications include the blending of concentrated solid-liquid slurries, polymerizations and the dissolution of solids or surfactants into liquids to form gels or complex surfactant/fluid phases. Due to the high apparent viscosities of some of these materials, the blending is performed under conditions which are predominantly laminar, which presents difficulties due to the lack of eddy diffusion which would assist mixing operations if the flow was turbulent (Todd D B, 2004). Overcoming this challenge has led to development of mixing strategies which aim to introduce chaotic flow to improve the performance; these have been employed in both batch stirred vessels (Alvarez *et al.* 2002) and in-line continuous static mixers (Etchells A W *et al.*,2004) which have been in use since the 1950's. Due to the complexity of the resultant flow fields formed in stirred vessels, substantial experimental and numerical studies on chaotic mixing have been undertaken to illustrate its potential to improve mixing (Alvarez *et al.* 2002; Arratia *et al.* 2004). Experimental work has focused on the use of optical flow diagnostic methods such as

Particle Image Velocimetry (PIV) or (Planar) Laser Induced Fluorescence (PLIF)(Arratia *et al.* 2004) on transparent systems, which have enabled the development of methods to quantify mixing performance as a function of the flow field and fluid viscosity. Modelling has involved direct numerical solution of the Navier-Stokes equations (DNS), as well as other forms of Computational Fluid Dynamics (CFD) (Zalc *et al.* 2002). More recent work has extended these approaches to consider the blending of non-Newtonian fluids in stirred vessels, focusing on yield stress fluids (Patel *et al.* 2011). This approach has raised understanding from an empirical level, where the entire mixing quality is based upon a single measured or derived parameter, to a multi-dimensional problem which considers the spatial distribution of mixing quality as a function of the fluid flow field and rheology.

In contrast, despite the industry drive towards continuous processing due to its improved sustainability (reductions in inventory and plant footprint), there has been little effort in obtaining equivalent understanding of non-Newtonian blending within continuous inline static (motionless) mixers, though limited design information for the blending of Newtonian fluids is in the public domain (Etchells A W *et al.*,2004). The blending of non-Newtonian fluids is complicated by a non-linear relationship between the applied shear stress and the shear rate obtained within the fluid. Newtonian design equations rely on the linear coupling between these quantities described by Newton's law of viscosity.

The CoV is often used as the sole criterion for characterising mixing efficiency or performance. However, the reality is much more complex since whilst CoV gives a measure of the range of a mixing property after a mixing operation, this is only one dimension of the problem. Kukukova *et al.*(2009) proposed segregation, which may be thought of as the degree to which a material is unmixed, as being composed of three separate dimensions.

This multi-dimensional approach has not yet been applied to determine mixing quality for non-Newtonian flows in static mixers. Of the limited information available in the open literature, work has generally focused on pressure drop measurements for time independent

(Shah *et al.* 1991; Li, Fasol *et al.* 1997; Kukukova *et al.* 2011) and viscoelastic (Chandra *et al.* 1992) non-Newtonian fluids in static mixers with only a few recent studies examining them in more detail (Chandra *et al.* 1992).

In this Chapter, a PLIF based method is used to characterise blending of non-Newtonian fluids in a Kenics KM mixer as function of number of mixer elements (6 and 12 elements) and fluid rheology. The transparent model fluids used are a Newtonian fluid (aqueous solution of glycerol) and two time-independent shear thinning fluids (aqueous solution of Carbopol 940 polymer) whose behaviour may be described using the Herschel-Bulkley model. The blending of two fluids is explored via addition of a secondary flow at the mixer inlet which has a volumetric flow equal to ~10% of the main flow, enabling the blending of fluids with different rheologies. As in previous work (Arratia *et al.*, 2004), the PLIF method is performed by doping the secondary fluid phase with fluorescent dye at the mixer inlet; the mixing pattern is thus obtained from images taken from a transverse section across the outlet of the mixer. From the images obtained, the scale and intensity of segregation are determined via calculation of values of $\text{Log}V_a$ and striation thicknesses respectively. A new criterion based on areal analysis of regions in the image with the same mixing intensity is proposed which combines aspects of both intensity and scale of segregation. Examination of these areal based distributions of mixing intensity enables a deeper understanding of the complexity of the mixing to be elucidated which has the potential to provide useful information for process designers.

4.2. Material and Methods

4.2.1. Fluids and Flow Conditions

The working fluids used were two different aqueous solutions of Carbopol 940 (Lubrizol Corp, Ohio, USA) and a glycerol solution (fluid n), as described in §3.2.1 where the less viscous fluid (fluid 1) was always used as the primary flow, whilst either fluid 1 or the more

viscous fluid 2 were used as the secondary flow doped with fluorescent dye and injected using the micro pump described in §3.4.1.

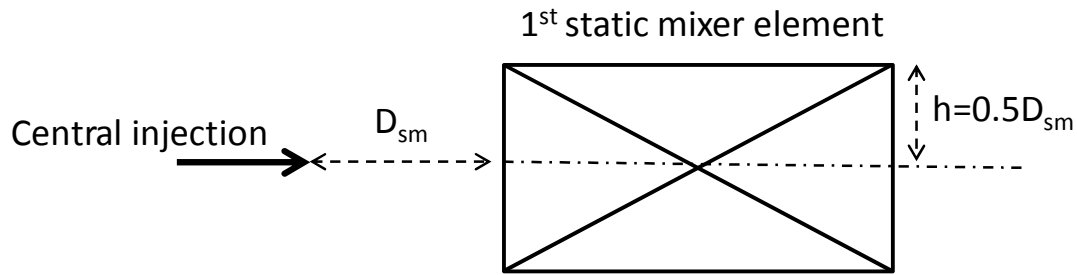
In this chapter a comparison between the mixing of Newtonian and non-Newtonian fluids in inline mixer is presented. The experiments are performed using the static mixer rig described in §3.4 in Chapter 3. A KM static mixer of diameter 12.7 mm (0.5”) with either 6 single blade 180° twisted elements or 12 elements is used, with lengths of 0.27 m ($L/D = 21$) and 0.53 m ($L/D = 42$) respectively. A constant total superficial velocity of 0.3 m s^{-1} , corresponding to a total volumetric flow rate of 184 L hr^{-1} , was used in all PLIF experiments. Three different experimental conditions were selected as shown in Table 4.1. This specific velocity has been selected from most common range of processing velocity used for static mixer in laminar regime (from 0.1 to 1 m s^{-1}).

Table 4.1: Summary of experimental conditions.

Experiment #	#1 _n	#1 _{nn}	#2
Primary flow	Fluid n	Fluid 1	Fluid 1
Secondary flow	Fluid n	Fluid 1	Fluid 2

Experiment #1_n involved use of the Newtonian glycerol solution (‘fluid n’) for both primary and secondary flows, thus providing a baseline for comparison with published data. Experiments #1_{nn} and #2 used the non-Newtonian Carbopol solutions. Experiment #1_{nn} used the non-Newtonian ‘fluid 1’ for both flows. Experiment #2 explored mixing of fluids with different rheology by using ‘fluid 1’ for the primary flow and the more viscous ‘fluid 2’ for the secondary flow. Each experiment was performed using both 6 and 12 KM mixing elements.

In Figure 4.1 all the specifics of static mixer dimensions are reported including secondary flow inlet dimensions and injection position.



	Flow ratio	Diameter static mixer (D_{sm}) [m]	Diameter injection (D_i) [m]
1/2"	10	0.0127	0.004

Figure 4.1 Injection position and static mixer dimension used for the experiments of Chapter 4.

The Reynolds number for the flows, based on a plain tube, is calculated as

$$Re = \frac{DV\rho}{\mu}, \quad (4.1)$$

leading to a value of 88 for the Newtonian experiment #1_n. Although transitional values of Reynolds number are somewhat dependent upon the geometry, this calculated value is well below those available in the literature, which quote values in the range of $Re > 500$ (Hirech *et al.* 2003). Calculation of Reynolds number for the non-Newtonian fluids is more complex since the viscosity is a function of shear rate. To provide an initial estimate for experiments #1_{nn} and #2, the apparent viscosity of fluid was calculated at wall shear rate obtained using equation (1) with $K = 28$ ($\dot{\gamma} = 650 \text{ s}^{-1}$), corrected for a shear thinning fluid (Chhabra and Richardson) by multiplying by $(3n+1/4n)$. The values of Re obtained were 88 and 91 respectively, confirming the flow was laminar.

Both advection and molecular diffusion are relevant possible mixing mechanisms in these experiments, although due to the viscous nature of the fluids (Table 3.1) it would be expected that advection would be the dominant mechanism since the value for Schmidt number,

$Sc = \nu/D_M \gg 1$ ($\sim 10^9$) for all the experiments (Todd D B, 2004). The spatial concentration distributions obtained in the PLIF images nevertheless arise from mixing by both mechanisms and are resolved to $10 \mu\text{m}$. It is not possible decouple the mixing effects due to each mechanism from the PLIF images.

To assess the temporal variation of the images, 10 images were acquired in three batches spaced several minutes apart for each experiment. No temporal variation was observed in any of the experiments, confirming the mixer was operating at steady-state.

4.2.2. Characterisation of mixing performance from the PLIF images

An alternative method of examining the mixing performance is proposed based on analysis of areas (striations) within the PLIF image which possess the same level of mixing, leading to an areal distribution of mixing intensity over the image which possesses some features of scale, as well as intensity.

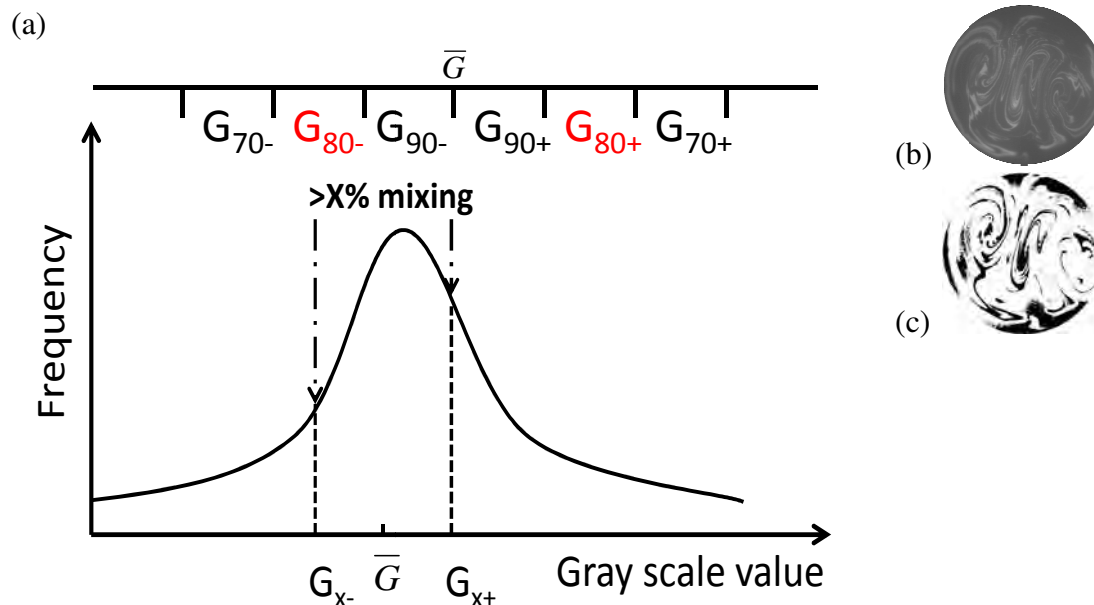


Figure 4.2 Development of areal analysis method. (a) Identification of regions in the grayscale distribution with a given mixing intensity; (b) raw image; (c) example of image processing for the experiment #1 12 elements with regions of mixing intensity $> 60\%$ in white.

This method is described with reference to Figure 4.2. Figure 4.2a displays a typical distribution of greyscale values (which are proportional to the dye concentration) which would be obtained from an image such as that shown in Figure 4.2b. From the distribution, mean value of grayscale in the image (corresponding to the fully mixed concentration,), can be easily evaluated. The mass balance of dye from the inlet to the PLIF measurement point can then be checked assuming steady state, i.e.

$$\bar{G} = \frac{F_{dye}G_{dye} + F_0G_0}{F_{dye} + F_0}; \quad (4.2)$$

where F_{dye} and F_0 are the volumetric flow rates of the primary and secondary flow and G_{dye} and G_0 are the gray scale values corresponding to the concentrations of dye present. The theoretical values calculated using eq. (4.2) were within 5% of the experimentally determined values for all experiments, thus the mass balance was closer to within an error of $\pm 5\%$ assuming plug flow. Using the experimental determined value, it is possible to calculate gray scale values corresponding to a given level of mixedness. Taking X% mixing as an example, this corresponds to gray scale values of either $G_{X-} = [1-(1-X)]$ or $G_{X+} = [1+(1-X)]$. So for 95% mixing, $G_{X-} = 0.95$ and $G_{X+} = 1.05$. Note that from eq. (4.2) both give the same log variance, as expected. Using MATLAB and the freeware image analysis tool Image J, the pixels in the image are identified which correspond to $G_{X-} < G < G_{X+}$, thus corresponding to a mixing intensity of $>X\%$: this arbitrary region is shown in Figure 4.2a. These pixels are then set to white ($G = 4095$) in the image, with the remaining out of range pixels being set to black ($G = 0$). An example of this procedure is shown in Figure 4.2c, where the fraction of the total cross-sectional area corresponding to this mixing intensity is then easily determined from the fraction of white pixels. By repeating this procedure over a range of values of X, both discrete and cumulative areal distributions of mixing intensity are thus obtained.

4.3. Results and Discussion

4.3.1. Pressure Drop

The pressure drops, ΔP , measured over an empty pipe for both continuous phase fluids, Fluid 1_n and Fluid 1_{nn}, are plotted in Figure 4.2 and compared with theoretical values obtained from eq. (4.3) for Fluid 1_n and eq. (4.4) (Non-Newtonian Flow and Applied Rheology (2nd edition), 2008) for non-Newtonian Fluid 1_{nn}.

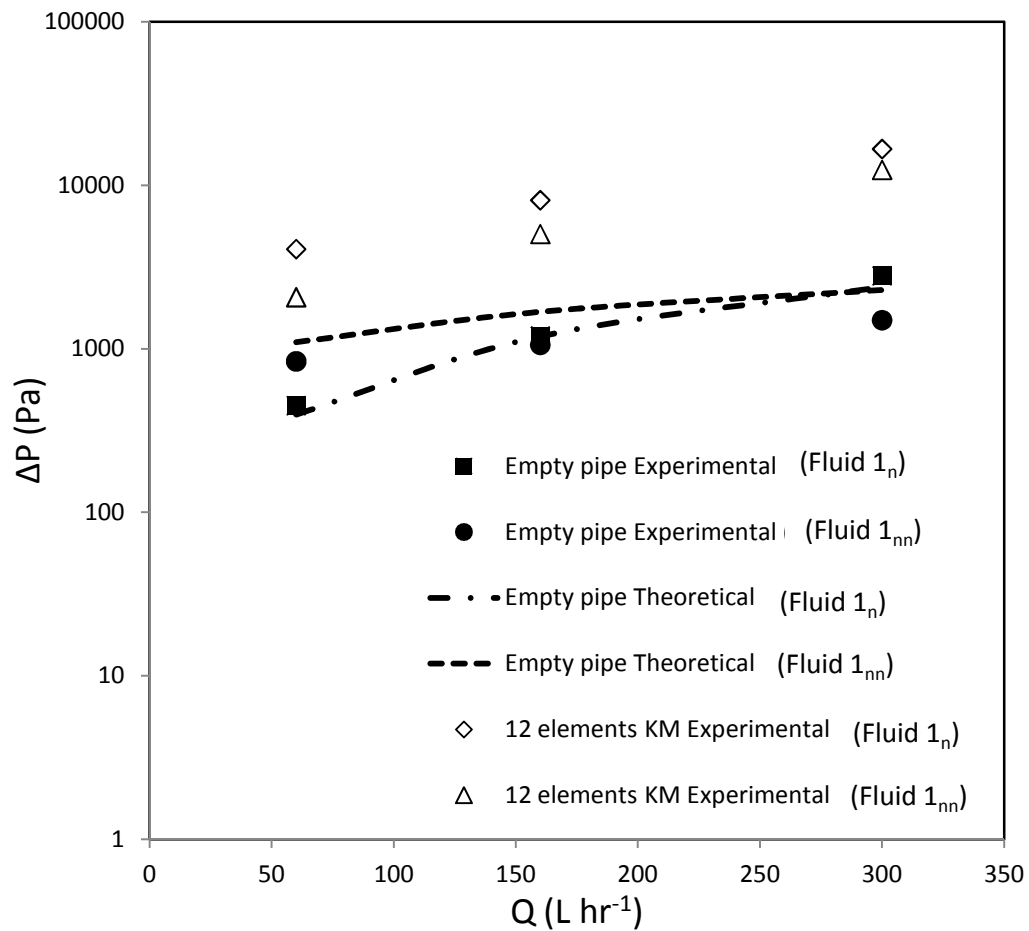


Figure 4.3 Pressure drop measurements made for both continuous phase fluids in the empty pipe and comparison with theoretical predictions.

$$Q = \frac{\pi D^4 \Delta P}{128 \mu L} \quad (4.3)$$

$$Q = \frac{8\pi^3}{\Delta P^3} \frac{1}{k^{1/n}} \left[\frac{n}{3n+1} \left(\left[\frac{\Delta P R}{L 2} \right] - \tau_y \right)^{\frac{3n+1}{n}} + \frac{2\tau_y n}{2n+1} \left(\left[\frac{\Delta P R}{L 2} \right] - \tau_y \right)^{\frac{2n+1}{n}} + \frac{\tau_y^2 n}{n+1} \left(\left[\frac{\Delta P R}{L 2} \right] - \tau_y \right)^{\frac{n+1}{n}} \right] \quad (4.4)$$

where Q is the volumetric flow rate and μ is the dynamic viscosity of the Newtonian fluid. Excellent agreement is observed for the Newtonian fluid and good agreement is observed with the non-Newtonian fluid, apart from at very low flow rates. Values of pressure drop for the same fluids in the empty pipe and after 12 KM mixer elements are given in Table 4.2. K_L values for the KM mixer are thus derived using eq. (4.5).

Table 4.2: Pressure drops over empty pipe (0.53 m) and 12 KM mixer elements (0.53 m) for the continuous phase fluids (Fluid 1_n and Fluid 1_{nn}).

	Pressure drop, ΔP (empty pipe) (Pa)	Pressure drop, ΔP (12 KM elements) (Pa)	Calculated value of K_L from eq. (4.5)	Re (-)
#1 _n (Newtonian)	1200	8122	6.77	88
#1 _{nn} (non-Newtonian)	1060	5040	4.77	91
#2 (non-Newtonian)	1120	5200	4.64	91

$$\Delta P_{sm} = \Delta P_{empty} K_L \quad (4.5)$$

The K_L value of 6.77 for the Newtonian fluid agrees well with the literature value (Allocca and Streiff, 1980) of 6.9. Although this approach is not applicable for the non-Newtonian fluid due to the Herschel-Bulkley constitutive law, the value of $K_L = 4.77$ is significantly

different from the Newtonian value. Notably, the pressure drops obtained from experiments #1_{nn} and #2 are quite similar, despite the addition of the minor flow of Fluid 2_{nn} in experiment #2.

4.3.2. Images obtained from PLIF technique

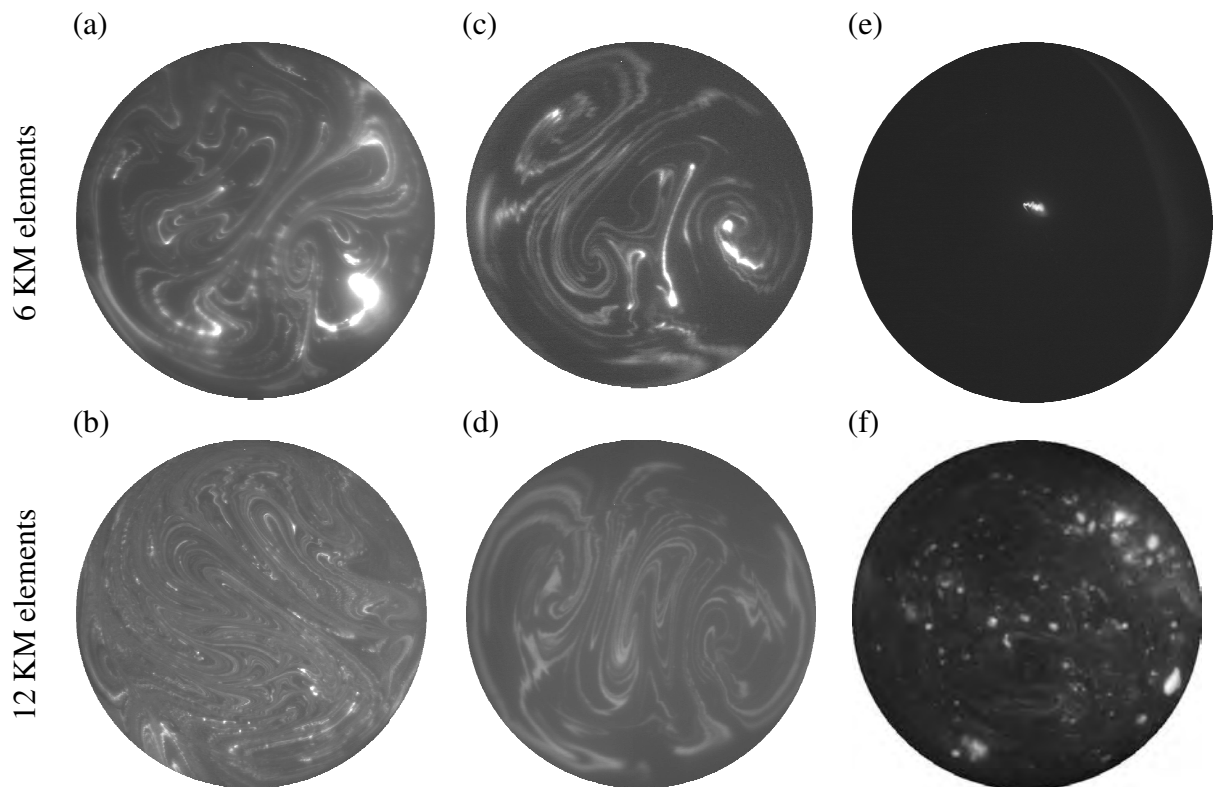


Figure 4.4: Raw PLIF Images. (a) and (b) show #1_n for 6 and 12 elements; (c) and (d) show #1_{nn} for 6 and 12 elements and (e) and (f) show #2 for 6 and 12 elements respectively.

Raw PLIF images obtained from each experiment are shown in Figure 4.4. The images show the distribution of dye tracer in the cross section of the pipe after both 6 and 12 elements of KM static mixer for each experiment. In the case of Newtonian blending (experiment #1_n), there is a notable reduction in the observed striation thickness when the number of elements is increased (Figure 4.4a and 4.4b), with the overall mixing pattern showing evidence of stretching and folding which is typical for KM static mixers (Alberini F *et al.*,2012). A bright spot of dye is observable in the bottom right hand corner of the image in Figure 4.4a suggesting some bypassing of the dye stream, however this is no longer noticeable in Figure 4.4b, after an additional 6 KM elements.

For the non-Newtonian blending experiment, a similar reduction in striation thickness is observed when the number of elements is increased (Figure 4.4c and 4.4d). However, the pattern of striations is markedly different. Since the flow conditions between experiments #1_n and #1_{nn} are identical, the differences must be due to the fluid rheology which leads to a different distribution of shear stresses, and thus shear rates and velocities, within the mixer geometry which manifests itself as changes in the striation patterns.

A dramatic change in mixing behaviour is observed for experiment #2. No mixing at all is observed after 6 elements (Figure 4.4e) and the dye remains as a central bright spot as injected into the mixer. This suggests that the dye stream has bypassed the elements. However, after 12 elements (Figure 4.4f), some splitting has occurred as the majority of the stream has been ‘shattered’ into a series of smaller bright spots. Some of the stream has, however, been blended by the mixer, leading to a conventional mixing pattern with thin striations observable in the background.

4.3.3. Analysis of Mixing Performance from PLIF Images

Values of CoV determined for all experiments using eq. (3.2) are given in Table 4.3.

Table 4.3: CoV_r from experimental data and eq. (2.31).

	Measured CoV	Measured $CoV_r = \frac{CoV}{CoV_0}$	Theoretical $CoV_r = K_i \frac{L}{D}$
#1 _n 6 elements	0.156	0.006	0.052
#1 _n 12 elements	0.089	0.003	0.003
#1 _{nn} 6 elements	0.264	0.101	0.052
#1 _{nn} 12 elements	0.089	0.003	0.003
#2 6 elements	0.484	0.186	0.052
#2 12 elements	0.193	0.074	0.003

Notable differences are observed between each experiment; unsurprisingly experiment # 2 gives by far the worst performance. Comparison of experimental values of CoV_r with eqn (2.31) with K_i = 0.87, shows good agreement for the Newtonian case (#1_n). CoV₀ was calculated based on the unmixed volume fraction at the inlet C_v = 0.13 using (Etchells A W *et al.*,2004)

$$CoV_0 = \left(\frac{1 - C_v}{C_v} \right)^{0.5} = 2.6 \quad (4.6)$$

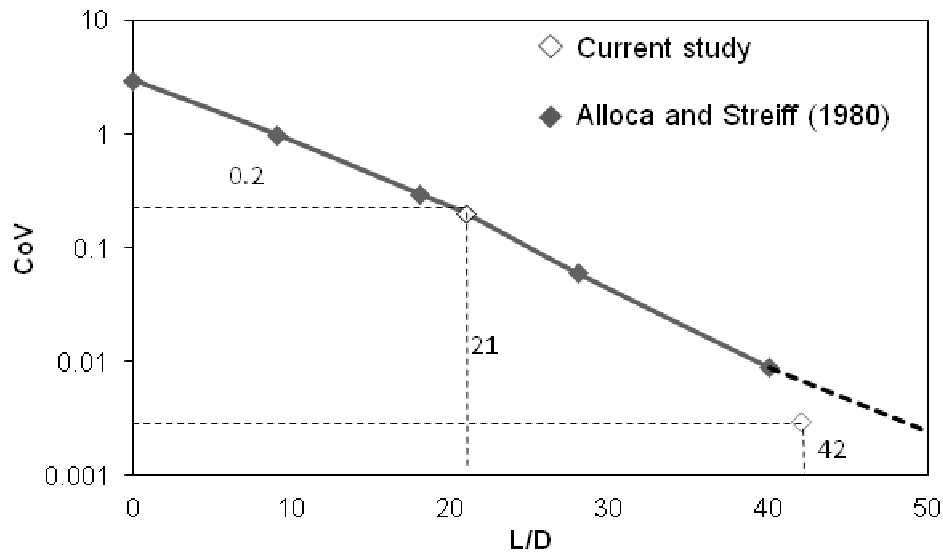


Figure 4.5: Coefficient of variation (CoV) data from Alloca and Streiff compared with the present study.

Figure 4.5 gives a comparison of the measured CoV with the CoV data obtained by Alloca and Streiff (1980) for a KM mixer blending Newtonian fluids where flow rate is 10% of the main flow, close to that in this work. Their range of L/D covers experiment #1_n with 6 elements where L/D is ~21. Their value of CoV is ~0.2 which is very close to the value of CoV = 0.17. Extrapolating their data to an L/D of 42 produces a CoV which is a conservative estimate of the result obtained from this study.

It is of interest to consider the mixing performance of the experiments in terms of the mechanical energy input to the process, since from an industrial perspective this defines the size of the pump and thus capital and running costs.

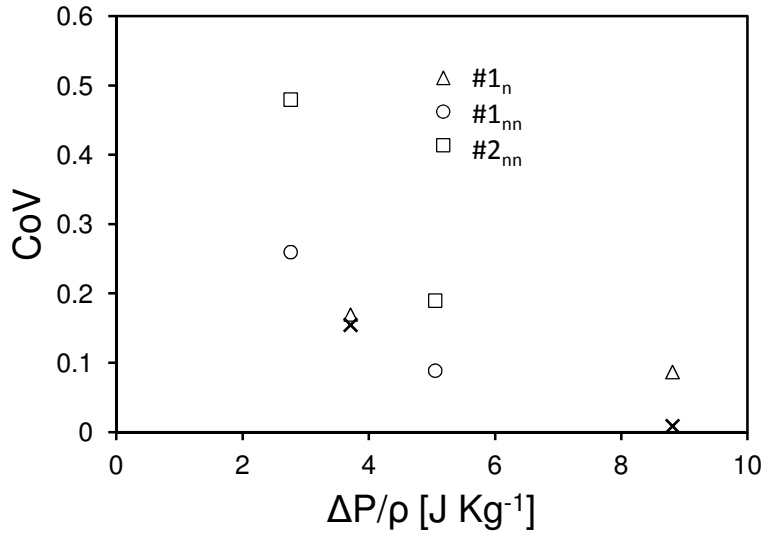


Figure 4.6: CoV versus $\Delta P/\rho$ for all the experiments developed for this work compared with eq. (2.31) (x in the plot).

Experimental and theoretical values of CoV from Table 4.3 are plotted in Figure 4.6 versus the energy inputted into the flow per unit mass of pumped fluid, expressed as the measured $\Delta P/\rho$ (J kg⁻¹), where ρ is the fluid density. Clear differences in the degree of mixing obtained are observed for each of the experiments. Since this parameter does not include viscosity ratio it does not collapse the data: experiments #1_{nn} and #2 have ostensibly the same pressure drop (Table 4.2), sharing the same continuous phase, yet a very different mixing performance is observed. Overall, experiment #1_n and experiment #2 give the best and worst performance, as before. Theoretical values of CoV using eq. (2.31) show some agreement with data from experiment #1_n. It is clear that existing published data cannot account for the effects of non-Newtonian rheology or viscosity ratio.

Kukukova *et al.* (2009) described the complexities of mixing processes and highlighted the need to consider a multidimensional approach to the problem, including the intensity and scale of segregation.

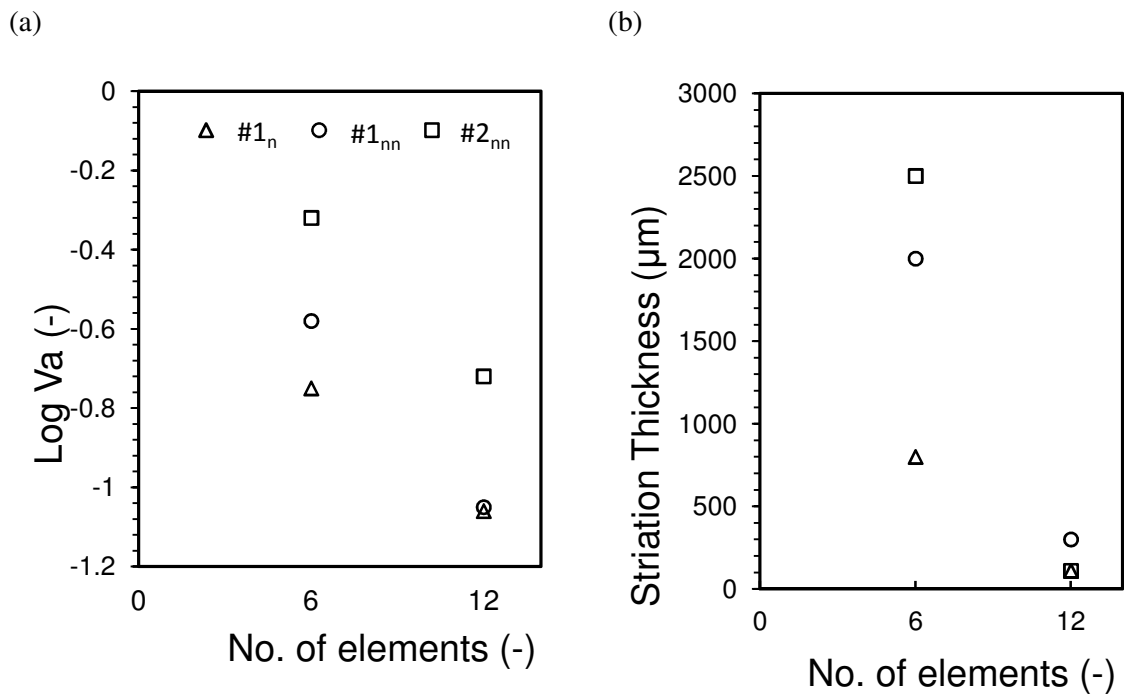


Figure 4.7: Comparison of (a) intensity (log-variance) and (b) scale of segregation (maximum striation thickness) obtained from the PLIF analysis.

The intensity (LogVa) and scale of segregation (maximum striation thickness), are plotted in Figures 4.7a and 4.7b respectively as a function of the number of KM mixer elements. Figure 4.6a shows that, unsurprisingly, values of LogVa decrease significantly when the number of mixing elements increases for all experiments. The final values produced are a function of the fluid rheology in all cases, apart from the agreement between experiments #1_n and #1_{nn} when 12 elements are used. In contrast, the average striation thicknesses (Figure 4.7b) show a different trend. It should be noted that the thicknesses of the measured striations are all much larger than the resolution of the PLIF camera. Remarkably, experiment #2 gives the ‘best’ performance with the lowest average striation thickness for 12 elements. This can be explained by the relatively few striations in experiment #2 skewing the striation distributions, due to lack of mixing and no distinction between striations where the fluids are mixed or where there is not mixing at all. This reinforces the danger of only considering either LogVa or striation thicknesses in isolation when determining overall mixing quality (Patel, Ein-

Mozaffari et al. 2011) and has led to the development of the approach proposed below which considers both the scale and intensity of segregation in conjunction.

4.3.4. Areal Distribution of Mixing Intensity

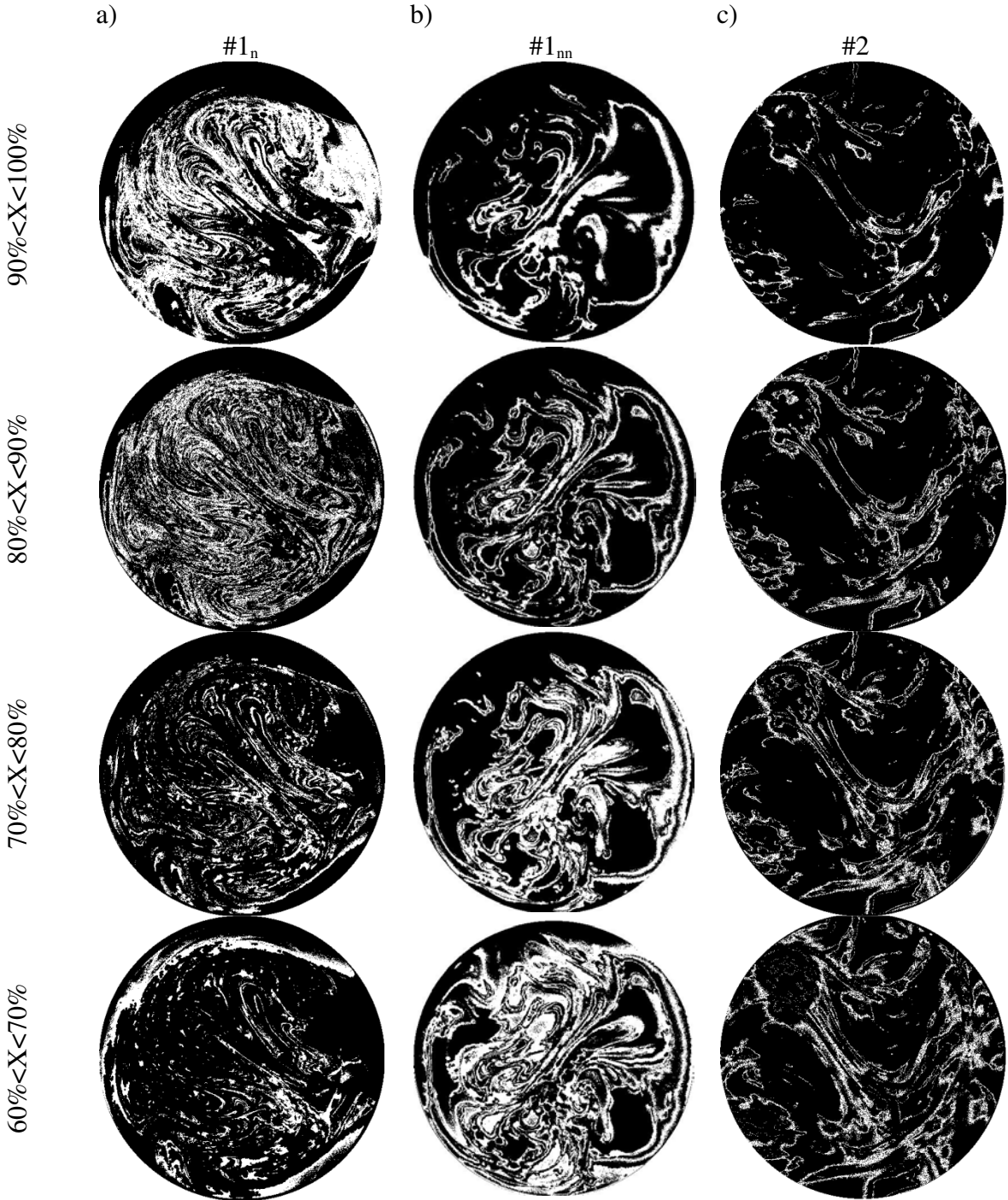


Figure 4.8. Application of the areal mixing analysis to the PLIF images obtained for 12 KM mixing elements. Discrete distributions are shown for (a) experiment #1_n, (b) experiment #1_{nn} and (c) experiment #2 respectively. Areas in white are within the range of interest.

Images obtained from the areal based analysis are given in Figure 4.8 for each experiment when performed using 12 KM mixing elements. The images show the areal regions corresponding to discrete distributions of intensity, X , as shown, between $60\% < X < 100\%$. Examining the images in Figure 4.8 further, white areas can be identified which are individual striations consistent with those observable in Figure 4.4. This is as would be expected from the mixing mechanism of stretching, cutting and folding which will produce striations with a similar CoV or log-variance. However, the analysis is not capable of determining the boundaries of individual contiguous striations (which would be a useful future development) since it only considers the intensity values on a pixel by pixel basis.

It is notable in all the images in Figures 4.4 and 4.8 that there is an alignment of the striations with the blade of the last element, which runs from the top left to the bottom right in all of the images. However, the striation distributions are not symmetrical from one side of the mixer to the other. This is most apparent for the non-Newtonian experiments shown in Figures 4.8 b and 4.8c and may be reflective of non-linearities introduced by the non-Newtonian rheology. Large black areas corresponding to unmixed regions ($X < 60\%$) are observable, these may be suggestive of regions where the fluid is travelling as a solid plug, with relatively low shear rates due to the yield stress and shear thinning nature of the fluid; however this cannot be proven without a full 3D flow simulation or experimental measurement. These regions are again much larger than for the Newtonian case. The distributions show that regions with mixing $>90\%$ are confined to a few striations which appear to be relatively thick compared with the large numbers of thin striations corresponding to lower mixing levels (e.g. $60\% < X < 70\%$). Regions of mixing intensity close to 100% would be identifiable as those where the mixing has led to homogeneity to within $10\ \mu\text{m}$ (the resolution of the experiments).

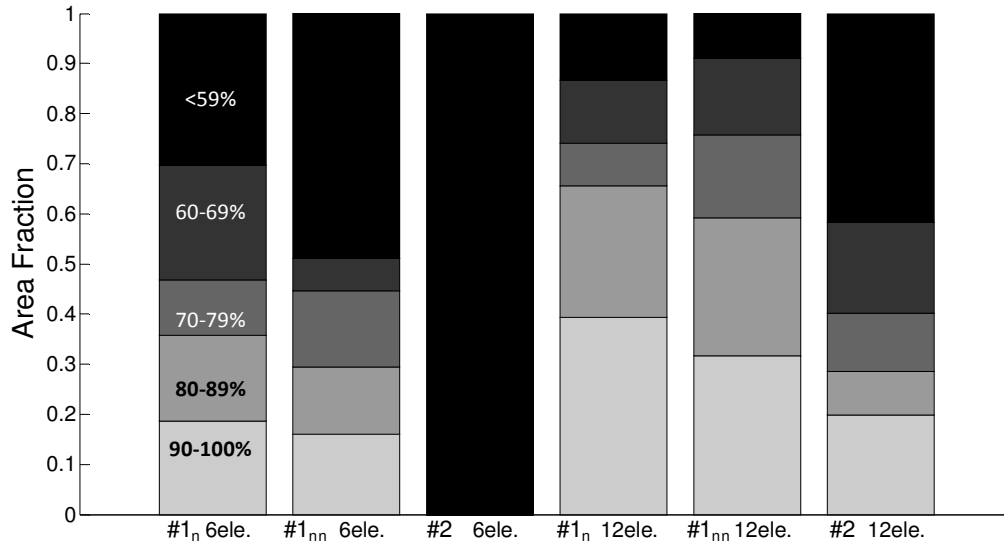


Figure 4.9: Bar graph showing discrete areal intensity distributions for each experiment.

The discrete distributions of area fraction as a function of mixing intensity are plotted as a bar graph in Figure 4.9. This presentation enables quantification of the mixing performance between each experiment and shows the improvement in all cases when 12 KM elements are used instead of 6 elements. The areal fraction for $X > 90\%$ approximately doubles from 19% to 39% for experiment #1_n; corresponding values for experiment # 2 are 15% and 32% for 6 and 12 elements respectively. Since no mixing occurred for experiment #2 when 6 KM elements are used (Figure 4.4e), this is reflected in an overall mixing intensity $<59\%$ across the whole cross section.

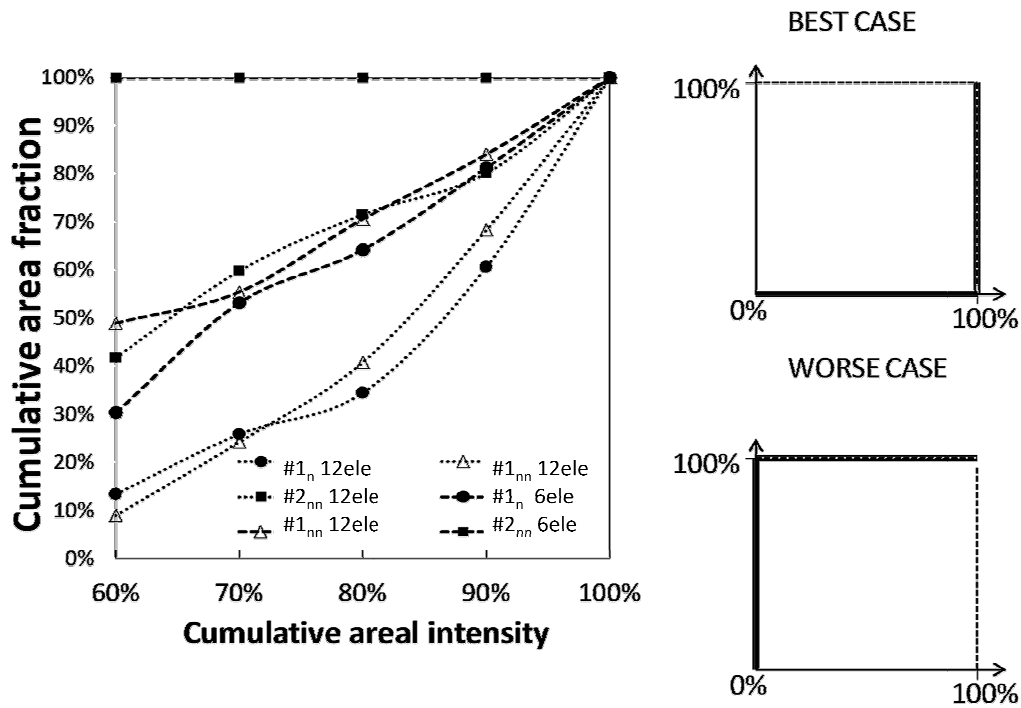


Figure 4.10: Cumulative areal intensity distributions as a means of determining relative mixing performance between experiments.

An alternative visualisation of the data is given using the cumulative distributions plotted in Figure 4.10, where the overall performance can be assessed compared with the idealised cases of 100% mixing (best case) and 0% mixing (worst case) given on the right hand side of the figure. This presentation enables the mixing performance between the experiments to be ranked as: #1_n 12 elements > #1_{nn} 12 elements > #1_n 6 elements > #1_{nn} 6 elements > #2 12 elements. In performing this comparison a higher weighting is given to the area fractions with a higher mixing intensity for the worst performing cases, since there is some overlap in the cumulative distributions.

Further insight into the mixing can be obtained by examination of the distribution of grayscale values, G , in the PLIF images, as shown in Figure 4.10 for the experiments performed with 12 KM elements.

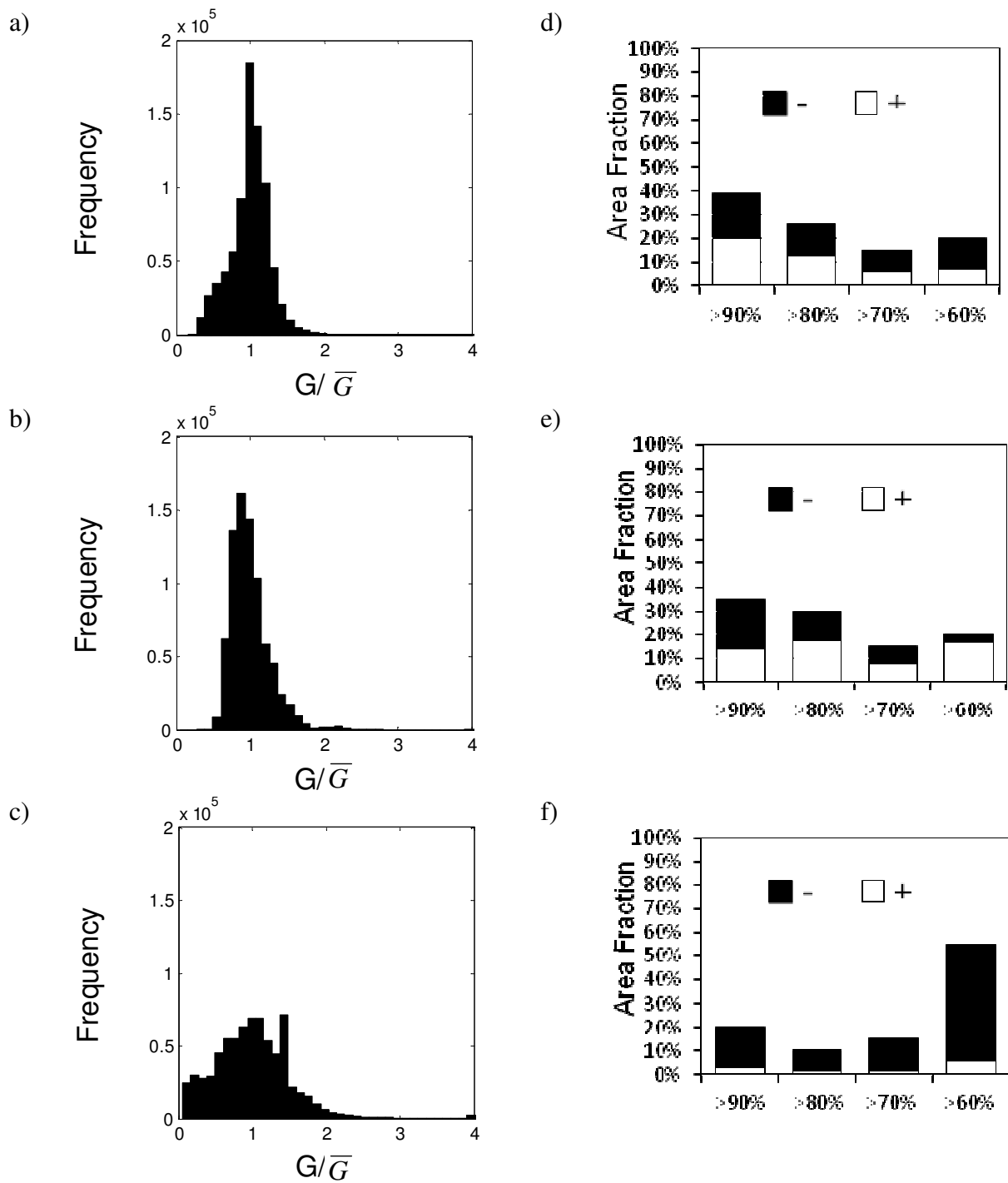


Figure 4.11: Gray scale distributions for (a) experiment #1_n and (b) experiment #1_{nn} and (c) experiment #2, all carried out with 12 KM elements. Sub figures (d), (e) and (f) show the breakdown of area fraction due to G_{X-} and G_{X+} for experiments #1_n, #1_{nn} and #2 respectively.

Grayscale distributions for experiments #1_n, #1_{nn} and #2, are shown in Figures 4.11a, 4.11b and 4.11c respectively. Values of \bar{G} are also marked on the figures. A greater skew in the distributions is observable for the non-Newtonian experiments, which has led to further analysis to determine the cumulative fractional contribution of both the G_{X-} and G_{X+} components for a given degree of mixing in Figures 4.11d, 4.11e and 4.11f. .

The G_{X-} and G_{X+} fractions are approximately even for experiment #1_n, but are biased towards the G_{X+} component for experiment #1_{nn}. Reasons for this are unclear, but may be related to the remarkably few pixels possessing low grayscale values in Figure 4.11b, leading to a negative skew on the distribution. For experiment #2 (Figure 4.11d) the G_{X-} fraction dominates: this can be attributed to the generally poor mixing performance for this experiment, with the higher concentrations of dye being isolated in the bright spots observed in Figure 4.4f.

4.4. Conclusions

Analysis of PLIF images has been performed to determine the mixing performance of KM static mixers using Newtonian and non-Newtonian aqueous solutions as a function of number of elements and viscosity ratio of the two fluids. Analysis of the data using log variance for intensity of segregation and striation thickness for scale of segregation has demonstrated the importance of considering both aspects in tandem for correct interpretation of the mixing performance; considering only a single measure is a known problem in the literature (Kukukova *et al.* 2009; Kukukova *et al.* 2011). A method is presented which considers the distribution of the cross sectional area with a given intensity of mixing, this areal analysis combines both intensity, in terms of log-variance, and scale, in terms of the fraction of the cross section with a given intensity. The method shows promise for the evaluation of mixing performance and can be considered as an addition to conventional approaches. The analysis does also to some extent identify striations of similar intensity, but identification of individual

contiguous striations would be a useful future development. The identification of areas in the pipe cross-section with a given range of log-variance enables identification of regions where the mixing is performed down to the micro-scale, but also unmixed or poorly mixed regions in the flow. The analysis of PLIF images allowed the detection of viscous stream filaments evident as spots when a fluid of higher viscosity was injected into a lower viscosity continuous phase, which is not predictable using conventional design approaches. This new method shows promise in unravelling the complexity of information-rich PLIF images, beyond a sole number-based mixing criterion.

CHAPTER 5

5. USE OF PLIF TO DETERMINE THE EFFECT OF SYSTEM AND FLUID PARAMETERS UPON THE BLENDING OF SHEAR-THINNING FLUIDS IN KM STATIC MIXERS.

5.1. Introduction

For industries manufacturing complex fluid products to remain competitive in the global marketplace, it is vital for them to maintain and retain leading edge technical capabilities for the development of new products and their manufacture. Across many sectors (e.g. food, pharmaceuticals, catalysis), these fluid products possess a complex (non-Newtonian) rheology. Whilst most traditional processing of complex fluids is carried out in batch plant, continuous processing is becoming increasingly attractive due to lower energy costs, decreased plant footprint and reduced inventory. However, development of reliable continuous plant requires that the capabilities of each unit operation are well understood; in terms of mixing and blending operations the in-line static mixer is a common choice and has established itself as a workhorse of the chemical industry (Paul et al., 2004).

Whilst there is a reasonable amount of data and design information available for static mixers to blend Newtonian materials (Shah and Kale, 1991), and analysis of mixing performance characterising the influence of viscosity in terms of the coefficient of variation (CoV) (Ventresca *et al.*, 2002), there is a lack of published material on non-Newtonian mixing. Understanding of blending non-Newtonian fluids has concentrated upon fluid dynamical aspects, which tend to focus on measured pressure drop as a function of rheology (Chandra and Kale, 1992), or to determine velocity profiles, (e.g. for the Kenics (KM) static mixer using Laser Doppler Anemometry (Adamaik and Jaworski, 2001), (Peryt-Stawiarska and Jaworski, 2011) or 3D Eulerian velocity maps using PEPT (Rafiee *et al.*, 2013) rather than mixing quality. Tozzi *et al.*, (2012) used a different approach to determine mixing performance in static mixers quantifying the mixedness from rheological perturbations using MRI. Although these data are fundamental for the understanding of non-Newtonian fluid behaviour and some have been used to verify CFD simulations (Peryt-Stawiarska *et al.*, 2008), (Rahmani *et al.*, 2006), it is difficult to find any experimental work using non-Newtonian fluids where an analysis based on concentration distribution is performed, even though this is the most direct way to define if two fluids are mixed. Of critical importance is the choice of method or algorithm used to determine mixing performance. The traditional approach for the calculation of mixing quality in low Reynolds number (laminar) flows is to assess either the distribution of the concentration of a passive scalar, C_i , via a statistical approach, leading to the calculation of CoV, or to examine the size of the striations (Kukukova *et al.*, 2011) present due to the chaotic flow pattern induced in the static mixer Alberini *et al.*,(2013) and Kukukova *et al.*,(2009) showed the importance of consideration of both these criteria together in assessing mixing performance. In isolation, misleading interpretations could be made since, for example, calculation of a maximum striation thickness as a mixing parameter does not consider whether fluid within each striation is well

mixed. Conversely, CoV does not give information on the spatial distribution of the concentration. Thus, both the scale (spatial distribution) and intensity (concentration variance, CoV) must be considered in tandem and not as separate independent criteria before conclusions are drawn. Different approaches to determine the scale of segregation have been compared by Kukukova *et al.*(2011)where the maximum striation thickness was considered the fastest method in terms of processing time, but with some limitations in terms of characterisation of the whole system. The results of this analysis are concentrated in sample data that cannot describe a complex mixing pattern generated by the blending of non-Newtonian fluids. Other approaches (Kukukova *et al.*, 2011) are proposed showing more accurate results but with very high processing times, however in all these approaches when the striation thickness decreases (Spencer *et al.*, 1951), the two viscous liquids are better mixed. Taking into account the complexity of the mixing of shear thinning fluids, a different point of view to determine the scale of segregation has to be considered. The striations, generated by the mixing of non-Newtonian fluids, have a complicated lamellar structure with a strongly asymmetric distribution. A precise analysis of striation shape, size and mixing intensity is key to understanding such complex systems and their mixing mechanisms. In this work, CoV, maximum striation thickness and the areal based analysis are combined with an additional characterisation of the number and area of striations with two ranges of mixing intensity $80 < X < 90\%$ and $X > 90\%$, i.e. when the striations are ‘well mixed’. These are used to assess the effect of critical physical parameters and scale upon the performance of a KM static mixer equipped with six elements for the blending of two shear thinning fluids, where a minor secondary flow is blended into a major primary flow. The physical parameters examined are fluid superficial velocity ($0.1 - 0.6 \text{ m s}^{-1}$), mixer size (0.5-1”), the volumetric flow ratio between the primary and secondary flows (10:1 and 25:1) and changing the

rheology of the secondary flow. Finally, the effect of the position of injection of the minor flow at the mixer inlet, either at the centre or at the wall, is considered.

5.2. Material and Methods

5.2.1. Fluids and Flow Conditions

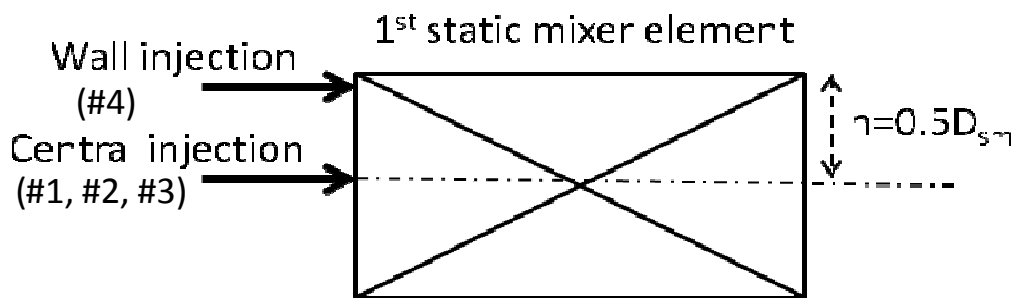
In this chapter non-Newtonian solutions are used. The fluids used are the same as used in Chapter 4 (Fluid 1 and Fluid 2) and their rheological characterisation and physical properties are given in §3.2.1. The two fluids were chosen to study the effect of injection of a more viscous fluid into a less viscous fluid, the core focus of this work. The remainder of the experimental design was made to consider the effect of superficial velocity, mixer scale, flow ratio, viscosity ratio and injection position whilst holding other variables constant. A baseline superficial velocity of 0.3 m s^{-1} was taken for all experiments, corresponding to a total volumetric flow rate of 180 L hr^{-1} at $1/2''$ scale and 600 L hr^{-1} for $1''$ scale. On the basis of these requirements, four different experiments were performed, as shown in Table 5.1 with the core effect of changing viscosity ratio being carried out for each experiment.

Table 5.1 Experimental conditions for all experiments.

Experiment	Injected fluid and position of injection	Superficial Velocity (v)			Flow ratio (FR)	ID	Codes
		0.1 [ms ⁻¹]	0.3 [ms ⁻¹]	0.6 [ms ⁻¹]			
#1a	1 Central	✓	✓	✓	10	½"	KM ₁ ID _{0.5} FR ₁₀
#1b	2 Central	✓	✓	✓	10	½"	KM ₂ ID _{0.5} FR ₁₀
#2a	1 Central	✓	✓	✓	10	1"	KM ₁ ID ₁ FR ₁₀
#2b	2 Central	✓	✓	✓	10	1"	KM ₂ ID ₁ FR ₁₀
#3a	1 Central	-	✓	-	25	1"	KM ₁ ID ₁ FR ₂₅
#3b	2 Central	-	✓	-	25	1"	KM ₂ ID ₁ FR ₂₅
#4a	1 Wall	-	✓	-	25	1"	KM ₁ ID ₁ FR _{25W}
#4b	2 Wall	-	✓	-	25	1"	KM ₂ ID ₁ FR _{25W}
Size		Re					
		0.1 [m s ⁻¹]	0.3[m s ⁻¹]	0.6 [m s ⁻¹]			
½" (#4)		20	91	245			
1 (#1,#2,#3)		26	150	394			

The effect of system and fluid parameters upon the blending of shear-thinning fluids were investigated systematically: the effect of superficial velocity is examined for the ½" mixer in experiment #1 and for 1" mixer in experiment #2. The effect of scale can thus be considered by comparing these two experiments. Similarly, the effect of flow ratio may be examined by

comparing experiments #2 and #3 and the effect of injection position by comparing experiments #3 and #4. The static mixer rig used in these experiments is described in §3.4.1 and equipped with six KM elements. In Figure 5.1 the static mixer dimensions are tabulated together with a figure showing the secondary flow inlet dimensions and injection position.



	Flow ratio	Diameter static mixer (D_{sm}) [m]	Diameter injection (D_i) [m]
1/2"	10	0.0127	0.004
1"	10	0.0254	0.008
1"	25	0.0254	0.005

Figure 5.2 Injection position and static mixer dimension used for the experiments of Chapter 5.

5.2.2. Characterisation of mixing performance from the PLIF images

The raw images are processed using MATLAB to evaluate CoV and striation thickness as described in §3.3.1.1 and §3.3.1.2. The areal method is also used and a full description is given in the previous Chapter in §4.2.2. The distribution of striations with high mixing intensity is obtained using a MATLAB script which has been developed to use both the MATLAB image toolbox and the DIPimage toolbox developed by TU Delft. The analysis allows the detection of the striations with a selected range of mixing intensity and the evaluation of their corresponding areas and perimeters. These features are evaluated using the

command ‘measure’ which produces a matrix where the number of columns are the number of detected objects on the image and different rows correspond to different measurement. In this analysis only two of the multiple options are used: they are ‘size’ for the area and ‘Perimeter’ for the perimeter.

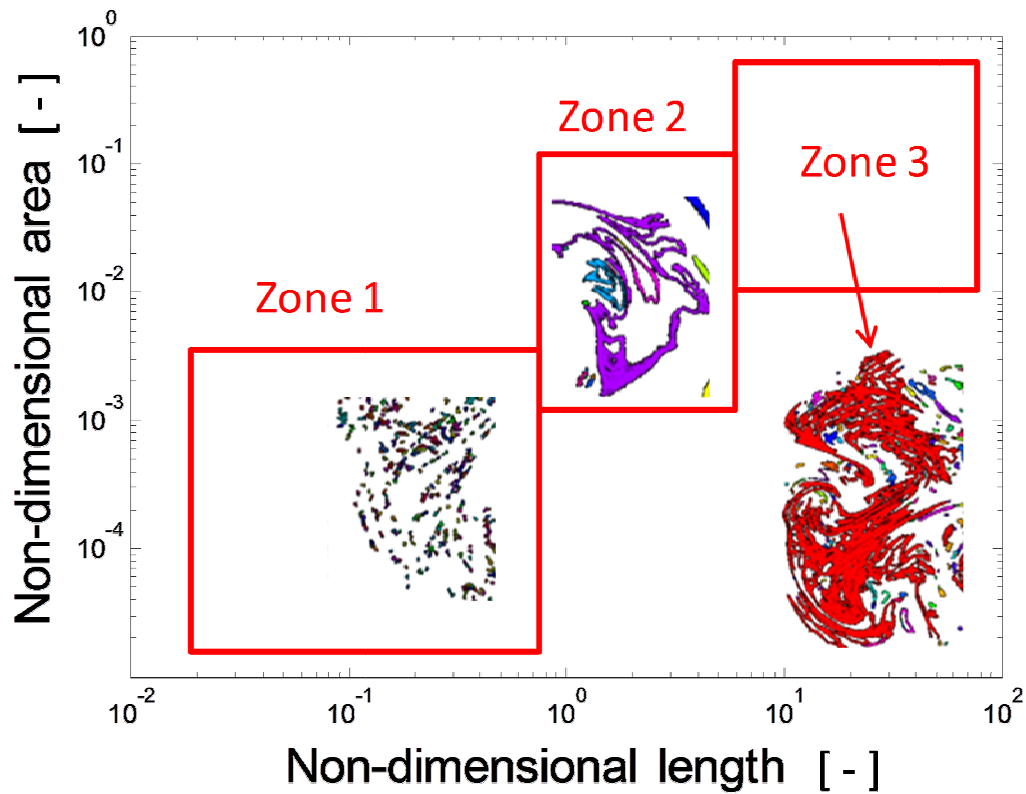


Figure 5.3 Three different zones that describe the size of striation with high mixer intensity in terms of non-dimensional area and perimeter.

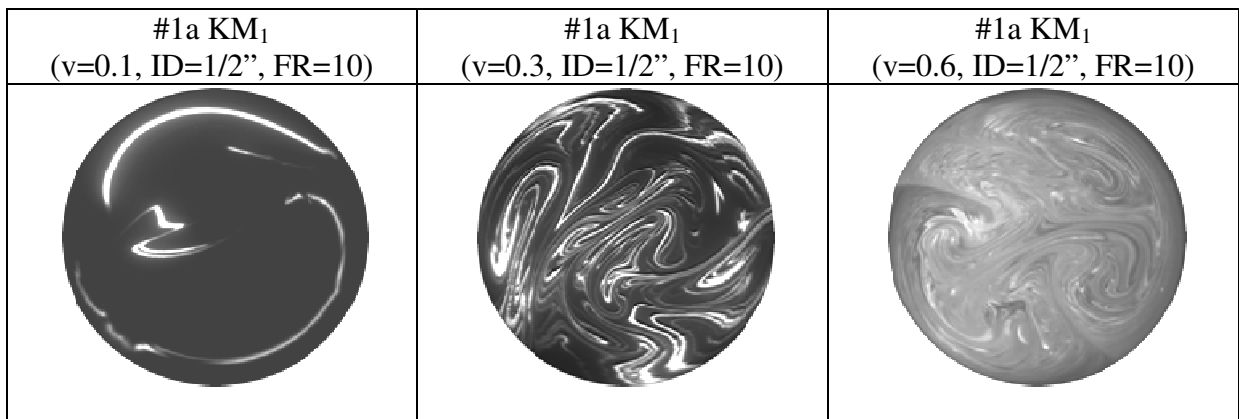
The obtained data are plotted following the structure presented in Figure 5.2. The y axis of the presented graph is a non-dimensional area that is given by the area of the striation over the area of the cross section of the injection; whilst the x axis is the non-dimensional length of the striation evaluated by the perimeter of the striation divided by the perimeter of the injection. The graph is divided in 3 main zones: zone 1 is characterized by striations with small areas and perimeters; if all measurements are in this zone then mixing is expected to be

poor. Zone 2 is where medium size striations are located: in this group all the striations typical of lamellar structures are included. Zone 3 is characterised by large striations. In this analysis the ranges of mixing intensity are the same as used in the area fraction method, focussing on the two ranges where the intensity is the highest ($X > 90\%$ and $80 < X < 90\%$).

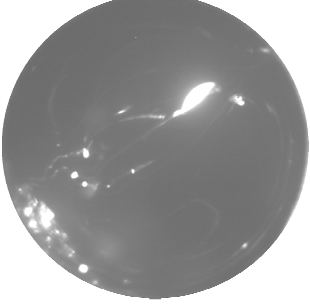
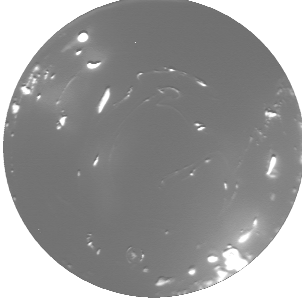
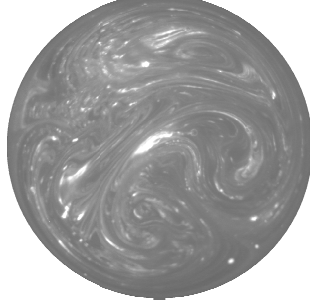
5.3. Results and Discussion

Raw PLIF images obtained for each experiment across the mixer outlet as a function of superficial velocity are shown in Figure 5.3. Again, as in Chapter 4, 10 images were acquired in three batches spaced several minutes apart for each experiment to check for temporal variations, which were not observed.

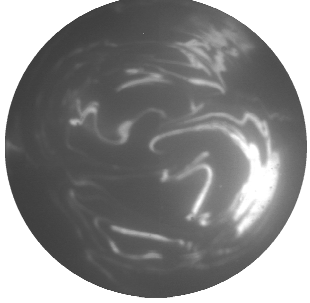

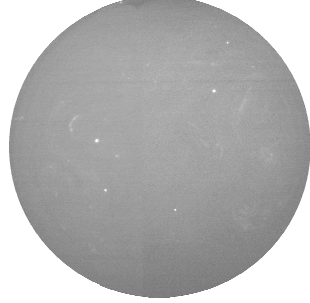
(a)



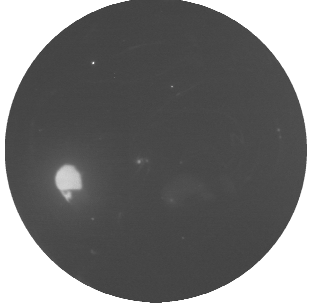
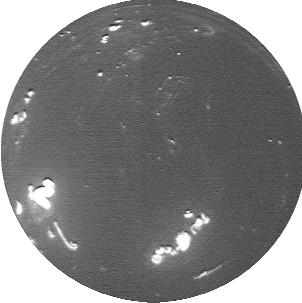
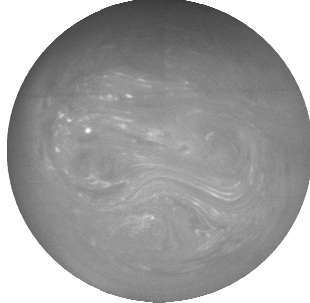
(b)

#1b KM ₂ ($\nu=0.1$, ID=1/2", FR=10)	#1b KM ₂ ($\nu=0.3$, ID=1/2", FR=10)	#1b KM ₂ ($\nu=0.6$, ID=1/2", FR=10)
		

(c)

#2a KM ₁ ($\nu=0.1$, ID=1", FR=10)	#2a KM ₁ ($\nu=0.3$, ID=1", FR=10)	#2a KM ₁ ($\nu=0.6$, ID=1", FR=10)
		

(d)

#2b KM ₂ ($\nu=0.1$, ID=1", FR=10)	#2b KM ₂ ($\nu=0.3$, ID=1", FR=10)	#2b KM ₂ ($\nu=0.6$, ID=1", FR=10)
		

(e)

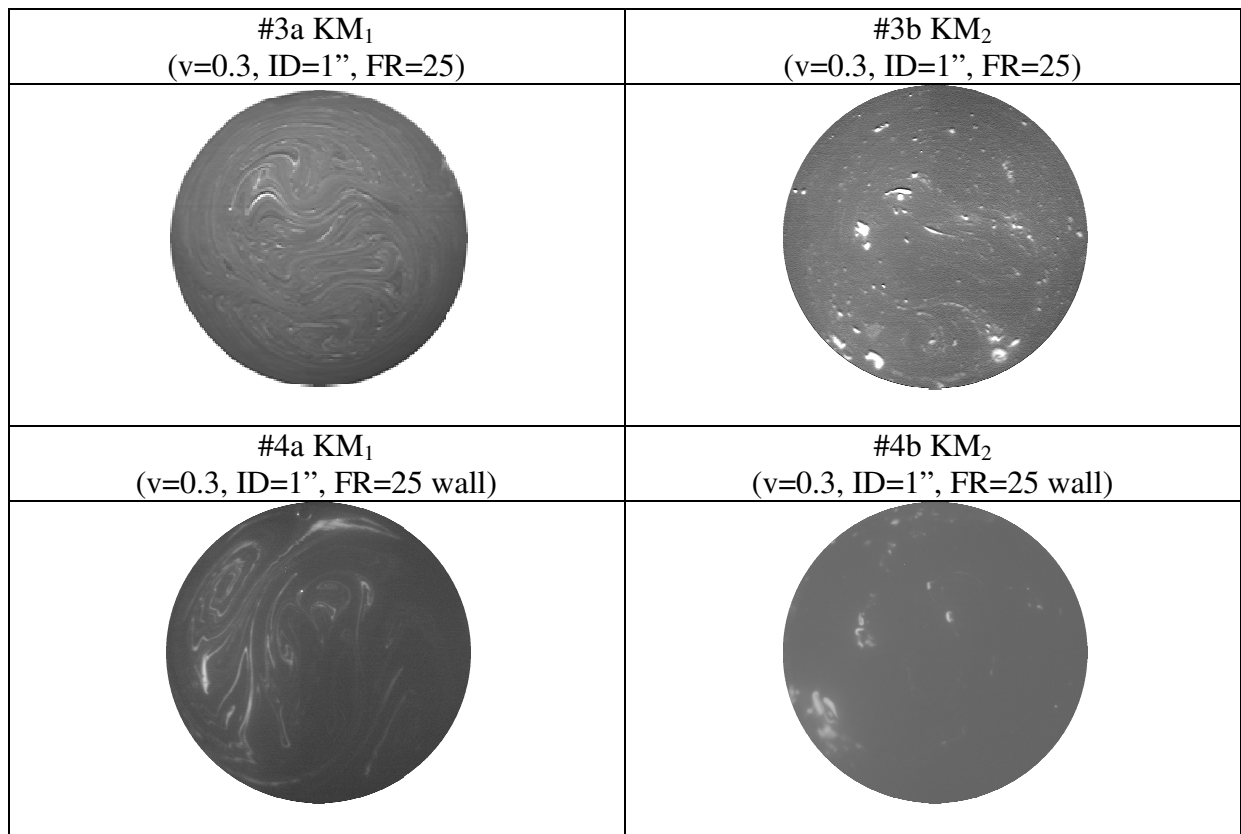


Figure 5.4 Raw images of all experiments: (a) Experiment 1a at different superficial velocities, (b) Experiment 1b at different superficial velocities, (c) Experiment 2a at different superficial velocities, (d) Experiment 2b at different superficial velocities, (e) Experiment 3a,b and 4a,b at the design velocity of 0.3 [ms⁻¹].

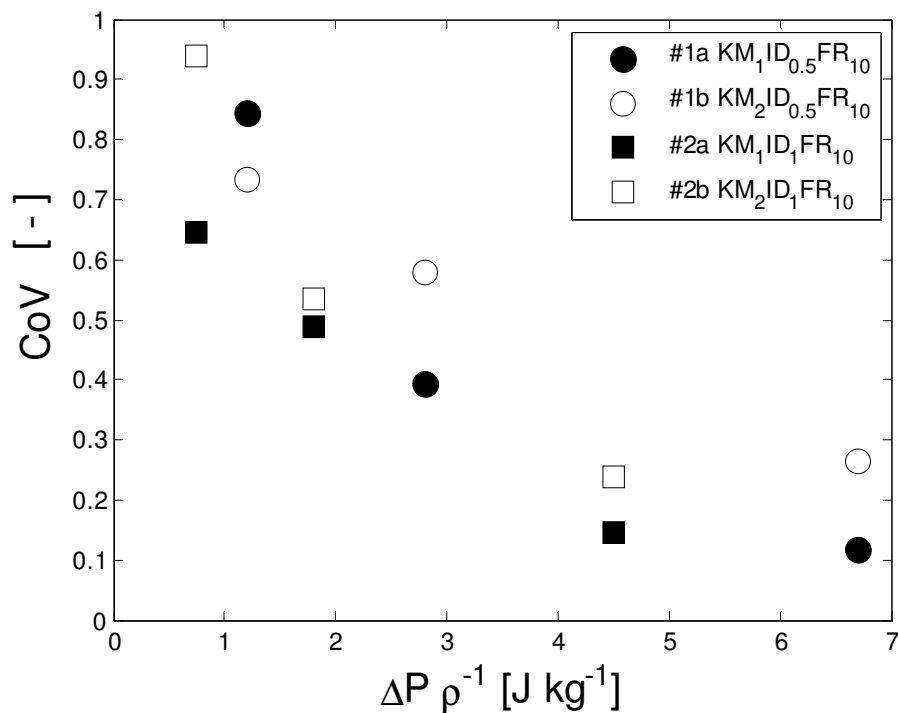
Figure 5.3a shows that pattern of striations radically changes with increasing superficial velocity for experiments carried out using ½" static mixer (#1a), as would be expected. At lower velocities the dye is concentrated in few striations while at higher velocities the number of striations is observed to increase. A similar behaviour is observed at the 1" scale, shown in Figure 5.3c; comparing both scales the PLIF images show the effect of stretching and folding due to the geometry of the mixer elements. As the mixing performance increases, the difference between gray scale values in different striations decreases drastically, and without proper image analysis it is impossible to detect any difference in gray scale values by eye in the cross section, for example, in Figure 5.3c at $v = 0.6 \text{ m s}^{-1}$.

Switching the injected fluid to fluid 2 illustrates the dramatic effect of changing viscosity ratio. Completely different patterns are observed in the images for experiments (#1b) and (#2b) shown in Figures 5.3 b and 5.3d respectively. The presence of fluid 2 causes the formation of viscous unmixed threads identified by spots on the cross section. As velocity increases the spots initially decrease in size then convert into striations as the velocity increases further. The patterns for the experiments performed at the design velocity (#1b, #2b and #3b) are similar but the experiment with higher flow ratio (#3b) is characterized by the presence of a greater number of smaller spots. Experiments carried out with injection of the minor fluid at the wall (#4a and #4b) shown in Figure 5.3e demonstrate completely different mixing patterns compared to similar experiments carried out with central injection (#3a and #3b). For wall injection the dye is concentrated only on half of the cross section.

5.3.1. Effect of velocity for different scales at constant flow ratio

The effects of superficial velocity and injected fluid rheology have been examined more closely by analysis of the PLIF images to obtain measures of mixing, with the aim of gaining a deeper understanding of the complexity of mixing non-Newtonian fluids at different scales. Values of CoV versus $\Delta P/\rho$ are shown in Figure 5.4a; they were determined for both ½” and 1” devices for both injected fluids (#1a&b and #2a&b) at each of the three different superficial velocities used.

(a)



(b)

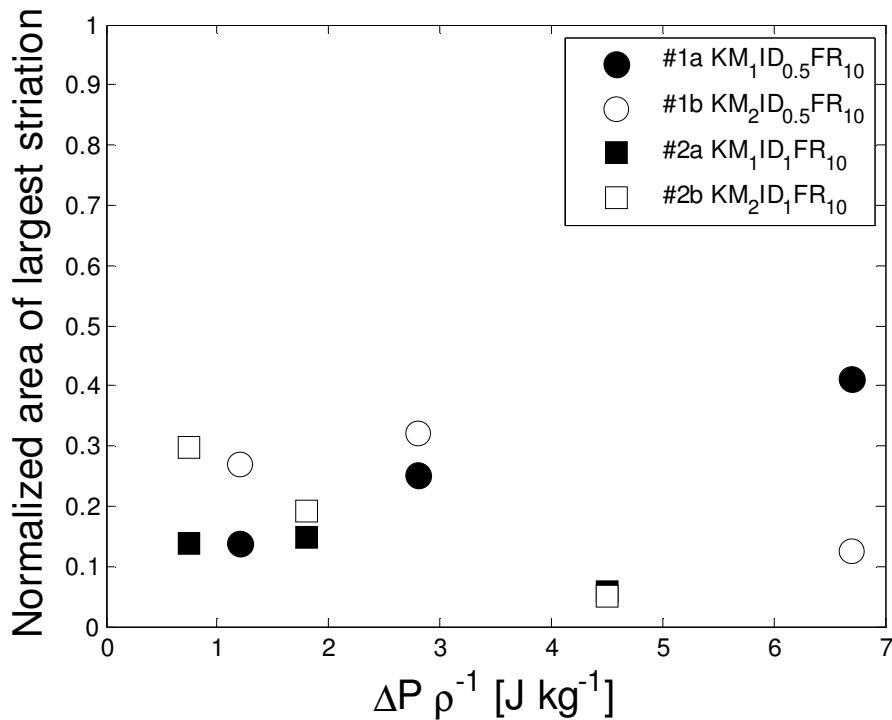
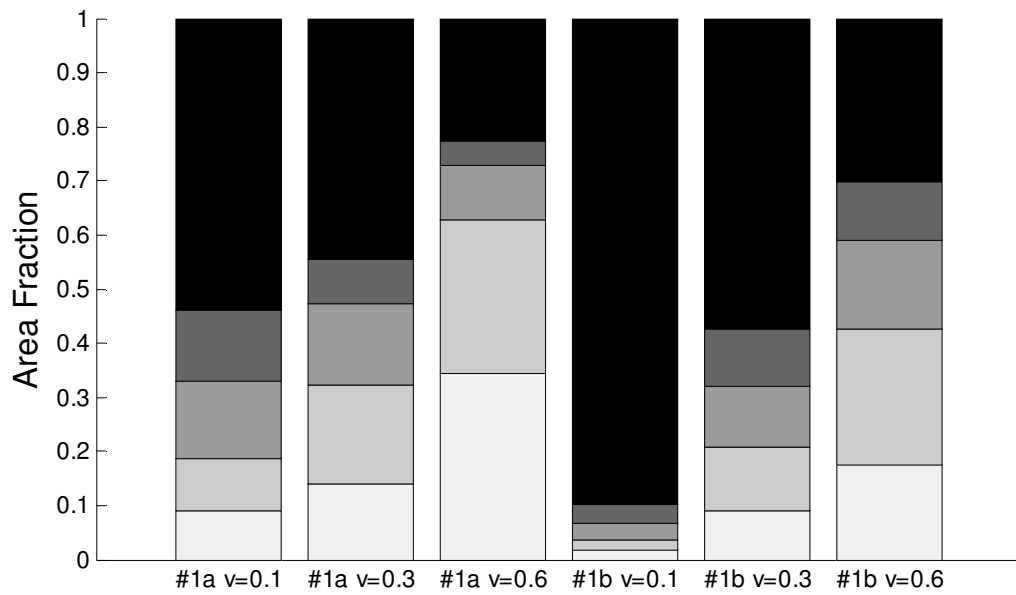


Figure 5.5 Effect of velocity for different scales at constant flow ratio: a) CoV (intensity of segregation) versus $\Delta P/\rho$ and b) max striation area (scale of segregation) versus $\Delta P/\rho$, for #1a&b and #2a&b at selected velocities.

Notable differences are observed between each experiment; unsurprisingly increasing $\Delta P/\rho$, and thus energy input, gives a much improved mixing performance. Injection of the more viscous fluid causes a worse mixing performance; a remarkable exception is observed when comparing values of the CoV between (#1a) and (#1b) at the lowest measured velocity. Also for the 1” experiments (#2a and #2b), the general trend for intensity of segregation is similar (CoV decreases with increasing energy input to the system). The values of CoV in Figure 5.4a are very similar when comparing #1a to #2a and #1b to #2b, though generally the ½” device performs slightly better. However in terms of energy consumed per reached level of mixedness, the 1” static mixer is more efficient. In terms of maximum striation area (Figure 5.4b) different trends are shown between the ½” experiments (#1a) and (#1b). By increasing

the velocity, the area increases in #1a while the opposite trend is observed for #1b. This phenomenon may occur because the mixing of non-Newtonian fluids does not involve a symmetric lamellar structure; the raw images in Figure 5.4 show the generation of many large zones of poor mixing. However the evaluation of mixing performance based upon a single criterion, as previously explained, can create misleading or uncertain results. For the 1” experiments (#2a and #2b), the trend of maximum striation thickness is unclear. The sizes (Figure 5.4b) are always greater for 1” and this can be explained by the larger dimensions of the system, but at both scales the injection of fluid 2 gives greater maximum striation thicknesses. Though a general conclusion may be extrapolated from this introductory analysis, a deeper approach is needed to classify and compare different experiments with such complex patterns. This has been carried out in the rest of this paper using the areal method and the distribution of striation size.

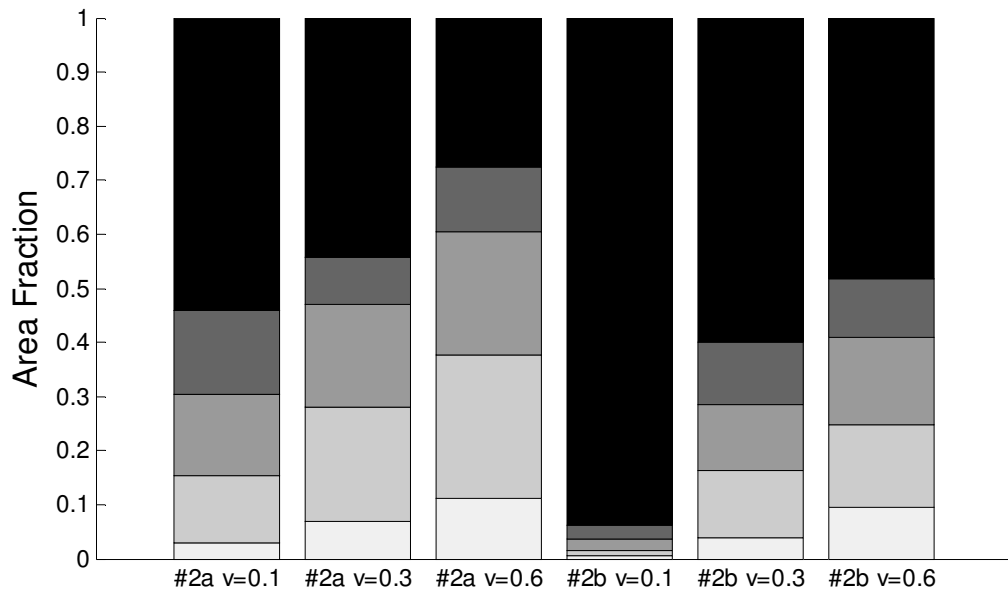
(a)



X<60% 60<X<70% 70<X<80% 80<X<90% 90<X<100%

Figure 5.6a Bar graph showing discrete areal intensity distributions (a) for #1a&b and (b) #2a&b at selected velocities (scale of static mixer: 1/2", central injection, flow ratio 10, KM).

(b)



X<60% 60<X<70% 70<X<80% 80<X<90% 90<X<100%

Figure 5.7b Bar graph showing discrete areal intensity distributions (a) for #1a&b and (b) #2a&b at selected velocities (scale of static mixer: 1", central injection, flow ratio 10, KM).

Figure 5.5a shows the distribution of different mixing intensities for experiments #1 and #2 in terms of area fraction from the areal method. As expected the fraction for $X > 90\%$ increases with increasing velocity, almost at the same rate as $X < 60\%$ decreases. The divergences between experiment #1a and #1b are clear in terms of absolute fraction values at different mixing intensities, where the experiment with the injection of fluid 1 (#1a) performs always better than the injection of fluid 2 (#1b). Whilst CoV analysis showed a higher coefficient for #1b at the lower velocity is clear on the bar graph that this evaluation was incorrect. The effect of increasing velocity is strongest in experiment (#1b). Figure 5.5b shows the distribution of mixing intensity for 1" experiments (#2a and #2b) at different velocities. The general trends are similar to the 1/2" experiments but the absolute values of different levels of mixing intensity are different. Increasing the velocity increases the fraction of mixing intensity for $X > 90\%$ as expected, but the ratio between #2a and #2b decreases. The fraction of mixing intensity for $80 < X < 90\%$ increases maintaining a constant ratio between the different injections (#2a and #2b). Comparing Figure 5.5a with Figure 5.5b, as expected the fraction of $X > 90\%$ is higher with the injection of fluid 1 at both scales, but is doubled for the 1/2" mixer when compared to the 1" mixer. The overall 'best' performance in terms of mixing intensity (#1a and #1b) is thus for the 1/2" static mixer.

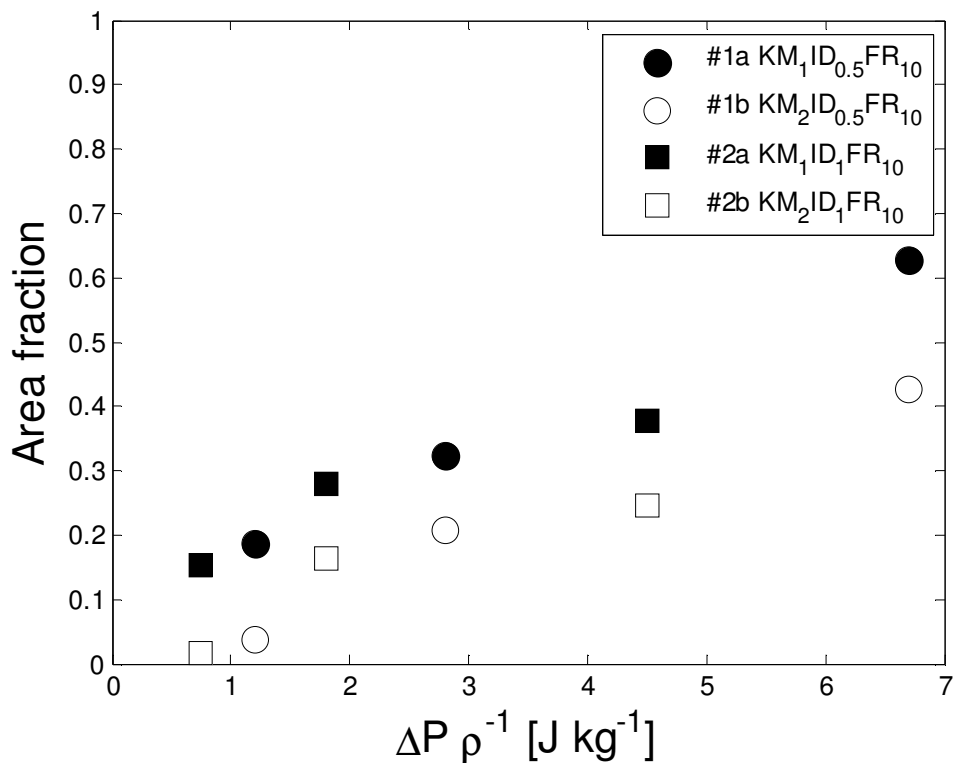
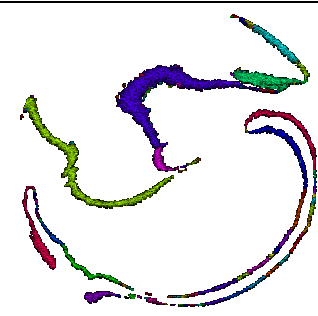
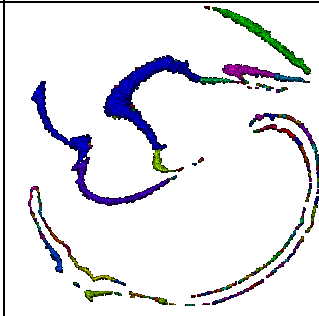
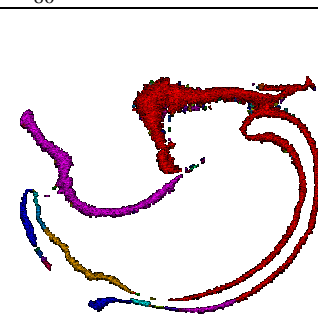
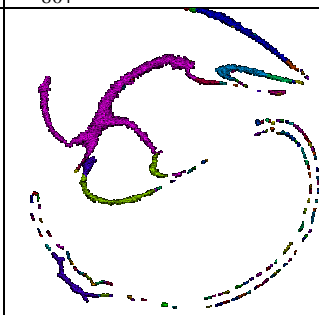


Figure 5.8 Fraction of mixing better than 80% ($X > 80\%$) versus $\Delta P/\rho$ for experiment #1a&b and #2a&b.

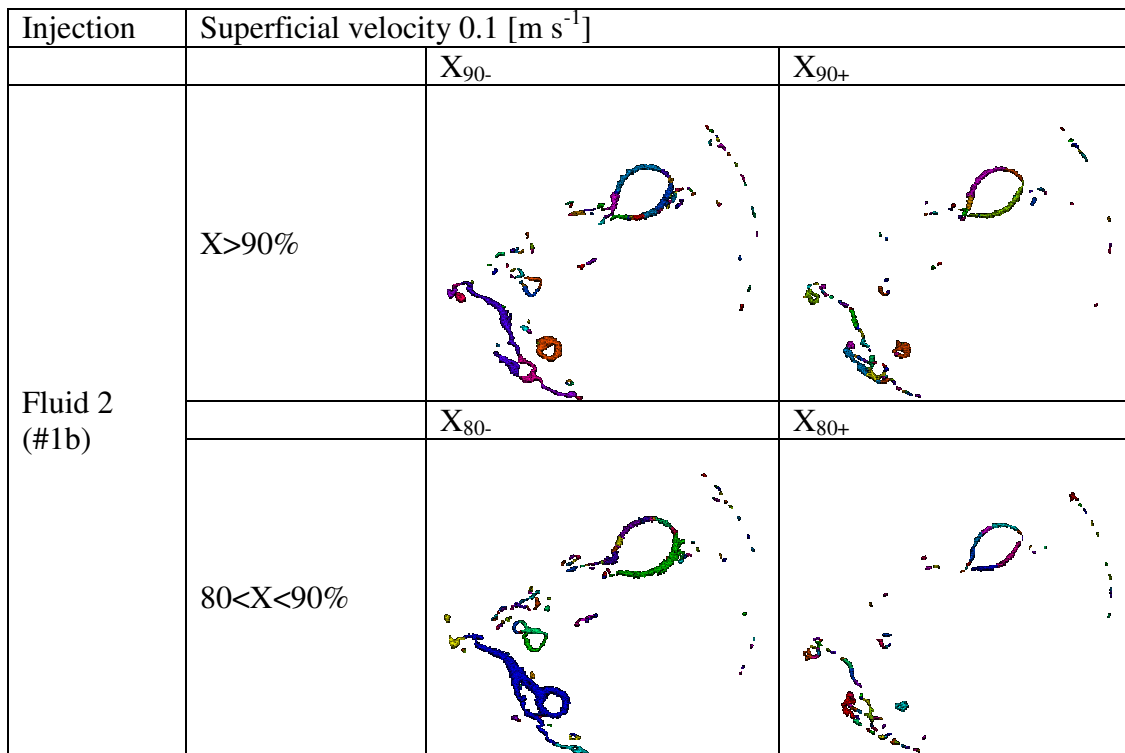
Figure 5.6 provides a general overview of the performance as a function of energy per unit mass. In this plot the area fraction plotted on the ordinate is for mixing intensity, $X > 80\%$. Referring to Figures 5.6a and 5.6b, the plotted points are the sum of the first two area fractions for the highest ranges of mixing intensity. Increasing energy input per unit mass increases the level of mixedness for both the systems where fluid 1 or fluid 2 are injected. The amount of “good mixing” increases proportionally with energy per unit mass and again, it appears to be independent of the size of static mixer. A characterisation of striations for selected ranges of mixing intensity is shown in Figure 5.7 for the ½” mixer and Figure 5.8 for the 1” mixture at each superficial velocity. The scale and viscosity ratio effects are visualised using this analysis. The striations within the range of interest ($X > 90\%$ and $80 < X < 90\%$) are presented for each experiment and superficial velocity highlighting the differences

between the upper bonds (X_{90+} , X_{80+}) and the lower bonds (X_{90-} , X_{80-}). The different striations detected by the MATLAB script are highlighted with different colours (due to limited number of colours, different striations can be identified by same colour). A contiguous striation is defined by corners contact between different pixels; where the edge pixel of a striation needs at least two free corners to be considered that. In addition, a plot which summarises the striation size distribution at selected mixing intensity of $X > 90\%$ is shown for both injections.

(a1)

Injection	Superficial velocity $0.1 \text{ [m s}^{-1}\text{]}$		
	X_{90-}	X_{90+}	
Fluid 1 (#1a)	$X > 90\%$		
	$80 < X < 90\%$		

(a2)



(a3)

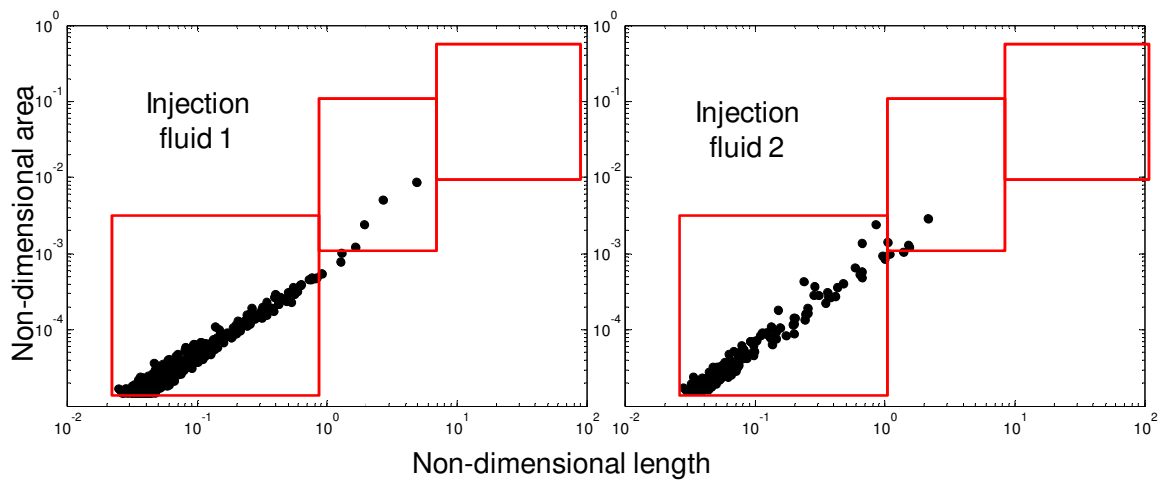
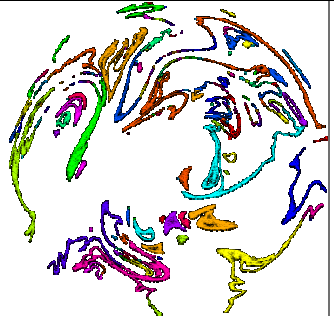
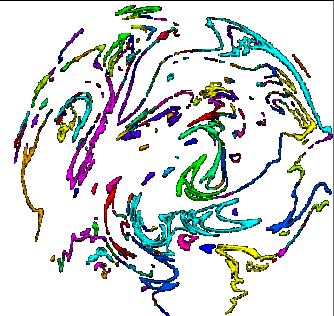
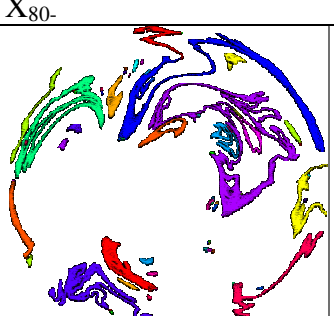
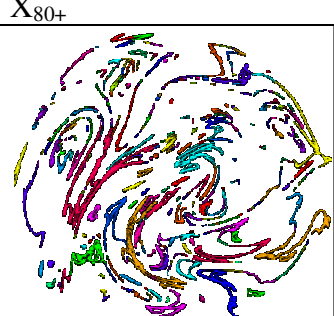
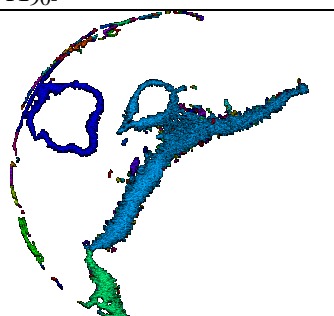
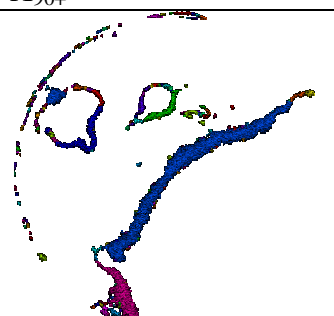
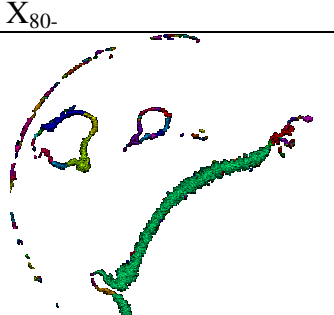
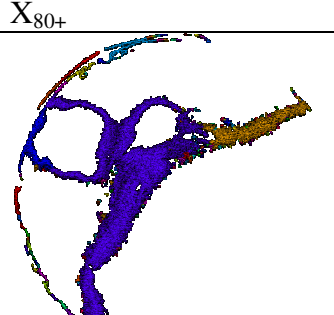


Figure 5.9a Striation areas for selected ranges of mixing intensity (injection fluid 1 and injection fluid 2) for $\frac{1}{2}$ " device including the plot of distribution of striation sizes for injection fluid 1 and for injection fluid 2 at $v=0.1\text{m s}^{-1}$.

(b1)

Injection	Superficial velocity 0.3 [m s ⁻¹]		
		X ₉₀₋	X ₉₀₊
Fluid 1 (#1a)	X > 90%		
	80 < X < 90%		

(b2)

Injection	Superficial velocity 0.3 [m s ⁻¹]		
		X ₉₀₋	X ₉₀₊
Fluid 2 (#1b)	X > 90%		
	80 < X < 90%		

(b3)

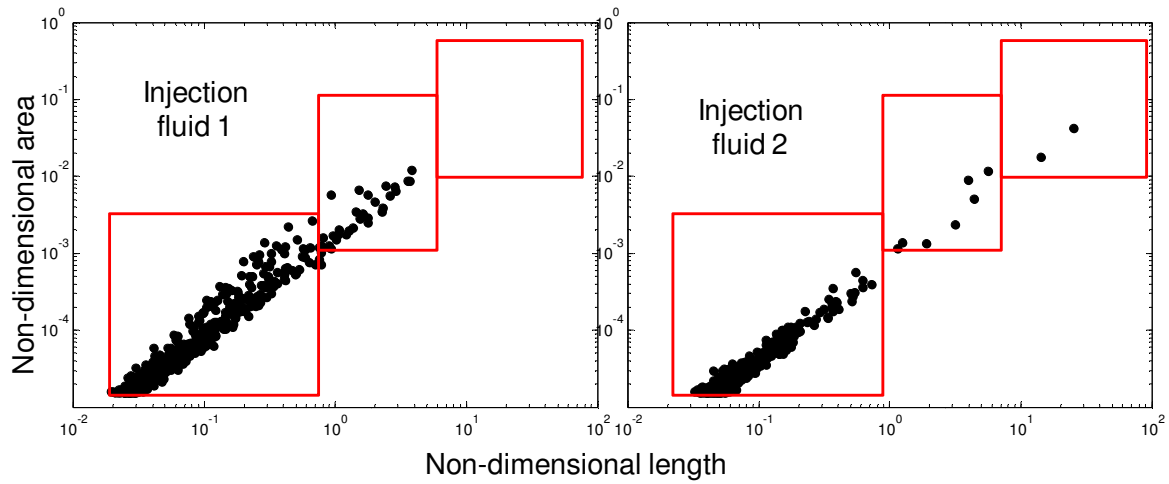
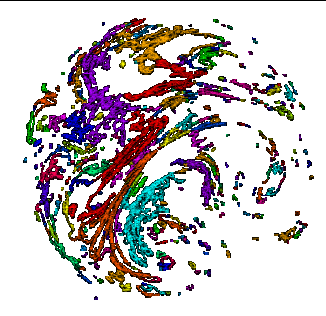
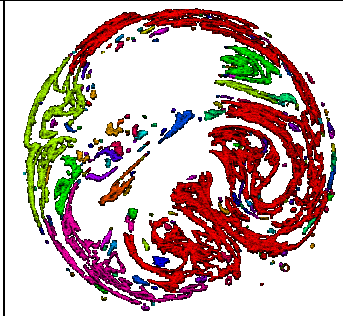
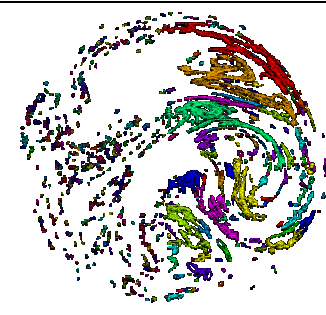
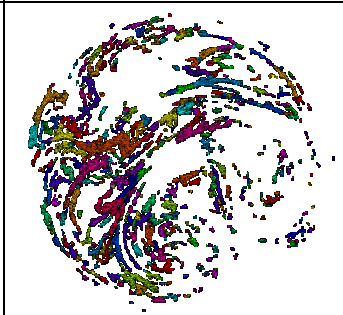


Figure 5.10b Striation areas for selected ranges of mixing intensity (injection fluid 1 and injection fluid 2) for 1/2" device including the plot of distribution of striation sizes for injection fluid 1 and for injection fluid 2 at $v=0.3\text{m s}^{-1}$.

(c1)

Injection	Superficial velocity $0.6 [\text{m s}^{-1}]$		
Fluid 1 (#1a)	$X > 90\%$	X_{90-}	X_{90+}
	$80 < X < 90\%$	X_{80-}	X_{80+}

(c2)

Injection	Superficial velocity $0.6 \text{ [m s}^{-1}\text{]}$	
	X_{90-}	X_{90+}
Fluid 2 (#1b)	$X > 90\%$ 	X_{90+} 
	$80 < X < 90\%$ 	X_{80+} 

(c3)

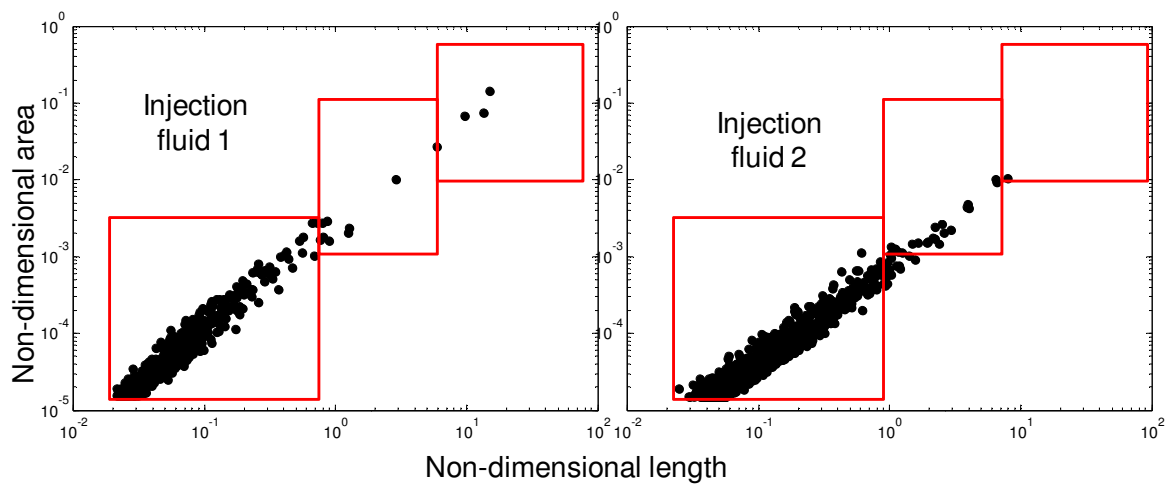


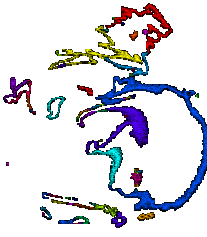



Figure 5.11c Striation areas for selected ranges of mixing intensity (injection fluid 1 and injection fluid 2) for $\frac{1}{2}$ " device including the plot of distribution of striation sizes for injection fluid 1 and for injection fluid 2 at $v=0.6 \text{ m s}^{-1}$.


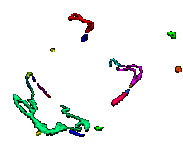

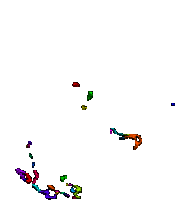
Figure 5.7 (a1), (b1), (c1) shows the shape of the striations for experiment #1a; if black pixels are located inside the coloured striation, the algorithm does not count this in the evaluation of total striation area. Increasing the velocity decreases the number of striations, but they all increase in area showing the progressing of mixing due to increasing the energy input in the system. The ideal trend is to reach a lower number of distinct striations with the highest value of mixing intensity ($G = \bar{G}$). Perfect mixing is a single uniform striation occupying the total cross sectional area of the mixer with a mixing intensity of $X = 100\%$. The pictures for X^- and X^+ show the different striations for the upper and lower bound of the selected ranges of mixing intensity (obtained from the areal method). Notable differences of striation shape are shown in the coloured images for the different velocities: the energy of the system drastically affects the spreading of the dye by increasing the size and swirl of the striations. In Figure 5.7 (a2), (b2), (c2), the detected striations are concentrated next to border of the unmixed zones. A possible explanation is that the yield stress of the fluid with a higher apparent viscosity imposes a limitation on the swirling generated by the static mixer elements. When the velocity increases up to 0.6 m s^{-1} the effect of yield stress on the formation of striations is lessened, potentially due to higher shear rates. The largest striations are found at the wall, where shear magnitudes are highest and local residence times longest. The striation size distribution is plotted in Figure 5.7 (a3), (b3), (c3), where the non-dimensional striation area versus non-dimensional length describes all the features of the detected striations. At the lowest velocity the points are concentrated in zone 1 (referring to Figure 5.2) underlining the presence of small zones of well mixed regions. At the intermediate velocity the number of points in zone 1 decreases whilst zone 2 becomes more populated. At the highest velocity the total number of points decreases, which confirms the generation of more concentrated zones of increased size. The presence of points in zone 3 is

an indication of improved mixing. Figure 5.7 (a3), (b3), (c3), shows also (right side) the shape and size distribution of the striations for the experiment #1b at the three velocities. The striations at the lowest velocity for both ranges of selected mixing intensity are lower in number and size. Clearly all the points in the plot are located in the zone 1. As velocity increases to 0.3 m s^{-1} , it is clear how the injection of different fluids affect mixing, with the injection of fluid 2 having a negative effect. General trends are summarized in the plots where increasing velocity, as for the experiment #1a, changes the distribution of the points in the different three zones. Comparing plots in Figure 5.7 (a3), (b3), (c3) it is apparent that the number of spots in zone 1 is always greater for the injection of fluid 2, identifying the formation of spots due to threads. A striation pattern without any structure is a consequence of low mixing performance, which is difficult to describe using CoV and maximum striation thickness, but it is detected by the proposed analysis of different mixing intensities. The quantification and localisation of different regions with different levels of mixing is the objective of this work, which gives an insight into the irregular pattern changes of the analysed system.

(a1)

Injection	Superficial velocity 0.1 [m s ⁻¹]		
		X ₉₀₋	X ₉₀₊
Fluid 1 (#2a)	X > 90%		
	80 < X < 90%		

(a2)

Injection	Superficial velocity 0.1 [m s ⁻¹]		
		X ₉₀₋	X ₉₀₊
Fluid 2 (#2b)	X > 90%		
	80 < X < 90%		

(a3)

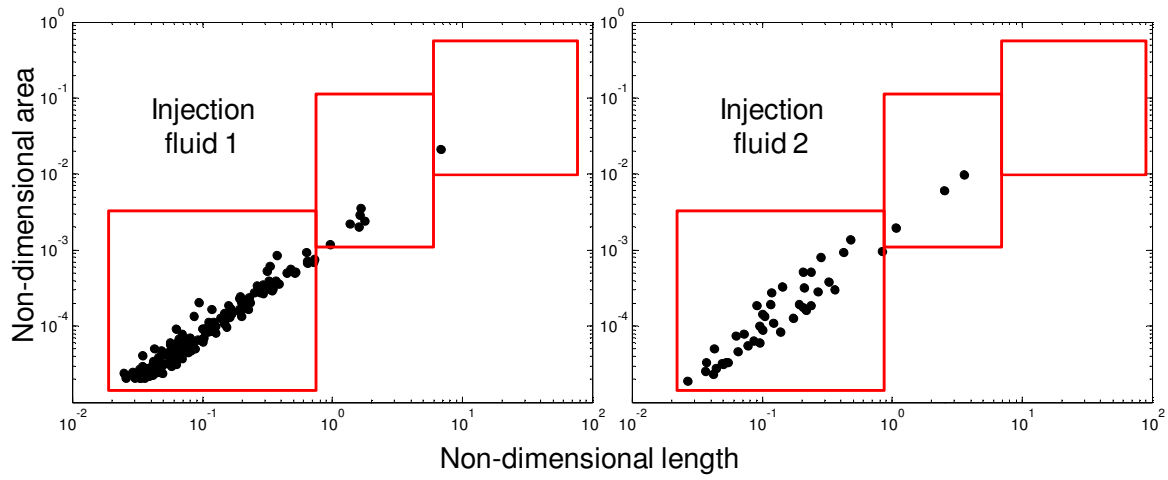






Figure 5.8a Striation areas for selected ranges of mixing intensity (injection fluid 1 and injection fluid 2) for 1" device including the plot of distribution of striation sizes for injection fluid 1 and for injection fluid 2 at $v=0.1\text{m s}^{-1}$.

(b1)

Injection	Superficial velocity $0.3 [\text{m s}^{-1}]$		
	X_{90-}	X_{90+}	
Fluid 1 (#2a)	$X > 90\%$		
	$80 < X < 90\%$		

(b2)

Injection	Superficial velocity $0.3 \text{ [m s}^{-1}\text{]}$		
		X_{90-}	X_{90+}
Fluid 2 (#2b)	$X > 90\%$		
	$80 < X < 90\%$		

(b3)

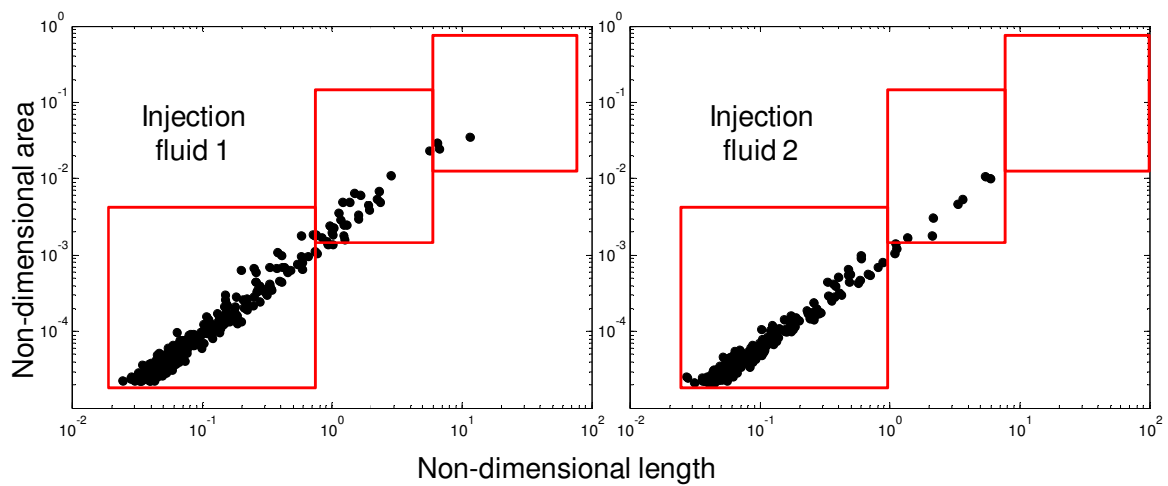
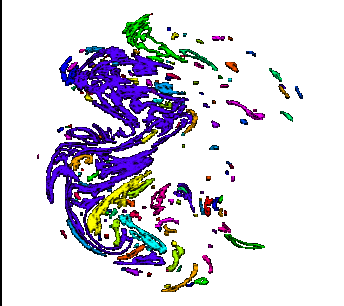
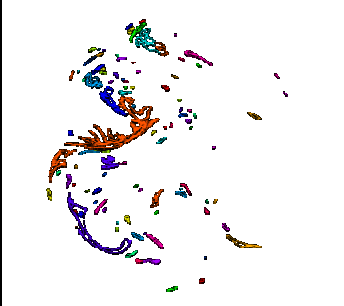
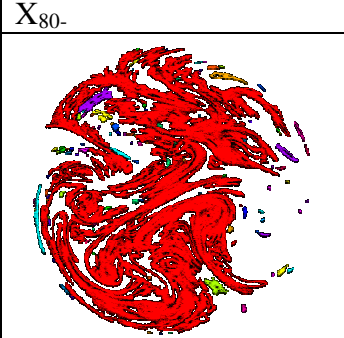
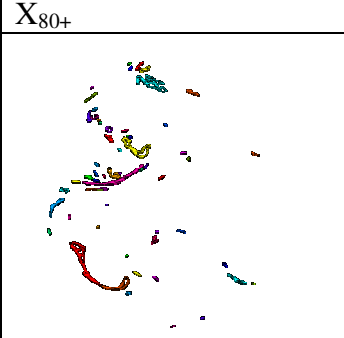

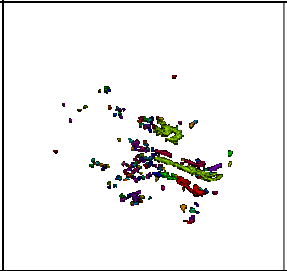
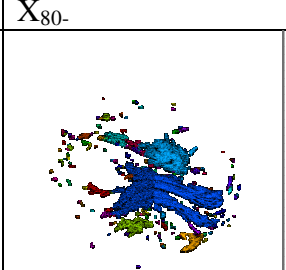
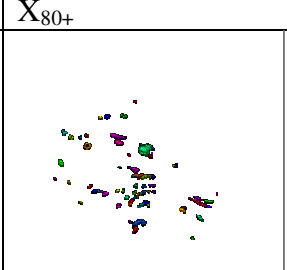


Figure 5.8b Striation areas for selected ranges of mixing intensity (injection fluid 1 and injection fluid 2) for 1" device including the plot of distribution of striation sizes for injection fluid 1 and for injection fluid 2 at $v=0.3\text{m s}^{-1}$.

(c1)

Injection	Superficial velocity 0.6 [m s ⁻¹]		
		X ₉₀₋	X ₉₀₊
Fluid 1 (#2a)	X > 90%		
	80 < X < 90%		

Injection	Superficial velocity 0.6 [m s ⁻¹]		
		X ₉₀₋	X ₉₀₊
Fluid 2 (#2b)	X > 90%		
	80 < X < 90%		

(c3)

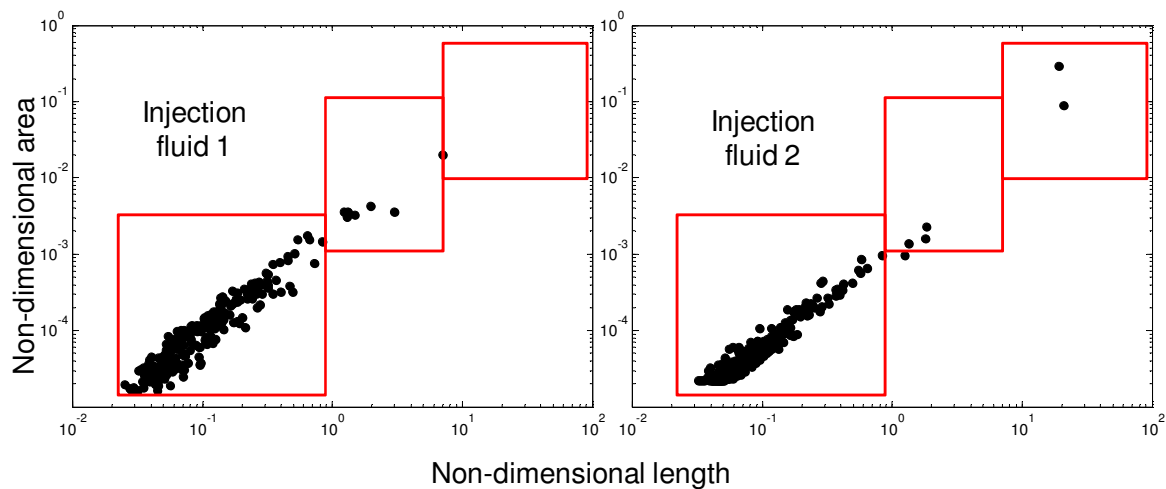


Figure 5.8c Striation areas for selected ranges of mixing intensity (injection fluid 1 and injection fluid 2) for 1” device including the plot of distribution of striation sizes for injection fluid 1 and for injection fluid 2 at $v=0.6\text{m s}^{-1}$.

Figures 5.8 show the shape and distribution of striations for experiments (#2a and #2b) where the 1” KM static mixer device was used. For the experiments run at the lowest velocity, the number of striations is similar to the ½” experiments for both injections. Comparing the two scales, further similarity is seen in the increasing striation elongation with velocity. The injection of fluid 2 limits the swirling and spreading of the dye, but for the 1” device the swirling is less affected than in the ½” KM static mixer. Clearly, the distribution of striations with high mixing intensity are different and in different regions with respect to ½” scale. Another difference between the different scales is the concentration of largest striations of better mixing ($X > 90\%$) for the lower bound (X_1) that was not evident in previous experiments. The asymmetry of the striation distribution on the cross section is accentuated for experiments #2a and #2b, underlining lower mixing performance for the 1” static mixer compared with the ½” (#1a and #1b). The analysis of the striation distribution gives a measure of the consequences of different flow conditions within the static mixer: with increasing velocity it seems that the geometry induces a rotational component to the fluid

motion that drastically increased the level of mixedness. This phenomenon was also noticed in the flow field results obtained using PEPT in the work of Rafiee *et al.* (2013). Referring to Figure 5.8 (a3), (b3), (c3) the general trend is similar to that seen in the previous set of experiments for ½”. The points of the graphs move from zone 1 where poor mixing affects the system, to zone 3 where striations have a consistent size, indicative of high mixing performance. However it is evident that the 1” device is characterized by lower performance in terms of the absolute level of mixing. Clearly, the effect of the injection of fluid 2 has a strong effect on the striations distribution limiting the location of points in zone 1 to superficial velocities of 0.1 and 0.3 m s⁻¹. To classify different trends of mixing based on the scale of the striations, the sum of all the striation perimeters for each experiment can be calculated to obtain the total interfacial length, non-dimensionalised by the perimeter of the injection. Generally, we can assume that the trend of the total interfacial length at the first stage, when the mixing in the system is very poor, it tends to increase. When the blending in the system reaches a high level of mixedness, the total interfacial length decreases due to the decreasing of striation number. Figure 5.9 shows the trend of total interface length for experiment #1a, b, 2a& b for all velocities. By increasing the energy per unit mass, the total length generally increases. However, for the injection of fluid 1 at the higher velocity, when there is the generation of large striations, the total length decreases. Whereas with the injection of fluid 2, the formation of large striations is limited and the total length always increases because the system does not reach a high level of mixedness.

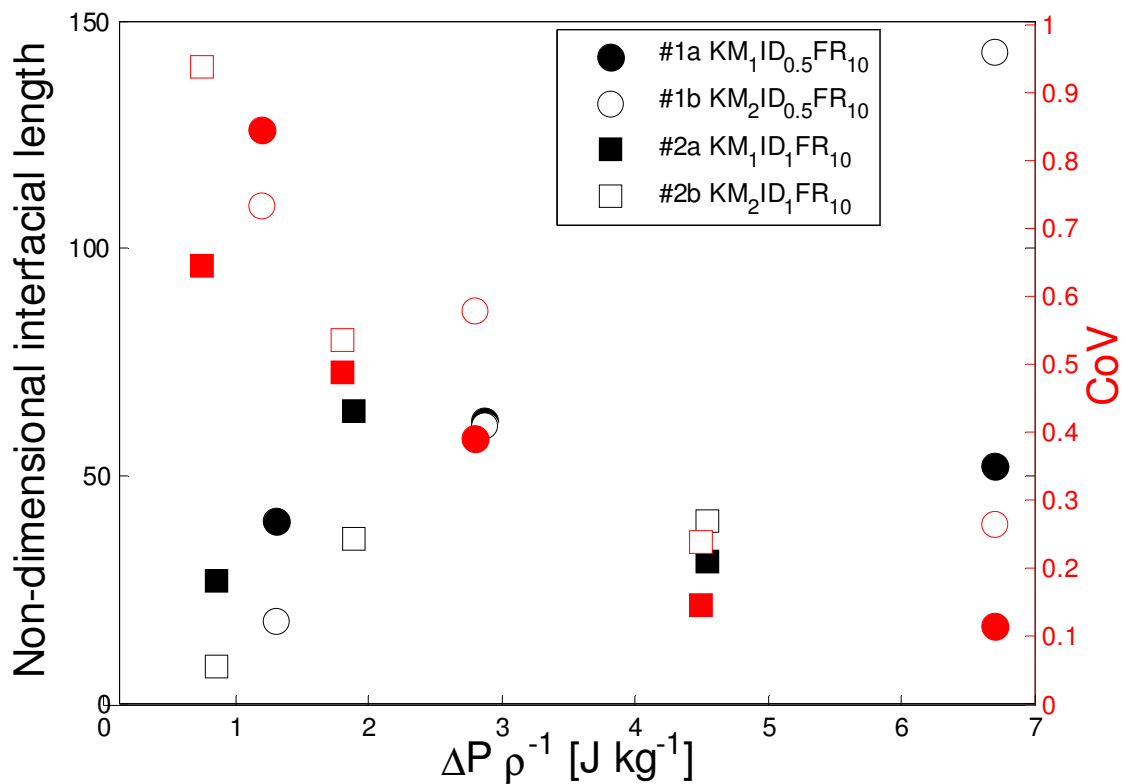
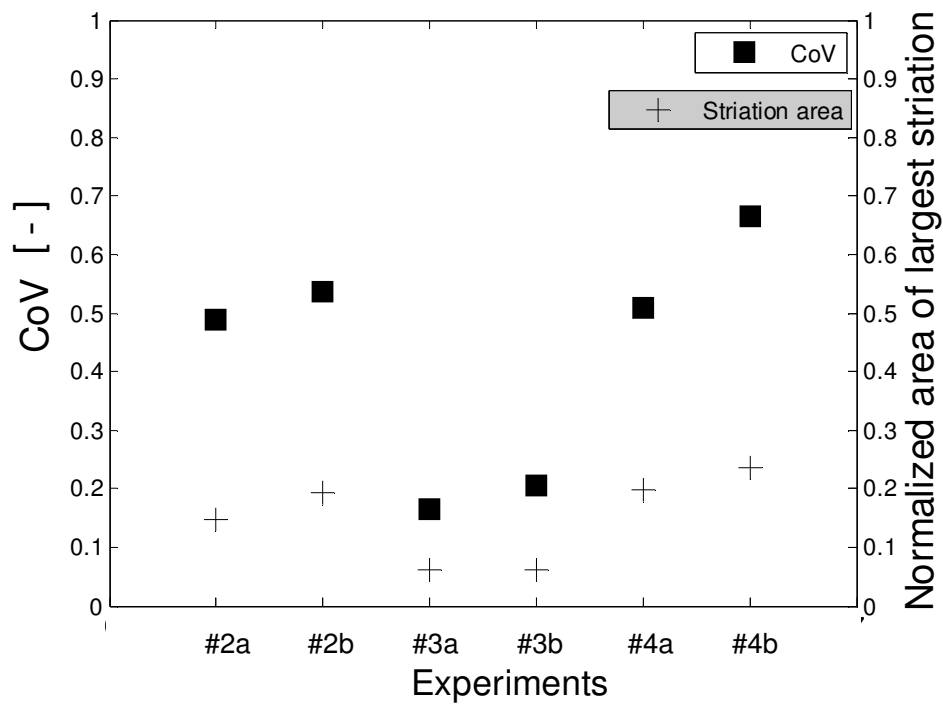


Figure 5.12 Total “interfacial length” over the static mixer perimeter for mixing intensity better than 80% ($X > 80\%$) versus $\Delta P/\rho$ for experiment #1a,b and #2a,b.

5.3.2. Effect of flow ratio and injection position at constant velocity and scale

Figure 5.10a shows values of CoV and maximum striation thickness at constant $\Delta P/\rho$, which shows a consistent difference between 1” experiments. Wall injection performs the poorest (#4a,#4b) whilst for central injection a flow ratio of 25 (#3a, #3b) gives a better result than a flow ratio of 10.

(a)



(b)

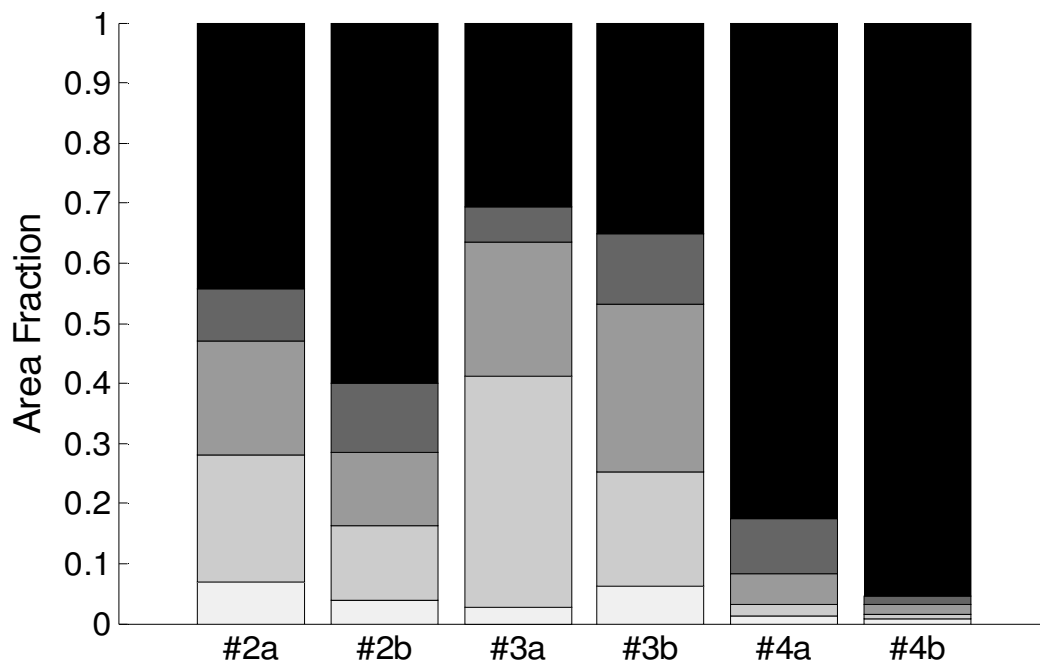

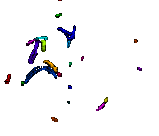
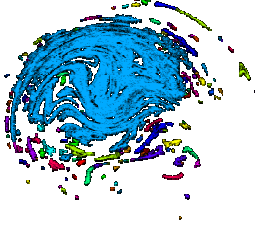
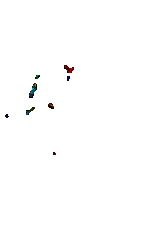


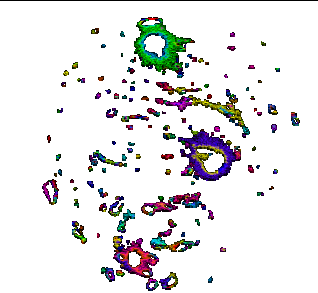
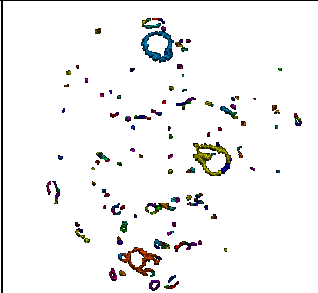
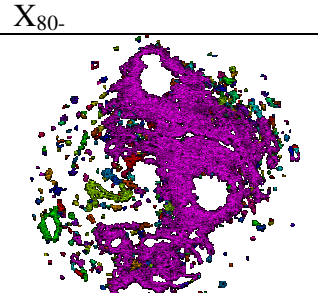
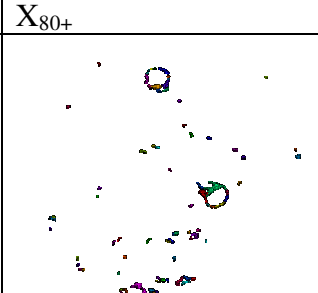
Figure 5.13 Effect of flow ratio and injection position at constant velocity and scale: a) CoV (intensity of segregation) and max striation area at constant $\Delta P/\rho$, b) bar graph showing discrete areal intensity distributions for #2a, #2b (central injection, flow ratio 10), #3a, #3b (central injection, flow ratio 25), #4a and #4b (wall injection, flow ratio 25) at $v=0.3 \text{ ms}^{-1}$.

Consistent changes are shown in Figure 5.10b, where the mixing performance is radically different compared to 1” experiments with flow ratio of 10 (#2a and b). Despite the fraction of $X > 90\%$ for #3a being lower than for #2a, the fraction of mixing intensity of $80\% < X < 90\%$ is much higher for (#3a, b) than in experiments (#2a, b). Thus the experiments with a flow ratio of 25 exhibit better performance. It can be seen that, by comparing Figures 11a and 11b, the position of injection drastically affects the mixing performance whilst all other parameters are kept constant; all the methods recognise the effect of different injection position. This is highlighted by CoV and maximum striation area analysis, with Figure 5.10b showing a large difference in the $X < 70\%$ area fraction for experiments with wall injection (#4a and #4b) compared to central injection (#3a and #3b), whilst there is also a much more limited area for $X > 90\%$. Striation size analysis for experiments #3 and #4 is presented in Figures 5.11 and 5.12.

(a)

Injection	Superficial velocity $0.3 \text{ [m s}^{-1}\text{]}$		
		X_{90-}	X_{90+}
Fluid 1 (#3a)	$X > 90\%$		
	$80 < X < 90\%$		

(b)

Injection		Superficial velocity 0.3 [m s ⁻¹]	
		X ₉₀₋	X ₉₀₊
Fluid 2 (#3b)	X > 90%		
	80 < X < 90%		

(c)

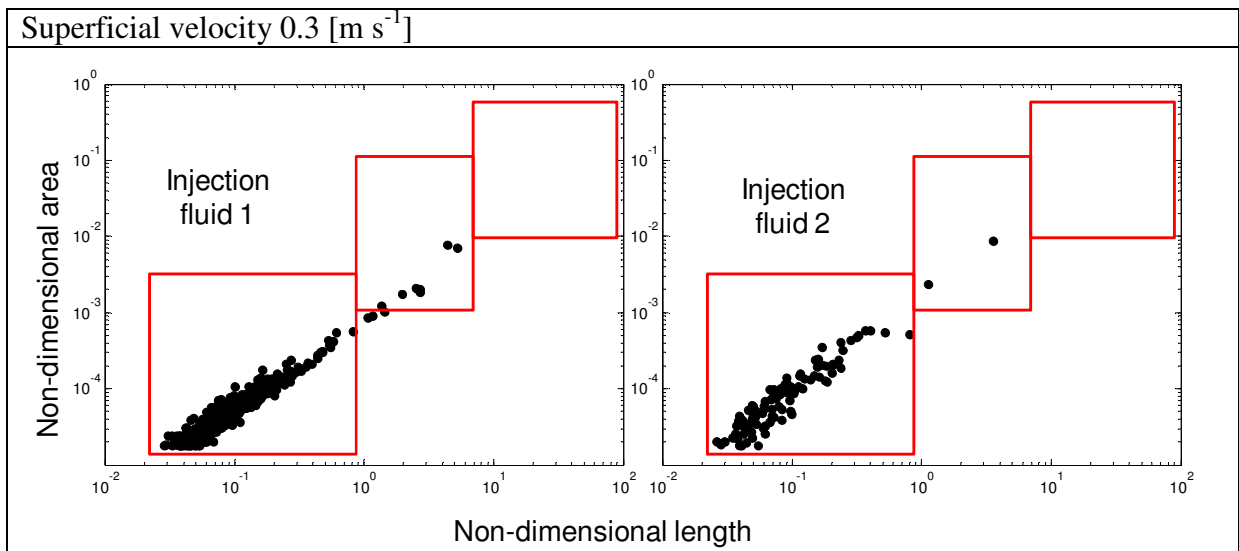

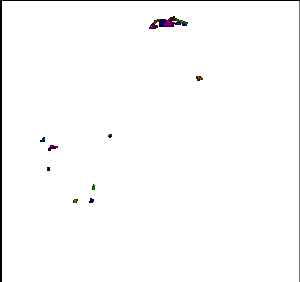


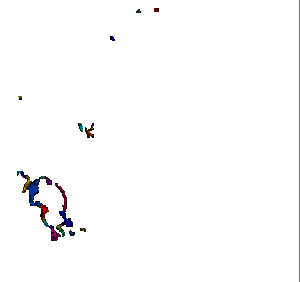
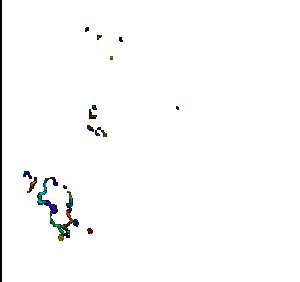
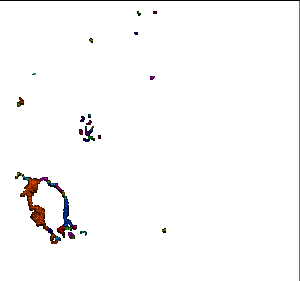
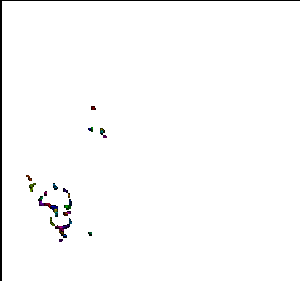


Figure 5.14 Effect of flow ratio and different injection for 1" device: a) striations area for selected ranges (injection fluid 1) (#3a) b) striations area for selected ranges (injection fluid 2) (#3b), c) distribution of striation size for injection fluid 1 and for injection fluid 2.

(a)

Injection	Superficial velocity 0.3 [m s ⁻¹]		
		X ₉₀₋	X ₉₀₊
Fluid 1 (#4a)	X > 90%		
	80 < X < 90%		

(b)

Injection	Superficial velocity 0.3 [m s ⁻¹]		
		X ₉₀₋	X ₉₀₊
Fluid 2 (#4b)	X > 90%		
	80 < X < 90%		

(c)

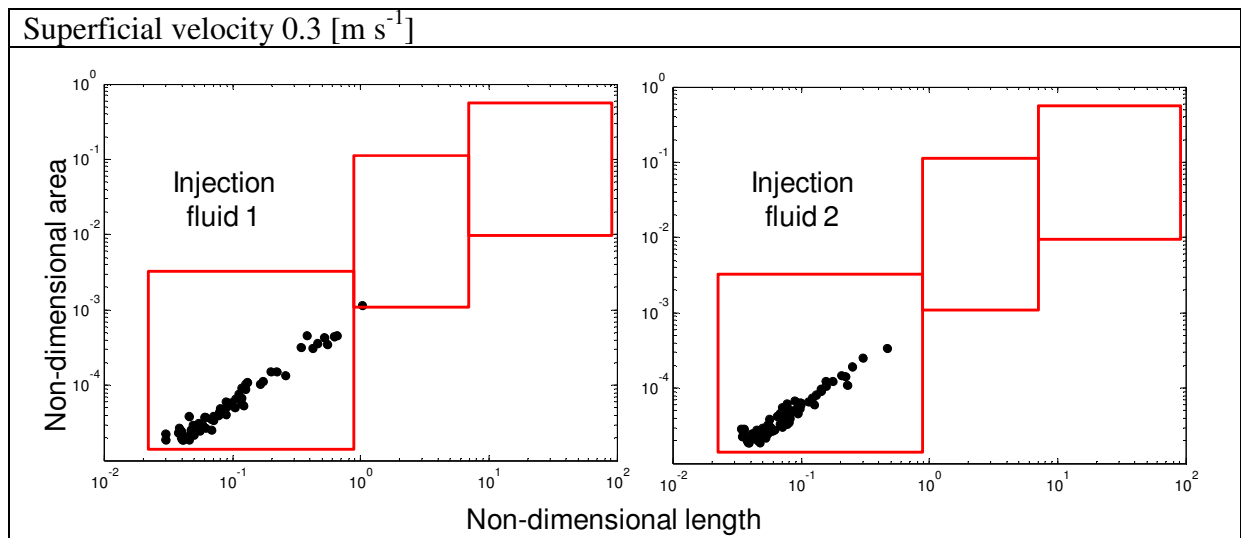


Figure 5.15 Effect of injection position and different injection for 1” device: a) striations area for selected ranges (injection fluid 1) (#4a) b) striations area for selected ranges (injection fluid 2) (#4b), c) distribution of striation size for the injection of fluid 1 and injection of fluid 2.

Figure 5.11a shows that even though the area fraction for $X > 90\%$ is lower for experiment (#3a), the biggest striations are concentrated in the lower bound range (X) as in experiment (#2a) shown in Figure 5.8 (b1). This may be due to the lower Reynolds number for the 1” device. The mixing performance for experiments with wall injection (#4a and #4b) is so poor that only a few spots have a mixing intensity of $X > 90\%$. Comparing the striation distribution of experiments #2a and #3a, it is clear how the region of ‘good mixing’ ($80 < X < 90\%$) is larger in size for experiment with flow ratio 25 (#3a) but concentrated in a more limited region than in #2a. For a given range of mixing intensity, experiments with injection of fluid 2 and different flow ratio #2b (Figure 5.8 (b2)) and #3b (Figure 5.11b) diverge giving the largest striations for experiments with a flow ratio of 10. The striation size distribution is shown in Figures 5.11c and 5.12c where the non-dimensional striation area versus non-dimensional length summarizes all characteristics of the detected striations. The

comparison between experiments with a flow ratio of 10 (#2a& b) and 25 (#3a& b) shown in Figures 5.8 (c2) and 5.11c show a lower number of points and a similar concentration in zone 1. For experiments #4a and b (Figure 5.12c), all striations are concentrated in zone 1, indicative of poor mixing. The poor performance thus be revealed by using the area fraction. When the mixing pattern is complex, the analysis of striations adds more information which is fundamental to distinguish and understand the mixing performance of different experiments.

5.4. Conclusion

Analysis of PLIF images has been performed to determine the mixing performance of KM static mixers using non-Newtonian aqueous solutions as a function of velocity, scale, flow ratio and injection position and comparing the effect of each these parameters with viscosity ratio of the two fluids (main flow: always fluid 1, injected fluid: fluid 1 and 2). Analysis of the data using CoV for intensity of segregation and striation area for scale of segregation have that shown in some cases one of the measures gives misleading results if the other is ignored, which is a well-known problem in literature (Kukukova *et al.*, 2009). A method previously presented (Alberini *et al.*, 2013) which considers the distribution of the cross-sectional area with a given intensity of mixing, has been used in combination with detailed striation analysis with high mixing intensity to characterize mixing performance, giving much more information than previous analyses. Analysis of striation area distribution is presented to schematize individual contiguous striations as a function of a non-dimensional area versus a non-dimensional length. The proposed scale of segregation analysis allows the determination of clear trends, recognising also small changes between different experiments.

This new method shows the complexity of information-rich PLIF images, and allows the classification of different experiments where CoV and striation thickness alone failed to clearly distinguish effects. As velocity increases the effect of varying the viscosity ratio becomes less important, whilst increasing the size of the static mixer decreases the mixing intensity. Scale has the greatest effect on the size of striations where poor mixing is observed. In terms of energy consumed per unit mass, the 1" size is more efficient due to possessing a lower pressure drop per unit length. Increasing the flow ratio between the injection and the main flow increases the overall mixing performance. Wall injection for the mixing of non-Newtonian fluids is not a suggested operating configuration as it negatively affects the overall mixing performance. Most of these effects are detected consistently only by the new proposed methods. These methods have industrial relevance since each method characterizes a different aspect of the mixing. For example, when an overview of the process is needed, the area fraction method can be used to estimate the amount of "lump" that has to be minimized in a downstream processing. But in a reactive system where the interface area is important, the striation method distribution can give an estimation of total interface length of the analysed cross section which is key aspect to take in account to determine the performance of the system.

CHAPTER 6

6. EFFECT OF SYSTEM AND FLUID PARAMETERS UPON THE BLENDING OF NON-NEWTONIAN FLUIDS: COMPARISON BETWEEN SMX PLUS AND KM STATIC MIXER

6.1 Introduction

This chapter is concerned with mixing studies using a SMX Plus static mixer. The design of the SMX Plus is based on the Sulzer SMX design which is well established for laminar mixing and dispersion duties; since its introduction in 1980 it has been applied successfully for a variety of different applications (Hirschberg *et al.*, 2009). Since this thesis is concerned with the blending of viscous non-Newtonian fluids, it is a logical choice for further study due to its known high efficiency for the laminar mixing of highly viscous fluids and also when the viscosities of the two fluids to be mixed differ strongly. According to Hirschberg *et al.* (2009), the SMX can handle the mixing task of two streams with viscosity ratios of up to 1,000,000. The SMX Plus design differs from the SMX by the use of a reduced number of

bars and gaps between the bars, allows a reduction of the pressure drop of the mixer to less than 50% while the mixing quality after a given number of elements remains nearly equivalent with the original SMX. As a result, significant cost savings can be achieved through reduced mixer and pipe diameters, or by using smaller pumps. Other important feature of SMX Plus is the size of the bars which change with the size of the static mixer instead of been constant as it was for the conventional SMX. Most of the research into SMX mixers applies computational fluid dynamics to calculate flow velocities, pressure drops, residence time distributions and heat transfer for both Newtonian and non-Newtonian power-law fluids. Visser *et al.* (1999) obtained velocity profiles for various cross-sections within the mixer and confirmed agreement between calculated pressure drops using CFD and experimental results. Use of the simulations to obtain heat transfer coefficients for cooling through the wall led to values lower than those observed experimentally; this highlighted the importance of heat conduction through the internals which was initially neglected in the simulations. Simulations assuming an infinitely high thermal conductivity of the plates resulted in higher heat transfer coefficients than experimentally observed. An experimental study of the flow pattern in the wall region of an SMX static mixer was performed using electrochemical shear rate sensors (Hirech *et al.*, 2003). Electrochemical signals were related to the local shear stress and the fluctuating velocity gradients in the flow due to turbulence. Analysis of these fluctuations was used to define the onset of turbulence and thus define flow regime to compare with CFD predictions. The transition from a laminar flow to an intermediate flow occurred at about $Re = 200$, whilst turbulent flow was observed at $1500 < Re < 3000$. The flow and mixing of power-law fluids in a standard SMX static mixer were simulated by Liu *et al.* (2006) using CFD. Their results showed that shear thinning reduces the ratio of pressure drop in the static mixer to pressure drop in empty tube when compared with Newtonian fluids in the range between 100 and 5000 s^{-1} using a power law fluid. The

correlations for pressure drop and friction factor were obtained at Reynolds number of 100, with the friction factor presented as a function of both Reynolds number and power-law index. An area-weighted average strain rate on the solid surface in mixing section was proposed to calculate pressure drop for a non-Newtonian fluid and the apparent viscosity which was used to calculate the Reynolds number. In terms of mixing performance of SMX mixers, only a few studies exist in the literature. Zalc *et al.* (2002) developed a detailed Lagrangian analysis of partially mixed structures in an SMX static mixer, with emphasis on laminar flows with Reynolds numbers between 1 and 100. Three injection positions (one centreline and two off-centre) were chosen. Mixing measures, such as the decrease in the coefficient of variation with axial distance, and the increase in the average rate of stretching, were discussed in order to quantify mixing performance. It was found that mixing rates for the centreline injections were larger than for the off-centre injection positions investigated. The required energy to maintain the flow across a unit length of SMX mixer (an element) is significantly higher when compared with the KM static mixer. However, it is believed that the SMX as it is designed today comes very close to the optimum in terms of mixing performance. In this Chapter, a geometrical modification of the well-known Sulzer SMX static mixer, called SMX Plus, is used for the blending of non-Newtonian fluids. The use of a reduced number of bars and gaps between the bars compared with the SMX design allows a reduction of the pressure drop of the mixer to less than 50% while the mixing quality after a given number of elements remains nearly equivalent with the original SMX. CFD simulations are being relied upon in order to show the performance of the SMX Plus with regard to pressure drop, mixing quality and residence time distribution by Hirschberg *et al.* (2009). These results are confirmed by their LIF measurements. The mixing performances for streams with different viscosities have been investigated using a decolourization technique. The choice of SMX Plus static mixer for this work was driven by the poor performance of the

KM static mixer for the blending of non-Newtonian fluids with different viscosities, shown in Chapters 4 and 5. Since the number of published works on the SMX Plus static mixer is very limited, this chapter could be a source of information suitable for industrial process development. In this chapter, the same sets of experiments carried out in Chapter 4 for the KM mixer are repeated using the SMX Plus mixer. For all different configurations the injections of same fluid as the base (fluid 1) or more thick fluid (fluid 2) are investigated. Mixer scale (1/2", 1"), superficial velocity, and flow ratio are the investigated fluid parameters.

6.2 Material and Methods

6.2.1 Fluids and Flow Conditions

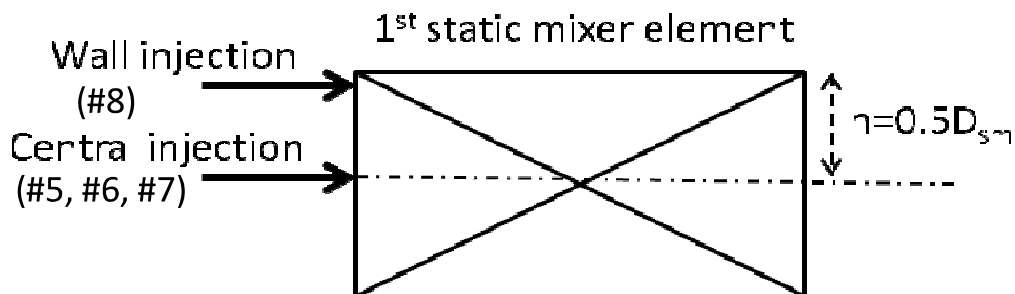
An introduction to the experimental conditions is reported in this paragraph. Full details of the static mixer rig used are given in §3.4. In this chapter, a baseline superficial velocity of 0.3 m s^{-1} was used in all experiments, corresponding to a total volumetric flow rate of 180 L hr^{-1} at 1/2" scale and 600 L hr^{-1} for 1" scale. The experimental design was made to consider the effect of superficial velocity, mixer scale, flow ratio, viscosity ratio and injection position whilst holding other variables constant. On the basis of these requirements, four different experiments were performed, as shown in Table 6.1, with the core effect of changing viscosity ratio being carried out for each experiment.

As described in Chapter 5, the effect of scale is examined as a function of superficial velocity by comparing experiments #5 and #6, the effect of flow ratio by comparing experiments #6 and #7 and the effect of injection position by comparing experiments #7 and #8. In Figure

6.1 all the specifics of static mixer dimensions are reported including secondary flow inlet dimensions and injection position.

Table 6.1. Experimental conditions for all experiments.

Exp	Injected fluid and position of injection	Superficial Velocity (v) (m s^{-1})			Flow ratio (FR)	ID	Codes
		0.1	0.3	0.6			
#5a	1 Central	✓	✓	✓	10	½"	SMX ₁ ID _{0.5} FR ₁₀
#5b	2 Central	✓	✓	✓	10	½"	SMX ₂ ID _{0.5} FR ₁₀
#6a	1 Central	✓	✓	✓	10	1"	SMX ₁ ID ₁ FR ₁₀
#6b	2 Central	✓	✓	✓	10	1"	SMX ₂ ID ₁ FR ₁₀
#7a	1 Central	-	✓	-	25	1"	SMX ₁ ID ₁ FR ₂₅
#7b	2 Central	-	✓	-	25	1"	SMX ₂ ID ₁ FR ₂₅
#8a	1 Wall	-	✓	-	25	1"	SMX ₁ ID ₁ FR _{25W}
#8b	2 Wall	-	✓	-	25	1"	SMX ₂ ID ₁ FR _{25W}
Size		Re					
		0.1 [m s^{-1}]	0.3 [m s^{-1}]	0.6 [m s^{-1}]			
½" (#5)		20	91	245			
1 (#6,#7,#8)		26	150	394			



	Flow ratio	Diameter static mixer (D_{sm}) [m]	Diameter injection (D_i) [m]
1/2"	10	0.0127	0.004
1"	10	0.0254	0.008
1"	25	0.0254	0.005

Figure 6.1 All the specifics of static mixer dimensions including secondary flow inlet dimensions and injection position.

6.3. Results and discussion

Very different mixing patterns, due to the different internal geometries between the KM and SMX Plus mixers, are illustrated in Figure 6.2. A comparison is presented between patterns for selected runs between both mixer types. The quality of mixing obtained by the two different geometries is radically different. The presented patterns (Figure 6.2) give a clear idea of the huge difference on the mixing performance; the striations are both smaller and more numerous when the SMX Plus geometry is used.

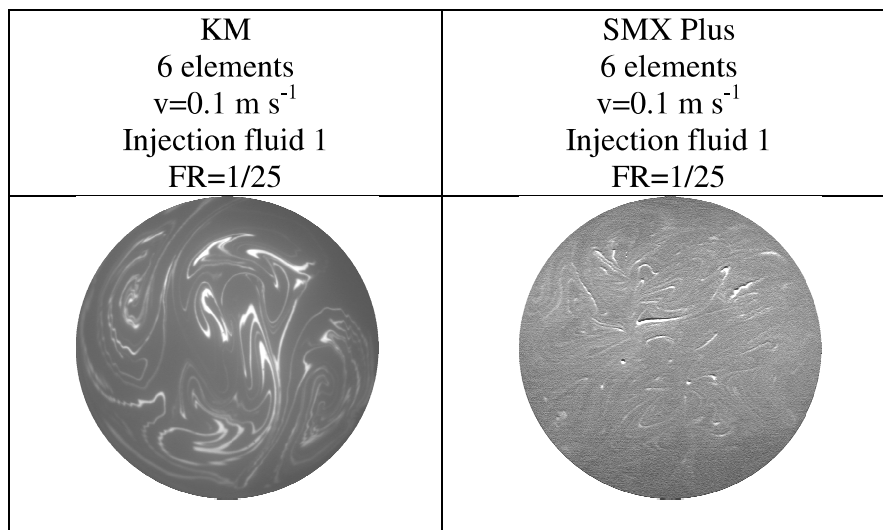


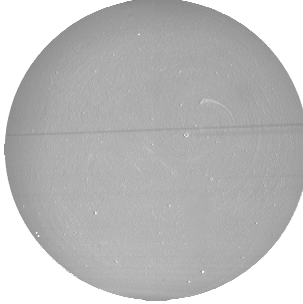


Figure 6.2. Flow pattern comparison between KM and SMX Plus static mixer designs.



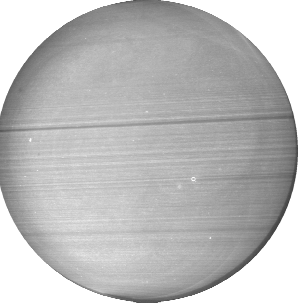
Raw PLIF images obtained for each experiment using SMX Plus at different superficial velocities are shown in Figure 6.3. The images show the distribution of dye tracer in the cross

section of the pipe after 6 elements of SMX Plus static mixer for each experiment. As previously done with the KM experiments, 10 images were acquired in three batches spaced several minutes apart for each experiment to check for temporal variations, which were not observed. In Figure 6.3a the patterns for experiments of SMX Plus static mixer ½” with central injection of fluid 1 (#5a) radically change by increasing superficial velocity as expected. At lower velocities the pattern is characterized by the typical pattern created by SMX Plus elements. The dye is concentrated in striations with high different grayscale values while at the higher velocities the grayscale values of striations tends to be more homogeneous. However, unlike the KM geometry, similar patterns are shown in the images for experiment when the injected fluid is switched to fluid 2 (#5b) as shown in Figure 6.3b but only where the presence of fluid 2 creates the formation of more concentrated zone of dye. Clearly the SMX Plus geometry generates lower number of threads identified by spots compared to the KM static mixer on the cross section. As velocity increases, it is clear how the patterns change due to higher number of cuts and folding based on same number of static mixer elements. At higher velocity the grey scale values are homogeneous in the whole cross section.



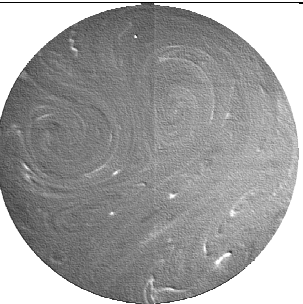
(a)

#5a SMX ₁ ($v=0.1$, ID=1/2", FR=10)	#5a SMX ₁ ($v=0.3$, ID=1/2", FR=10)	#5a SMX ₁ ($v=0.6$, ID=1/2", FR=10)
		




(b)

#5b SMX ₂ ($v=0.1$, ID=1/2", FR=10)	#5b SMX ₂ ($v=0.3$, ID=1/2", FR=10)	#5b SMX ₂ ($v=0.6$, ID=1/2", FR=10)
		

(c)

#6a SMX ₁ ($v=0.1$, ID=1", FR=10)	#6a SMX ₁ ($v=0.3$, ID=1", FR=10)	#6a SMX ₁ ($v=0.6$, ID=1", FR=10)
		

(d)

#6b SMX ₂ ($v=0.1$, ID=1", FR=10)	#6b SMX ₂ ($v=0.3$, ID=1", FR=10)	#6b SMX ₂ ($v=0.6$, ID=1", FR=10)
		

(e)



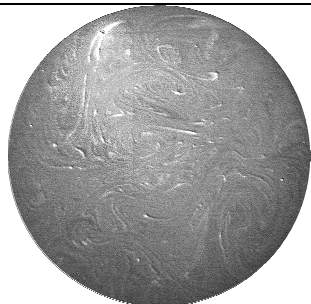

#7a SMX ₁ ($v=0.3$, ID=1", FR=25)	#7b SMX ₂ ($v=0.3$, ID=1", FR=25)
	
#8a SMX ₁ ($v=0.3$, ID=1", FR=25 wall)	#8b SMX ₂ ($v=0.3$, ID=1", FR=25 wall)
	

Figure 6.3 Raw images of all SMX Plus experiments: (a) Experiment 5a at different superficial velocities, (b) Experiment 5b at different superficial velocities, (c) Experiment 6a at different superficial velocities, (d) Experiment 6b at different superficial velocities, (e) Experiment 7a,b and 8a,b at the design velocity of 0.3 [ms⁻¹].

The characteristic pattern generated by the SMX Plus geometry is showed in Figure 6.3c for the 1” device, showing the effect of stretching and folding due to the geometry of the mixer elements. Increasing the size it seems that the formation “dye loops”, due to multi flow direction generated by the SMX Plus element geometry, is limited in 1” static mixer may be affect by a lower shear. In both scales Reynolds number is in the range of laminar flow (see Table 6.1). The pattern observed in experiment for 1” device shows pretty similar behaviour to the ½”, promising similar mixing performance. The patterns for the experiments performed at the “design” velocity of 0.3 m s^{-1} for 1” device for experiments #6b, #7b and #8b are similar but surprisingly #7b and 8b seem to be characterized by the presence of a greater number of spots due to different flow ratio between the injection and the main flow (FR = 25). Comparing the experiments, where the flow ratio was kept constant at 25 but a different position injection was used, comparing #8a vs #7a and #7b vs #8b shows that the effect of wall injection does not affect the mixing performance as for the KM design.

6.3.1. Pressure drops comparison between KM and SMX Plus static mixer

Pressure drops were evaluated using always the non-Newtonian solution (fluid 1, Carbopol 0.1% w/w) varying the superficial velocity of the flow and size of static mixer for both devices (KM and SMX Plus) and empty pipes for the two diameter sizes. In terms of energy consumed, the SMX Plus static mixers have higher pressure drops than KM, as expected due to the more complicated geometry of the mixing elements. Figure 6.4 shows the pressure drop for both devices at selected velocities at both ½” and 1” scales. As expected, the pressure drops are higher for ½” diameter than 1” both for SMX Plus and KM. The higher values of pressure drop for SMX plus are justified by the higher wet perimeter per unit length compared to the KM. Increasing the diameter of the static mixer the wet perimeter increase proportionally to the size of the device for both geometries (KM and SMX Plus).

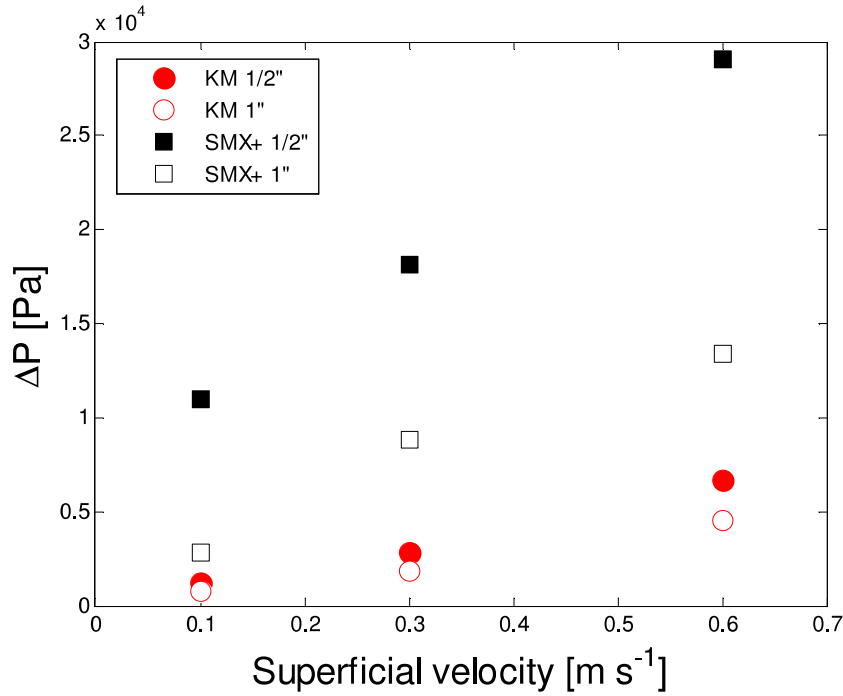


Figure 6.4 $\Delta P/\rho$ versus superficial velocity for all experiments and both geometries.

In the following table (Table 6.2) the K_L values are reported for both static mixers at different superficial velocities where K_L is the ratio between the pressure drops of the static mixer to the pressure drops of an empty pipe with the same dimension. For KM static mixer there is a marked difference with scale at the same velocity and from expected data of 6.9 cited by the literature (Handbook of Industrial Mixing). More constant K_L values are found for the SMX Plus where the velocity and the diameter appear to have a much less significant influence. Besides, the K_L values match better the value cited in the literature.

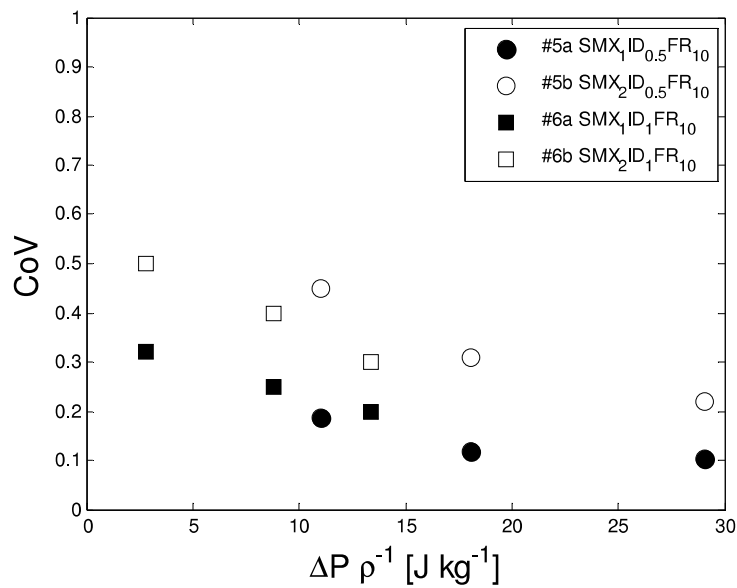
Table 6.2 K values for KM and SMX Plus static mixer at different superficial velocity.

$K_L = \frac{\Delta P_{static_mixer}}{\Delta P_{empty_pipe}}$	Superficial Velocity (ms ⁻¹)	KM 1/2"	KM 1"	SMX Plus 1/2"	SMX Plus 1"
	0.1	2.2	5.5	33.3	27.4
	0.3	2.7	7.5	29.9	36.6
	0.6	4.3	12.6	31.6	37.4

6.3.2. Effect of velocity for different scales at constant flow ratio

The influence of velocity and the injection of fluid with different rheological behaviour are investigated in order to gain a deeper understanding of the complexity of mixing non-Newtonian fluids at different scales.

(a)



(b)

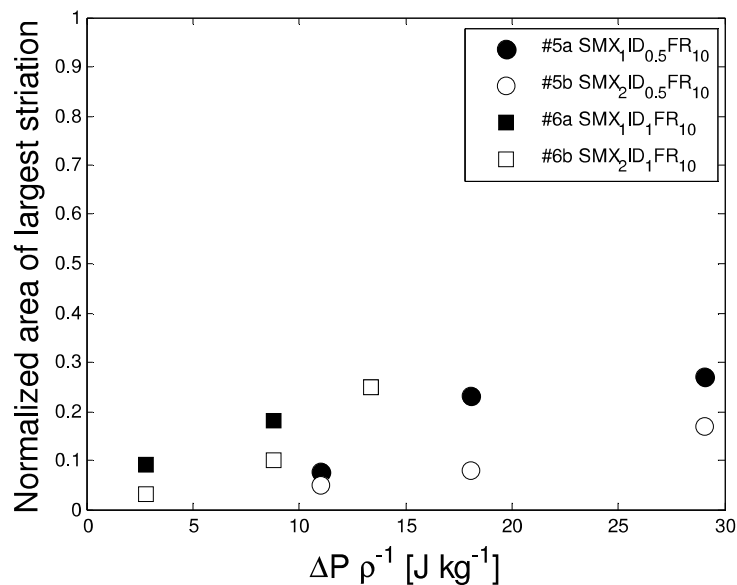


Figure 6.5 Effect of velocity for different scales at constant flow ratio: a) CoV (intensity of segregation) versus $\Delta P/\rho$ and b) max striation area (scale of segregation) versus $\Delta P/\rho$, for #5a, b and #6a,b at selected velocities.

Values of CoV versus $\Delta P/\rho$ are shown in Figure 6.5a; they were determined at three different velocities for ½” and 1” for both injections at constant flow ratio of 10. Again, the increasing $\Delta P/\rho$ leads to improved mixing performance. Mixing with the injection of fluid with different rheology leads to generally worse performance compared with when the injected fluid is the same as the main flow. Also for both scales, the general trend for intensity of segregation is similar to the previous experiments (CoV decreases by increasing energy input to the system). The values of CoV in Figure 6.5a are very similar between experiments, though generally the ½” device performs slightly better. However in terms of energy consumed per reached level of mixedness, the 1” static mixer proves to be more efficient.

In terms of maximum striation area (Figure 6.5b) different trends are shown for experiments with the ½” SMX Plus. By increasing the velocity, the area increases. However the evaluation of a sample data, as previously explained, can create misleading or uncertain results because it does not explain the overall scale of segregation of the system. For experiments for 1” SMX Plus, the maximum striation trend is analogous to the ½” device except at highest velocity where the values of area are similar between experiments with different injections. The sizes of normalized maximum striation thickness (Figure 6.5b) are not greater for 1” and this can be explained by the structure of the SMX Plus element where the gaps increase proportionally to the scale of the device. In SMX static mixer the size of the ‘net’ of the element was constant for all the scales which drastically influenced the pressure drops of the system.

In the following sections a deeper analysis of mixing intensity and scale of segregation are obtained using the areal analysis and the distribution of striation sizes used in Chapter 5. Figure 6.6a shows the distribution of different mixing intensities described by area fraction. The bars graph refers to three runs for the experiments SMX Plus ½” for injection of both fluids (#5a, #5b) at different velocities. As expected, the fraction for $X > 90\%$ increases by

increasing velocity, and clearly the amount of $X < 60\%$ much larger than for the KM experiments. The divergences between experiment for the injection of fluid 1 (#5a) or fluid2 (#5b) are clear in terms of absolute fraction values at different mixing intensities, where #5a performs always better than #5b. The performances at higher velocity are pretty similar also if different injection is used. These findings match the earlier CoV analysis. Only at $v=0.3 \text{ m s}^{-1}$ are clear differences observed.

(a)

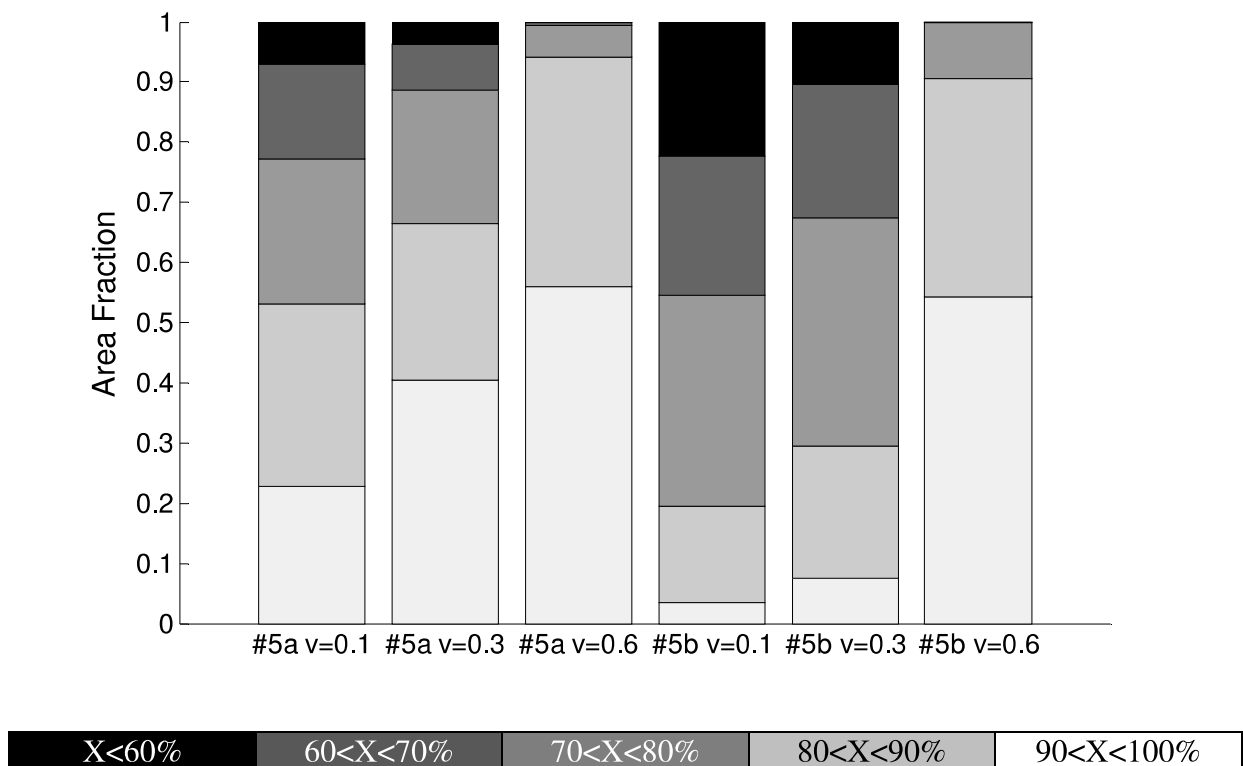


Figure 6.6a. Bar graph showing discrete areal intensity distributions for #5a,b at selected velocities (scale of static mixer: $\frac{1}{2}$ " , central injection, flow ratio 10, SMX Plus).

(b)

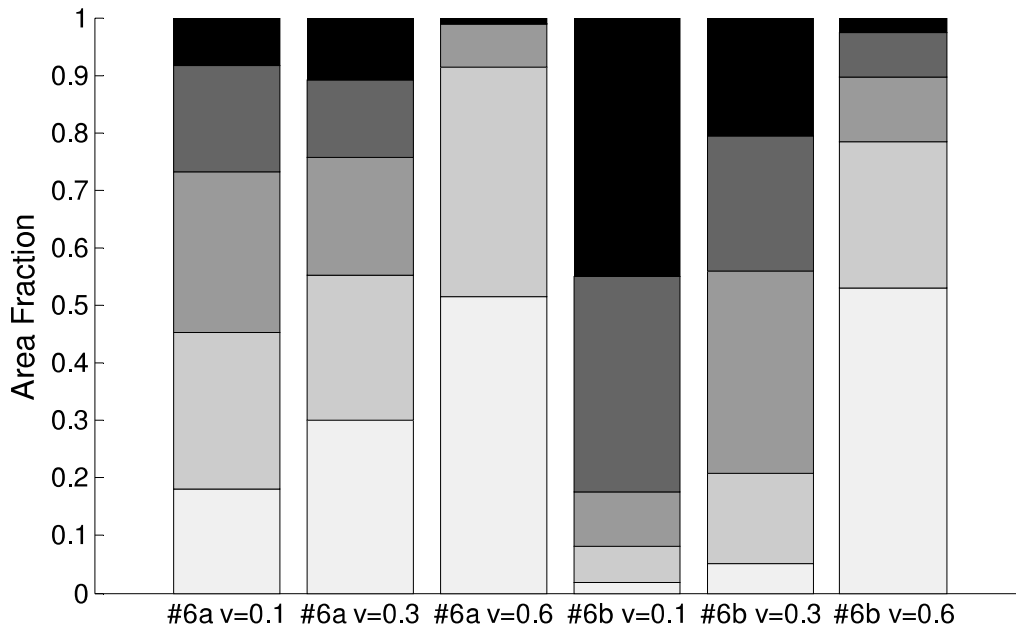


Figure 6.7b. Bar graph showing discrete areal intensity distributions for #6a,b at selected velocities(scale of static mixer: 1”, central injection, flow ratio 10, SMX Plus).

Figure 6.6b shows the distribution of mixing intensity for experiments of 1” SMX Plus at different velocities. The general trends are similar to the previous experiments but the absolute values of different levels of mixing intensity are different. By increasing the velocity the fraction of mixing intensity for $X > 90\%$ increases with a big jump at higher velocity, as expected. Comparing Figure 6.6a with Figure 6.6b, as expected the fraction of $X > 90\%$ is higher with the injection of fluid 1 at both scales, and the difference between the scales are not so marked as they were for the KM geometry. Nevertheless, the overall ‘best’ performance in terms of mixing intensity is with ½” static mixer.

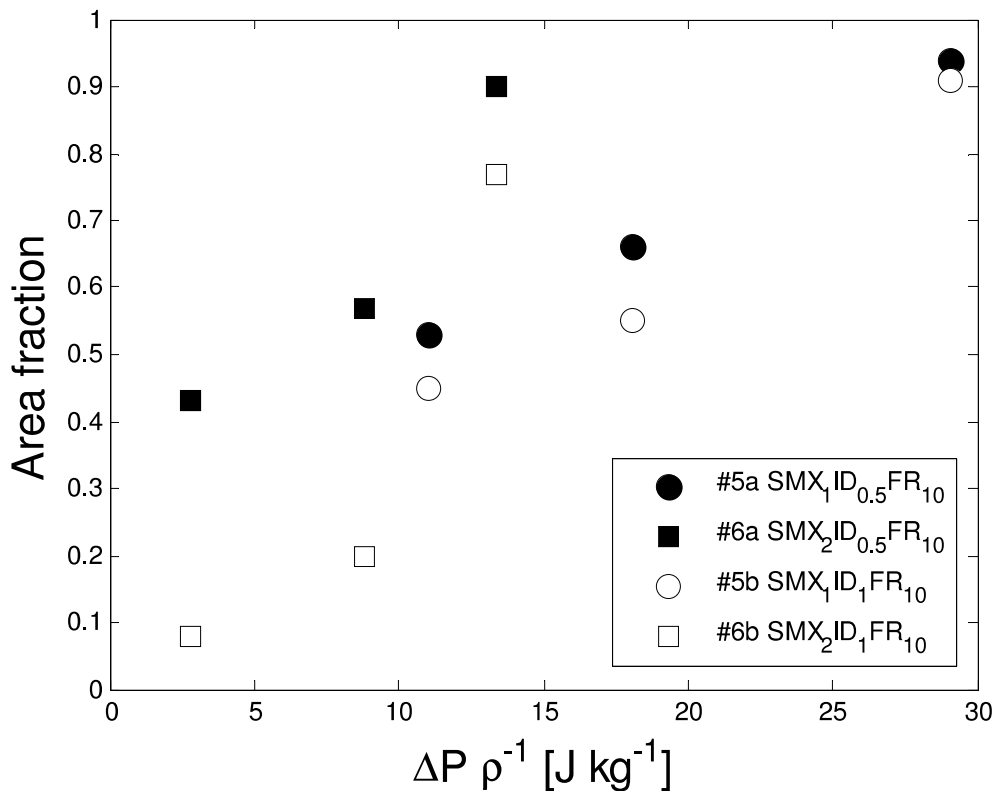
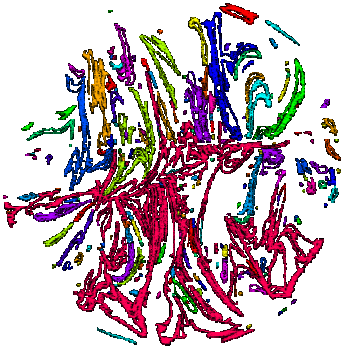
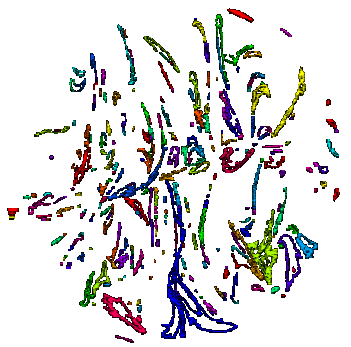
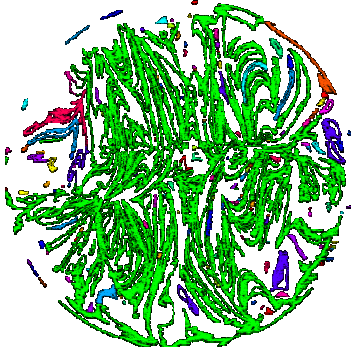




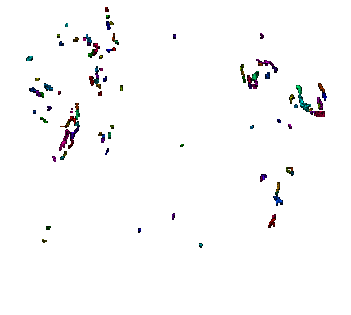
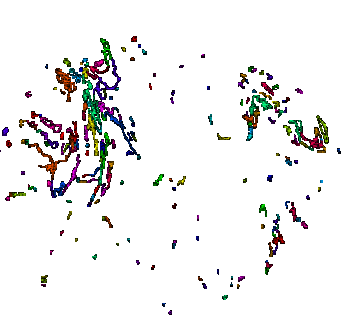
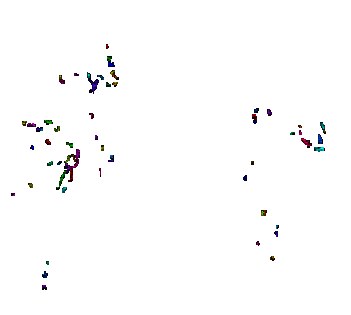
Figure 6.8 Fraction of mixing better than 80% ($X > 80\%$) versus $\Delta P/\rho$ for experiment #5a&b and #6a&b.

Figure 6.7 provides a general overview of the performance as a function of energy per unit mass. In this plot the mixing intensity is for $X > 80\%$. By increasing energy input per unit mass the level of mixedness increases for both systems where fluid 1 or fluid 2 are injected. The amount of ‘good mixing’ increases proportionally with energy per unit mass and it appears to be dependent from the size of static mixers which means that the Reynolds number affects the overall performance of the device. This effect is clearly shown by the points at higher $\Delta P/\rho$ for the 1” device where they are completely out of the trend for both injections. Besides, it seems that the ½” device performs better for the injection of fluid 2 (more thick), however the increase of energy per unit mass seems not really impact the overall mixing performance for the injection of the other fluid (fluid 1).

(a1)

Injection	Superficial velocity 0.1 [m s ⁻¹]		
		X ₉₀₋	X ₉₀₊
Fluid 1 (#5a)	X > 90%		
	80 < X < 90%		

(a2)

Injection	Superficial velocity 0.1 [m s ⁻¹]		
		X ₉₀₋	X ₉₀₊
Fluid 2 (#5b)	X > 90%		
	80 < X < 90%		

(a3)

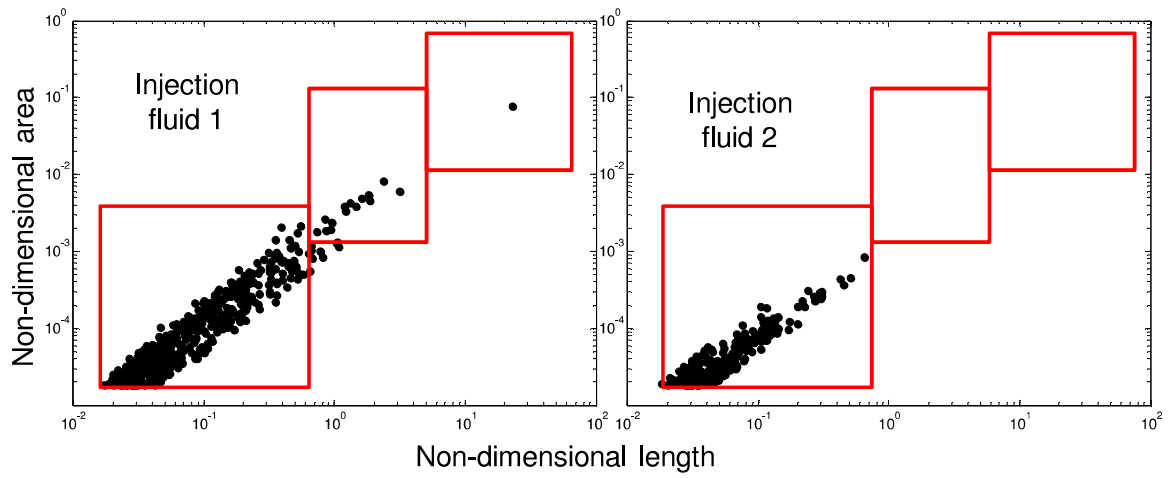
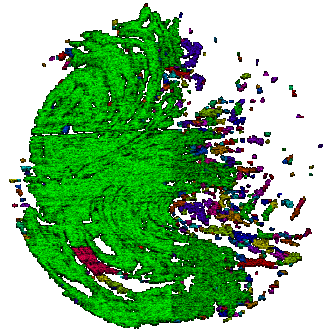
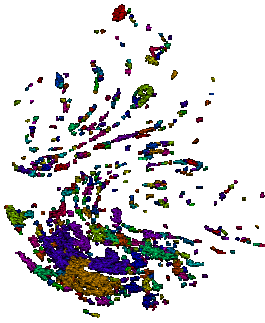
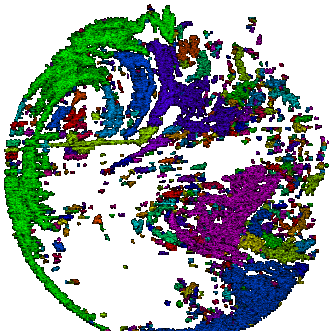

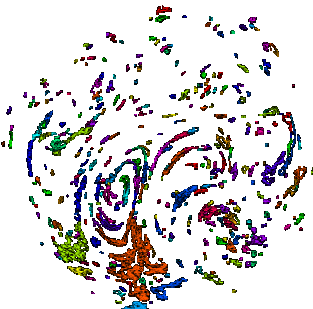
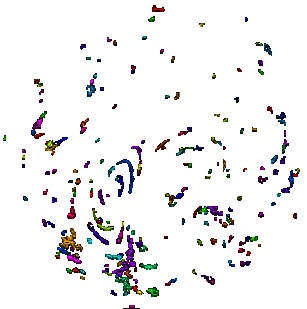
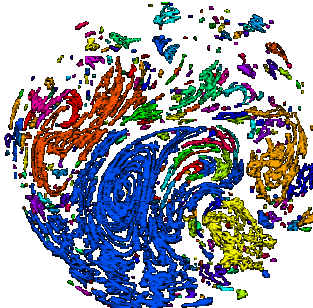
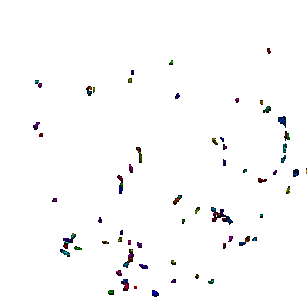


Figure 6.8a Striation areas for selected ranges of mixing intensity (injection fluid 1 and injection fluid 2) for $\frac{1}{2}$ " device including the plot of distribution of striation sizes for injection fluid 1 and for injection fluid 2 at $v=0.1\text{m s}^{-1}$.

(b1)

Injection	Superficial velocity 0.3 [m s ⁻¹]		
		X ₉₀₋	X ₉₀₊
Fluid 1 (#5a)	X > 90%		
	80 < X < 90%		

(b2)

Injection	Superficial velocity 0.3 [m s ⁻¹]		
		X ₉₀₋	X ₉₀₊
Fluid 2 (#5b)	X > 90%		
	80 < X < 90%		

(b3)

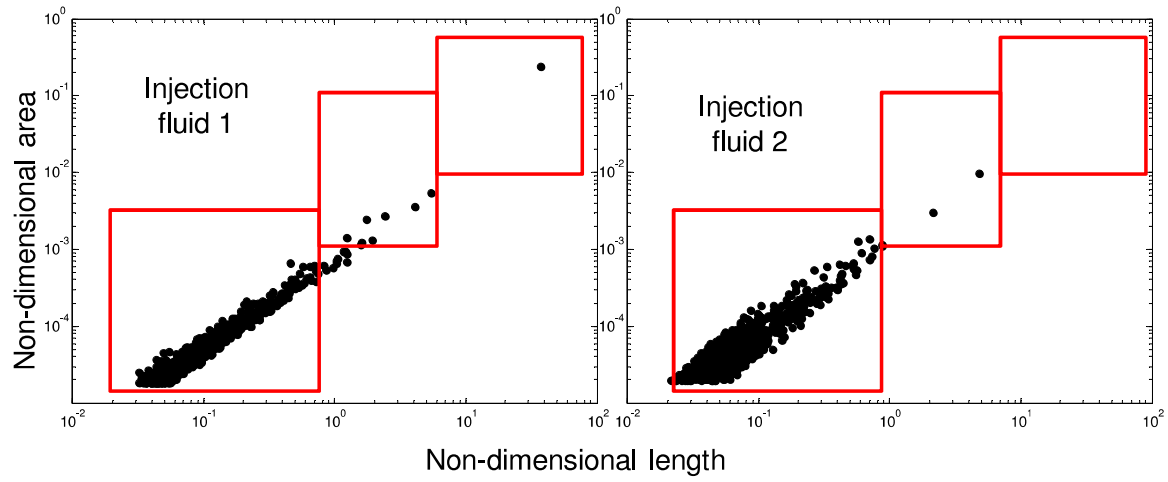

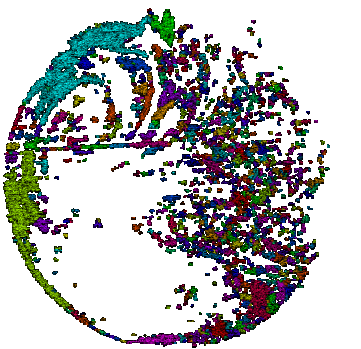
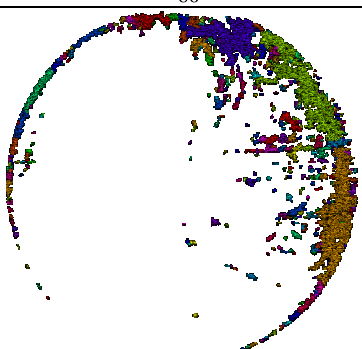
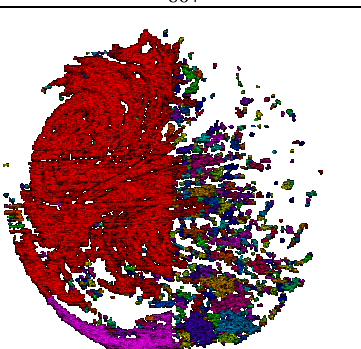
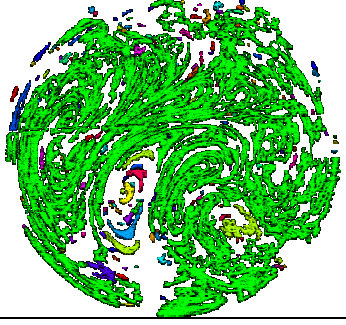
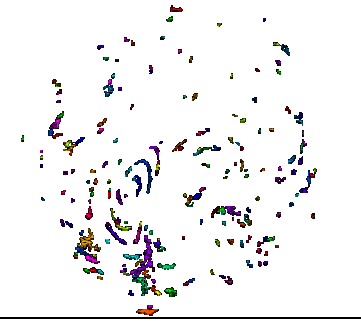
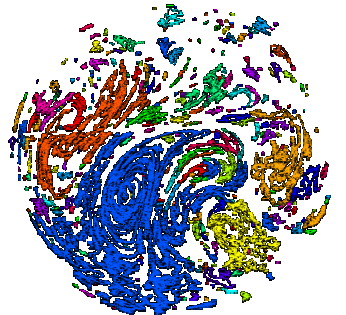
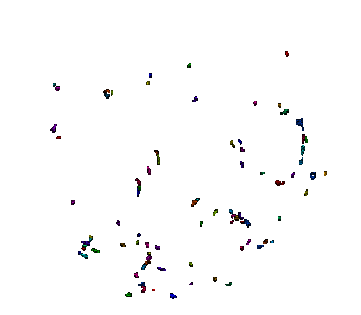


Figure 6.8b Striation areas for selected ranges of mixing intensity (injection fluid 1 and injection fluid 2) for 1/2" device including the plot of distribution of striation sizes for injection fluid 1 and for injection fluid 2 at $v=0.3\text{m s}^{-1}$.

(c1)

Injection		Superficial velocity 0.6 [m s ⁻¹]	
		X ₉₀₋	X ₉₀₊
Fluid 1 (#5a)	X > 90%		
	80 < X < 90%		

(c2)

Injection		Superficial velocity 0.6 [m s ⁻¹]	
		X ₉₀₋	X ₉₀₊
Fluid 2 (#5b)	X > 90%		
	80 < X < 90%		

(c3)

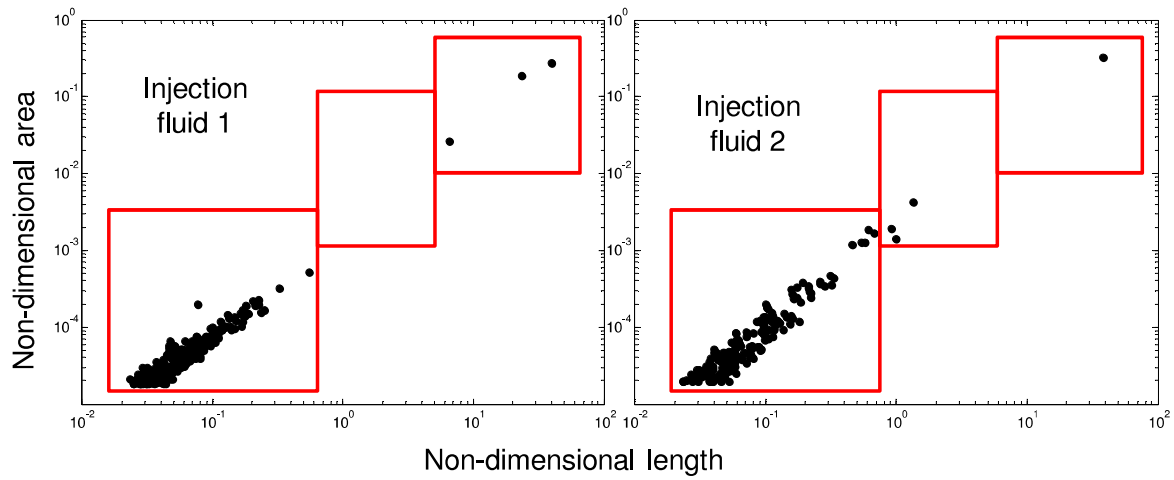


Figure 6.8c Striation areas for selected ranges of mixing intensity (injection fluid 1 and injection fluid 2) for $\frac{1}{2}$ " device including the plot of distribution of striation sizes for injection fluid 1 and for injection fluid 2 at $v=0.6\text{m s}^{-1}$.

(a1)

Injection	Superficial velocity 0.1 [m s ⁻¹]		
		X ₉₀₋	X ₉₀₊
Fluid 1 (#6a)	X > 90%		
	80 < X < 90%		

(a2)

Injection	Superficial velocity 0.1 [m s ⁻¹]		
		X ₉₀₋	X ₉₀₊
Fluid 2 (#6b)	X > 90%		
	80 < X < 90%		

(a3)

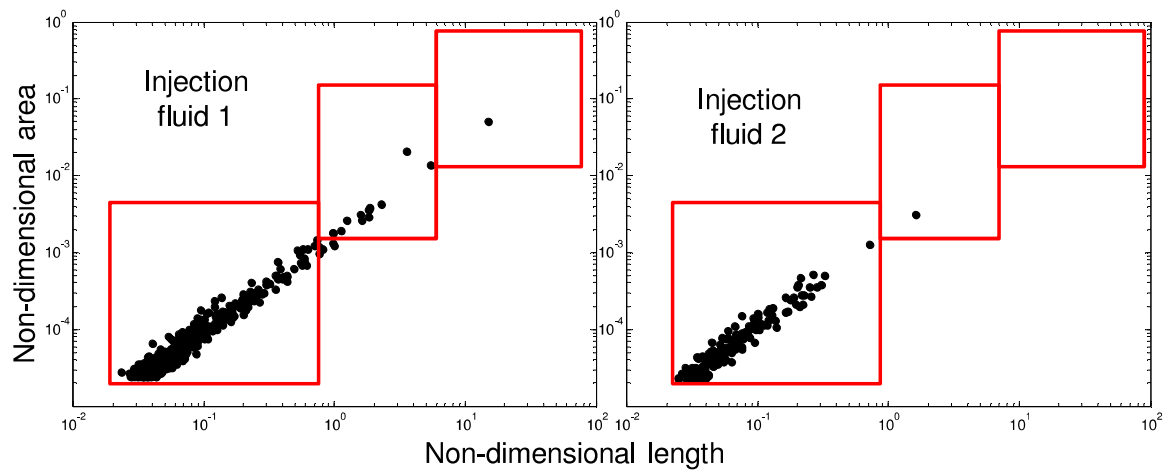
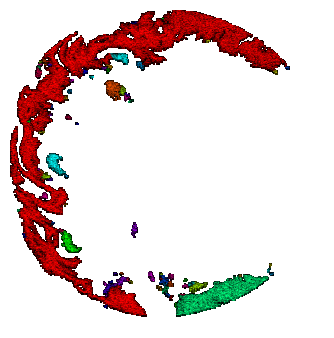
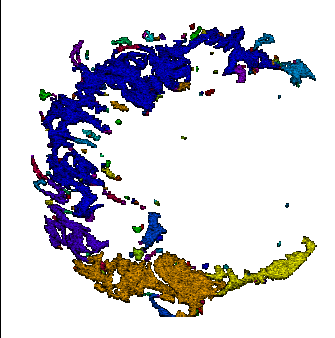
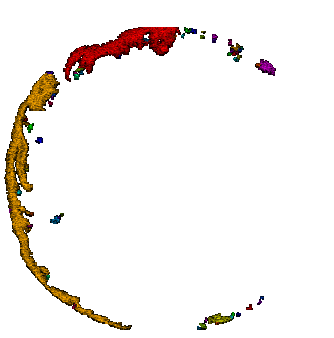
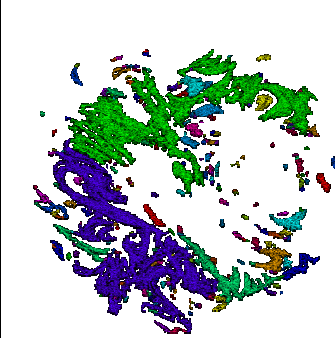
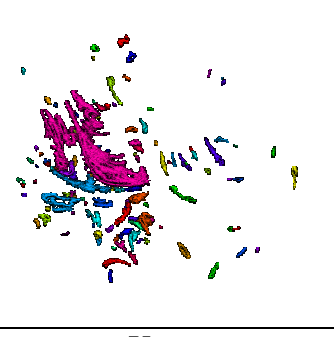

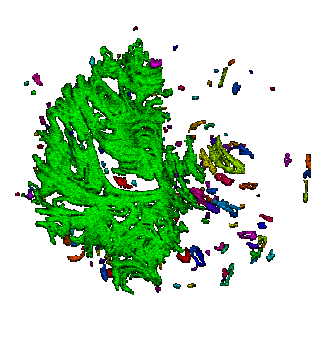
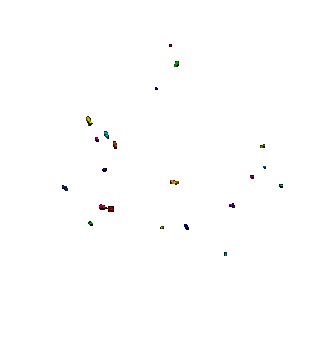


Figure 6.9a Striation areas for selected ranges of mixing intensity (injection fluid 1 and injection fluid 2) for 1" device including the plot of distribution of striation sizes for injection fluid 1 and for injection fluid 2 at $v=0.1\text{m s}^{-1}$.

(b1)

Injection	Superficial velocity 0.3 [m s ⁻¹]		
		X ₉₀₋	X ₉₀₊
Fluid 1 (#6a)	X > 90%		
	80 < X < 90%		

(b2)

Injection	Superficial velocity 0.3 [m s ⁻¹]		
		X ₉₀₋	X ₉₀₊
Fluid 2 (#6b)	X > 90%		
	80 < X < 90%		

(b3)

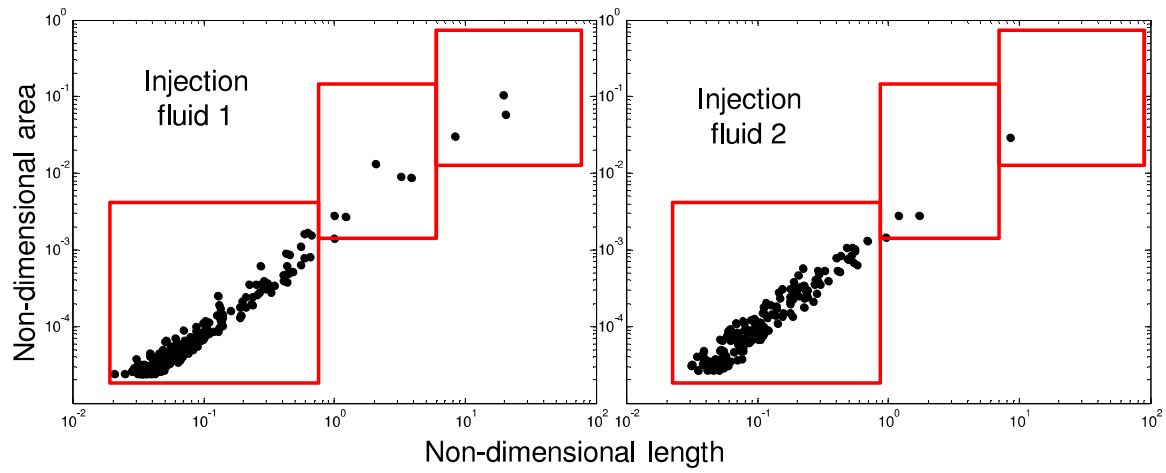
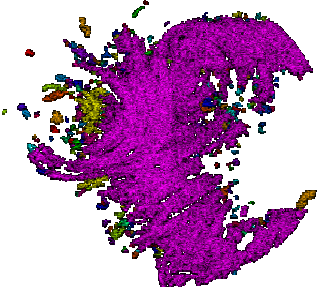
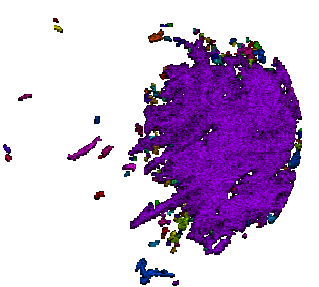
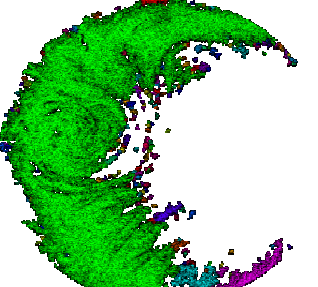
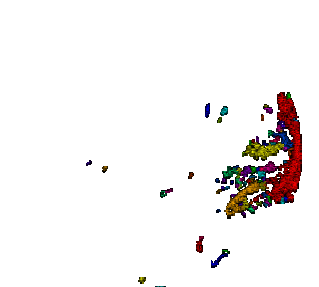
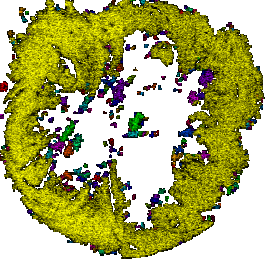
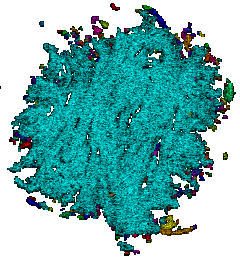
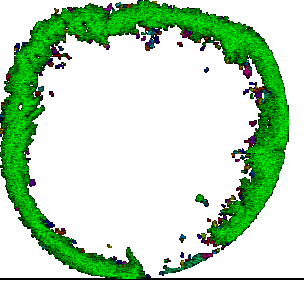
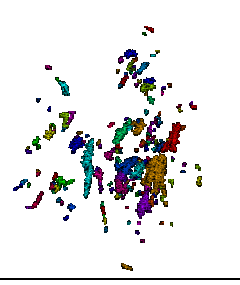


Figure 6.9b Striation areas for selected ranges of mixing intensity (injection fluid 1 and injection fluid 2) for 1" device including the plot of distribution of striation sizes for injection fluid 1 and for injection fluid 2 at $v=0.3\text{m s}^{-1}$.

(c1)

Injection	Superficial velocity 0.6 [m s ⁻¹]		
		X ₉₀₋	X ₉₀₊
Fluid 1 (#6a)	X > 90%		
	80 < X < 90%		

(c2)

Injection	Superficial velocity 0.6 [m s ⁻¹]		
		X ₉₀₋	X ₉₀₊
Fluid 2 (#6b)	X > 90%		
	80 < X < 90%		

(c3)

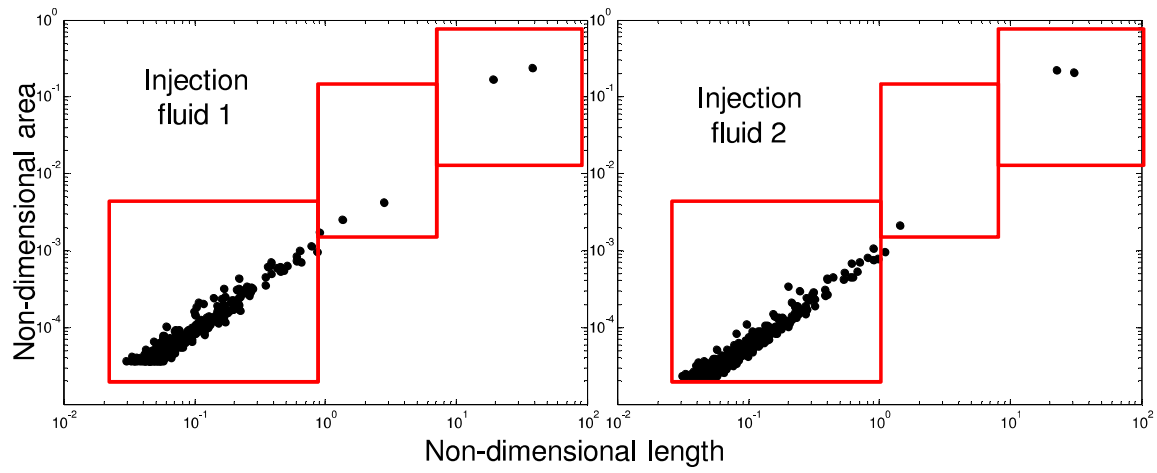


Figure 6.9c Striation areas for selected ranges of mixing intensity (injection fluid 1 and injection fluid 2) for 1" device including the plot of distribution of striation sizes for injection fluid 1 and for injection fluid 2 at $v=0.6\text{m s}^{-1}$.

A distribution of striations for selected ranges of mixing intensity is shown in Figure 6.8 for ½” and Figure 6.9 for 1” at three superficial velocities; the analysis method is the same as used in Chapter 5. The scale and viscosity ratio effects are visualised and schematised using this analysis. The striations within the range of interest $X > 90\%$ and $80 < X < 90\%$ and selected superficial velocities are presented for each experiment. The different striations detected by the MATLAB script are highlighted with different colours. In addition, plots (Figure 6.8c and 6.9c) are displayed where the striation size distribution for $X > 90\%$ is shown classifying it in 3 zones.

Figure 6.8 shows the shape of the striations for the experiment where ½” SMX Plus was used at three velocities. By increasing the velocity the number of striations decreases, but they all increase in area size showing the progressing of mixing due to increasing the energy input in the system. Notable differences of striation shape are shown in the coloured images for the different velocities showing the characteristic pattern generated by the SMX Plus element at lower velocities.

In Figure 6.8(a2), (b2), (c2) it is clear how the size of the striations increases by increasing the velocity and how they are generated from a side of the cross section and increasing the velocity their occupancy in the cross section increases. As it was for KM static mixer the injection of fluid 2 decreases the performance of static mixer but SMX plus generates high number of striation also at lower velocity. When the velocity increases up to 0.6 m s^{-1} the non-Newtonian behaviour on the formation of striations is lessened, potentially due to higher shear rates. According to the experiments undertaken, very large striation with similar range of mixing is typical for this flow condition.

The striation size distribution is plotted in Figure 6.8 (a3), (b3), (c3) , where the non-dimensional striation area versus the non-dimensional length schematises all the features of

the detected striations. At lower velocity the points are concentrated in zone 1 but distributed also in the other zones for the injection of fluid 1. However for the injection of fluid 2 the number of striation is lower and the distribution is limited to zone 1. At the intermediate velocity the number of points in zone 1 decreases whilst zone 2 becomes more populated. At higher velocity for the injection of fluid 1 the total number of points decreases, which confirms the generation of more concentrated zones of increased size. Instead, the number of striations increases (zone 1) when the fluid 2 is used for the injection, showing the generation of new areas with higher mixing intensity. Bigger areas are also detected, demonstrating the progressing of the overall mixing. At higher velocity (Figure 6.8(c3)) the distributions are more similar compared to the experiment of injection of fluid 1 indicating the progressing of the mixing detected also by the area fraction method. General trends are summarized in the plots where increasing velocity, as for the experiment #5a, the total number of striations decreases in zone 1 and in number. Comparing plots for different injections it looks like that the number of spots in zone 1 decreases slowly for the injection of fluid 2, identifying the limitations caused by the yield stress.

Compared to the results obtained for KM, the striation pattern for SMX Plus has a clearer and more symmetric structure also at lower velocity, which proves the effectiveness of the SMX Plus device. Figure 6.9 (a1), (b1), (c1) and 6.9 (a2), (b2), (c2) show the shape and distribution of striations for experiments #6a and #6b where the 1" SMX Plus static mixer device was used. For the experiments run at a lower velocity, the striations are more localized compared to ½" device showing more asymmetry on the mixing. Then the general trend is similar to the previous experiments for both injections. Comparing the two scales, further similarities are seen in the increasing striation size with velocity. At velocity 0.3 m s^{-1} it is clear how the zones with high mixing intensity are concentrated on the side and this may be due to the rotational component of the flow which directs the flow where the effect is

stronger. The injection of fluid 2 creates similar pattern to the 1/2" device, at lower and middle velocity the size of striations is limited and at higher velocity there is a formation of big striations. As for the KM static mixer, the yield stress plays an important role limiting the swirling and stretching of the injected flow. Despite that, a classification of different effects on the mixing can be done following the information of area fraction and striation distribution for different devices. Referring to Figures 6.9 (a3), (b3), (c3) the general trend is similar to that seen in the previous set of experiments for 1/2". Injecting fluid 1 at low velocity, the striations are concentrated in zone 1, while they move towards zone 2 and then zone 3 after increasing the velocity. Comparing the injections of fluid 1 and 2, in the latter the number of striations increases. At first rise of velocity the distribution of size of striations remains concentrated in zone 1 and then at last stage the striations tend to increase in size and decrease in number.

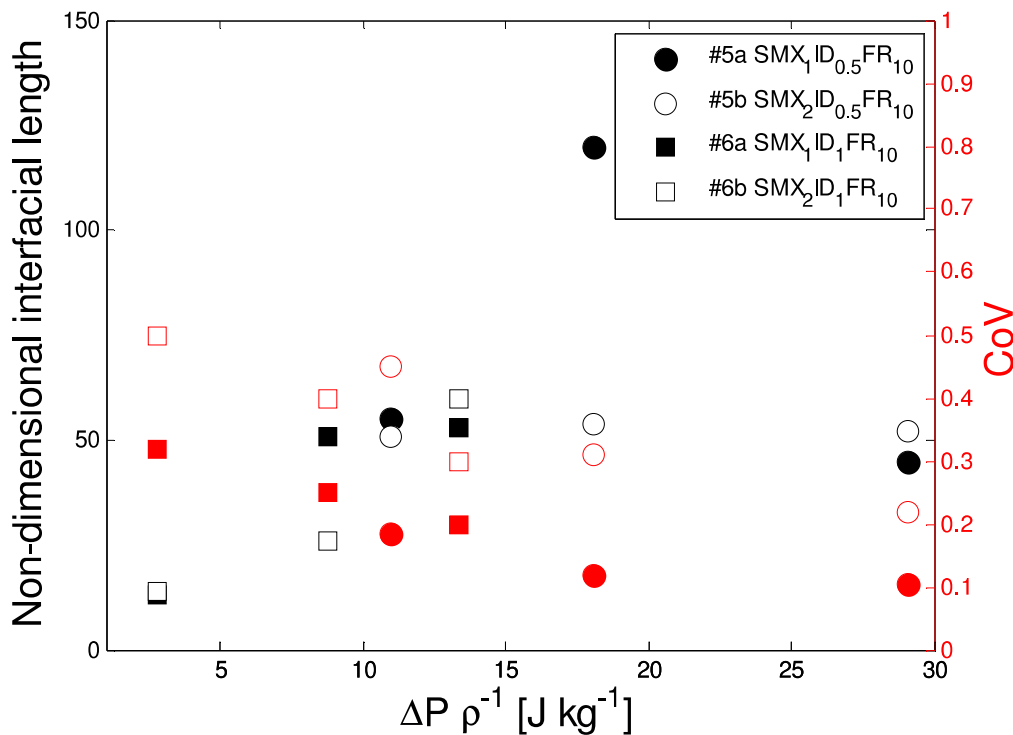


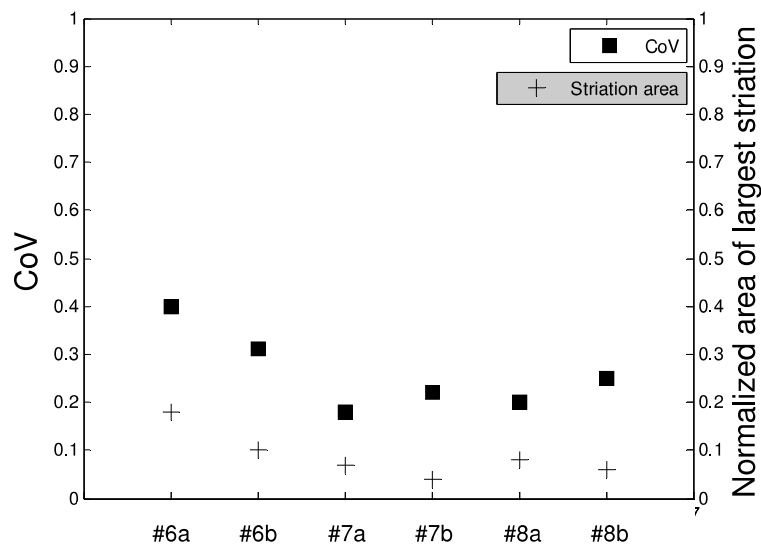
Figure 6.10 Total “interfacial length” over the static mixer perimeter for mixing intensity better than 80% ($X > 80\%$) versus $\Delta P/\rho$ for experiment #5a&b and #6a&b.

As previously evaluated for KM static mixer, the ‘interfacial length’ is calculated also for SMX Plus (Figure 6.10) showing interesting trends. From the results it can be extrapolated that interfacial length is less affected by the injection as before for KM, except for the experiment #5a at 0.3 m s^{-1} where the “interfacial length” increases of an order of magnitude compared to #5b. Again the CoV analysis does not give precise information and it does not recognise changes of system. The proposed analysis allows the determination of clear trends, recognising also small changes between different runs and experiments. The performed experiments are repeatable keeping constant all the experimental set up which can influence the mixing performance or the sensitivity of images (inlet position, superficial velocity, dye concentration, laser power, etc). Besides, the experiments can be considered time independent after a few seconds which is the time spent by the system when is switched on, to reach steady condition.

6.3.3. Effect of flow ratio and injection position at constant velocity and scale

In Figure 6.11a there are the values of CoV and maximum striation thickness at constant $\Delta P/\rho$, which show a consistent difference between experiments with a flow ratio of 10 (#6a, #6b) and a flow ratio of 25 (#7a&b, #8a&b), the latter generally seems to have better performance.

(a)



(b)

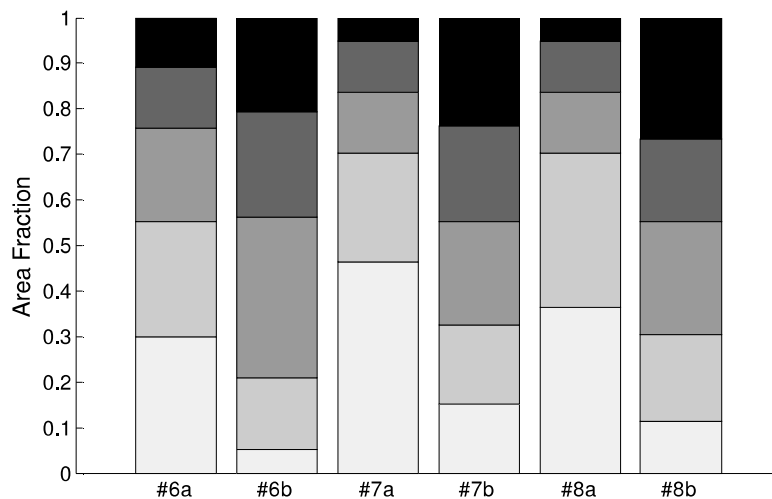


Figure 6.11b Effect of flow ratio and injection position at constant velocity and scale: CoV (intensity of segregation) and max striation area at constant $\Delta P/\rho$ bar graph showing discrete areal intensity distributions for #6a, #6b(central injection, flow ratio 10),#7a,

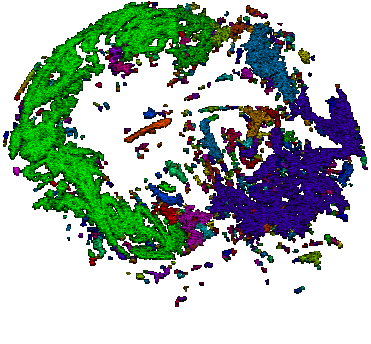
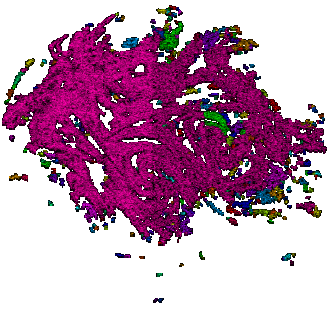
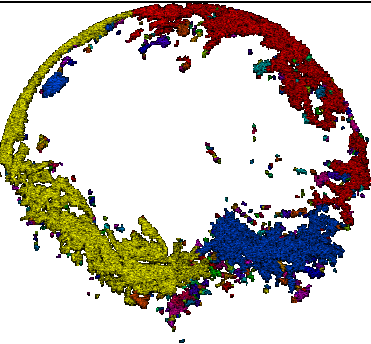
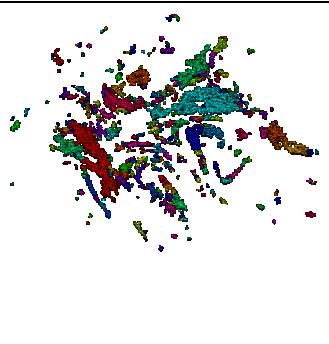
#7b(central injection, flow ratio 25), #8a and #8b (wall injection, flow ratio 25) at $v=0.3 \text{ ms}^{-1}$.

Consistent changes are shown in Figure 6.11b, where the mixing performances for 1" with flow ratio 10 are radically different compared to experiments the flow ratio 25:

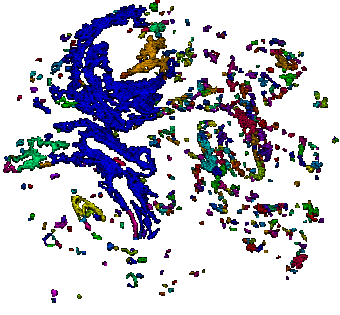
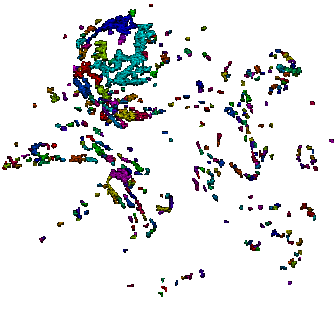
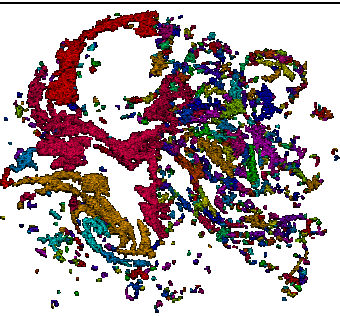
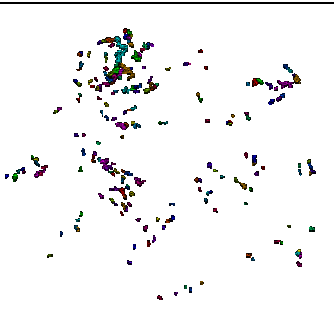
- the fraction of $X>90\%$ for #6a is lower than for #7a;
- the fraction of mixing intensity of $80\%<X<90\%$ is similar;
- the fraction of $X<60\%$ is reduced by 1/2 for the experiment with the injection of fluid 1 (#7a) and slightly increase for the other (#7b).

By analysing the results of experiment with same flow ratio of 25 but with different injection position (#7a vs #8a and #7b vs #8b in Figure 6.11), it is clear that the position of the injection does not really affect the mixing performance as for KM. Keeping all parameters constant the overall mixing performance slightly decreases. This information follows previous results obtained by Zalc (2002) which explains this lack of performance in SMX static mixer. A misaligned nozzle of the injected stream exhibits channelling behaviour while significant mixing only begins further downstream. Due to the small difference between mixing performance, CoV and maximum striation thickness do not recognise the effect of different injection positions. This is highlighted by area fraction and distribution of size of striations analysis. Figure 6.11b shows differences in the $X>90\%$ area fraction for experiments with flow ratio 25 but with different injection position (#8a and #8b compared to #7a and #7b). Even more significant differences are visible for area fraction of $X<60\%$. Striation size analysis for experiments #7 and #8 is presented in Figures 6.12 and 6.13.

(a)

Injection	Superficial velocity 0.3 [m s ⁻¹]		
		X ₉₀₋	X ₉₀₊
Fluid 1 (#7a)	X > 90%		
	80 < X < 90%		

(b)

Injection	Superficial velocity 0.3 [m s ⁻¹]		
		X ₉₀₋	X ₉₀₊
Fluid 2 (#7b)	X > 90%		
	80 < X < 90%		

(c)

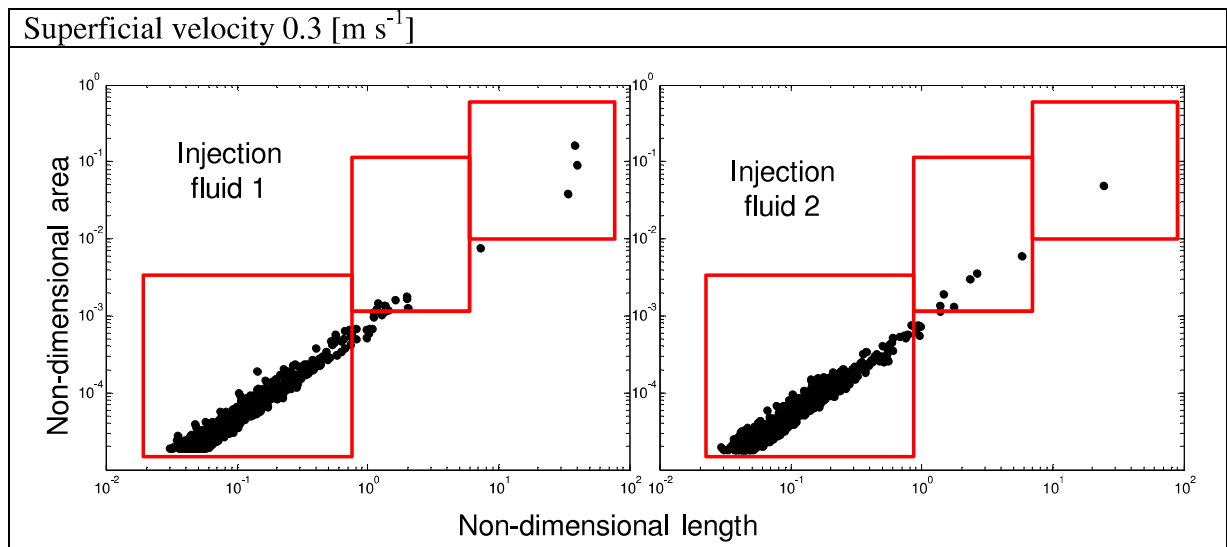
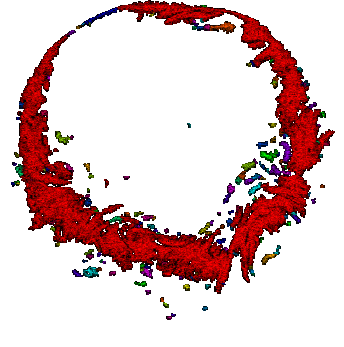
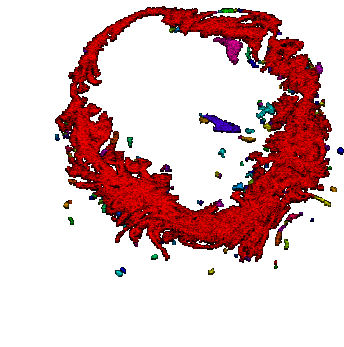
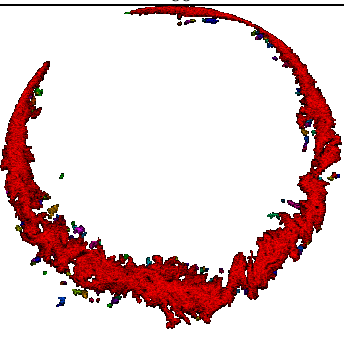
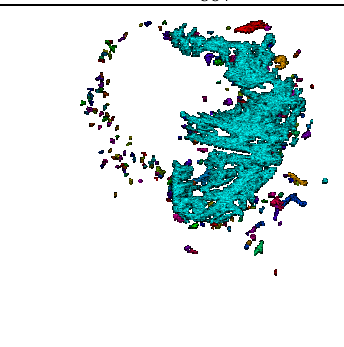
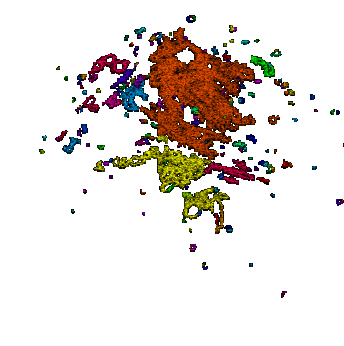
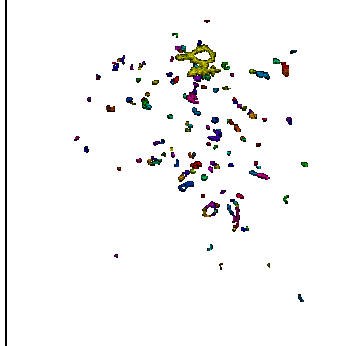
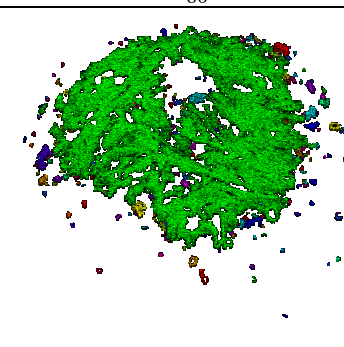
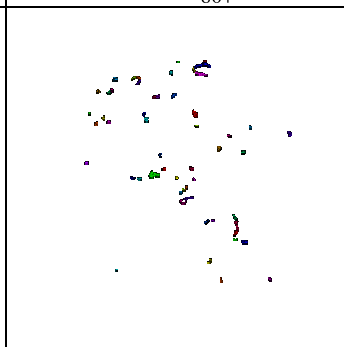


Figure 6.12 Effect of flow ratio 25 for a central injection for 1” device: a) striations area for selected ranges (injection fluid 1) b) striations area for selected ranges (injection fluid 2), c) distribution of striation size (injection fluid 1vs injection fluid 2).

(a)

Injection		Superficial velocity 0.3 [m s ⁻¹]	
		X ₉₀₋	X ₉₀₊
Fluid 1 (#8a)	X > 90%		
	80 < X < 90%		

(b)

Injection		Superficial velocity 0.3 [m s ⁻¹]	
		X ₉₀₋	X ₉₀₊
Fluid 2 (#8b)	X > 90%		
	80 < X < 90%		

(c)

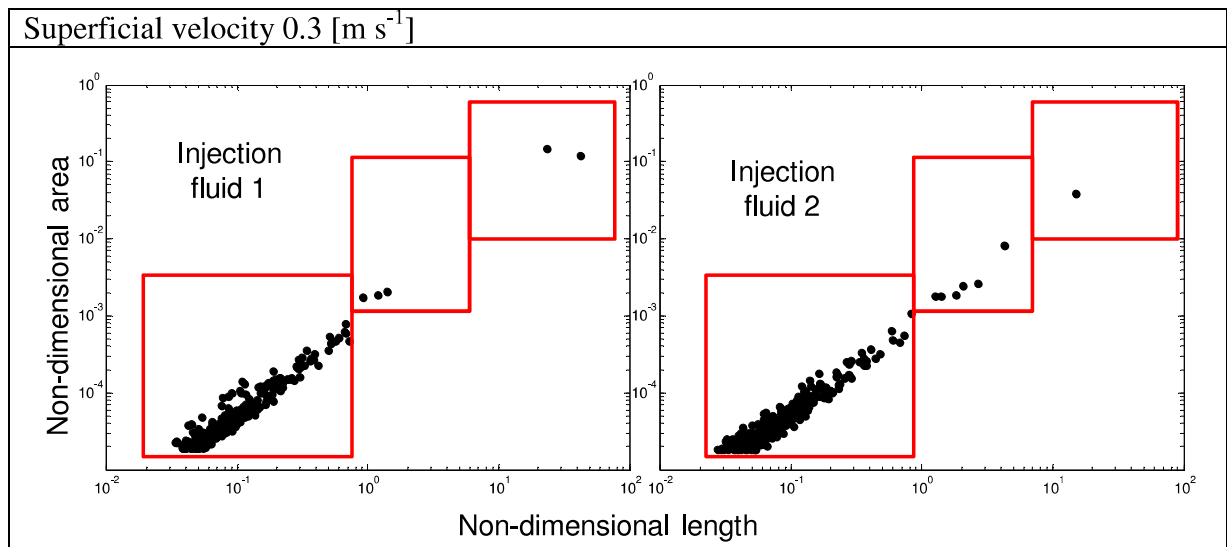


Figure 6.13 Effect of injection position at wall for 1'' device at constant flow ratio of 25: a) striations area for selected ranges (injection fluid 1) b) striations area for selected ranges (injection fluid 2), c) distribution of striation size for the injection of fluid 1 and injection of fluid 2.

The biggest striations are distributed on the whole cross section as on the side for lower bound range (X.) as in experiment for flow ratio 10, and in the centre for the higher bound (X+) which was not on the cross section for the experiment for flow ratio 10. Also the injection of fluid 2 changes the system for the better because the striations are bigger in size and in “interfacial length” (Figure 6.12c). The mixing performance for experiments #8a and #8b are quite similar to the previous results obtained using flow ratio 10. The ‘good mixing’ is concentrated on the sides for both bounds but after the injection of fluid 2 the striations have a consistent size compared to experiment #5b and a larger number of threads are detected too.

The striation size distribution is shown in Figures 6.12c and 6.13c, where the non-dimensional striation area versus non-dimensional length summarizes all characteristics of the detected striations. The comparison between experiments with 1” SMX Plus but with different flow ratios 10 (#6a&b) and 25 (#7a&b) (Figures 6.9 (b3) versus Figure 6.12c) shows a lower number of points in zone 2 and but similar concentration in zone 1. For experiments for the wall injection and flow ratio 25 (#8a and b) (Figure 6.12c), all striations are not concentrated in zone 1 as it was for the KM static mixer where they were much more affected by the wall injection. In this paragraph it is shown how the proposed methods give detailed information which allows a comparison between different devices that have different effects on the blending of non-Newtonian fluids.

6.3.4. Time independency

From the beginning of this study the time independent nature of fluids was known. In other words, the fluid properties do not change with time but they do if different stress is applied. However, important feature of the blending of non-Newtonian fluids using static mixer has been taken into account when gear pumps is used to pump the main flow and for the injection of secondary flow. As mentioned previously 10 different images were captured for each experiment in order to get consistent results. If the location of the laser is maintained in the same position the 10 images prove to be exactly the same. Examples of images detected at different times are reported in Figure 6.14; both kind of devices (KM and SMX Plus) show that the pattern at the end of static mixer is independent of the time of capture.

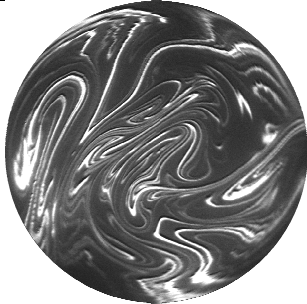
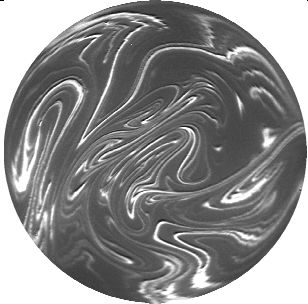
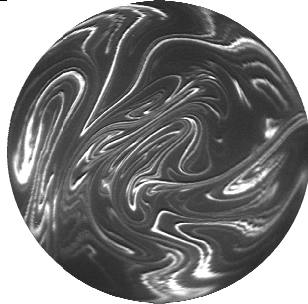



Time	t_1	t_2	t_3
KM 6 elements $v=0.3 \text{ m s}^{-1}$ Injection fluid 1			
SMX Plus 6 elements $v=0.3 \text{ m s}^{-1}$ Injection fluid 1			

Figure 6.14 Flow pattern for selected experiments at different detection time for KM and SMX Plus static mixers.

This information has an industrial relevance because it means that the system is stationary. Besides, depending on the parameter of the system considered (pH, temperature, etc) it can involve problems in the process. A classical example to explain this phenomenon is the reaction which can be in function of pH or temperature. Constant patterns can create fixed zones where a hypothetical reaction does not take place due to wrong pH or high temperature which can be a negative consequence for the overall process efficiency.

6.3.5. Energy consumed in KM and SMX Plus static mixers

In order to compare the energy consumed and the mixing performance, area fractions with mixing intensity $X > 80\%$ versus energy per unit mass are plotted in Figure 6.15 for all devices with $\frac{1}{2}$ " diameter.

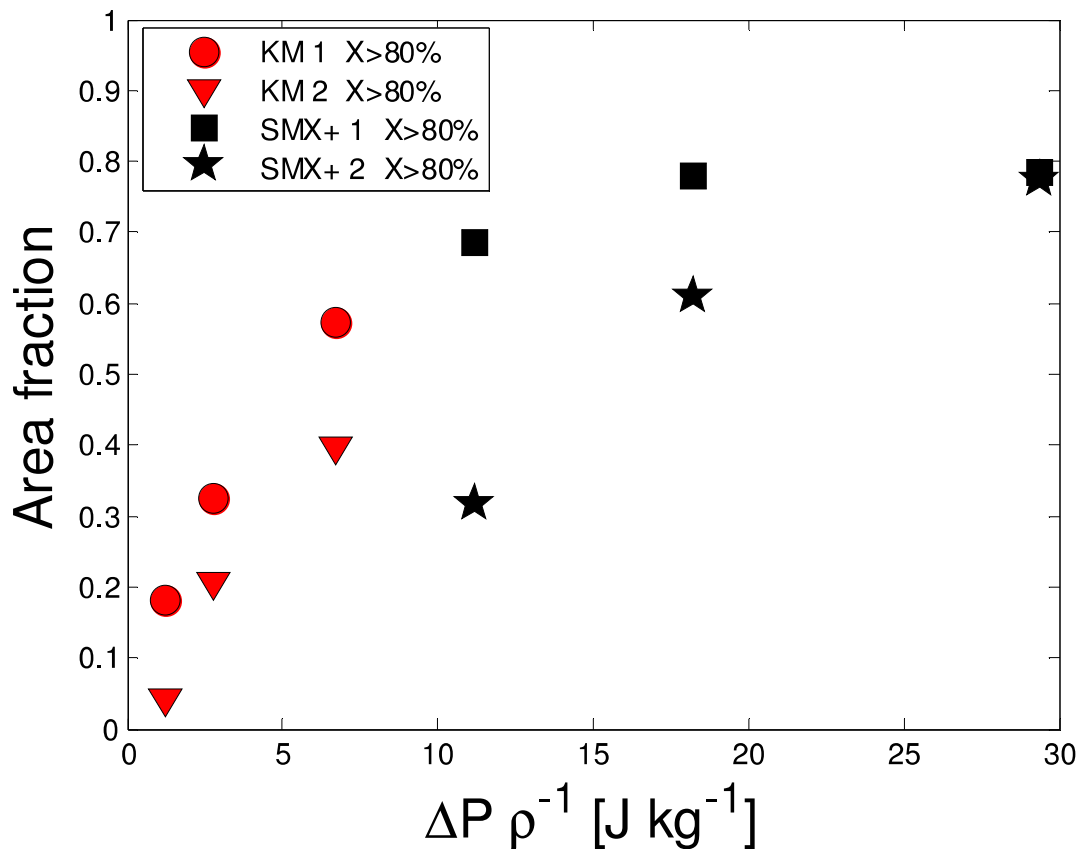


Figure 6.15 Fraction of mixing better than 80% ($X > 80\%$) versus $\Delta P/\rho$ for experiments with different geometries using $\frac{1}{2}$ " device.

Generally KM2 and SMX Plus2 (injection of fluid 2) have lower area fractions. However, for both injections the data show a general trend in which increasing the energy per unit mass, the fraction of ‘good mixing’ increases independently from the static mixer used. As showed in the graph, at the highest value of energy per unit mass the effect of the injection of fluid 2 is negligible.

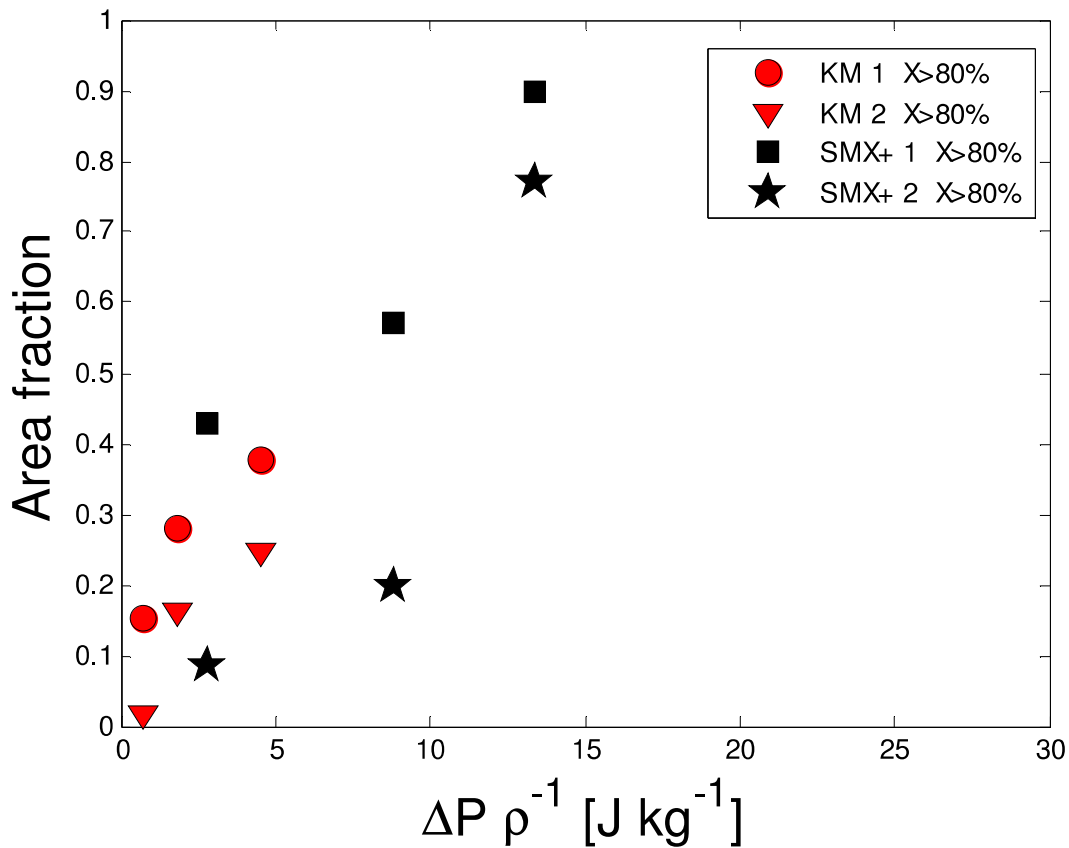


Figure 6.16 Fraction of mixing better than 80% ($X > 80\%$) versus $\Delta P/\rho$ for experiments with different geometries using 1” device.

In Figure 6.16 the area fractions for 1” devices are plotted keeping the same parameters of the previous graph. For the injection of fluid 1, the area fraction increases proportionally to the energy per unit mass, with the exception for the highest velocity for KM 1. For the injection of fluid 2 the trends of KM 2 and SMX Plus 2 are very diverse and it may be due to the lower Reynolds number that cannot generate a sufficient stress on the fluid, compared to the ½” diameter. These results show the strongest effect of rotational component of the flow which seems to affect the blending of non-Newtonian fluids. This happens in particular with the injection of fluid 2, where the flow field plays a more important role than the energy per unit mass in the system.

Another important value which has to be calculated in order to clearly understand the energy spent by devices per unit time, is the power used for the blending. As mentioned before, the energy spent per unit mass was calculated as:

$$\text{Energy per unit mass [J/Kg]} = \Delta P/\rho. \quad (6.1)$$

However, pressure drops (ΔP), flow rates (Q) and an estimation of mass of fluid in the devices were used to calculate the power per unit mass as:

$$\text{Power per unit mass [W/kg]} = (Q * \Delta P)/\text{mass fluid in static mixer}. \quad (6.2)$$

The mass of fluid in all devices was estimated subtracting the volume of the static mixer frame to the volume of the pipe and multiplying it by the density of the fluid. KM and SMX Plus geometries are different; therefore the volumes of the frames were calculated considering the following instructions.

For KM static mixer the geometry can be considered as parallelepiped twisted of 180 degrees. To determine the volume of the frame for 6 elements the volume of single parallelepiped will be multiplied by the number of elements (eq. 6.3). The three dimensions (d =diameter of pipe, L = length of element and t =thickness) which describe the parallelepiped are listed in the following table for 1" and 1/2" diameters.

$$\text{Volume KM frame} = 6 \times (d_e \times L_e \times t_e) \quad (6.3)$$

Table 6.3 KM element geometry dimensions

Static mixer	d_e	L_e	t_e
1"	0.025	0.04	0.003
1/2"	0.0125	0.025	0.002

For SMX Plus the geometry is more complicated but it can be assumed that the single element consists of 4 long sticks and 9 short ones (eq. 6.4). The dimensions (x =width of the sticks, l =short length, L =long length and t =thickness) of long and short sticks are described in the following table.

$$\text{Volume SMX Plus frame} = 6 \times [4 \times (L_e \times x_e \times t_e) + 9 \times (l_e \times x_e \times t_e)] \quad (6.4)$$

Table 6.4 SMX Plus element geometry dimensions

	d_e	L_e	x_e	l_e	t_e
1"	0.025	0.04	0.003	0.025	0.001
1/2"	0.0125	0.025	0.001	0.0125	0.001

The values of energy per unit mass and the power per unit mass are showed in table 6.5.

Table 6.5 Values of energy per unit mass and power per unit mass for KM and SMX Plus at three different superficial velocities.

KM ½"	m s ⁻¹	L hr ⁻¹	J kg ⁻¹	W kg ⁻¹
	0.1	60	1.20	0.51
	0.3	160	2.80	3.17
	0.6	300	6.70	14.23
KM 1"				
	0.1	180	0.75	0.40
	0.3	540	1.80	2.89
	0.6	1080	4.50	14.46
SMX Plus ½"				
	0.1	60	11.00	4.41
	0.3	160	18.10	19.33
	0.6	300	29.10	58.13
SMX Plus 1"				
	0.1	180	2.80	1.29
	0.3	540	8.80	12.17
	0.6	1080	13.36	36.96

As expected, SMX Plus mixers need higher values of power per unit mass for both static mixer diameters. Increasing the superficial velocity the power increases as expected and the ½” diameter (KM and SMX Plus) always has higher values of power per unit mass compared to 1”. Clearly, the difference in absolute values between 1” and ½” SMX Plus at the same superficial velocity are much higher compared to KM static mixer. This is maybe can explain previous results showed in Figure 6.16 where the comparison between different devices of area fractions versus energy per unit were not proportional to energy spent, unlike for ½” static mixer showed in Figure 6.15. However, the scale effect on the overall mixing performance, for the blending of non-Newtonian fluids in terms of energy consumed, is relevant for SMX Plus geometry whilst for KM it is not.

6.4. Conclusions

The analysis of PLIF images has been performed to determine the mixing performance of SMX Plus static mixers using non-Newtonian aqueous solutions as a function of velocity, scale, flow ratio and injection position; and to compare the effect of these parameters to the viscosity ratio of the two fluids (main flow: always fluid 1, injected fluid: fluid 1 and 2).

A method previously presented (Alberini et al., 2013), which considers the distribution of the cross-sectional area with a given intensity of mixing, has been used. In combination to that, a detailed striation analysis for high mixing intensity has been considered to characterize mixing performances, giving much more information than previous analysis. As velocity increases the effect of varying the viscosity ratio becomes more negligible, whilst increasing

the size of the static mixer the mixing intensity performance decreases. In terms of energy consumed per unit mass, the 1" size is more efficient due to lower pressure drop per unit length. Increasing the flow ratio between the injection and the main flow does not affect much the overall mixing performance. The wall injection for the mixing of non-Newtonian fluids is not suggested as an operating configuration but it does not decrease the overall mixing performance as it was for KM static mixer. As described in the results, the SMX Plus device performs better using the same number of elements but the pressure drops increase drastically compared to KM. SMX Plus static mixer generates similar amount of 'interfacial length' to KM but using much more energy per unit mass. KM static mixer has more sensitivity to different configurations compared to SMX Plus. The 1" devices are more efficient in terms of energy spent for the blending of non-Newtonian in both devices. The 1" SMX Plus static mixer does not perform proportionally to the energy per unit mass as the KM. According to that the scale effect is more significant for SMX Plus than for KM.

7. UNDERSTANDING OF NON-NEWTONIAN BLENDING: FOCUSING ON FILAMENT STRETCHING AND DROP STRETCHING

7.1. Introduction

It is well known that advection is critical for the mixing of fluids over the timescales typically present within the chemical and physical processes used by industry. The previous results chapters have demonstrated how advective processes lead to the blending of non-Newtonian fluids within both KM and SMX Plus static mixers, and how the input parameters and mixer geometry influence the achievable mixing performance. Within the static mixer, fluid elements experience both shearing and stretching due to their path through the local flow field. As the PLIF images generated in Chapters 4-6 demonstrate, this flow field is complex and leads to the creation of an intricate pattern of striations. The striation pattern has been shown to be strongly influenced by the fluid rheology, both of the continuous phase and the injected fluid. Analysis of the data has shown that this performance can be characterised from an energetic argument, with the power per unit mass being a reasonable scaling criterion for a given set of initial conditions. In this Chapter, a preliminary study is made which aims

to unpick the individual mixing events occurring within static mixers, via individual experiments under closely controlled conditions to determine the behaviour of fluid drops or filaments of non-Newtonian fluids under the action of shear or elongation. By obtaining a better understanding of the response of individual events to the flow field, it is hoped to gain insight into the integral behaviour due to the combined effect of shear and elongation within static mixers. Usually, shear viscosity and extensional viscosity are the two parameters used to classify the behaviour of fluids under shear and elongation respectively. The aim of this chapter is not only focused on the characterization of the rheological behaviour, but also to investigate the consequences of these mechanisms (shearing and stretching) on drops of fluid in terms of interface topology and work done (energy).

The two aspects studied in this chapter are:

- how a shear field affects the shape of a drop of non-Newtonian fluid (fluid 1 or fluid 2) immersed in a Newtonian continuous phase;
- how the stretching of a filament of non-Newtonian fluid (fluid 1 or fluid 2) is affected by the rheological behaviour of the fluids and the energy spent to cause the breakage of the filament.

In the literature, similar studies on drop deformation or breakage and filament stretching are extensively developed. However, the final objectives of the researchers have concentrated on aspects other than mixing performance. Usually, drops in a continuous phase are used to calculate the interfacial tension using experimental approaches (Germann, 2012) (Megias-Alguacil, 2013). Other studies on this subject are concentrated on the investigation of drop breakage to estimate the performance of a device on the drop size distribution for emulsions, for example (Pacek, 1997) (Megias-Alguacil, 2006). However, all these investigations have

in common the use of parameters such as perimeter, area of drops and stretching rate which allow the description of the effect of different stress on drops.

Many studies on filament stretching are concerned about the investigation of rheology of the fluids in terms of extensional viscosity and Trouton ratio (Alves, 2008) (Arratia, 2006) (Yao, 2000) (Bandalusena 2012) (Shridar *et al.*, 1991), for more information the reader is referred to §2.1.3.2. Extensional viscosity has been extensively used to characterise polymer solutions (McKinley, 2005) because the progressive break-up of smaller droplets is an important dynamic process which covers a wide range of different industrial applications such as fertilizer and pesticides production, paint application, roll-coating of adhesives and food processing operations such as container and bottle-filling. The progressive thinning of a fluid filament is driven by capillarity and resisted by inertia, viscosity and additional stresses resulting from the extensional deformation of the fluid microstructure within the thread. In such cases, the transient extensional viscosity of the fluid plays an important role in controlling the dynamics of break-up. All these aspects are taken in account to characterise the single stretching mechanism on the investigated non-Newtonian solutions.

7.2. Experimental methods

7.2.1. Shear drop stretching

The equipment used for this preliminary study is a modified Bohlin rheometer (see §3.2.2) which has been used to impose fixed values of shear (50, 150, 300, 500 s⁻¹) to the continuous phase.

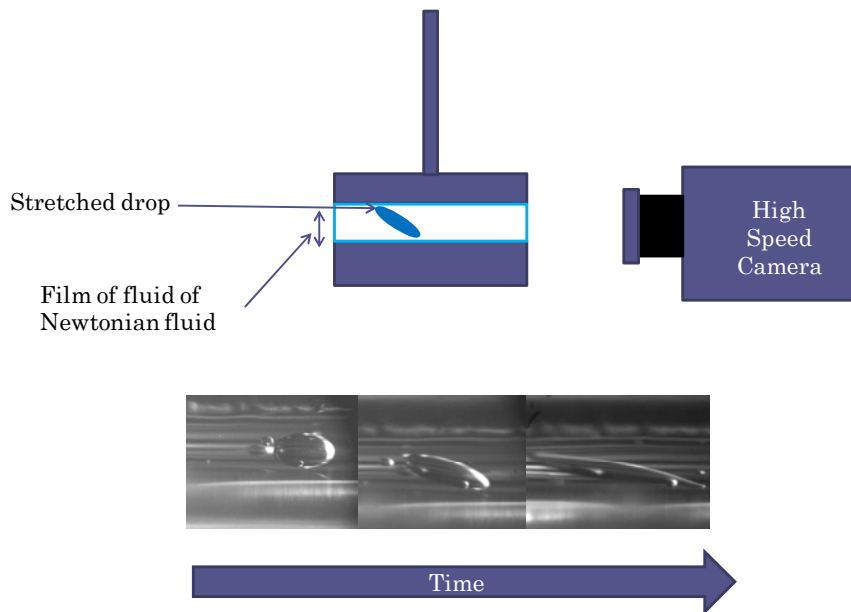


Figure 7.1 Drop stretching experiments

The drop stretching rig (Figure 7.1) involves also the use of high speed camera which is located on the size of the sample platform to detected how the shape of drops, with volume of 0.1 μL , changes with the time under different shear.. Due to the small size of the drops a microscope is attached to the camera using C-mount connection. The geometry used is a 60 mm plate which allows a larger gap (1000 μm) between the geometry and the sample platform for a better visualisation of the drops, compared to the cone/plate geometry that generally works at constant gap of the order of 50 μm at the centre of the cone. The continuous phase is silicon oil with a viscosity of 0.35 Pa s, which has a Newtonian behaviour. The interfacial tensions between the two non-Newtonian fluids and the silicon oil were measured. The measurements were done using a KRUSS K100 tensiometer, applying the ring method, which showed a small difference in the values between the two fluids giving values of $\sigma_{1S}=0.0035 \text{ N m}^{-1}$ and $\sigma_{2S}=0.0030 \text{ N m}^{-1}$ for fluid 1 and fluid 2 respectively.

The choice of this fluid has been determined by the properties of Newtonian fluid where the viscosity is not affected by the shear. That allows the application of a more uniform stress on

the non-Newtonian drops simplifying the phenomenon in a pure shear deformation, avoiding also non-Newtonian effects on the interface between the continuous phase and the drop. For all the experiments the drop was located in the same position which was one edge of camera view (Figure 7.2a). The effect of shear on the drop of fluids has been calculated from the variation of perimeter and the energy spent. Using the image J tools the area and perimeter of drops were calculated (Figure 7.2b).

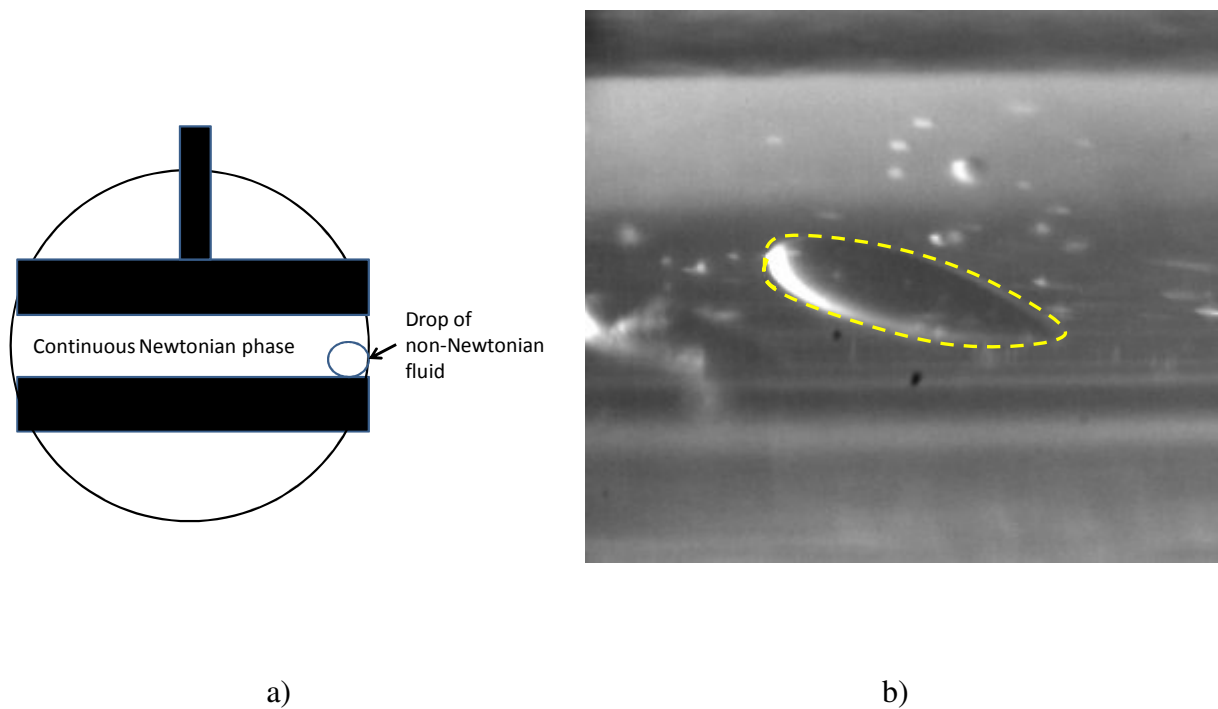


Figure 7.2. a) Location of the drop in each experiment and b) example of measurement of drop perimeter.

The variation of perimeter has been calculated as a dimensionless quantity P (perimeter at selected time) divided by P_0 (perimeter at time 0). The analysis has been developed at constant time steps for all ranges of shear. Four equal time steps are calculated from a maximum time defined as the time spent by the drop within the field of view of the camera at an applied shear rate of at 500 s^{-1} (0.0485 s). This time is then used to to select the

corresponding number of images.. From the images the dimension of the drops are calculated using Image J software. In the following results the variation of perimeter is plotted as a function of the energy applied to the system, to visualise at constant time steps the rate of deformation of the drops. The energy spent has been calculated using the torque values of the rheometer, Γ , the rotational speed (ω) and the calculated time (t) as;

$$E = \Gamma \omega t \quad (7.1)$$

Furthermore, the power (P) spent in the system is plotted in function of the perimeter variation at constant maximum time for all the selected shear values, where:

$$P_w = \Gamma \omega \quad (7.2)$$

Initial observations showed that the presence of the drops did not affect the rheology of the system; the torque remained constant and thus constant values of viscosity were detected for each run at different shear rates. The experiments were repeated two times for each run without showing any difference between the rheometer measurements and the drop size.

7.2.2. Filament stretching

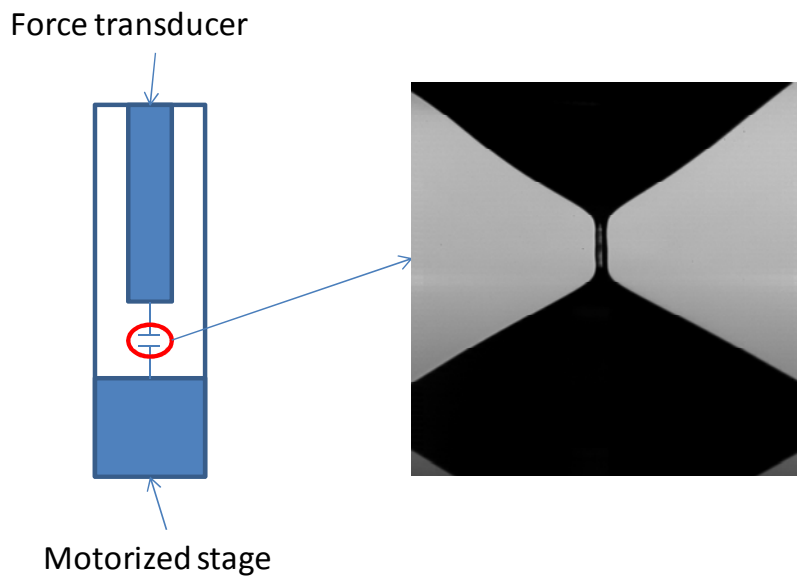


Figure 7.3 Filament stretching rig

The filament stretching rig consists of a motorized stage and a force transducer (Appendix A2) mounted on a vertical stand. Both the transducer and the stage have a plate connected to an extremity which is used for locating the drop of fluid, bottom plate and to pull up the filament of fluid, the top plate. The motorized stage can move in three directions giving the possibility to locate the bottom plate precisely under the top one. The high speed camera is used and located in front of the rig to visualize the breakage and the stretching of the fluid filament. The drop is created between two metallic disks one of which is connected to the force transmitter and the other to the motorized stage. A wide range of velocity has been used for the experiments (from 0.25 to 1.5 mm s⁻¹ in steps of 0.25 mm s⁻¹), and the behaviour of both fluids 1 and 2 have been studied. The diameter variation as a function of the energy input has been investigated. D is the perimeter at selected time, and D_0 is the perimeter at $t = 0$ when the motorized stage is not moving yet. The stretching rate at which the diameter changes is determined from the ratio between D at time just before the filament breakage over D_0 divided by the time of breakage (see Figure 7.4).

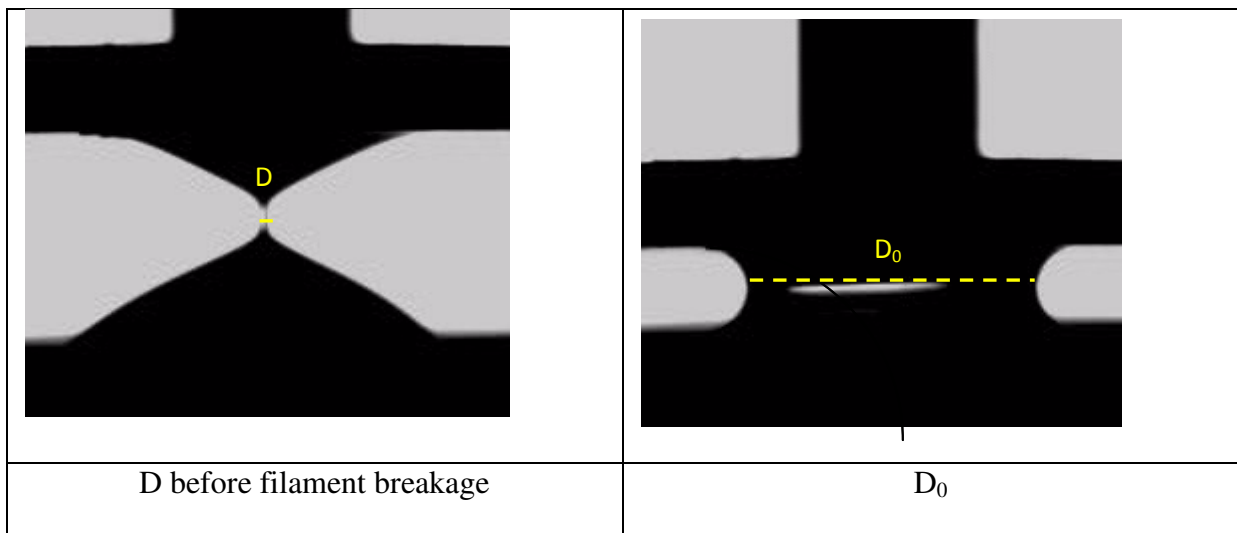


Figure 7.4 Selected images for D just before the breakage and D_0 using fluid 1 at the velocity of 1.25 mm s⁻¹.

The results are interpreted as

- a) the filament diameter evolution as a function of time and velocity of stretching for both fluids;
- b) the force values applied to the filament as a function of time and velocity of stretching for both fluids;

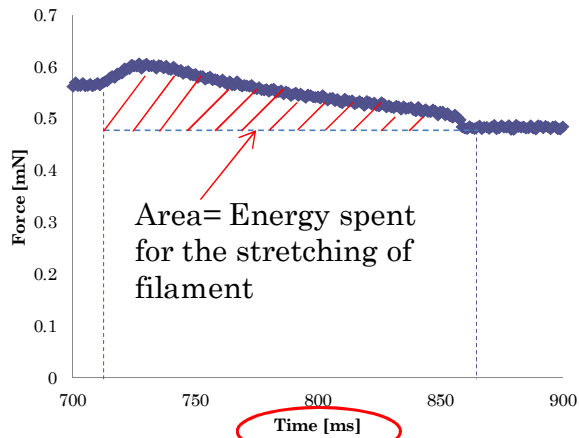
Using the force measurement data, an estimation of energy spent for the breakage of the filament has been calculated. Furthermore, apparent extensional viscosity (η_e) plotted versus Hencky strain is presented where η_e is calculated following the equation (McKinley, 2005):

$$\eta_e = \frac{\sigma}{\frac{dD(t)}{dt}} \quad (7.3)$$

where σ is the superficial tension and D is the diameter of the filament and Hencky strain is defined as:

$$\varepsilon = \ln\left(\frac{D(t)}{D_0}\right) \quad (7.4)$$

An estimation of energy spent for the stretching of the filament is also evaluated using the information obtained from the tracking of force versus sample points. The number of samples per experiment is reasonably high due to the frequency of 100 s^{-1} which gives the possibility of a detailed description of force variation with time. In Figure 7.5 the experimental approach to evaluate the energy spent is explained. The raw measurements consist of force versus sample rate which can be converted to force versus time by dividing the number of samples by the frequency. Then, by multiplying the time by the velocity of the motorized stage, the x axis becomes displacement ([m]). The value of energy is evaluated from the area under the curve to the lower base value using the trapezium rule.



Multiplied by the velocity of the motorized stage

—————>
Displacement [m]

Figure 7.5 Example of force measurement and explanation of how the energy spent for the stretching has been calculated.

7.3. Results

7.3.1. Drop stretching under a continuous shear field

The scope of this preliminary study is to seek new information on the requirements of non-Newtonian mixing. In order to track the deformation of the drops, P/P_0 is plotted as a function of energy applied by the rheometer for the shearing of the continuous phase (Figure 7.6 and 7.7). The data are recorded at fixed time steps as previously defined. In Figure 7.6, the trend of P/P_0 for the drops of fluid 1 is shown. Different symbols have been used for the different shear rates applied and as expected, the energy increases as the shear applied to the fluids increases.

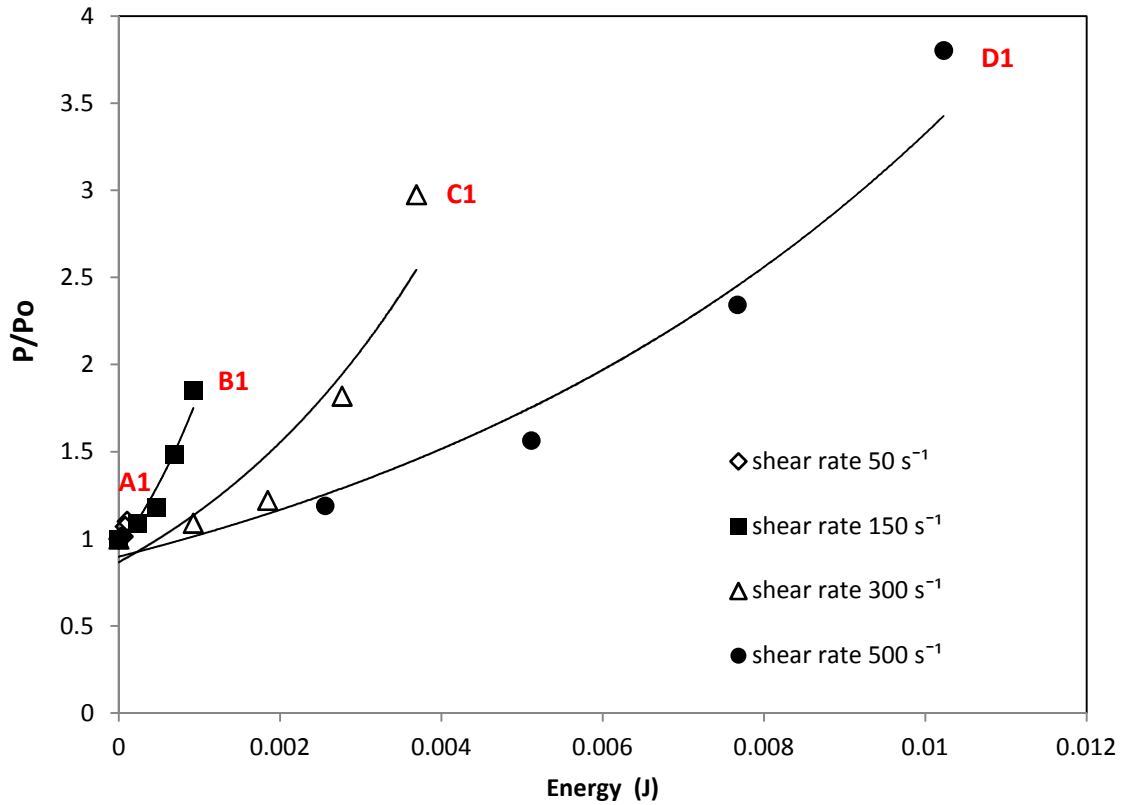


Figure 7.6 P/P_0 versus the energy applied by the rheometer for fluid 1.

Generally the perimeter of the drops increases as a function of the energy spent by the rheometer. This is due to a combination of drag and interface force between the drop and the continuous phase; the correlation between the energy spent and the perimeter increasing rate is directly proportional as expected. The deformation of the drop is affected by the surface tension forces; the Laplace pressure is inversely proportional to the radius of curvature of the drop. Comparing the perimeter of the drops at constant energy, the data does not collapse because there is a clear effect of shear rate which may be affected by the changing apparent viscosity of the dispersed phase.

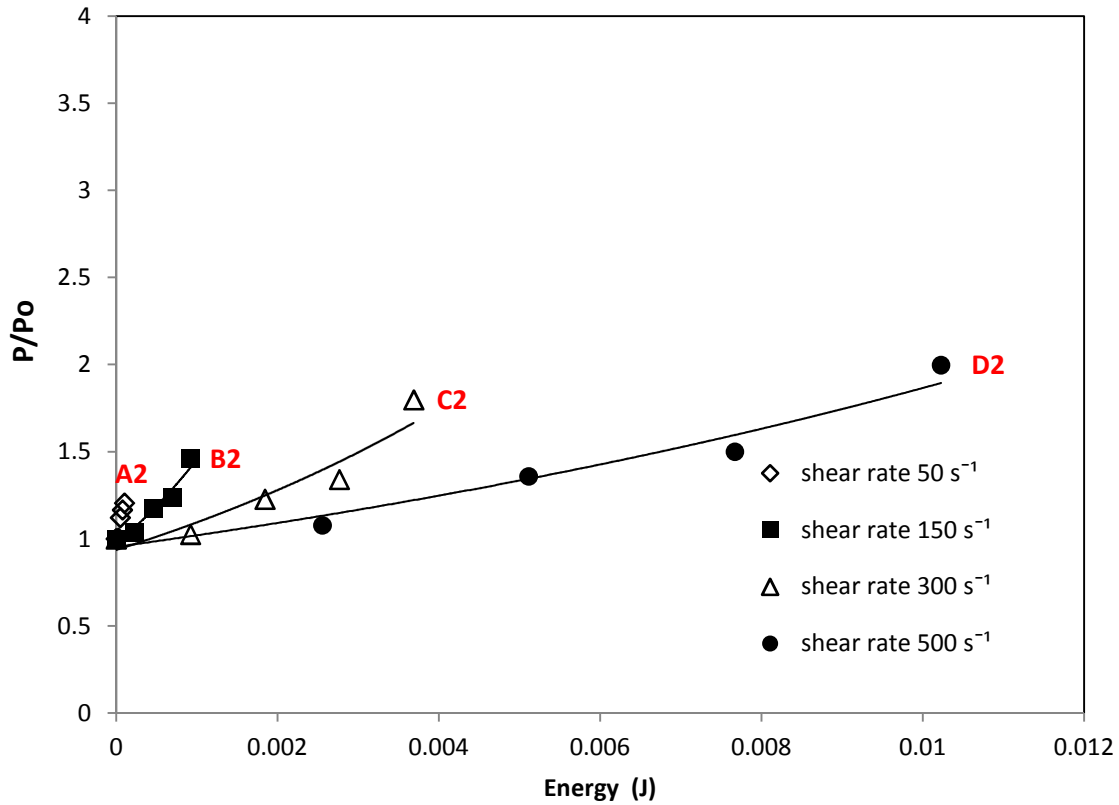
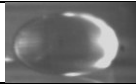
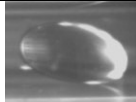
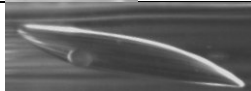
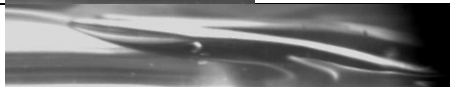



Figure 7.7 P/P_0 versus the energy applied by the rheometer for fluid 2.

Figure 7.7 shows the experimental data obtained for the drops made of fluid 2 where the general trends are similar to the previous plot (Figure 7.6). The overall values of P/P_0 are lower than the previous case due to the nature of fluid 2. Due to the limited difference between the fluids in terms of interfacial tension, the trends of the shearing of drops, shown in Figure 7.6 and 7.7, may be affected mainly by the rheology behaviour of the non-Newtonian fluids. Comparing the results of Figure 7.6 with Figure 7.7 shows that P/P_0 decreases drastically for the fluid 2 compared to fluid 1; the results show that when the same energy is spent to apply same shear to the drops, the deformation a drop of fluid 2 is almost half that of a drop of fluid 1. This aspect has a critical importance when referring to the behaviour of drops of fluid in the static mixer. Figure 7.8 presents all the images of the drops

after constant time (maximum time) at different shears. In Figures 7.6 and 7.7 the points to which the images correspond are labelled.

a)		
Dispersed phase =Fluid 1 (0.1 % Carbopol solution) Continuous phase= Silicon oil 0.35 Pa s		
	Shear rate 0 s^{-1}	
A1	Shear rate 50 s^{-1}	
B1	Shear rate 150 s^{-1}	
C1	Shear rate 300 s^{-1}	
D1	Shear rate 500 s^{-1}	


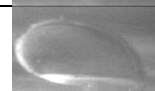



b)		
Dispersed phase =Fluid 2 (0.2 % Carbopol solution) Continuous phase= Silicon oil 0.35 Pa s		
	Shear rate 0 s^{-1}	
A2	Shear rate 50 s^{-1}	
B2	Shear rate 150 s^{-1}	
C2	Shear rate 300 s^{-1}	
D2	Shear rate 500 s^{-1}	

Figure 7.8 Images at maximum time for all the runs for fluid 1(a) and 2 (b).

Figure 7.8 shows clear evidence of the different behaviour of the drops of different fluids under the same shear field. The drops of fluid 2 better conserve their shape under high shear (Figure 7.8b) which is not true for the drop of fluid 1 (Figure 7.8a). Clearly, the different rheological behaviours affect the shape of the drops under different shear rate. These data are summarised in Figure 7.9, where a plot of P/P_0 versus the power spent is presented. The P/P_0 values are determined at a constant time step for all the experiments with both fluid 1 and

fluid 2. The selected time is the maximum time of 0.0485 s defined in the previous section. . At low power input (the lowest applied shear rate of 50 s^{-1}), the values of P/P_0 are similar for the two different fluids. This may be due to yield stress effects dominating at low shear, which are similar for both fluids. However at higher powers (applied shear rates) it is clear how the deformation of the drops of fluid 2 is limited compared to the drops of fluid 1. This graph gives a clear comparison of the performance using different fluids where the deformation of drop of fluid 2 does not increase as drop of fluid 1 increasing the power input.

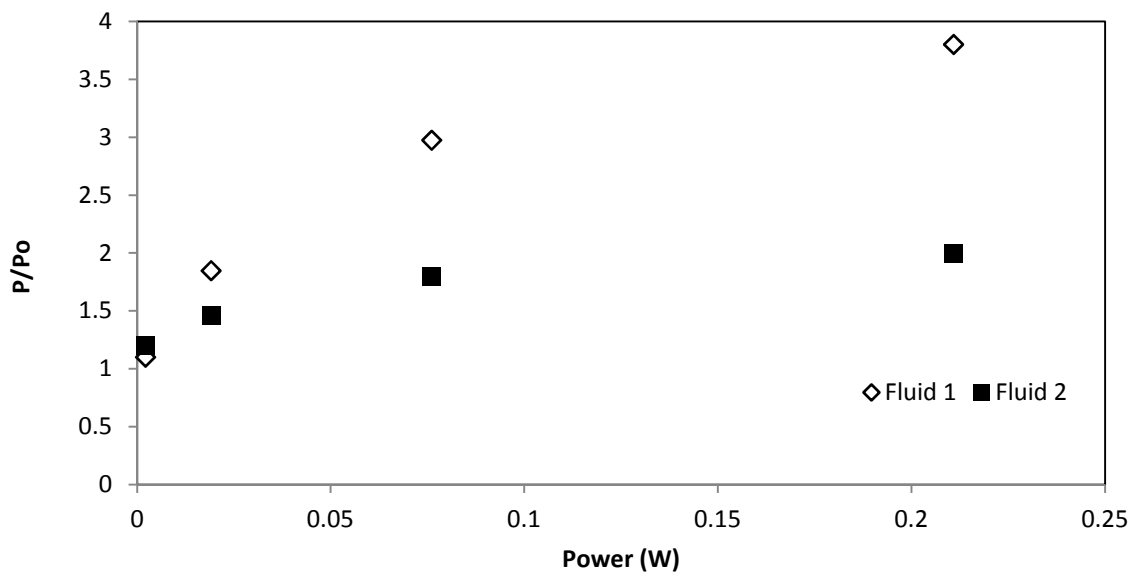


Figure 7.9 P/P_0 at maximum selected time versus power spent for both fluids.

7.3.2. Filament stretching

Figures 7.10 and 7.11 show force versus displacement measurements for the filament stretching at different velocities for fluids 1 and 2 respectively. Figure 7.10 shows the results for the filament made of fluid 1. By increasing the velocity, the filament breakage happens faster. The slope of the force versus time increases with the velocity but the upper base value and the lower base value remain constant for all the experiments.

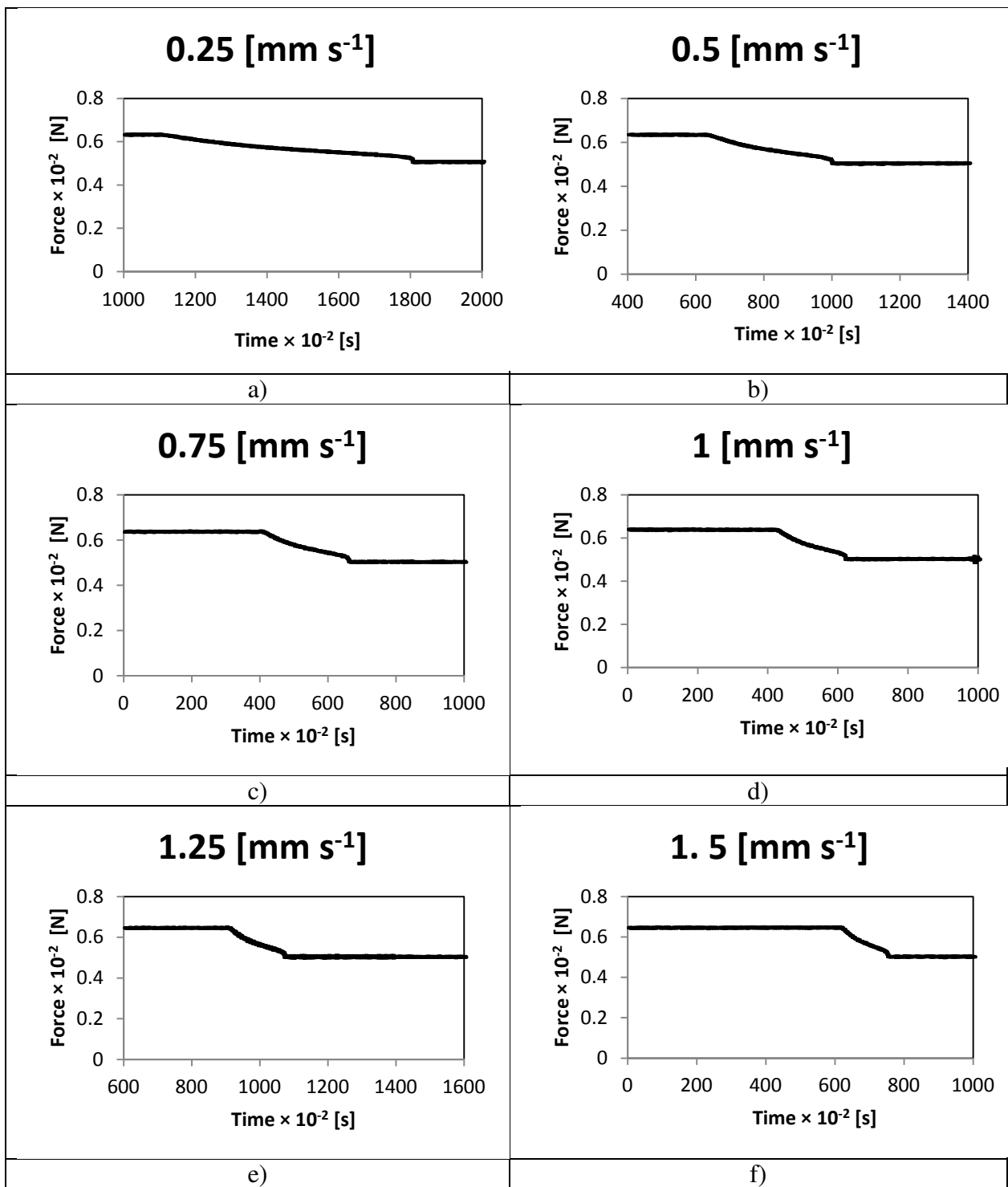


Figure 7.10 Force measurement at different speeds for filaments of fluid 1 at constant volume.

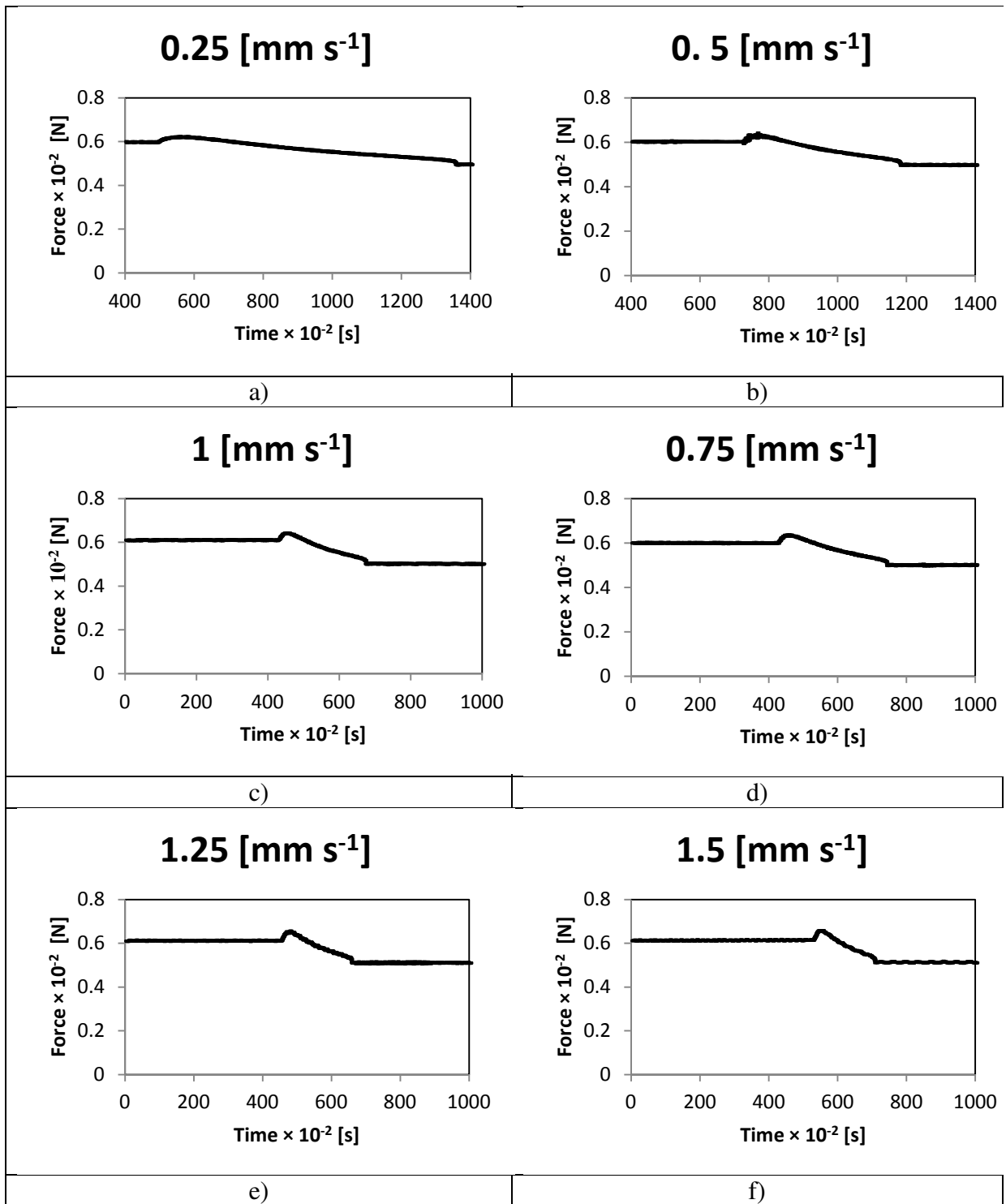


Figure 7.11 Force measurement at different speeds for filaments of fluid 2 at constant volume.

Remarkable differences can be found comparing Figure 7.10 and 7.11 where force measurements of different non-Newtonian filaments are presented. Clearly the upper base and lower base values change slightly for the two different settings. The upper base value is a combination of capillary force and the gravitational force; the sum of weight of the upper

sample platform which is used to pull the filament and fluid weight, gives the total gravitational contribute. Otherwise, the lower base value of the force is only due to the gravitational force of remain fluid on the platform and weight of it. An estimation of the capillary force (F) for both fluids can be calculated using the values of surface tension, ($\sigma_1=0.062$ [Nm] and $\sigma_2=0.056$ [Nm]) the radius of curvature (R) and the area of filament contact (A) as:

$$F = \frac{\sigma}{R} A \quad (7.5)$$

$$R = \frac{h}{2} \cos \theta \quad (7.6)$$

where h is the distance between the lower and upper sample platform at t_0 .

	$F \times 10^{-2}$ [N]	$F \times 10^{-2}$ [N] (Exp)	A [mm ²]	σ [Nm]	R [mm]	θ [°]	h [mm]
Fluid 1	0.187	0.162	19.63	0.062	0.65	20	5.15
Fluid 2	0.123	0.115	15.97	0.056	0.73	22	4.51

Table 7.1 Values of capillary force and the physical quantities for the evaluation of them.

Referring to Figure 7.12, the curvature angle is calculated from the images at t_0 .

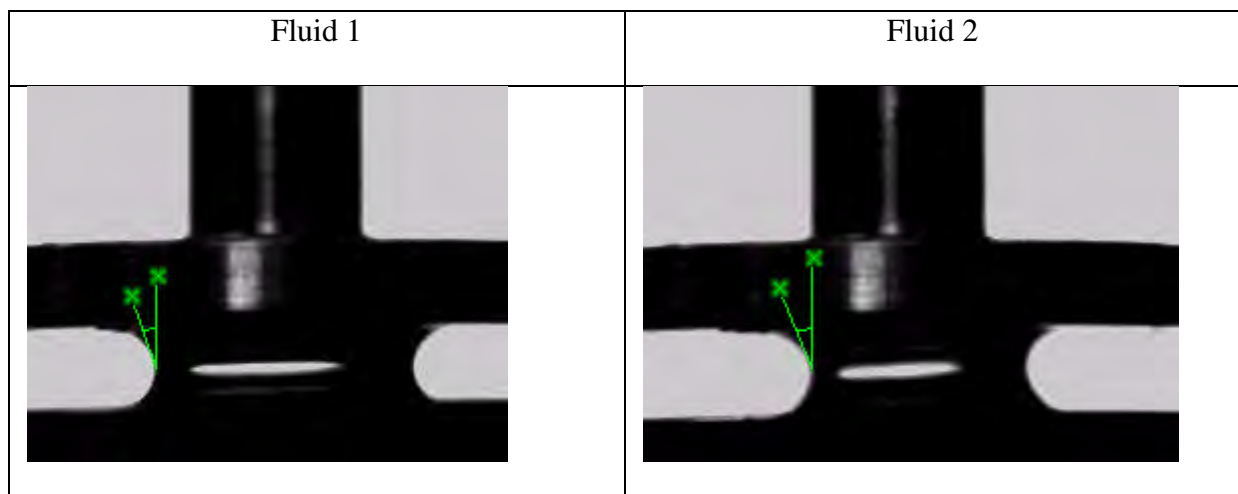
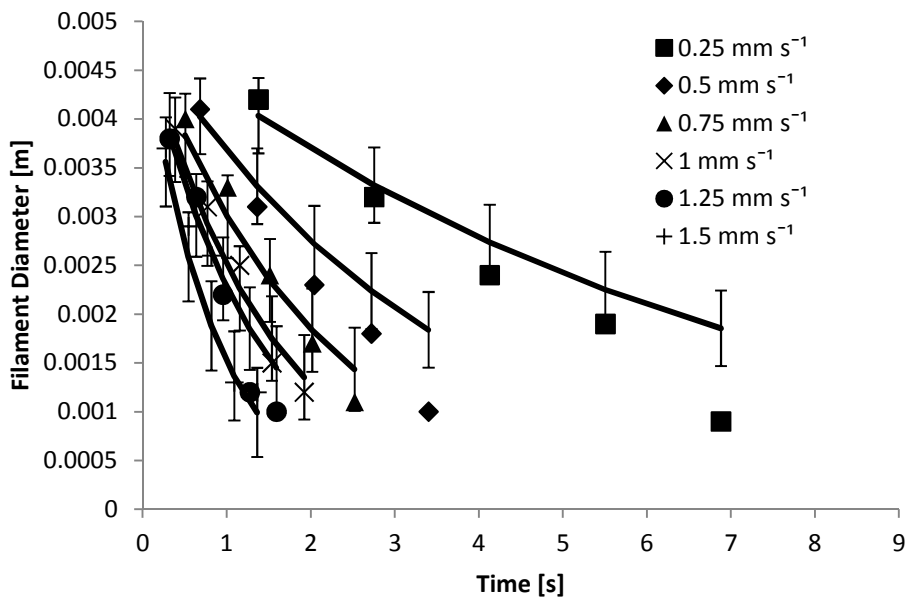


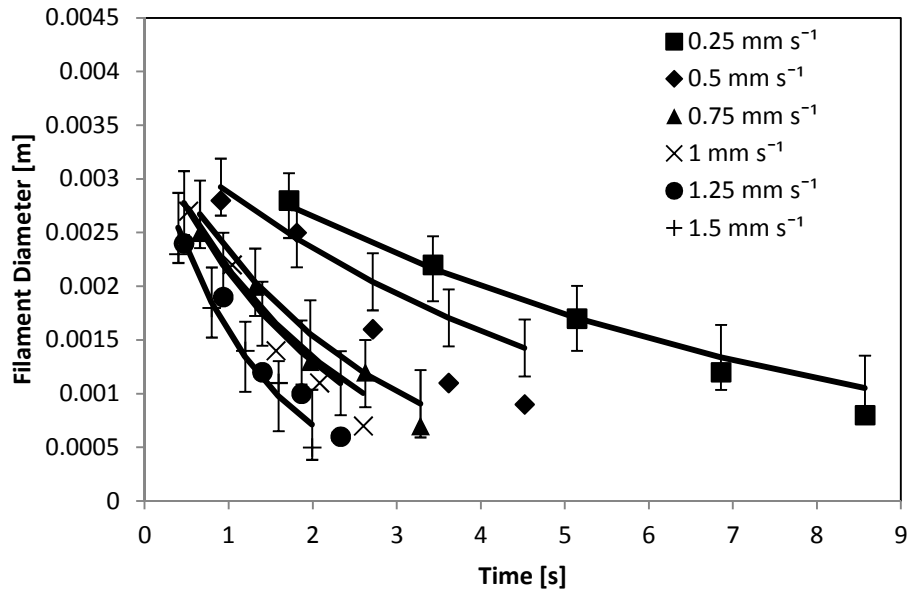
Figure 7.12 Filament of fluid at t_0 with highlighted contact angle (θ) for both fluids.

The calculated values of the capillary force (Table 7.1) match with the differences (ΔF) between the upper value and lower value of the force of figure 7.10 and 7.11 within an error

~10%. As for the experimental data ΔF is lower for the filament of fluid 2 than fluid 1. Since the reliability of the obtained experimental results is now proved, a description of effects of filament stretching on different non-Newtonian fluids is presented. In Figures 7.12a and 7.12b the variation of the diameter filaments as a function of the time for both fluids is presented. The points correspond to the experimental values measured from the high speed images and the line corresponds to the model values obtained from the correlation presented in the equation 2.17 which relates the D_0 (diameter at time t_0) and D (diameter of filament just before the breakage). An average stretching rate (ϵ_r) is calculated and used to evaluate the diameter at different times. Generally, the model underestimate the values of diameter but with in an error range $< 10\%$.



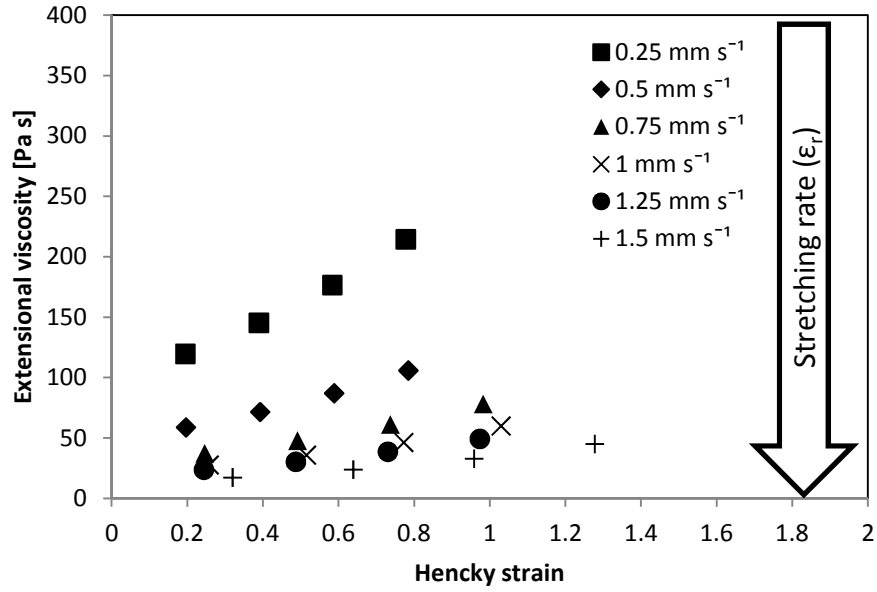
a)



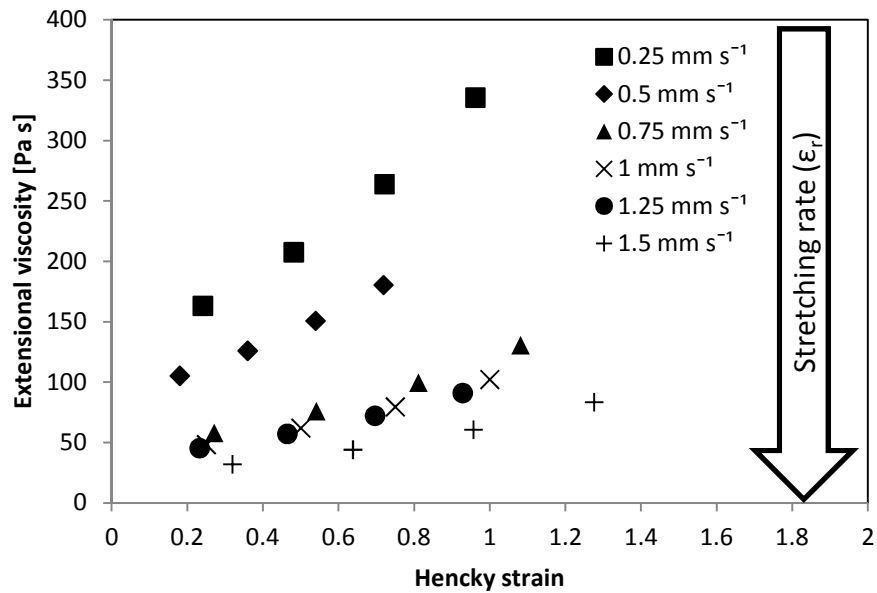
b)

Figure 7.13 Variation of filament diameter versus time: a) filament of fluid 1, b) filament of fluid 2.

Comparing the slopes of the correspondent curves of Figure 7.13a and 7.13b, it is clear the different tendencies of the two fluids to stretch. The values of D_0 for the two filament of non-Newtonian fluids are slightly different ($D_0=0.0049$ [m] for fluid 1 and $D_0=0.0035$ [m] for fluid 2) although the initial volumes of the drops are the same. That is may be due to the small differences in surface tension between the two fluids which affects the initial curvature.



a)



b)

Figure 7.14 Extensional viscosity versus Hencky strain at different stretching rates for Fluid 1 a) and 2 b).

A common approach to verify the properties under stretching of a fluid is the measurement of extensional viscosity as a function of the Hencky strain and stretching rate. In Figure 7.14a and b the trend of extensional viscosity for the two fluids is presented.

As expected for a shear thinning fluid, increasing the stretching rate causes the extensional viscosity to decrease. However at constant stretching rate the viscosity increases with the decrease of the filament diameter. Marked differences can be noticed between the values obtained for fluid 1 and fluid 2. The higher consistency of Fluid 2 is evident when compared to fluid 1. Both shearing and stretching are influenced by the behaviour of the fluid which suggests that it is more difficult to stretch filaments of fluid 2. The next step of this study is to investigate the energy consumed to stretch a filament of fluid. Combining the data from the model and the experimental values of the force a description of diameter variation (D/D_0) versus energy is presented in Figure 7.15. The D/D_0 data plotted in Figure 7.15 corresponds to the estimated values of the verified model as a function of time and stretching rate. 5 equal intervals of time were chosen based on the time of breakage evaluated from the high speed images; this value of breakage time is also compared with the one obtained from the force measurements. From a direct comparison between time and diameter size, using the high speed images, 5 ranges of D/D_0 (A, B, C....etc) were determined for all the different stretching velocities. As explained in § 7.2.2, the energy is calculated on base of force time and velocity with which the filament is stretched. The collected data of D/D_0 and the correspondent energy spent can be use to compare the stretching response of the fluids with others that can be found in the literature. Hencky strain or extensional viscosity are the most common parameters used in literature which can be easy calculated from the proposed results.

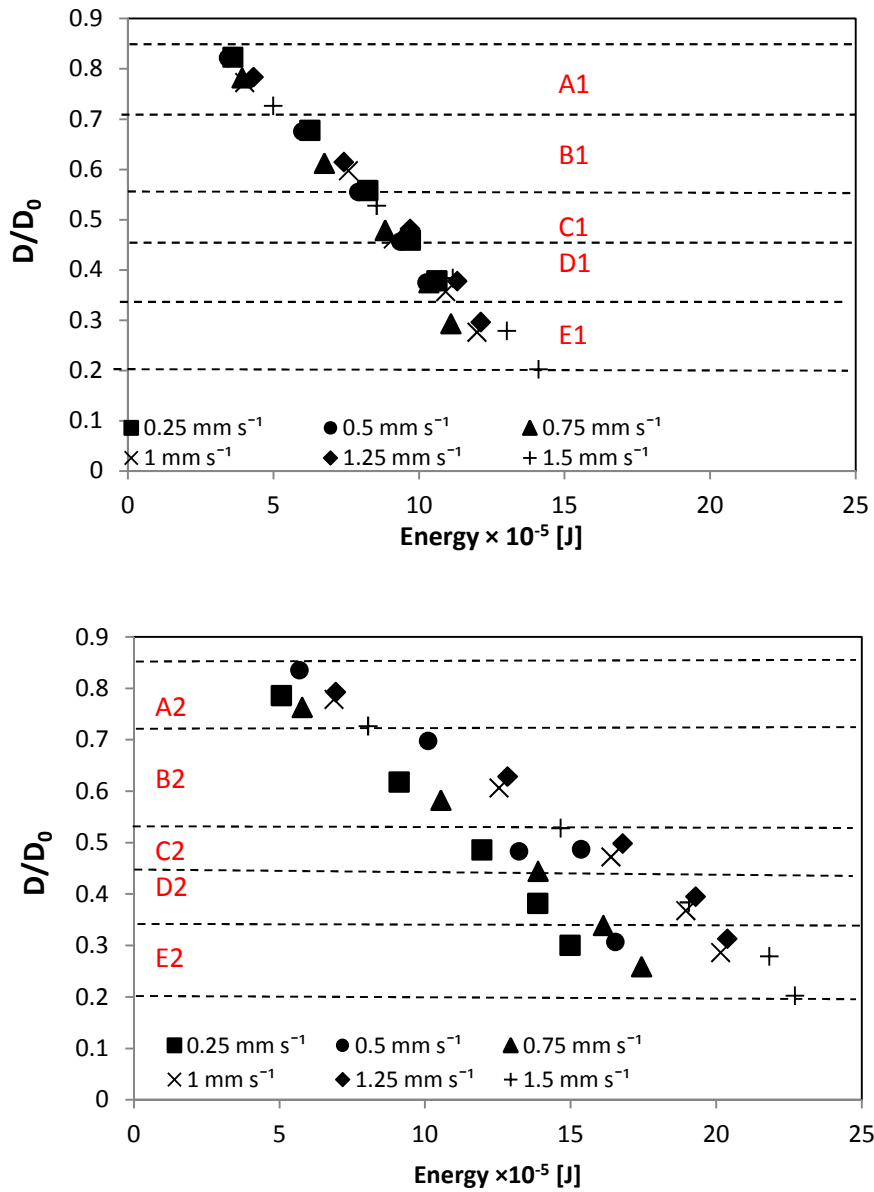


Figure 7.15 Variation of filament diameter versus energy: a) filament of fluid 1 and b) filament of fluid 2.

Analysing more in details the Figure 7.15a, as expected the energy spent for the stretching increases decreasing D/D_0 . The stretching velocity is shown to not largely affect the energy values for fluid 1. Comparing Figure 7.15a with Figure 7.15b many differences can be observed. Firstly, the overall values of energy are always higher for fluid 2 compared to fluid 1. This result matches perfectly with the previous results on the drop shearing where clearly the shear of a drop was correlated to the rheology of the fluid.

For the stretching of fluid 2 the values of energy for experiments at similar range of D/D_0 but run at different velocity are not similar as in the previous case. At constant D/D_0 increasing the velocity of stretching the energy spent increases; the difference in term of energy increase with the decreasing of filament diameter. This trend can be reconnected to the Figure 7.11 where for the velocities above 0.5 mm s^{-1} there was the formation of peak on the force measurement which can explain this difference in terms of energy. Increasing the velocity the peak increases in size as the energy spent for the stretching of fluid 2. The causes of this peak can be reconnected to the contribution of viscous forces and capillary forces which cannot be clearly distinguish at this stage of research. Images for different ranges of D/D_0 for the used fluid are shown in Figure 7.16a. Due to the different initial dimensions of the filament the images cannot directly compared but the ratio of D/D_0 is the same.

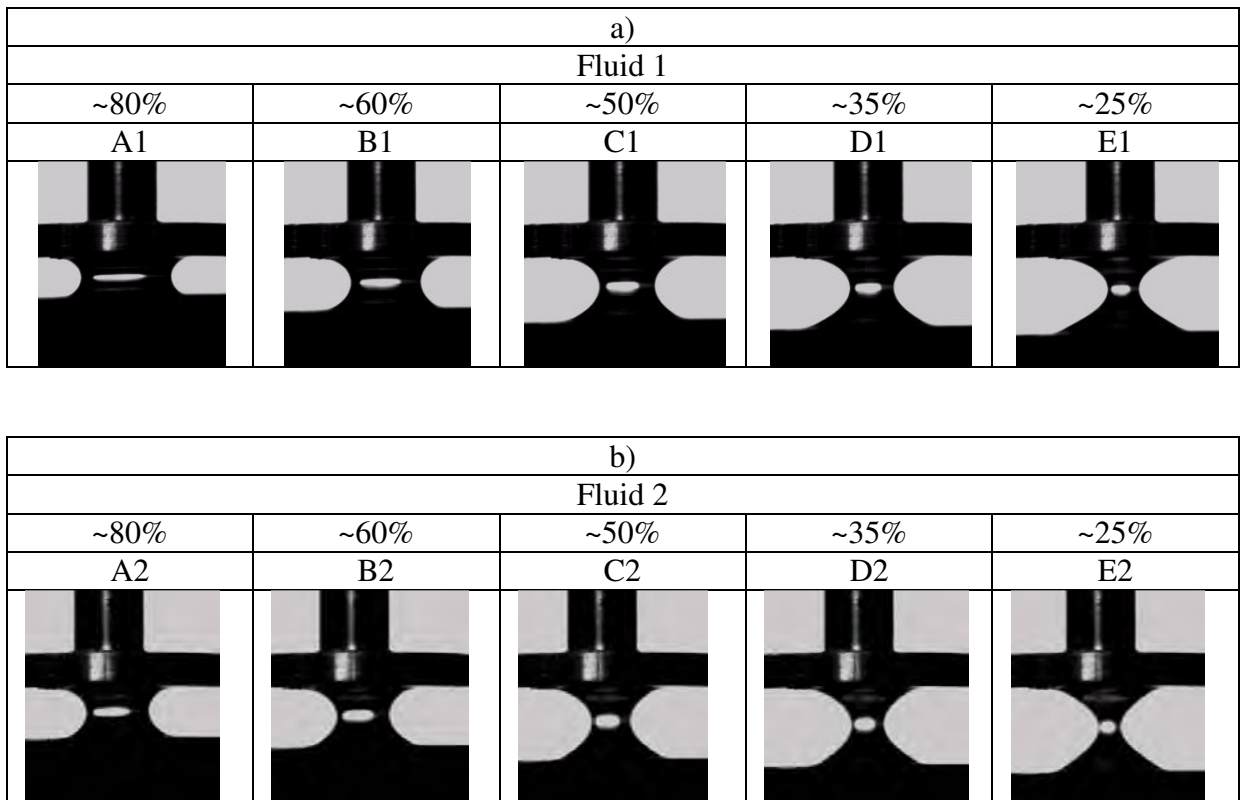


Figure 7.16 Images of filament at different values of D/D_0 for fluid 1 a) and 2 b) at selected velocity.

The main difference between the two fluids is the time spent to approach the following range of D/D_0 (for example from A1 to B1 and A2 to B2). Clearly the time spent is directly connected to how it is hard to stretch the different filament. The areas of contact for the filament of fluid 2 at similar D/D_0 are always lower than for fluid 1. In Table 7.2 are summarised the dimension of the filament of the two fluids before breakage. Considering the volume of the drop was the same, consistent differences are shown on the final dimensions of the filament which may be affected by the rheology of the different fluids.

Table 7.2 Final dimensions of filament before the breakage.

	Final length of filament [mm]	Final diameter of filament [mm]
Fluid 1	3.19	0.24
Fluid 2	3.6	0.20

Finally, in Figure 7.17 a comparison between the values of energy spent for the filament stretching for all experiments at different velocities and for different ranges of D/D_0 is shown. Clearly, the energy spent for the stretching of fluid 2 is almost double than fluid 1 for the experiment run at same conditions. In addition, the energy for the stretching of fluid 2 is more affected by the velocities and D/D_0 than for fluid 1.

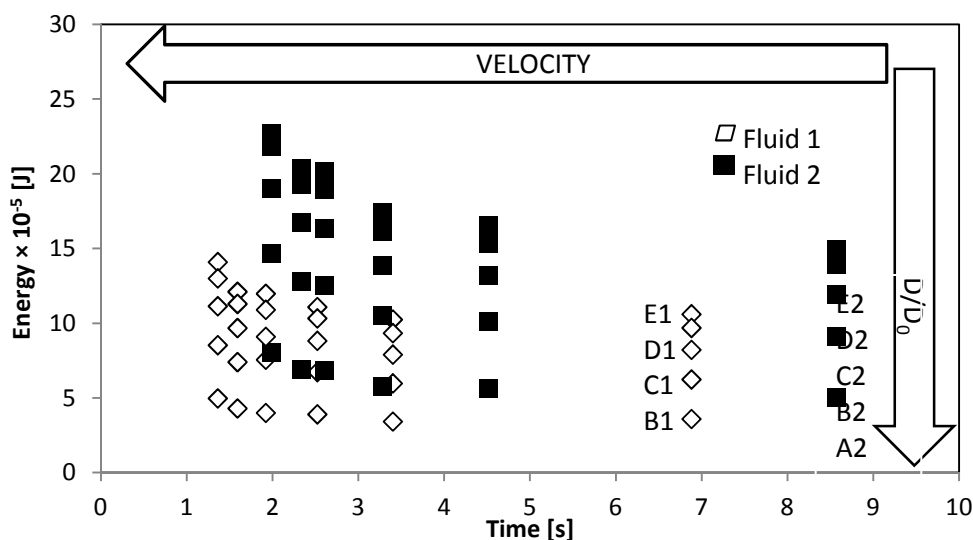


Figure 7.17 Comparison of energy spent values for the stretching of the two fluids at different velocities and range of D/D_0

These results are consistent with the observed behaviour of the fluids when mixed using the static mixers. In Chapters 4-6, the effect of different fluid injections in static mixer was debated; assuming that the flow field in the static mixer is constant, then if filaments, streams or drops of a given fluid follow the same fluid path through the static mixer, they will experience the same shear history yet they will behave differently due to their rheology. An additional complication exists if their presence modifies the flow field.

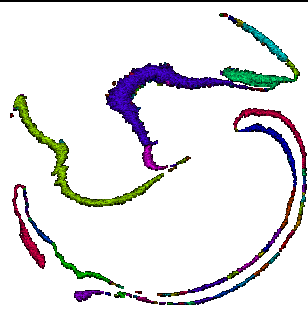
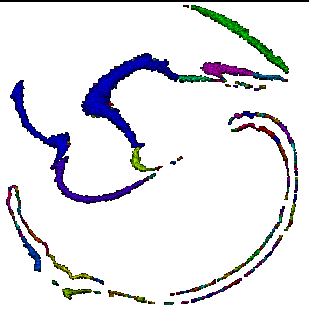
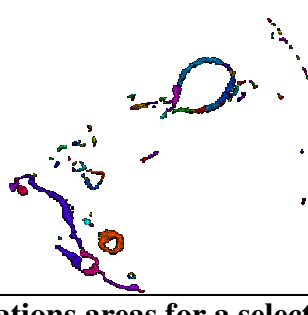
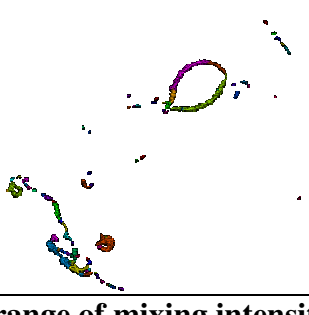
Injection		Superficial velocity 0.1 [m s ⁻¹]	
		X ₋	X ₊
Fluid 1	X>90%		
Injection		Superficial velocity 0.1 [m s ⁻¹]	
		X ₋	X ₊
Fluid 2	X>90%		

Figure 7.18 Selected images of striations areas for a selected range of mixing intensity for two experiment run at same conditions but using different injection.

In Figure 7.18, results of striation areas for a selected range of mixing intensity are shown. The two selected experiments were carried out at same flow ratio, same superficial velocity and same pipe size but with injection of different fluid. Clearly the effect of fluid 2 is remarkable as in the shear drop experiments. The striations, generated in the blending of

non-Newtonian fluids in static mixer, are lower in number and in size for the injection of fluid 2 than for the injection of fluid 1. The data presented in Chapter 5 show that over the range of measured superficial velocities, the level of mixedness for the injection of fluid 2 never reached the level obtained for fluid 1. The shear drop stretching results show exactly the same general trends obtained from the static mixer experiments. It is clear how much more difficult it is to shear an element of fluid 2 than fluid 1.

7.4. Conclusions

Two different aspects of the behaviour of the two different non-Newtonian fluids have been considered in the chapter:

- the behaviour of drops under a constant shear field;
- breakage of fluid filaments under elongation;

The results of this chapter are generic and can be related easily to any mixing system, as stirred tank or inline mixing, since individual phenomena relevant to mixing processes are considered. The information gained in this preliminary study is fundamental to improve the research in the direction of more complex systems. Obviously, for the experiment where the rheometer was used to apply a constant shear to the system, the values of energy are directly correlated to measurements; however these energy values are used for a comparison assuming similar conditions. The main assumption is that interfacial forces behave similarly for drops of different fluids. No marked differences have been found between interface or surface tension values of the two fluids, which is the most effective force at the interface. These values have been calculated for both the experiment where it was required.

The validity of models is proposed for the stretching of non-Newtonian fluid using solution with low concentration of polymer. Data are proposed for possible CFD validations in terms

of perimeter for drop shearing stretching and perimeter and diameter for the filament stretching. A wide range of work can be elaborated from these approaches focussing on the understanding of mixing bases.

8. CONCLUSIONS AND FUTURE RECOMMENDATIONS

8.1. Conclusions

This chapter presents some overall conclusions to give a general overview of how the research objectives have been met. Individual conclusions for each study undertaken can be found at the end of each results chapter. This chapter also contains recommendations for future work.

- *Development of a new method to characterise mixing performance using an areal distribution of mixing intensity to describe blending of non-Newtonian fluids in Kenics static mixer and comparison of the new analysis methods with conventional mixing parameters which represent the scale and intensity of segregation. (Chapter 4).*

The primary objective of this thesis was to investigate how to determine the mixing performance using static mixer in laminar flow. In most of the previous studies for the quantification of mixing intensity, coefficient of variation was the most often used parameter

to determine the level of mixedness. Statistically averaged values based on concentration distribution and empirical correlations based on length and diameter of static mixer, were used as methodology to evaluate the coefficient of variation. To the best of current knowledge, for the quantification of scale of segregation, striation thickness is the most used method to evaluate the mixing performance. This thesis has debated the importance of considering both aspects in tandem for correct interpretation of the mixing performance; considering only a single measure is a known problem in the literature (Kukukova, Aubin et al. 2009; Kukukova, Aubin et al. 2011). This issue has been addressed in the methods and analysis presented. Analysis of PLIF images has been performed to determine the mixing performance of KM static mixers using Newtonian and non-Newtonian aqueous solutions as a function of number of elements and viscosity ratio of the two fluids. A method has been developed which considers the distribution of the cross sectional area with a given intensity of mixing, this areal analysis combines both intensity, in terms of log-variance, and scale, in terms of the fraction of the cross section with a given intensity. The method shows promise for the evaluation of mixing performance and can be considered as an addition to conventional approaches.

- *Development of a new analysis to characterise scale of segregation more deeply based on previous developed method. (Chapter 5).*

The developed method allows the identification of striations of similar intensity. Analysis of striation area distribution is presented to schematize individual contiguous striations as a function of a non-dimensional area versus a non-dimensional length. This new method shows the complexity of information-rich PLIF images, and allows the classification of different experiments where CoV and striation thickness alone failed to clearly distinguish the effects of different parameters. The methods developed have different industrial relevance as each method characterizes a different aspect of the mixing. For example, when an overview of the

process is needed, the area fraction method can be used to estimate the amount of “lump” that has to be minimized in a downstream processing. But in a reactive system where the interface area is important, the striation method distribution can give an estimation of total interface length of the analysed cross section which is key aspect to take in account to determine the performance of the system.

- *Study of the effect of system and fluid parameters as flow rate, flow ratio, size of static mixer, different injection and different injection position upon the blending of Non-Newtonian fluids in a KM static mixer. Different experiments are carried out and compared for the understanding of the behaviour of shear thinning fluids upon different conditions. (Chapter 5).*

Analysis of PLIF images has been performed to determine the mixing performance of KM static mixers using non-Newtonian aqueous solutions as a function of velocity, scale, flow ratio and injection position and comparing the effect of these parameters to the viscosity ratio of the two fluids (main flow: always fluid 1, injected fluid: fluid 1 and 2). The identification of areas in the pipe cross-section with a given range of log-variance enables identification of regions where the mixing is performed down to the micro-scale, but also unmixed or poorly mixed regions in the flow. The analysis of PLIF images allowed the detection of viscous stream filaments evident as spots when a fluid of higher viscosity was injected into a lower viscosity continuous phase, which is not predictable using conventional design approaches. This new method shows promise in unravelling the complexity of information-rich PLIF images, beyond a sole number-based mixing criterion. As velocity increases the effect of varying the viscosity ratio becomes less important, whilst increasing the size of the static mixer decreases the mixing intensity performance since energy inputted per unit mass decreases, at constant velocity. Scale has the greatest effect on the size of striations with poor mixing evident. However when the data is presented in terms of energy consumed per unit

mass, the 1" size is more efficient due to possessing a lower pressure drop per unit length. Increasing the flow ratio between the injection and the main flow increases the overall mixing performance. The wall injection for the mixing of non-Newtonian fluids is not a suggested operating configuration as it negatively affects the overall mixing performance.

- *Comparison of the behaviour of different static mixers at the same inlet conditions, in terms of performance and energy consumed, focussing on KM and SMX Plus designs (Chapter 6).*

As for the KM static mixer, when velocity increases the effect of varying the viscosity ratio becomes negligible, whilst increasing the size of the static mixer the mixing intensity performance decreases. In terms of energy consumed per unit mass, the 1" size is more efficient due to lower pressure drop per unit length. Increasing the flow ratio between the injection and the main flow does not affect much the overall mixing performance as for the KM. The wall injection for the mixing of non-Newtonian fluids is not a suggested as an operating configuration but it does not decrease the overall mixing performance as was the case for the KM static mixer. The SMX Plus device performs better using the same number of elements but the pressure drops increase drastically compared to the KM design. SMX Plus static mixer generates similar amount of 'interfacial length' to KM but using much more energy per unit mass. KM static mixer has more sensitivity to different configurations compared to SMX Plus. The 1" devices are more efficient in terms of energy spent for the blending of non-Newtonian in both devices. The 1" SMX Plus static mixer does not perform proportionally to the energy per unit mass as the KM. According to that the scale effect is more significant for SMX Plus than for KM.

- *Understanding of non-Newtonian blending: focusing on filament stretching and drop stretching.*

The last chapter refers to a preliminary study based on results which can be related easily to any mixing system, as stirred tank or inline mixing, since individual phenomena relevant to mixing processes are considered. The information gained in this preliminary study is fundamental to improve the research in the direction of more complex systems. Obviously, for the experiment where the rheometer was used to apply a constant shear to the system, the values of energy are direct correlated to measurements; however these energy values are used for a comparison assuming similar conditions. The main assumption is that interfacial forces behave similarly for drops of different fluids. No marked differences have been found between interface or surface tension values of the two fluids, which is the most effective force at the interface. These values have been calculated for both the experiment where it was required.

8.2. Future recommendations

This work has shown that the mixing performance of non-Newtonian fluids can be investigated in details by using the developed method. The complexity of the mixing pattern of the blending of shear thinning non-Newtonian fluids highlights the need for further research in this area or similar which can build on the results reported here. Suggestions for further work are provided below. The developed method is suitable for investigations of different mixing apparatus and for the development of new correlations for the design of static mixer rig. The same approach used for the investigation of mixing in

static mixer, can be applied in any system where transparent fluids are used and where a window or glass part of the equipment can be installed. These two aspects are fundamental to be able to use PLIF technique or other optical approaches. Possible future applications can concern the understanding of the blending of other complex fluids with different behaviour (shear thickening or other). In future work also the applicability of this method for multiphase systems can be considered. The detailed information obtained by the developed image analysis can afford the determination of a drop size distribution in-situ (example emulsions inside static mixer or other apparatus). In this thesis work the study of fluid dynamics inside a static mixer has been studied for non-Newtonian fluids using optical methods. A future investigation can be developed on the basis of proposed experiment maybe using a comparison of different technique as for example PEPT, which in addition allows interrogation of opaque fluids. The use of CFD to model the blending of non-Newtonian can be another step forward for the optimisation of non-Newtonian mixing process. The use of same methodologies for the characterisation of mixing performance and the comparison with experimental data can create strong bases for the development of models for the description of blending for complex fluids. Finally regarding the last chapter of this thesis, a lot of work can be carried out for a better understanding how the viscous forces and capillary forces act on the fluids filaments or drops. An investigation related to all specific components of the filament stretching force can be considered for future work. The understanding of all the components of the stretching force and how they change with the rheology is the final step to reach a more deep understanding of fluid behaviours under different stress (shearing or stretching).

APPENDIX

APPENDIX A: Equipment specification.

A1. Cone and plate geometries.

Dimensions				Form Factors		
Angle (°)	Diameter (mm)	Truncation (µm)	Sample volume (ml)	Shear rate	Shear stress	Viscosity (Pa s)
0	20					
0.5	20	13	0.03	114.6	0.4774	0.00416
1	20	26	0.06	57.3	0.4774	0.00833
1.5	20	39	0.09	38.16	0.4774	0.01251
2.0	20	52	0.12	28.65	0.4774	0.01666
4.0	20	105	0.24	14.33	0.4774	0.03331
0	40					
0.5	40	13	0.15	114.6	0.0596	0.00052
1	40	26	0.30	57.3	0.0596	0.00104
1.5	40	39	0.45	38.16	0.0596	0.00156
2.0	40	52	0.60	28.65	0.0596	0.00208
4.0	40	105	1.20	14.33	0.0596	0.00416
0	60					
0.5	60	13	0.60	114.6	0.0177	0.00015
1	60	26	1.20	57.3	0.0177	0.00031
1.5	60	39	1.80	38.16	0.0177	0.00046
2.0	60	52	2.40	28.65	0.0177	0.00618
4.0	60	105	4.80	14.33	0.0177	0.00124

Table.A1 Cone and plates features (AR100 Manual)

A2. Force transducer

The measurement of the filament stretching or breakage force has been carried out using an Aurora scientific 403A transducer which has a range of measurable forces between 0.1 to 100 mN. In combination with the transducer the software DMC v5.294 is used to record the measurements in ASCII files. 400A Series Force Transducers are designed for applications where fast response, high resolution and very low compliance or the visco-elastic properties of a sample are important. This force transducer provides a high-level analogical output as soon as the sample is attached. The transducers are rugged, compared with semi-conductor strain gauges, and they are repairable. The design is based on two variable displacement capacitors formed from cantilevered quartz beams. The load is attached to the active beam while the other beam acts as a reference. The reference beam, which is identical in size and construction to the active one, nullifies most ambient vibrations and electrical interference. This unique design results in excellent thermal stability and allows the instrument to operate without unusual or troublesome laboratory techniques. The low compliance of the quartz beams means that there is essentially no motion in the sample being tested (Aurora Scientific Brochure).

The frequency of response is 4 kHz. Some specifications of the device are listed below.

Force Specifications (Aurora scientific 403A Brochure)

Force Range: 0 to 5.0 mN (0 to 0.5 grams)

- **Sensitivity:** 0.5 mN (0.05 gram) per volt
- **Resolution:** 100.0 nN (10.0 micrograms)
- **Linearity:** $\pm 0.2\%$ of full scale over 50% of full scale , $\pm 1.0\%$ of full scale over full scale
- **Step Response Time:** 1.0 msec
- **Resonant Frequency:** 0.6 kHz

- **Compliance:** 1.0 micron/mN (10.0 micron/gram)
- **Zero Drift:** 0.1 mg/deg C
- **Gain Drift:** 0.01 %/deg C
- **Hysteresis:** 0.01 %
- **Maximum Overload Force:** 100.0 mN (10.0 gram)
- **Output Tube Length:** 7.0 mm
- **Output Tube Diameter:** 1.0 mm

General Specifications

- **Warm Up Time:** 30 minutes to rated accuracy
- **Operating Temperature:** 0 to 40 deg C
- **Power Requirements:** 120VAC \pm 10%, 50/60Hz, 20 Watts max. 100, 220 and 240VAC available.
- **Dimensions Electronics Enclosure:** 9cm high x 21cm wide x 25cm deep
- **Weight: Electronics:** 2.7 kg, Head: 120 grams
- **Transducer Cable Length:** 6 feet.
- **Power Cable Length:** 6 feet.

A3. Photron SA3 fastcam

.General Specifications (FASTCAM SA3 brochure)

- **Sensor** 12-bit ADC (Bayer system color, single sensor) with 17 μm pixel size
- **Shutter** Global electronic shutter from 16.7ms to 2 μs independent of frame rate
- **Lens Mount** Interchangeable F-mount and C-mount using supplied adapters (Optional High-G block mount available)
- **Extended Dynamic Range** Selectable in twenty steps (0 to 95% in 5% increments) to prevent pixel over-exposure
- **Memory** 2GB (standard), 4GB (optional) and 8GB (optional)
- **Video Outputs** NTSC /PAL composite VBS (BNC). Ability to zoom, pan and scroll within image via keypad (option). Live video during recording
- **Camera Control** Through optional keypad with integrated viewfinder and Gigabit Ethernet or RS-422
- **User Preset Switch** User selectable camera function control mounted on the camera's rear panel
- **Low Light Mode** Low light mode for simple camera adjustment when working in low ambient light, high frame rate or short exposure modes
- **Triggering** Selectable positive or negative TTL 5Vp-p or switch closure
- **Trigger Delay** Programmable delay on selected input and output triggers, 100ns resolution
- **Timing** Internal clock or external source
- **IRIG Time Code** IRIG/GPS timing is recorded in real time on every frame
- **Event Markers** Ten user entered event markers mark specific events within the image sequence in real time. Immediately accessible through software
- **Variable** User selectable Variable Framerate/Resolution function

- Framerate/Resolution** adjustable in 128 x 16 pixel steps
- **Selectable Recording Bit Depth** User selectable 12-bit (high-dynamic range) or 8-bit (50% frame increase) recording mode
- **Trigger Modes** Start, End, Center, Manual, Random, Random Reset
- **Saved Image Formats** JPEG, AVI, TIFF, BMP, RAW, PNG, MOV, and FTIF. Images can be saved with or without image or comment data
- **Data Display** Frame Rate, Shutter Speed, Trigger Mode, Date or Time, Status (Playback/Record), Real Time, Frame Count, Resolution and LUT
- **Partitioning** Up to 8 memory partitions may be set by the user
- **High-G** Tested to 100G, 10ms, six-axis
- **Operating Temperature** 0-40 degrees C (32-104 degree F)
- **Mounting** 1 x 1/4-20 UNC, 6 x M5 on all four sides
- **Dimensions** 120mm (4.72")H x 120mm (4.72")W x 215.8mm (8.50")D
*excluding protrusions
- **Weight** 9.48 lbs (4.3kg)
- **Power Requirements** 100V-240V AC ~ 1.5A, 50-60Hz optional DC operation 22-32VDC, 60VA

APPENDIX B: V3V apparatus

B1. Volumetric 3-Component Velocimetry (V3V)

The V3V is a powerful and versatile 3D flow measurement system created by TSI system. The device is equipped with 3 Powerview 4MP (2048 × 2048 pixels) 12 bit CCD camera using a synchronizer attached to a personal computer. A Nd-Yag laser (New Wave Solo III) pulsing at 7 Hz, is used to create a volumetric laser projection on the analysed sytem. The V3V system was controlled using TSI Insight V3V 4G software. As it can be seen in Figure B.1.1 the cameras are inserted in the V3V probe giving a triangular location.



Figure B1.1. Probe and cameras of V3V (TSI V3V Brochure)

For the alignment of the cameras the probe has to reach the optimal position which is achieved using the two laser diodes and the V3V calibration target. The operation of V3V is determined by 4 important elements: 3D3C imaging technique, illumination, 3D camera and the algorithm. The 3D imaging is based on Defocusing Digital Particle Image Velocimetry (DDPIV) which is a volumetric flow mapping technique that can measure the 3 components

of velocity in a volume of fluid, thus allowing the calculation of full derivative quantities. The illumination is achieved using a 2 pulse laser as for PIV equipped with lenses which give a cone shape laser at output. The illumination volume has a maximum size of 140×140×100 mm. The measurement volume (Figure B1.2) is defined by overlap of 3 viewing angles. Combining information from the 3 apertures yields, a particle triplet is characterized by 3 different points of view.

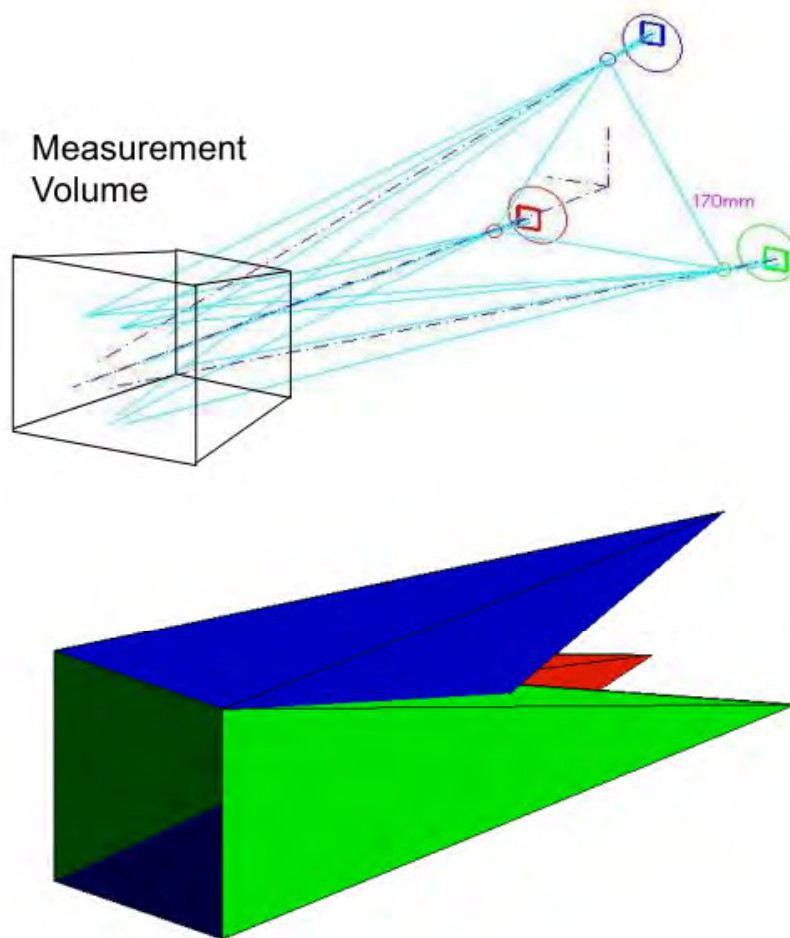


Figure B1.2 Measurement volume of V3V (TSI V3V Brochure)

To better understand the principle of triplets, the operation of the eyes in a 2D space can be taken as example. Referring to the Figure B1.3 the main difference between the operation of

eyes and V3V is the possibility of the second one to detect the third dimension thanks to the 3 cameras.

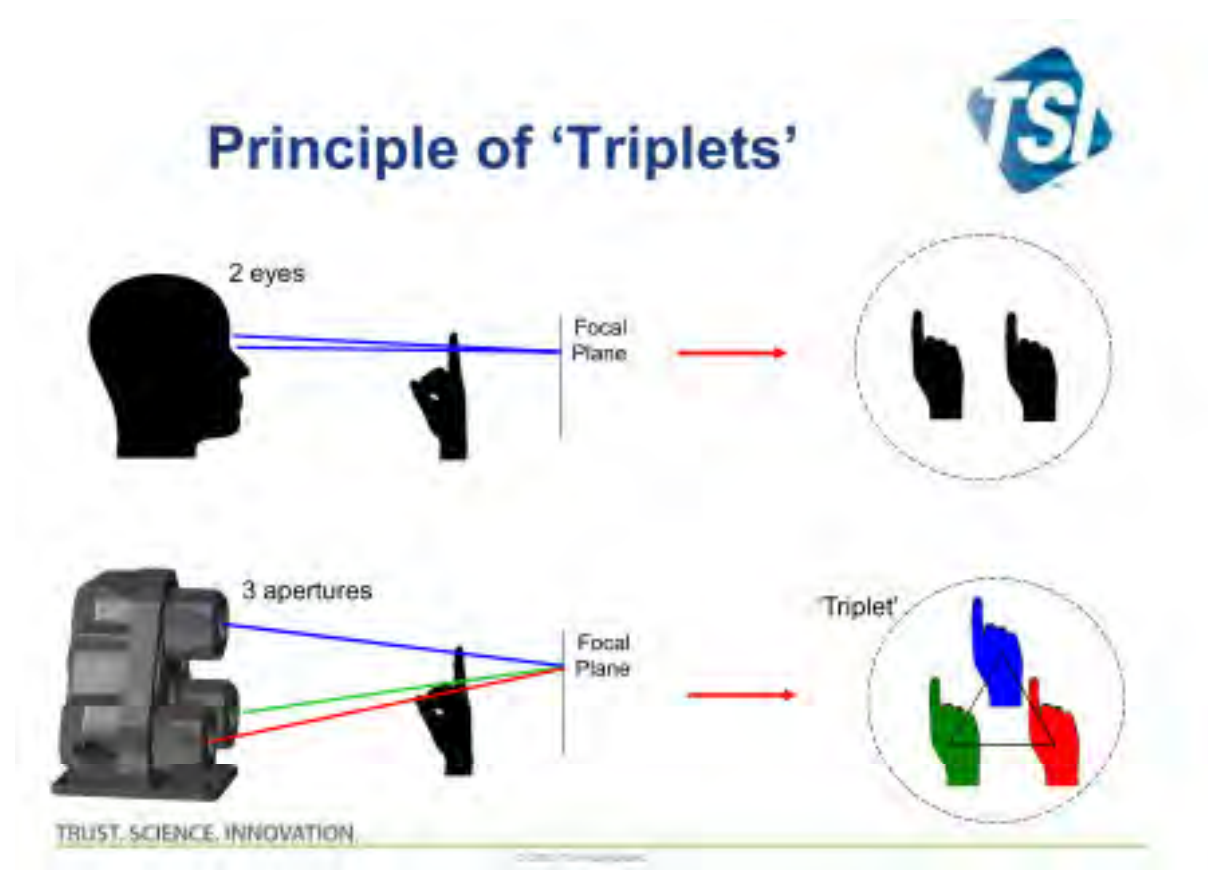


Figure B1.3 Principle of triplets for the V3V (TSI V3V brochure).

A fundamental step in order to get reliable results is the calibration. An automated multi-plane calibration is carried out capturing target images in the parallel plane to the camera. This type of calibration is essential to correct misalignment error, to correct lens distortion and to correct pinhole deviation.

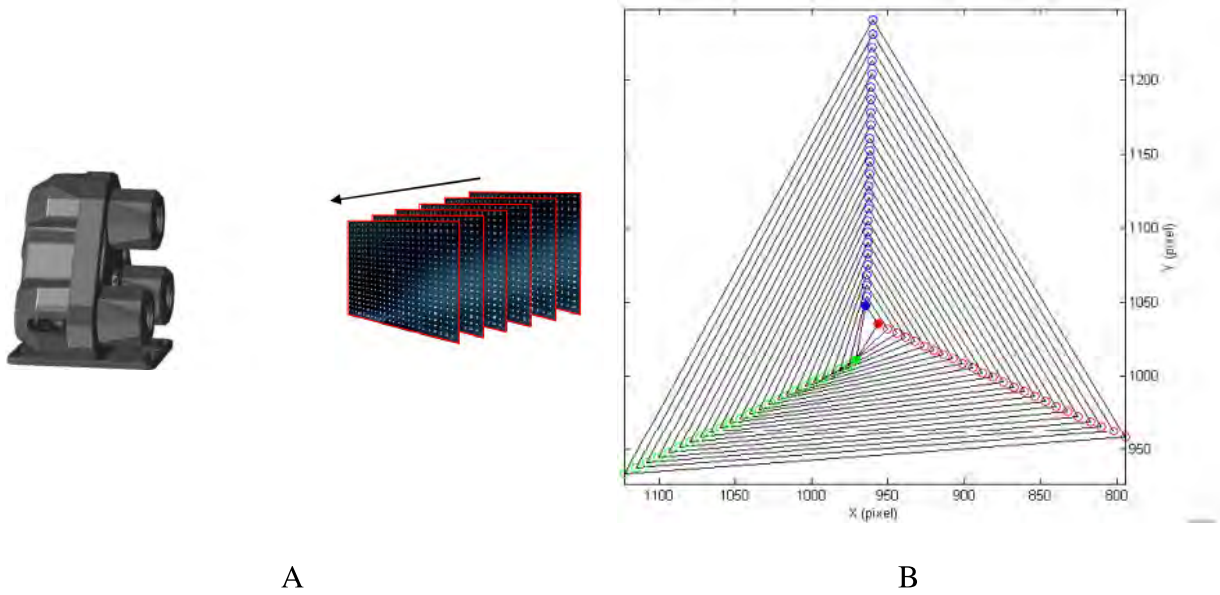


Figure B1.4. Calibration procedure for V3V: a) automated multi-plane calibration and b) triplet size at each calibration plane (TSI V3V Brochure).

The last step to achieve the results of 3D measurement is the analysis of the raw image using the algorithm developed by TSI. Using the 2 frames as a normal PIV system, the velocity of the particles is calculated on individual particle displacement in time among different laser pulses. The triplet search algorithm is based on 3 steps: first identifying a particle in the top aperture, second searching for matches according to the calibration triplets (right image) and finally checking potential matches for a match in the left image. If a sufficient number of particles is detected the Insight software allows the characterization of the vector field. In the following paragraphs it will be show the apparatus used and it will be described the experiment using static mixer.

APPENDIX C: Minor experiments

C1: Fluid dynamic of a Kenics KM static mixer.

In Appendix C two different optical techniques are used to describe the fluid dynamic in inline mixer. Firstly, V3V technique is used to characterize the flow field inside a 6 elements KM static mixer at constant flow rate. The superficial velocity which is used to carry out the experiment is 0.3 ms^{-1} . The other session of this appendix concerns about flow visualisations using the high speed camera in order to investigate the effect of different injection positions. Referring to Figure C1 a matrix of experiments has been studied combining the wall and centre (quotes are in Figure C1) with far and close positions of injection. The far position is about one diameter pipe from the first element of the static mixer while for the close position the injection is attached to it. The flow ranges are the same used for PLIF experiments: 0.1 , 0.3 , 0.6 ms^{-1} are the selected velocities.

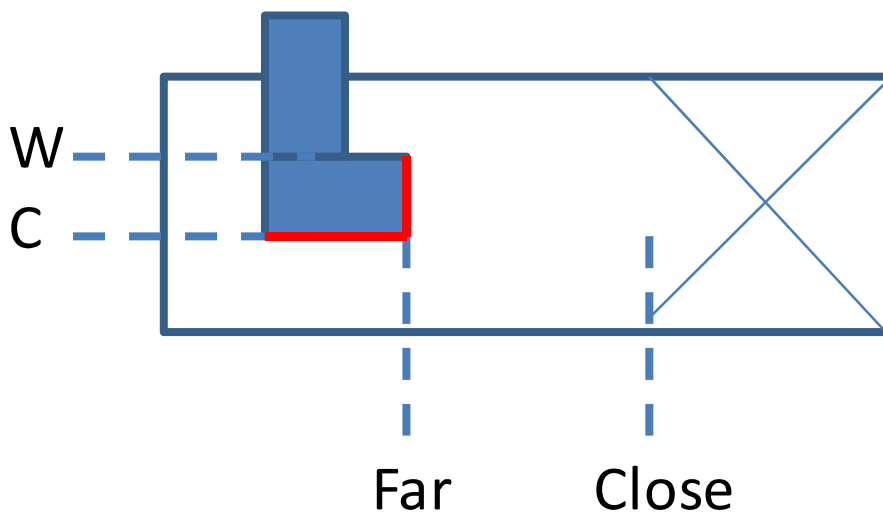


Figure C1.1 a) Different positions of injection

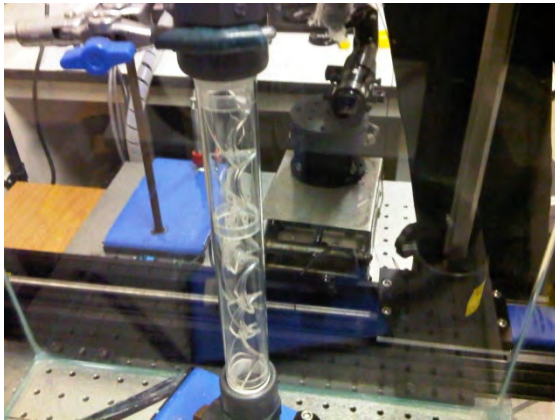
C2: V3V experiment

C2.1 Introduction

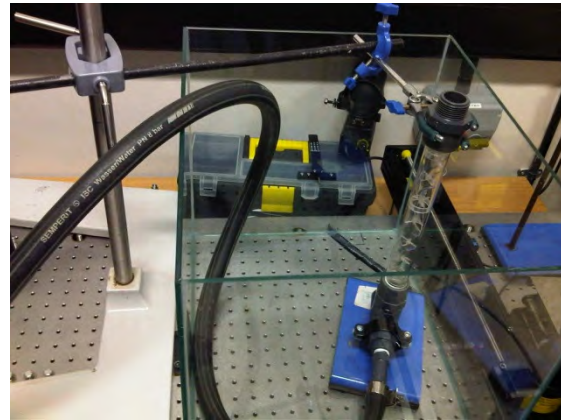
This part of work deals with the investigation of flow dynamic inside the Kenics static mixer and a qualitative characterization of the effects on the flow along the static mixer changing the injection position. Refer to material and method chapter for a full description of the used techniques. In particular, the 3D flow inside the KM static mixer is characterised by V3V technique developed by TSI and the effects of the injection position is detected using a high speed camera. In the following paragraph an overall overview of the recent progress on these studies are presented. In the literature there are some recent works where the core of the study is to evaluate the flow dynamics in a wide range of system. In his work Troolin (2010) studied the vortex rings generated by driving pistons within circular cylinders at a constant velocity. The flow downstream of circular and inclined exits was examined using V3V. The use of this technique allows a better understanding of the vortex ring propagation which is more difficult with 2D standard technique. In the same group of research Kireitseu (2010) studied the vortex ring but in a completely different system as heart valve and Cheng (2013) investigated the three-dimensional vorticity dynamics of the flows generated by revolving wings. Most of the works in the literature where the flow dynamics of KM static mixer is investigated are based on CFD. In his work Hobbs (1997) developed a numerical characterisation of low Reynolds number flow in Kenics static mixer which is correlated to the other work done in collaboration with Muzzio (1997) where the three dimensional chaotic flow was investigated. Avalosse (1997) developed numerical tools for the analysis of complex 3-D mixing devices. The calculation of the flow dynamic has been developed combining streamlines with a fairly large number of material points; along these stream lines, relevant kinematic variables, which are subjected to a statistical treatment, are evaluated. The statistical treatment was performed on some 8, 000 material points crossing the entry section

to evaluate mixing quality. More recently Saatdjian (2012) in his work studied the mixing by chaotic advection in two types of three-dimensional open flows. The first flow is spatially periodic; it consists of a cylindrical tube with a finite number of KM static mixer elements inside. The mixing is characterized by 3-D flow numerically solving the momentum equations using computational fluid dynamics. The second mixer considered is the time-periodic 3-D flow between two co focal elliptic cylinders whose inner and outer boundaries glide at constant or variable velocity. One of the few experimental works has been developed by Rafiee *et al.*(2013) where positron emission particle tracking (PEPT) is used to determine mixing performance. In this work, PEPT has been used to study laminar flow for different types of fluids in a Kenics static mixer (KM) with a left-right blade combination: a high viscosity Newtonian and non-Newtonian fluid. Using the analysis of the tracer particle trajectories through the mixer, Rafiee *et al* computed the overall flow field and to visualise how the fluid twists and folds as it passes along the mixer. The stretching and folding mechanism of mixing was observed.

C2.2 Experimental setup



a)



b)

Figure C2.1 a) 6 elements of KM static mixer made by transparent material, b) enclosure box and static mixer used for V3V experiment.

The V3V technique has been used to investigate the flow field inside a KM static mixer provided with 6 elements. In Figure C.2.1a, it is shown the device structure which is completely made of transparent materials. The pipe is made of glass with a thickness of 2 mm and the static mixer elements are made of Perspex with a thickness of 2 mm too. To avoid distortions on the images due to the static mixer pipe curvature, an enclosure box (Figure C.2.1b) filled with a solution of glycerol was used. Glycerol 98% was used to match the refractive index among all transparent materials. A tie-rod was used to ensure the stability of the apparatus.

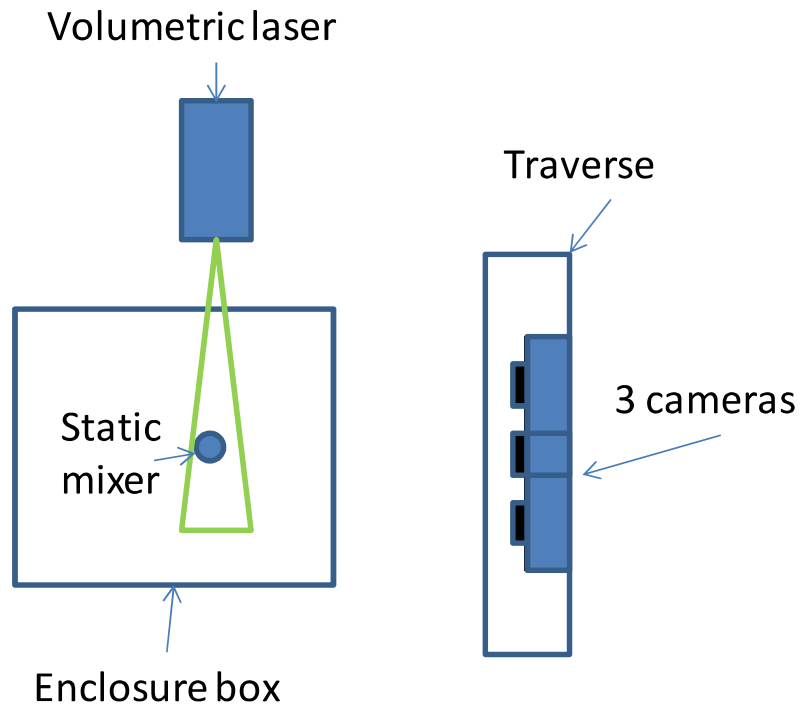


Figure C2.2 V3V rig

Figure C2.2 shows a schematic rig of the V3V system with the rest of the equipment. The enclosure box was orthogonal to the laser and to the 3 cameras which were attached to a traverse. With this set up the cameras were able to move in the 3 directions to find the right focus and to help with the calibration. The laser was positioned in order to create a cone of light which has illuminated the entire static mixer. Finally the device was located almost in the centre of the enclosure box in order to have less reflection due to the wall of box. The refractive index is a key parameter which affects drastically the quality of the data for this technique. The only experiment where the refractive index was completely matches is the one carried out using a Glycerol solution of 80% w/w. This solution is the same used for the experiments in the chapter 4. For the details of rheology of the cited fluid refer to material and method in the session of rheology of model fluids (§3.1.1). The static mixer consists of 5 KM elements (R-R) with 1 inch diameter and 1.5" length. The flow field has been characterized only for 3 of 5 KM elements due to the limited size of volumetric laser

projection. A single flow condition has been chosen setting the superficial velocity to 0.3 m s^{-1} which is used as standard velocity for all the experiments in this thesis work.

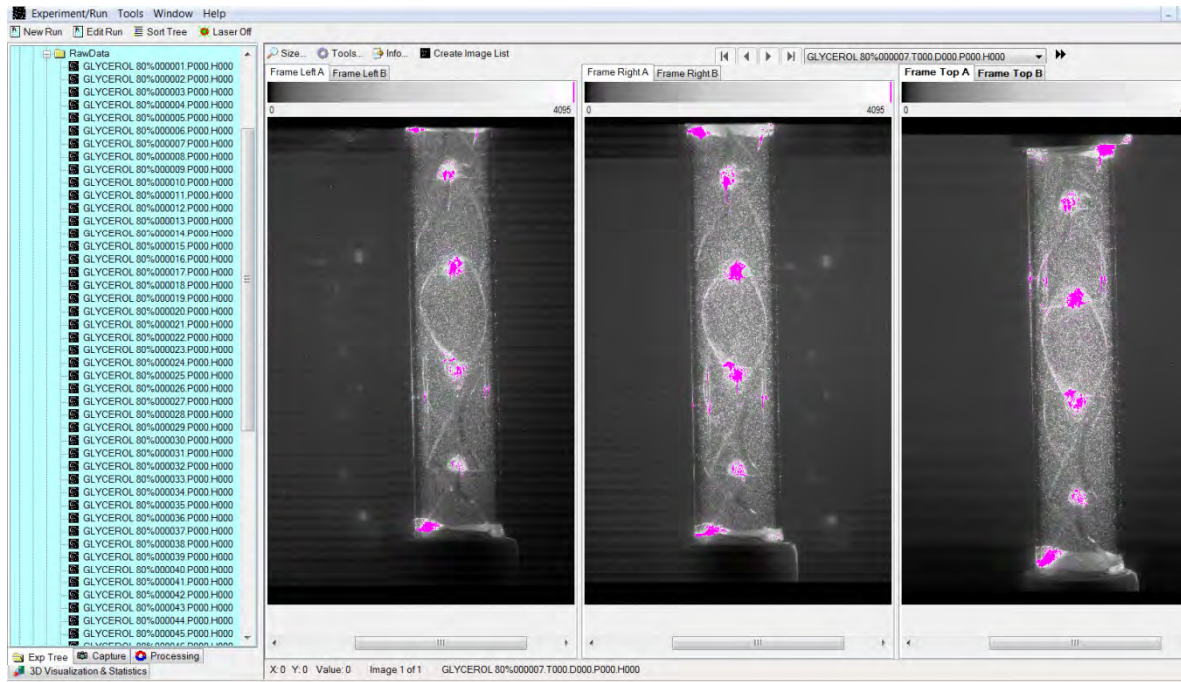


Figure C2.3 Raw images of the three views of V3V cameras.

In the above Figure the raw images of the three views of V3V cameras are showed. Using the Insight V3V software, the group of three images are processed by the TSI algorithm which is based on the principle of triplets explained in the Appendix B.

C2.3 Results

Figure C.5 represents the vector scatter for the V3V experiment where the refractive index was matched among all static mixer parts, fluid and enclosure box. As expected the flow is direct from the top to the bottom (Y direction) but not following a straight path. The presence of KM static mixer generates swirling flow around the elements.

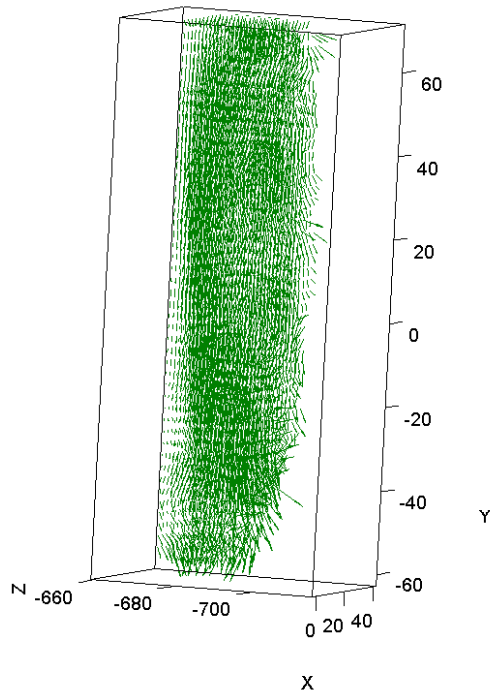


Figure C.2.4 Vector scatter of static mixer system using 80% w/w glycerol solution

Processing the raw data obtained by the V3V apparatus, it is possible to create velocity maps for different plane or volumetric maps; series of data statics are calculated by the software to allow a general characterisation of flow dynamic for the analysed system. Figure C2.5 presents a series of velocity maps for different projections of plane YX for different Z positions, where Y is the axial direction of the static mixer, X is one of the perpendicular directions to Y which is in front of the cameras and Z is the other one. The projections start from the middle of static mixer in Z direction and each different image represents the cross section at intervals of 2 mm distance. From the velocity maps it is clear how the flow behaves inside the static mixer, as expected high velocity is reached always in the centre of the zone between the element and the wall of the pipe. The flow field of three out of five elements is characterised by the different sections. The highest velocity of the system is in close to 0.4 m s^{-1} ; the superficial velocity of the system is 0.3 m s^{-1} . Observing the different sections and the correspondent flow projections for element 2 and 4, it is evident the

similarity of the patterns; as expected the element 3 shows a different pattern due to the orthogonal position unlike element 2 and 4. Obviously the pattern between element 2 and 4 are not identical in the intensity level of velocity and this maybe due to a not complete developed flow or for the shape of static mixer element which are not identical.

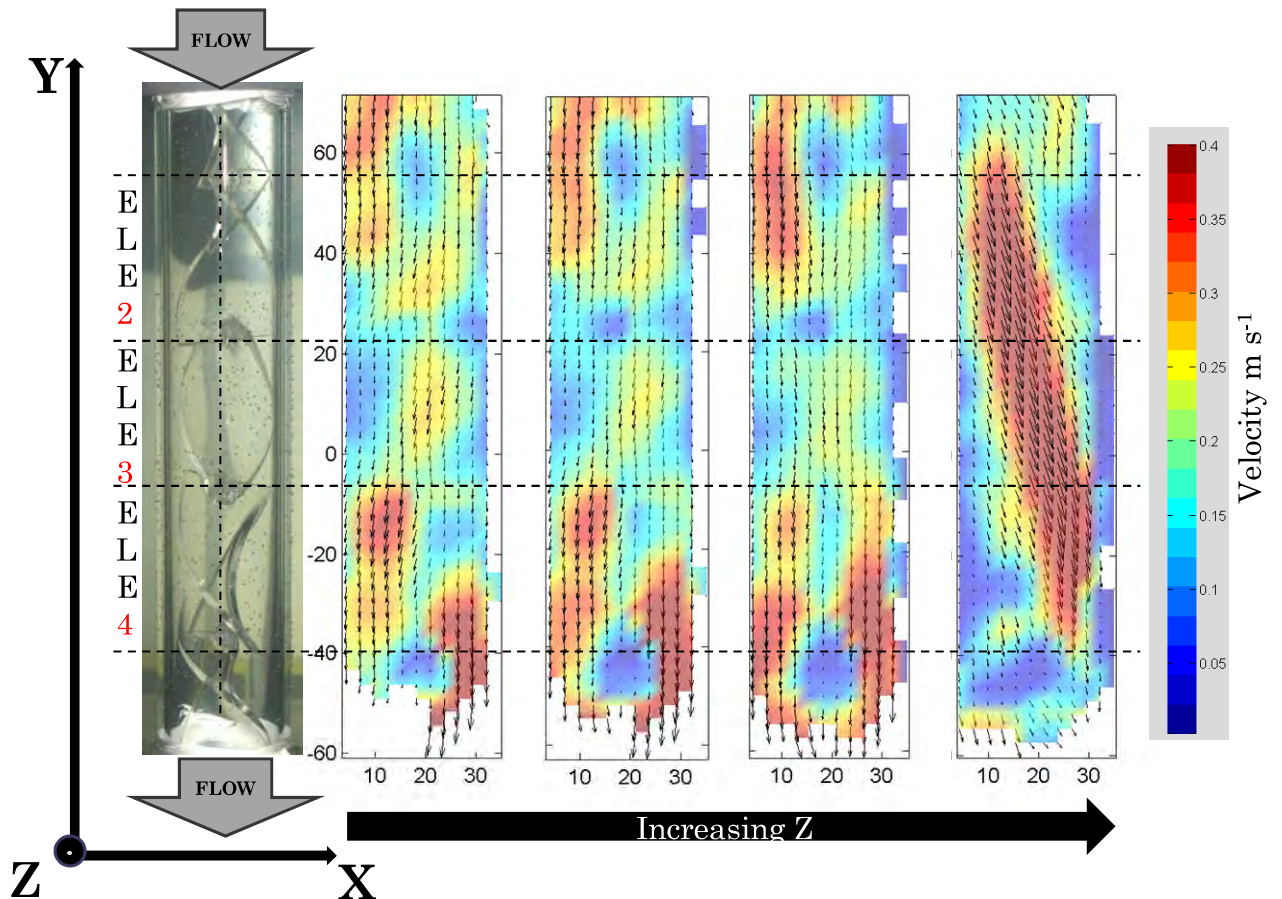
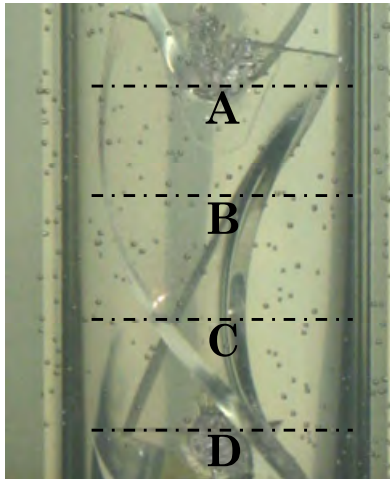


Figure C2.5 Flow field of different YX cross sections of static mixer.

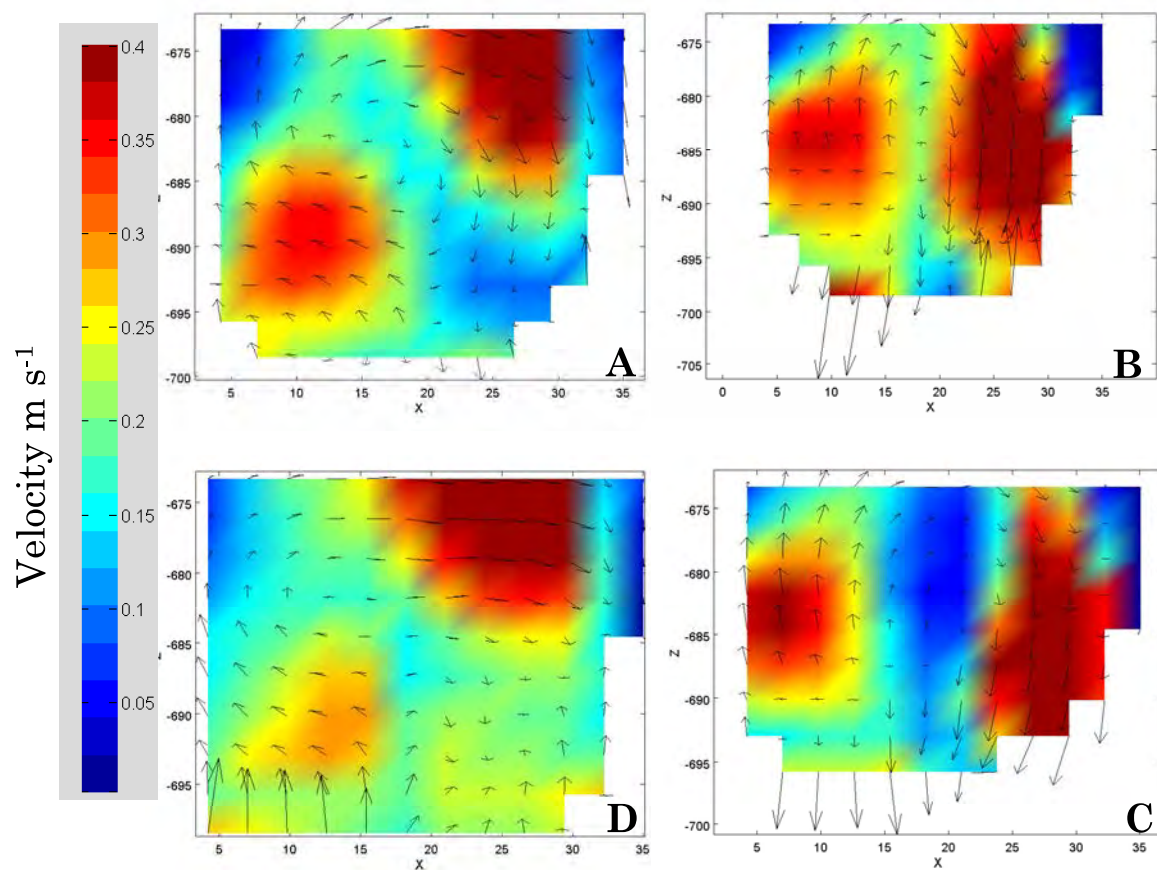
Figure C2.6a shows different cross sections of the plane ZX for the element 4 which are evidenced in Figure C2.6a with the sections A, B, C, D. Figure C2.7b shows the characteristic flow pattern for a Kenics static mixer element. As expected there are two peaks in velocity where the flow is faster; these peaks are situated in different locations in each different section following the shape of the static mixer element. The maximum peaks in velocity are at the furthest distance from the solid boundaries of the geometry between the inner wall of

the pipe and the blade. Towards the inner wall of the mixer, the velocity decreases significantly.

Element 4



a)



b)

Figure C2.6 a) Sections of static mixer; b) Flow field of different YX cross sections of static mixer element.

In the plot of Figure C2.7 the distribution of Reynolds number for the whole volume of the static mixer is presented. As expected, the range of interest is only in the laminar regime which gives the possibility of comparing of the results with previous works.

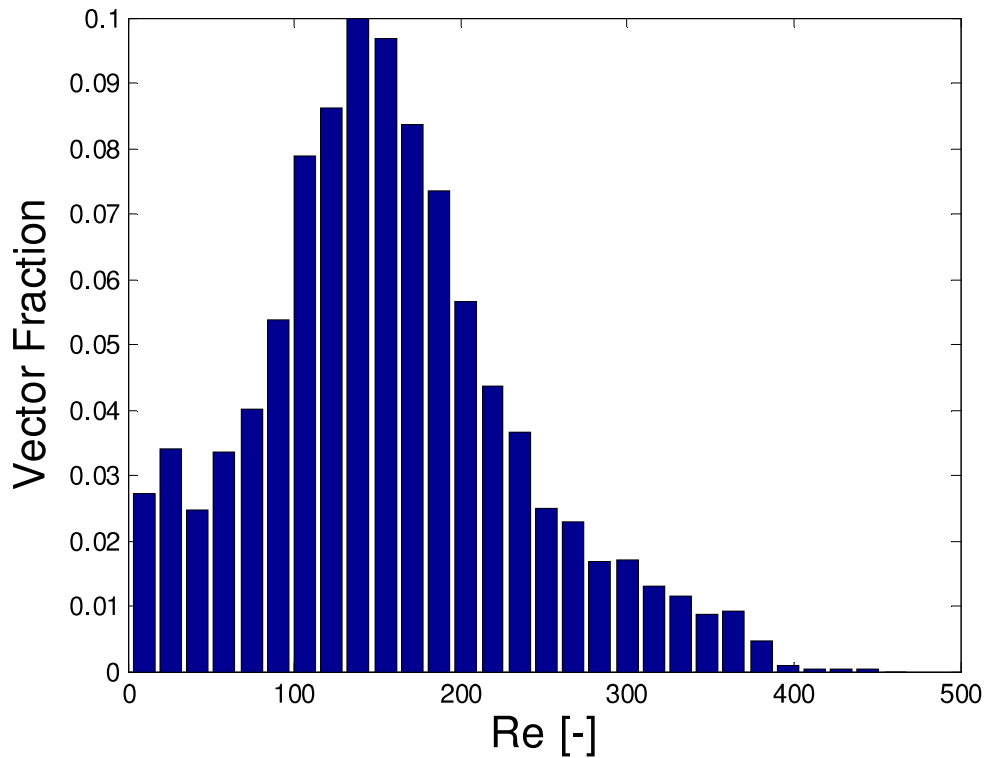


Figure C2.7. Reynolds number distribution inside the static mixer volume

Finally in Figure C2.8 a and b the vorticity distribution of the whole static mixer system are presented. In Figure C2.8a the distribution of vorticity γ is presented; the Insight software calculate this value following the equations below:

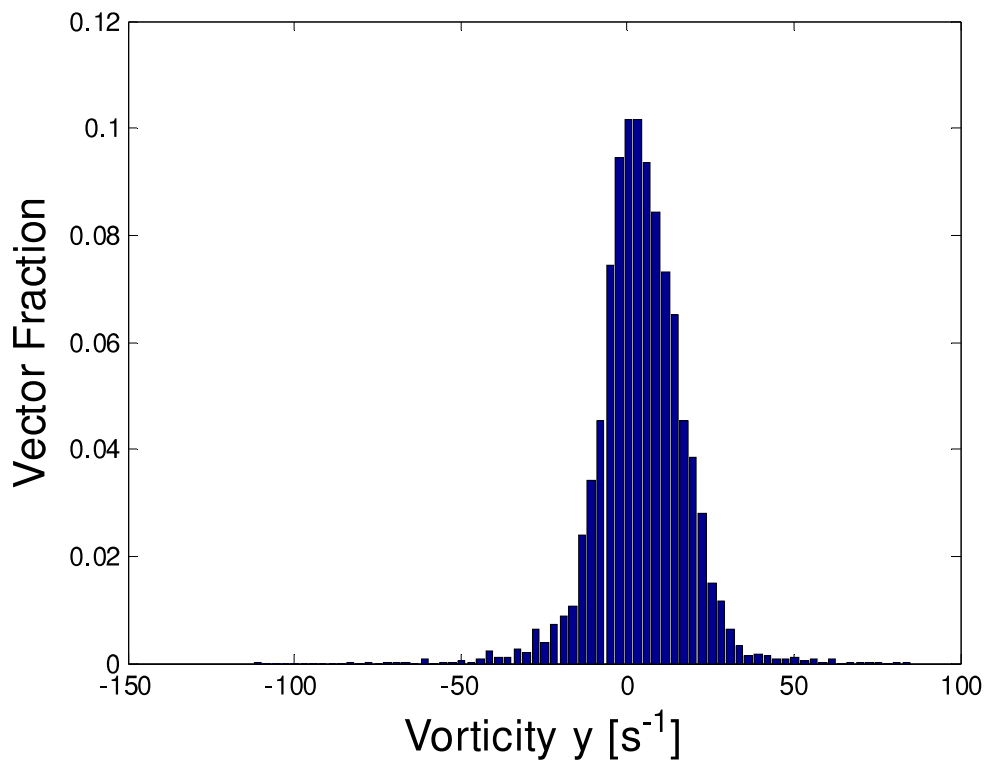
$$\text{VorticityX} = dW/dy - dV/dz,$$

$$\text{VorticityY} = dU/dz - dW/dx,$$

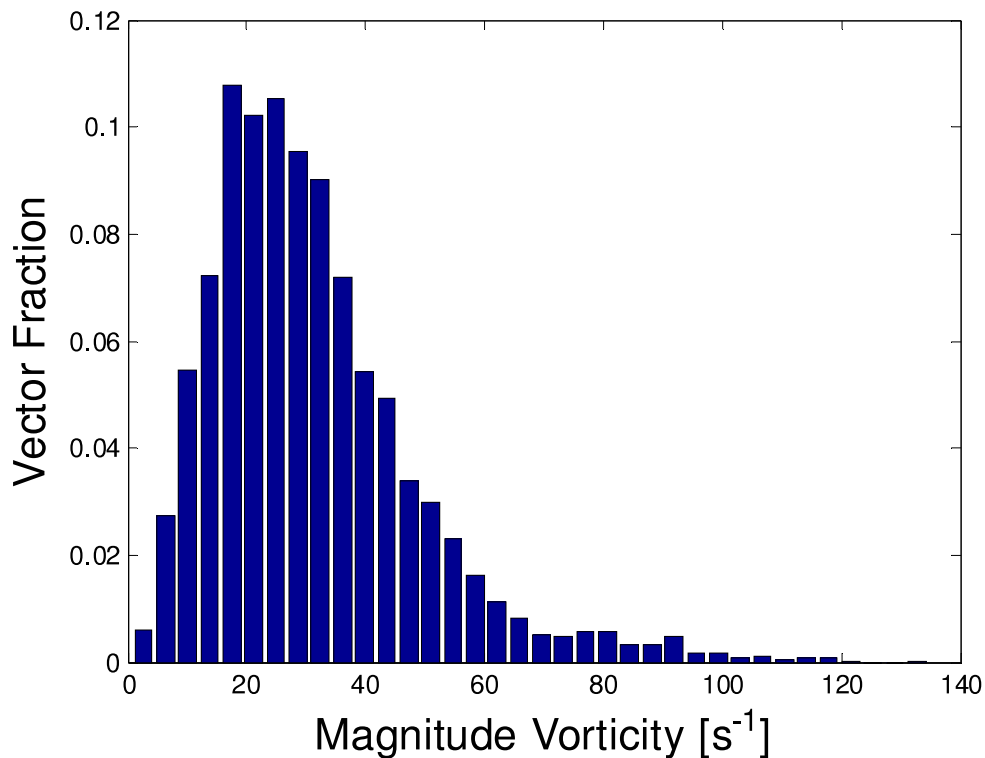
$$\text{VorticityZ} = dV/dx - dU/dy,$$

$$\text{Vorticity Magnitude} = \text{Sqrt}(\text{VorticityX}^2 + \text{VorticityY}^2 + \text{VorticityZ}^2),$$

where U is the velocity in X direction, V is the velocity in Y direction and W is the velocity in Z direction. As expected in laminar regime, a symmetric shape distribution of the positive and negative values of the vorticity is reported. In terms of magnitude vorticity the maximum values is close to 140 s^{-1} but more often the magnitude vorticity is in the range between 20 and 50 s^{-1} . These values can be compared to the values calculated using the empirical equation which relate the shear to the velocity over the diameter multiply by a constant K ($K=8$ empty pipe and $K=28$ KM static mixer); for an empty pipe the maximum shear is 96 s^{-1} and for a KM the value of the shear is 336 s^{-1} . Considering that the equation for the shear and the values of K are empirical, the experimental values can be considered for a qualitative analysis, maybe not for the absolute values.



a)



b)

Figure C2.8 a) Vorticity distribution in the static mixer;b) Magnitude vorticity distribution in the static mixer

C2.4 Conclusion

This part of this thesis work is a preliminary approach to a novel technique for the characterisation of a 3D flow field which can be developed and used as valid instrument for the validation of CFD (computational fluid dynamic). These preliminary results confirm the validity of the proposed technique; furthermore a qualitative analysis has been approached to verify the validity of an empirical correlation applied to a more complex geometry than an empty pipe, as KM static mixer is. A comparison with another experimental and computational work is done to confirm the truthfulness of the obtained results. The limitation of this technique is the need of transparent fluid which matches the refractive index of all parts of the system.

C.3 Injection position effects

C3.1 Introduction

Hobbs (1997) is the first who investigated the importance of injection position in static mixers. The performances of the Kenics static mixer for mixing small streams of passive tracer into the bulk flow have been investigated as a function of injection location and flow ratio. Mixing is evaluated qualitatively by examining the spread of the tracer on cross-sectional slices from the mixer and quantitatively by computing the CoV as a function of axial position. The conclusions of this work underline the strong effect of different injection position for the standard Kenics geometry in particular for the first few elements, after which the mixing rate is independent from the injection location. Zalc (2003) in his work characterized mixing behaviour in a four-element SMX static mixer. CFD has been used for a high resolution and high-accuracy computational results for multiple flow rates in the laminar regime. Mixing simulations were used to expose mixture topology central injection and off-centre injections and to illustrate stretching fields at various axial distances. The mixing patterns provide strong evidence of self-similarity and asymptotic directionality. The main conclusions of this work describe the mixing rate to be relatively insensitive to Reynolds number for the central injection, but it depends on flow rate when the injection is off-centre. The development of new technologies determines the production of an intermediate piece for connecting static mixer to the injection in the last few years. The advantages of this piece is that it can optimize the manufacture of the static mixer and the connection piece in injection moulding process and avoid contamination of to-be-mixed products reliably before entering into the mixer while avoiding errors in the assembly.

C3.2 Experimental setup

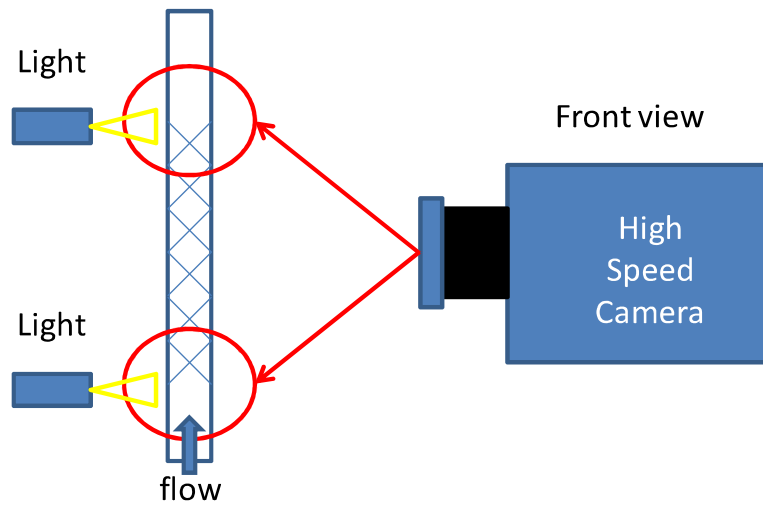


Figure C3.1 a) Positions where the camera was pointed; first element and at the bottom of static mixer. b) Different position of injection investigated.

The static mixer made of transparent materials has been used for the investigation of effect injection positions and velocities of the flow. The device was locked on the horizontal stand used also for the PLIF experiments. In particular two locations were investigated: the first elements and the last elements of 6. These experiments were performed using a black dye which was more visible for a monochrome camera instead of Rhodamine 6G used for PLIF experiments. A light was located perpendicular to the device in the longitudinal direction like the camera but it was located opposite to the light source. For these experiments the main parameters considered are superficial velocity, axial distance between the first element of static mixer and injection, the central or wall injection position and type of fluid injected. The two fluids are injected which are extensively used in this thesis work; they are based on Carbopol solution. Refer to material and method for specifications about the rheology and composition of the solution (§3.2.1). Three different velocities are selected to investigate their importance. Two axial positions have been chosen to visualize the effects along the

static mixer. The positions were selected following the distances with which the experiments of chapter 4 and chapter 5 have been developed. The 'FAR' distance corresponds to 1 inch diameter distance between first element and injection; the 'CLOSE' distance is when the injection is attached to the first element. Selected images which represent the inlet of static mixer and the outlet are reported to give a qualitative view of the problem.

C3.3 Results

In this thesis work a qualitative analysis of the flow dynamic in 6 elements of KM static mixer is done. Thanks to the information obtained from the proposed mixing performance analysis (area fraction method and striation area distribution), the injection position has been detected as significant parameter which influences drastically the mixing performance for the KM static mixer. The influence on the mixing performance has been discussed extensively in chapter 5; however this chapter shows what influences those performances using flow visualisation for a better understanding. Following the structure of previous analysis the effect of velocity is characterized. In addition, the analysis of axial distance between first element and injection (FAR or CLOSE) and wall or central injection position have been studied. The effect of velocity is extensively discussed for KM in chapter 5 but the aim of these results is to explain what happens to the flow before and when the two stream pass through the static mixer. In Figure C3.2 a and f, the view of the central injection (primary fluid: fluid 1 and secondary fluid: fluid 1) in an empty pipe at two selected velocities is shown. Comparing the two injections in an empty pipe it is clear how the trajectories of the secondary flows change increasing the distance from the injection point. Increasing the velocity, this effect seems to decrease but it is clear how only if attached to the injection point the dye is perfectly in the centre. The axial section of the injection in an empty pipe has been analysed using PIV (Figure C.3.2 c and h). The trajectory of the secondary flow is influenced by the velocity distribution which is slightly modified by the presence of the 'L' injection

inside the pipe. The main flow is concentrated in a smaller section just where the 'L' injection is located, generating an acceleration in the flow that creates a sort of 'jet' which pulls up the injected flow. After a distance of a pipe diameter, the flow becomes a plug flow as expected. In Figure C3.2 b and g the view of 2nd and 3rd element of KM static mixer are shown; the injection of the secondary flow is attached to the first element (CLOSE injection) for both selected velocities. Observing the two views of the 2nd and 3rd element of KM static mixer it is evident how the velocity influences the mixing of the injected dye among static mixer elements. To quantify the effect of the mixing in the two proposed views, gray scale values distributions are presented (Figure C3.2 d and i). The same experiments are run without the injection of dye in order to obtain a background image. Thanks to that, a range of gray scale values is determined. In the proposed graphs the black zone is where the gray scale values are influenced by the dye concentration. Clearly increasing the velocity the distribution is getting smoother due to the mixing effect on the dye.

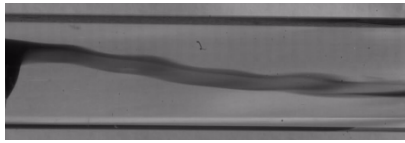
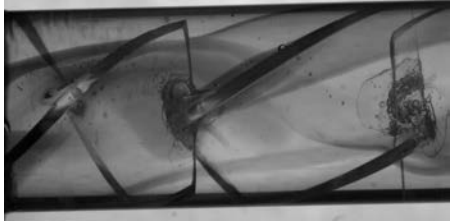

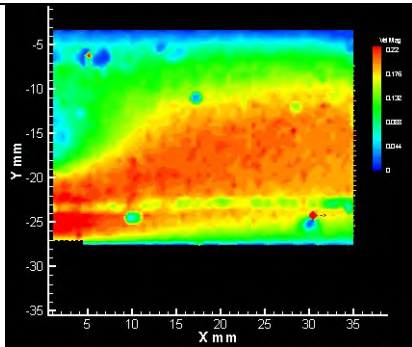
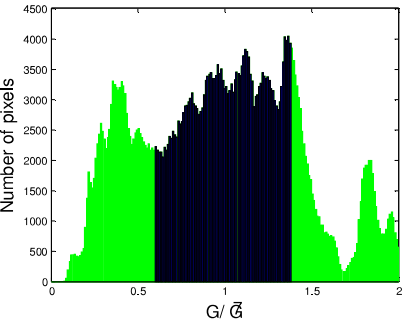
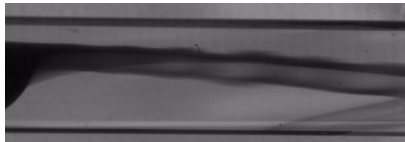
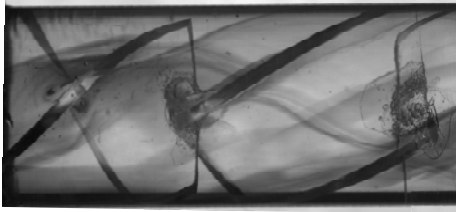
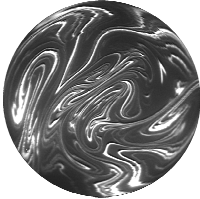
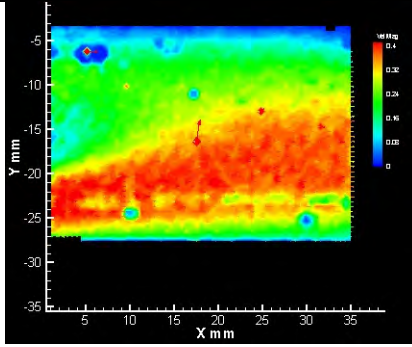
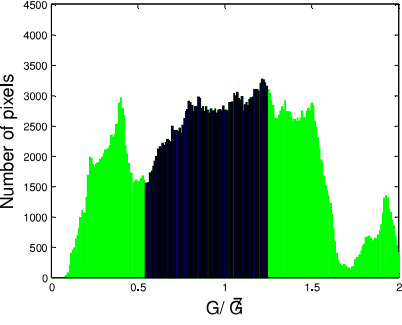
Vel.	View of the central injection in an empty pipe	View of 2 nd and 3 rd element of KM static mixer	PLIF image of the cross section
0.1 [ms ⁻¹]			
	a)	b)	
			
	c)	d)	e)
0.3 [ms ⁻¹]			
	f)	g)	
			
	h)	i)	l)

Figure C3.2. View of the central injection in an empty pipe (a and f), the view of 2nd and 3rd element of KM where the injection of the secondary flow is attached to the first element (b and g), the raw PLIF images at the end of 6 element of KM static are

presented (e and l), PIV analysis (axial section) for central injection in an empty pipe (c and h) and gray scale values distribution of static mixer section (d and i).

Figure C3.3 and C3.4 is a summary of the consequences of a different injection location for the two model fluids (fluid 1 and 2) extensively used in this thesis work. Figure C3.3 shows the trajectory of the injected fluid at 'FAR' and 'CLOSE' positions for fluid 1 and 2. It is clear how the flow overpasses the first element when the injection it is located in the 'FAR' position. The consequence is that the main flow directs the secondary towards the wall over passing the first elements of the static mixer. However when the injection is located in the 'CLOSE' position, the first elements is not over passed anymore. Clearly, differences on the mixing pattern are evidenced on the proposed PLIF images for both injected fluids which represent the consequences of different settings. For detailed information about mixing performance refer to chapter 4 and 5.



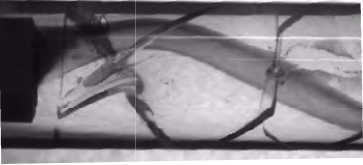

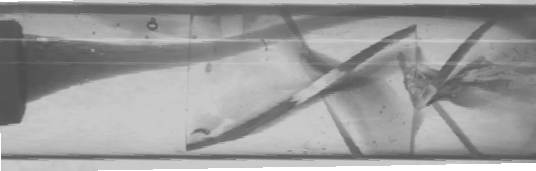

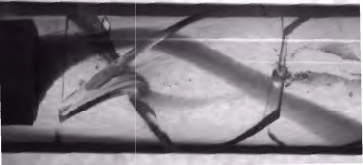
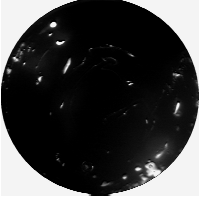
Fluid	View of the injection	'FAR' injection (PLIF image)
Fluid 1	'FAR' position	
		
	'CLOSE' position	
		
Fluid 2	'FAR' position	
		
	'CLOSE' position	
		

Figure C3.3 Visualisation of injection in the two selected position, FAR and CLOSE at superficial velocity of 0.3 m s^{-1} . Raw PLIF images for selected experiment using 6 elements KM static mixer.

In Figure C3.4 wall and central injection in an empty pipe are proposed for both fluids with the correspondent PLIF images for KM 6 elements with the ‘CLOSE’ injection. Wall injection accentuates the trajectory towards the wall of the pipe which results a half mixed cross section (PLIF image). From the selected images it seems that the injection of fluid 1 is slightly affected by the perturbation of the flow due to the ‘L’ injection which slightly dissolves the injected dye. This phenomenon is neglected for the injection of fluid 2 where it is likely that the higher yield stress plays an important role to contrast the mixdness of the injection.

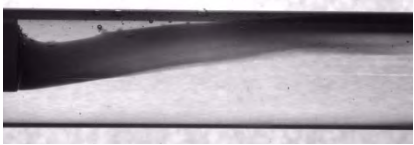

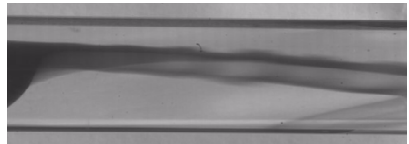
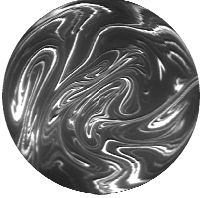
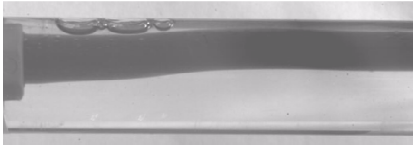
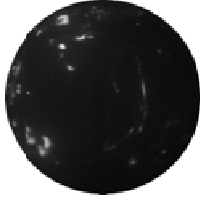
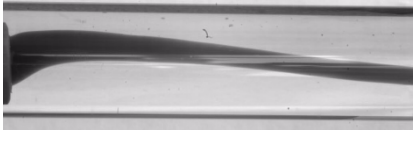
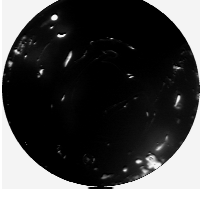
Inj. Pos.	Injected Fluid	View of the injection	Cross section (PLIF image)
wall	Fluid 1		
central			
wall	Fluid 2		
central			

Figure C3.4 Visualisation of injection in the two selected position, central and at wall at superficial velocity of 0.3 m s^{-1} . Raw PLIF images for selected experiment using 6 elements KM static mixer.

C3.4 Conclusions

This part of work has been developed to visualize the effects of injection position which is a critical step and sometime is an underestimated parameter for a correct setting of a static mixer. A summary of the possible injection conditions are reported in this part of thesis chapter; relevant importance is given to central injection attached to the first elements which avoids the fluid to overpass the first elements. Perturbations of the flow due to the 'L' obstruction can facilitate the mixing of the injected dye if the yield stress is not high to contrast this trend. For different treated conditions, PLIF raw images are reported, for more information about the mixing performance referring to previous chapters (4 and 5). This part of the work has been developed to formalise assumptions which have been made during this thesis work as negligible diffusion in the system and the not correct functioning of KM static mixer without a precise setting.

APPENDIX D: MATLAB codes

D1: Script of intensity of segregation: Coefficient of variation and LogVa

```
%location of the centre of cross section in pixels
xc=600;
yc=600;
r=500;
l=2*r/sqrt(2);
ls=round(l);

%%%Define boundaries of ROI%%%
Y1A=yc-ls/2;
Y1B=yc+ls/2;
X1A=xc-ls/2;
X1B=xc+ls/2;
nn=ls^2;

%Import image file%%%
f1='F:\plif\fedo october 1inch';
f2='180 l per hr 18 l per h 01 carb kenics\RawData';%name folder
f3='cut180 l per hr 18 l per h 01 carb kenics';%name file

nni=7;% image number

fname=[f1,'\',f2,'\',f3,'00000',num2str(nni),'.T000.D000.P000.H000.tif'];
A = imread(fname);
y=A;
Aa=y;
sizeA=size(A);
imgCutci = zeros(sizeA(1,1),sizeA(1,1));%mask to remove section outside area of interest

for i=1:sizeA(1,1);
for j= 1: sizeA(1,1);
    tmp = (i-xc)*(i-xc)+(j-yc)*(j-yc);
    if (tmp<=r*r)

        imgCutci(i,j)=Aa(i,j);
    else
        imgCutci(i,j)=0;
    end
end
end
end
```

```

GI=find(imgCutci>0);
GIs=imgCutci(GI);
GIss=151; % number for G infinity determined experimetically using solution of dye pre-
mixed

szGI=size(GIs);
szGIs=szGI(1,1);
GCinf=zeros(szGIs,1);

for j=1:szGIs-1

    GCinf(j,1)=GIss;
end

GCinf=double(GCinf);
GIs=double(GIs);

%%%Nominal Grey scale%%%

GIF=GIs;
GCIF=GCinf;

%%Calculate Variance%%

GT=zeros(szGIs,1);
GTCOV=zeros(szGIs,1);
VA=zeros(szGIs,1);
lgva=zeros(szGIs,1);
for i=1:szGIs-1

    dv=abs(GIF(i,1)-GCIF(i,1));

    GTCOV(i,1)=sqrt((dv)^2)/GIss;

    if GIF(i,1)>=2*GCIF(i,1);
        VA(i,1)=1;
    elseif 2*GCIF(i,1)>GIF(i,1)>GCIF(i,1)
        GT(i,1)=(((GIF(i,1)-GCIF(i,1)))/GCIF(i,1))-1;
        VA(i,1)=((GT(i,1)-1)^2);
    else
        GT(i,1)=(GIF(i,1)/GCIF(i,1));
        VA(i,1)=((GT(i,1)-1)^2);
    end
end

VAm=mean(VA);
CoV=mean(GTCOV);
LogVA=log(VAm)

```

D2: Script for scale of segregation: Striation thickness

%%location of the centre of cross section in pixels

clear all

xc=1000;

yc=1000;

r=500;

l=2*r/sqrt(2);

ls=round(l);

%%Define boundaries of ROI%%

Y1A=yc-ls/2;

Y1B=yc+ls/2;

X1A=xc-ls/2;

X1B=xc+ls/2;

nn=ls^2;

f1='f:\plif\fedo november';

f2='GLYCERO12ELE\RawData';

f3='GLYCERO12ELE';

%GLYCERO12ELE

nni=29;

%nnf=47;

%n=nnf-nni;

fname=[f1,'\f2,\f3','0000',num2str(nni),'T000.D000.P000.H001.LA.TIF'];

A = imread(fname);

y=A;

Aa=y;

imgCutci = zeros(2048,2048);

for i=1:2048;

for j= 1: 2048;

tmp = (i-xc)*(i-xc)+(j-yc)*(j-yc);

if (tmp<=r*r)

imgCutci(i,j)=Aa(i,j);

end


```

    end
end
mn=find(imgCutci>0);
mns=imgCutci(mn);
mnss=151; % number for G infinity determined experimetically using solution of dye pre-
mixed

At1 = zeros(2048,2048);
% selection area of interest
for i=1:2048
    for j=1:2048
        if abs(imgCutci(i,j)-mnss)~=mnss
            At1(i,j)=imgCutci(i,j)-mnss;
        else
            At1(i,j)=1;
        end
    end
end
At2 = zeros(2048,2048);
% location striations per mixing intensity
for i=1:1:2048
    for j=1:1:2048

        if At1(i,j)>(mnss*(0.3))% selection of range onf mixing intensity
            At2(i,j)=0;

        else
            At2(i,j)=1;

        end
    end
end
At3 = zeros(2048,2048);

for i=1:1:2048
    for j=1:1:2048

        if At1(i,j)<(mnss*(-0.3))
            At3(i,j)=0;

        else
            At3(i,j)=1
        end
    end
end
end

```

%evaluation of striations

```
HH= zeros(1,2048);
HH3= zeros(1,2048);
HV= zeros(1,2048);
HV3= zeros(1,2048);
for i=1:1:2048
    if find(At2(:,i)==0)~=0;
        tempV=find(At2(:,i)==0);
        if size(tempV)==1
            HV(1,i)=1;
        else
            temppV=diff(tempV);
            HV(1,i)=max(temppV);
        end
    else
        HV(1,i)=0;

end

if find(At2(i,:)==0)~=0;
    tempH=find(At2(i,:)==0);
    if size(tempH)==1
        HH(1,i)=1;
    else
        temppH=diff(tempH);
        HH(1,i)=max(temppH);
    end
else
    HH(1,i)=0;

end

end

for i=1:1:2048
    if find(At3(:,i)==0)~=0;
        tempV3=find(At3(:,i)==0);
        if size(tempV3)==1
            HV3(1,i)=1;
        else
            temppV3=diff(tempV3);
            HV3(1,i)=max(temppV3);
        end
    else
        HV3(1,i)=0;

end
```

```
if find(At3(i,:)==0)~=0;
    tempH3=find(At3(i,:)==0);
    if size(tempH3)==1
        HH3(1,i)=1;
    else
        temppH3=diff(tempH3);
        HH3(1,i)=max(temppH3);
    end
else
    HH3(1,i)=0;
end
end
end
```

D3: Script for scale and intensity of segregation: Area fraction and striation area distribution

```
% location of the centre of cross section in pixels
xc=600;
yc=600;
r=500;
l=2*r/sqrt(2);
ls=round(l);

%% Define boundaries of ROI
Y1A=yc-ls/2;
Y1B=yc+ls/2;
X1A=xc-ls/2;
X1B=xc+ls/2;
nn=ls^2;

%% Import image file
f1='F:\plif\fedo october 1 inch';
f2='180 l per hr 18 l per h 01 carb kenics\RawData'; %name folder
f3='cut180 l per hr 18 l per h 01 carb kenics'; %name file

nni=7; % image number

fname=[f1,'\',f2,'\',f3,'00000',num2str(nni),'T000.D000.P000.H000.tif'];
A = imread(fname);
y=A;

Aa=y;

sizeA=size(A);
imgCutci = zeros(sizeA(1,1),sizeA(1,1)); %mask to remove section outside area of interest

for i=1:sizeA(1,1);
for j= 1: sizeA(1,1);
    tmp = (i-xc)*(i-xc)+(j-yc)*(j-yc);
    if (tmp<=r*r)

        imgCutci(i,j)=Aa(i,j);
    else
        imgCutci(i,j)=0;
    end
end
end
end
```

```

GI=find(imgCutci>0);
GIs=imgCutci(GI);
GIss=151; % number for G infinity determined experimentally using solution of dye pre-
mixed

szGI=size(GIs);
szGIs=szGI(1,1);
GCinf=zeros(szGIs,1);

for j=1:szGIs-1

    GCinf(j,1)=GIss;
end

GCinf=double(GCinf);
GIs=double(GIs);

%%%Nominal Grey scale%%%

GIF=GIs;
GCIF=GCinf

a = readim(fname);

%range of gray scale to define range of mixing intensity

l1=GIss*0.1;
l2=GIss*0.2;
l3=GIss*0.3;
l4=GIss*0.4;
l1p=GIss+l1;
l1m=GIss-l1;
l2p=GIss+l2;
l2m=GIss-l2;
l3p=GIss+l3;
l3m=GIss-l3;
l4p=GIss+l4;
l4m=GIss-l4;

%selection of ranges in the image

b1= a>=l1m & a<l1p;

b2m= a>=l2m & a<l1m;

b2p= a>=l1p & a<l2p;

b3m= a>=l3m & a<l2m;

b3p= a>=l2p & a<l3p;

```

```
b4m= a>=l4m & a<l3m;
```

```
b4p= a>l3p & a<l4p;
```

```
b5m= a<=l4m;
```

```
b5p= a>=l4p;
```

```
b1 = brmedgeobjs(b1,2);
```

```
%selection of striation with similar mixing intensity
```

```
image_out1 = label(b1,Inf,0,0);
```

```
image_out2m = label(b2m,Inf,0,0);
```

```
image_out2p = label(b2p,Inf,0,0);
```

```
image_out3m = label(b3m,Inf,0,0);
```

```
image_out3p = label(b3p,Inf,0,0);
```

```
image_out4m = label(b4m,Inf,0,0);
```

```
image_out4p = label(b4p,Inf,0,0);
```

```
image_out5m = label(b5m,Inf,0,0);
```

```
image_out5p = label(b5p,Inf,0,0);
```

```
% measure of the size and perimeter of striations
```

```
data1 = measure(b1,[],{'size','perimeter'});
```

```
data2m = measure(b2m,[],{'size','perimeter'});
```

```
data2p = measure(b2p,[],{'size','perimeter'});
```

```
data3m = measure(b3m,[],{'size','perimeter'});
```

```
data3p = measure(b3p,[],{'size','perimeter'});
```

```
data4m = measure(b4m,[],{'size','perimeter'});
```

```
data4p = measure(b4p,[],{'size','perimeter'});
```

```
data5m = measure(b5m,[],{'size','perimeter'});
```

```
data5p = measure(b5p,[],{'size','perimeter'});
```

```

sz1 = data1.size;

sz2m = data2m.size;
sz2p = data2p.size;

sz3m = data3m.size;
sz3p = data3p.size;

sz4m = data4m.size;
sz4p = data4p.size;

sz5m = data5m.size;
sz5p = data5p.size;

sz2=[sz2m sz2p];
sz3=[sz3m sz3p];
sz4=[sz4m sz4p];
sz5=[sz5m sz5p];

s1=sum(sz1);
s2=sum(sz2);
s3=sum(sz3);
s4=sum(sz4);
s5=sum(sz5);

totn=(s1+s2+s3+s4+s5);

%area fraction values
areafraction90=100*s1/totn;
areafraction80=100*s2/totn;
areafraction70=100*s3/totn;
areafraction60=100*s4/totn;
areafraction50=100*s5/totn;

areafra=[areafraction90 areafraction80 areafraction70 areafraction60 areafraction50];

```

REFERENCES

- ADAMIAK, I. & JAWORSKI, Z. 2001. An experimental investigation of the non-Newtonian liquid flow in a Kenics static mixer. *Inzynieria Chemiczna I Procesowa*, 22, 175-180.
- ADAMS, L. W. & BARIGOU, M. 2007. CFD analysis of caverns and pseudo-caverns developed during mixing of non-newtonian fluids. *Chemical Engineering Research & Design*, 85, 598-604.
- ALBERINI F, SIMMONS MJH, INGRAM A, STITT EH. A combined criterion to identify mixing performance for the blending of non-Newtonian fluids using a Kenics KM static mixer, 14th European Conference on Mixing, Warszawa, 10-13 September 2012.
- ALBERINI F, M.J.H. SIMMONS, ET AL. (2013). Use of an areal distribution of mixing intensity to describe blending of non-Newtonian fluids in a Kenics KM static mixer using PLIF. *AIChe journal*.
- ALLAN, J. J., GREATED, C. A. & MCCOMB, W. D. 1984. LASER-DOPPLER ANEMOMETER MEASUREMENTS OF TURBULENT STRUCTURE IN NON-NEWTONIAN FLUIDS. *Journal of Physics D-Applied Physics*, 17, 533-549.
- ALLOCA, P., AND F. A. STREIFF (1980). presented at the AICHe Annual Meeting, Chicago.
- ALVAREZ, M., ZALC, J., SHINBROT, T., ARRATIA, P. & MUZZIO, F. 2002a. Mechanisms of mixing and creation of structure in laminar stirred tanks. *AICHe Journal*, 48, 2135-2148.
- ALVAREZ, M. M., ZALC, J. M., SHINBROT, T., ARRATIA, P. E. & MUZZIO, F. J. 2002b. Mechanisms of mixing and creation of structure in laminar stirred tanks. *Aiche Journal*, 48, 2135-2148.
- ALVES, M. A. (2008). Design of a cross-slot flow channel for extensional viscosity measurements. *Xvth International Congress on Rheology - the Society of Rheology 80th Annual Meeting, Pts 1 and 2*. A. Co, L. G. Leal, R. H. Colby and A. J. Giacomin. 1027: 240-242.
- ANDERSON, P. D., GALAKTIONOV, O. S., PETERS, G. W. M., VAN DE VOSSE, F. N. & MEIJER, H. E. H. 2000. Mixing of non-Newtonian fluids in time-periodic cavity flows. *Journal of Non-Newtonian Fluid Mechanics*, 93, 265-286.
- AREF, H. 1984. Stirring by chaotic advection. *Journal of Fluid Mechanics*, 143, 1-21.
- ARRATIA, P., KUKURA, J., LACOMBE, J. & MUZZIO, F. 2006. Mixing of shear-thinning fluids with yield stress in stirred tanks. *AICHe Journal*, 52, 2310-2322.
- ARRATIA, P. E. & MUZZIO, F. J. 2004. Planar laser-induced fluorescence method for analysis of mixing in laminar flows. *Industrial & Engineering Chemistry Research*, 43, 6557-6568.
- ARRATIA, P. E., C. C. THOMAS, ET AL. (2006). "Elastic instabilities of polymer solutions in cross-channel flow." *Physical Review Letters* 96(14).
- ASMAR, B. N., LANGSTON, P. A. & MATCHETT, A. J. 2002. A generalised mixing index in distinct element method simulation of vibrated particulate beds. *Granular Matter*, 4, 129-138.

- AUBIN, J., FLETCHER, D. F., BERTRAND, J. & XUERE, C. 2003. Characterization of the mixing quality in micromixers. *Chemical Engineering & Technology*, 26, 1262-1270.
- AUBIN, J., NAUDE, I., BERTRAND, J. & XUERE, C. 2000. Blending of Newtonian and shear-thinning fluids in a tank stirred with a helical screw agitator. *Chemical Engineering Research & Design*, 78, 1105-1114.
- AVALOSSE, T. & CROCHET, M. J. 1997. Finite-element simulation of mixing .2. Three-dimensional flow through a Kenics mixer. *AIChE Journal*, 43, 588-597.
- BALDYGA, J. 2001. Applications of Computational Fluid Mechanics (CFD) in chemical and process engineering. *Inżynieria Chemiczna I Procesowa*, 22, 3-14.
- BANDALUSENA, H. C. H., W. B. ZIMMERMAN, ET AL. (2009). "Microfluidic rheometry of a polymer solution by micron resolution particle image velocimetry: a model validation study." *Measurement Science & Technology* 20(11).
- BOGER, D. V. & BINNINGTON, R. 1977. Separation of Elastic and Shear Thinning Effects in the Capillary Rheometer. *Transactions of the Society of Rheology*, 21, 515-534.
- BROWN DAR, JONES PN, MIDDLETON JC, PAPADOPOULOS G ARIK, EB. Experimental methods. In: Paul EL, Atiemo-Obeng VA, Kresta SM. *Handbook of industrial mixing: science and practice* . New Jersey: John Wiley & Sons Inc., 2004:145-256.
- CHANDRA, K. G. & KALE, D. D. 1992. PRESSURE-DROP FOR LAMINAR-FLOW OF VISCOELASTIC FLUIDS IN STATIC MIXERS. *Chemical Engineering Science*, 47, 2097-2100.
- CHENG, B., SANE, S. P., BARBERA, G., TROOLIN, D. R., STRAND, T. & DENG, X. Y. 2013. Three-dimensional flow visualization and vorticity dynamics in revolving wings. *Experiments in Fluids*, 54.
- CHHABRA, R. P. & RICHARDSON, J. F. *Non-Newtonian Flow and Applied Rheology - Engineering Applications* (2nd Edition). Elsevier.
- COULSON, J. M., RICHARDSON, J. F., BACKHURST, J. R. & HARKER, J. H. *Coulson and Richardson's Chemical Engineering Volume 1 - Fluid Flow, Heat Transfer and Mass Transfer* (6th Edition). Elsevier.
- DANCKWERTS, P. V. 1952. THE DEFINITION AND MEASUREMENT OF SOME CHARACTERISTICS OF MIXTURES. *Applied Scientific Research Section a-Mechanics Heat Chemical Engineering Mathematical Methods*, 3, 279-296.
- DAS, P. K., LEGRAND, J., MORANCAIS, P. & CARNELLE, G. 2005. Drop breakage model in static mixers at low and intermediate Reynolds number. *Chemical Engineering Science*, 60, 231-238.
- ELYUKHINA, I. 2013. Oscillating-cup technique for yield stress and density measurement. *Journal of Materials Science*, 48, 4387-4395.
- ETCHELLS AW, MEYER CF, *Mixing in pipelines*. In: Paul EL, Atiemo-Obeng VA, Kresta SM. *Handbook of industrial mixing: science and practice* . New Jersey: John Wiley & Sons Inc., 2004:391-478.
- FAN, L. T., LIN, S. T. & AZER, N. Z. 1977. AUGMENTATION OF RATE OF FORCED FLOW BOILING HEAT-TRANSFER BY MEANS OF IN-LINE STATIC MIXERS. *Letters in Heat and Mass Transfer*, 4, 425-428.
- FANGARY, Y. S., SEVILLE, J. P. K. & BARIGOU, M. 1999. Flow studies in stirred tanks by positron emission particle tracking (PEPT), *Rugby, Inst Chemical Engineers*.
- FAVELUKIS, M. & LAVRENTEVA, O. M. 2013. Mass transfer around prolate spheroidal drops in an extensional flow. *Canadian Journal of Chemical Engineering*, 91, 1190-1199.

- FRADETTE, L., TANGUY, P., LI, H. Z. & CHOPLIN, L. 2007. Liquid/Liquid Viscous Dispersions with a SMX Static Mixer. *Chemical Engineering Research and Design*, 85, 395-405.
- GALINDO-ROSALES, F. J., ALVES, M. A. & OLIVEIRA, M. S. N. 2013. Microdevices for extensional rheometry of low viscosity elastic liquids: a review. *Microfluidics and Nanofluidics*, 14, 1-19.
- GALINDO, E. & NIENOW, A. W. 1992. MIXING OF HIGHLY VISCOUS SIMULATED XANTHAN FERMENTATION BROTHS WITH THE LIGHTNIN A-315-IMPELLER. *Biotechnology Progress*, 8, 233-239.
- GELARO, R., REYNOLDS, C. A. & ERRICO, R. M. 2002. Transient and asymptotic perturbation growth in a simple model. *Quarterly Journal of the Royal Meteorological Society*, 128, 205-227.
- GERMANN, N. AND E. J. WINDHAB (2012). "On the rheology and microstructure of immiscible polymer blends in eccentric Taylor-Couette flow." *Journal of Non-Newtonian Fluid Mechanics* 169: 54-60.
- GHANEM, A., LEMENAND, T., DELLA VALLE, D. & PEERHOSSAINI, H. Static mixers: Mechanisms, applications, and characterization methods – A review. *Chemical Engineering Research and Design*.
- GRACE, H. P. 1982. DISPERSION PHENOMENA IN HIGH-VISCOSITY IMMISCIBLE FLUID SYSTEMS AND APPLICATION OF STATIC MIXERS AS DISPERSION DEVICES IN SUCH SYSTEMS. *Chemical Engineering Communications*, 14, 225-277.
- HABIB, S. & RYNE, R. D. 1995. Symplectic Calculation of Lyapunov Exponents. *Physical Review Letters*, 74, 70-73.
- HALL, J. F., BARIGOU, M., SIMMONS, M. J. & STITT, E. H. 2004a. Mixing in unbaffled high-throughput experimentation reactors. *Industrial & Engineering Chemistry Research*, 43, 4149-4158.
- HALL, J. F., BARIGOU, M., SIMMONS, M. J. H. & STITT, E. H. 2004b. Mixing in Unbaffled High-Throughput Experimentation Reactors. *Industrial & Engineering Chemistry Research*, 43, 4149-4158.
- HANKS, R. W. 1979. The Axial Laminar Flow of Yield-Pseudoplastic Fluids in a Concentric Annulus. *Industrial & Engineering Chemistry Process Design and Development*, 18, 488-493.
- HENICHE, M., TANGUY, P. A., REEDER, M. F. & FASANO, J. B. 2005. Numerical investigation of blade shape in static mixing. *Aiche Journal*, 51, 44-58.
- HIRATA, Y., NIENOW, A. W. & MOORE, I. P. T. 1994. ESTIMATION OF CAVERN SIZES IN A SHEAR-THINNING PLASTIC FLUID AGITATED BY A RUSHTON TURBINE BASED ON LDA MEASUREMENTS. *Journal of Chemical Engineering of Japan*, 27, 235-237.
- HIRECH, K., ARHALIASS, A. & LEGRAND, J. 2003. Experimental Investigation of Flow Regimes in an SMX Sulzer Static Mixer. *Industrial & Engineering Chemistry Research*, 42, 1478-1484.
- HIRSCHBERG, S., KOUBEK, R., F.MOSER & SCHÖCK, J. 2009. An improvement of the Sulzer SMX™ static mixer significantly reducing the pressure drop. *Chemical Engineering Research and Design*, 87, 524-532.
- HOBBS, D. M. & MUZZIO, F. J. 1997. The Kenics static mixer: a three-dimensional chaotic flow. *Chemical Engineering Journal*, 67, 153-166.

- ISHIKAWA, T., OHNUMA, S. & KAMIYA, T. 1996. Transitional process of flow and heat transfer in a circular pipe with short static mixer. *Kagaku Kogaku Ronbunshu*, 22, 875-881.
- JAWORSKI, Z., PIANKO-OPRYCH, P., MARCHISIO, D. L. & NIENOW, A. W. 2007. CFD modelling of turbulent drop breakage in a Kenics static mixer and comparison with experimental data. *Chemical Engineering Research & Design*, 85, 753-759.
- JOSHI, P., NIGAM, K. D. P. & NAUMAN, E. B. 1995. The Kenics static mixer: new data and proposed correlations. *The Chemical Engineering Journal and the Biochemical Engineering Journal*, 59, 265-271.
- KALBITZ, H. & BOHNET, M. 1991. INFLUENCE OF STATIC MIXERS ON HEAT-TRANSFER AND PRESSURE-DROP IN TUBE HEAT-EXCHANGERS. *Chemie Ingenieur Technik*, 63, 270-271.
- KAWASE, Y., SHIMIZU, K., ARAKI, T. & SHIMODAIRA, T. 1997. Hydrodynamics in three-phase stirred tank reactors with non-newtonian fluids. *Industrial & Engineering Chemistry Research*, 36, 270-276.
- KELLER, D. S. & KELLER, J. D. V. 1990. An investigation of the shear thickening and antithixotropic behavior of concentrated coal-water dispersions. *Journal of Rheology*, 34, 1267-1291.
- KIREITSEU, M. V., TROOLIN, D. R. & KAUNAS UNIV OF, T. 2010. Turbulence Flow Dynamics and Vortex Rings of Heart Valve. *Mechanika 2010: Proceedings of the 15th International Conference*.
- KM KM static mixer brochure. <http://www.chemineer.com/products/kenics/km-mixers.html>.
- KU, D. N. & LIEPSCH, D. 1986. THE EFFECTS OF NON-NEWTONIAN VISCOELASTICITY AND WALL ELASTICITY ON FLOW AT A 90 DEGREE BIFURCATION. *Biorheology*, 23, 359-370.
- KUKUKOVA, A., AUBIN, J. & KRESTA, S. M. 2009. A new definition of mixing and segregation: Three dimensions of a key process variable. *Chemical Engineering Research and Design*, 87, 633-647.
- KUKUKOVA, A., J. AUBIN, S. KRESTA (2011). "Measuring the scale of segregation in mixing data." *The Canadian Journal of Chemical Engineering* 89(5): 1122-1138.
- KUKUKOVÁ, A., NOËL, B., KRESTA, S. M. & AUBIN, J. 2008. Impact of sampling method and scale on the measurement of mixing and the coefficient of variance. *AIChE Journal*, 54, 3068-3083.
- KUMAR, G. & UPADHYAY, S. N. 2008. Pressure drop and mixing behaviour of non-Newtonian fluids in a static mixing unit. *The Canadian Journal of Chemical Engineering*, 86, 684-692.
- KUPTSOV, P. V. & PARLITZ, U. 2012. Theory and Computation of Covariant Lyapunov Vectors. *Journal of Nonlinear Science*, 22, 727-762.
- LAROSA, P. & MANNING, F. S. 1964. INTENSITY OF SEGREGATION AS MEASURE OF INCOMPLETE MIXING. *Canadian Journal of Chemical Engineering*, 42, 65-&.
- LEHWALD, A., JANIGA, G., THEVENIN, D. & ZHRINGER, K. 2012. Simultaneous investigation of macro- and micro-mixing in a static mixer. *Chemical Engineering Science*, 79, 8-18.
- LEHWALD, A., THEVENIN, D. & ZHRINGER, K. 2010. Quantifying macro-mixing and micro-mixing in a static mixer using two-tracer laser-induced fluorescence. *Experiments in Fluids*, 48, 823-836.
- LI, H. Z., FASOL, C. & CHOPLIN, L. 1996. Hydrodynamics and heat transfer of rheologically complex fluids in a Sulzer SMX static mixer. *Chemical Engineering Science*, 51, 1947-1955.

- LI, H. Z., FASOL, C. & CHOPLIN, L. 1997. Pressure drop of Newtonian and non-Newtonian fluids across a Sulzer SMX static mixer. *Chemical Engineering Research & Design*, 75, 792-796.
- LI, H. Z., FASOL, C. & CHOPLIN, L. 1998. Heat transfer to Newtonian and non-Newtonian fluids flowing in a sulzer SMX static mixer. *Chemical Engineering Communications*, 170, 23-37.
- LING, F. H. 1993. CHAOTIC MIXING IN A SPATIALLY PERIODIC CONTINUOUS MIXER. *Physics of Fluids a-Fluid Dynamics*, 5, 2147-2160.
- LIPSCOMB, G. G. & DENN, M. M. 1984. Flow of bingham fluids in complex geometries. *Journal of Non-Newtonian Fluid Mechanics*, 14, 337-346.
- LIU, S. P., HRYMAK, A. N. & WOOD, P. E. 2006. Laminar mixing of shear thinning fluids in a SMX static mixer. *Chemical Engineering Science*, 61, 1753-1759.
- LOBRY, E., THERON, F., GOURDON, C., LE SAUZE, N., XUEREB, C. & LASUYE, T. 2011. Turbulent liquid-liquid dispersion in SMV static mixer at high dispersed phase concentration. *Chemical Engineering Science*, 66, 5762-5774.
- MACOSKO, C. W. *Rheology - Principles, Measurements and Applications*.
- MADANI, A., MARTINEZ, D. M., OLSON, J. A. & FRIGAARD, I. A. 2013. The stability of spiral Poiseuille flows of Newtonian and Bingham fluids in an annular gap. *Journal of Non-Newtonian Fluid Mechanics*, 193, 3-10.
- MAITI, S. & MISRA, J. C. 2013. Non-Newtonian characteristics of peristaltic flow of blood in micro-vessels. *Communications in Nonlinear Science and Numerical Simulation*, 18, 1970-1988.
- MALKIN, A. Y. & ISAYEV, A. I. *Rheology - Concepts, Methods, and Applications* (2nd Edition). ChemTec Publishing.
- MCKINLEY, G. H. (2005). *Visco-elasto-capillary thinning and break-up of complex fluids*.
- MEIJER, H. E. H., SINGH, M. K. & ANDERSON, P. D. 2012. On the performance of static mixers: A quantitative comparison. *Progress in Polymer Science*, 37, 1333-1349.
- MEGIAS-ALGUACIL, D. (2013). "Surface Rotation of Liquid Droplets Under a Simple Shear Flow: Experimental Observations in 3D." *Soft Materials* 11(1): 1-5.
- MEGIAS-ALGUACIL, D. AND E. J. WINDHAB (2006). "Experimental study of drop deformation and breakup in a model multitoothed rotor-stator." *Journal of Fluids Engineering-Transactions of the Asme* 128(6): 1289-1294.
- MEN, Y., HESSEL, V., LÖB, P., LÖWE, H., WERNER, B. & BAIER, T. 2007. Determination of the Segregation Index to Sense the Mixing Quality of Pilot- and Production-Scale Microstructured Mixers. *Chemical Engineering Research and Design*, 85, 605-611.
- MOYERS-GONZALEZ, M., ALBA, K., TAGHAVI, S. M. & FRIGAARD, I. A. 2013. A semi-analytical closure approximation for pipe flows of two Herschel-Bulkley fluids with a stratified interface. *Journal of Non-Newtonian Fluid Mechanics*, 193, 49-67.
- NIENOW, A. W. 1997. On impeller circulation and mixing effectiveness in the turbulent flow regime. *Chemical Engineering Science*, 52, 2557-2565.
- OTTINO, J. 2000. Chaotic mixing in a bounded three-dimensional flow. *J. Fluid Mech*, 417, 265-301.
- OTTINO, J. M. 1990. MIXING, CHAOTIC ADVECTION, AND TURBULENCE. *Annual Review of Fluid Mechanics*, 22, 207-253.
- OTTINO, J. M., MUZZIO, F. J., TIAHJADI, M., FRANJIONE, J. G., JANA, S. C. & KUSCH, H. A. 1992. Chaos, Symmetry, and Self-Similarity: Exploiting Order and Disorder in Mixing Processes. *Science*, 257, 754-760.
- PACEK, A. W. & NIENOW, A. W. 1997. Breakage of oil drops in a Kenics mixer.

- PAHL, M. H. & MUSCHELKNAUTZ, E. 1980. Statische Mischer und ihre Anwendung. *Chemie Ingenieur Technik*, 52, 285-291.
- PARKER, D. J., BROADBENT, C. J., FOWLES, P., HAWKESWORTH, M. R. & MCNEIL, P. 1993. POSITRON EMISSION PARTICLE TRACKING - A TECHNIQUE FOR STUDYING FLOW WITHIN ENGINEERING EQUIPMENT. *Nuclear Instruments & Methods in Physics Research Section a-Accelerators Spectrometers Detectors and Associated Equipment*, 326, 592-607.
- PATEL, D., EIN-MOZAFFARI, F. & MEHRVAR, M. 2011. Dynamic Performance of Continuous-Flow Mixing of Pseudoplastic Fluids Exhibiting Yield Stress in Stirred Reactors. *Industrial & Engineering Chemistry Research*, 50, 9377-9389.
- PAUL, E. L., ATIEMO-OBENG, V. A. & KRESTA, S. M. *Handbook of Industrial Mixing - Science and Practice*. John Wiley & Sons.
- PELOT, D. D., SAHU, R. P., SINHA-RAY, S. & YARIN, A. L. 2013. Strong squeeze flows of yield-stress fluids: The effect of normal deviatoric stresses. *Journal of Rheology*, 57, 719-742.
- PERYT-STAWIARSKA, S. JAWORSKI 2011. The CFD numerical analysis of non-Newtonian fluid flow through Kenics static mixer. *Przemysl Chemiczny*, 90, 1661-1663.
- PERYT-STAWIARSKA, S. & JAWORSKI, Z. 2008. Fluctuations of the non-Newtonian fluid flow in a Kenics static mixer: An experimental study. *Polish Journal of Chemical Technology*, 10, 35-37.
- POOLE, R. J., ESCUDIER, M. P., PRESTI, F., DALES, C., NOUAR, C., DESAUBRY, C., GRAHAM, L., PULLUM, L. & ASME 2005. Asymmetrical flow behaviour in transitional pipe flow of non-Newtonian liquids.
- PRADIPASENA, P. & RHA, C. 1977. PSEUDOPLASTIC AND RHEOPECTIC PROPERTIES OF A GLOBULAR PROTEIN (β -LACTOGLOBULIN) SOLUTION1. *Journal of Texture Studies*, 8, 311-325.
- RAFIEE, M., SIMMONS, M. J. H., INGRAM, A. & STITT, E. H. Development of positron emission particle tracking for studying laminar mixing in Kenics static mixer. *Chemical Engineering Research and Design*.
- RAHMANI, R. K., T. G. KEITH (2006). "Numerical simulation and mixing study of pseudoplastic fluids in an industrial helical static mixer." *Journal of Fluids Engineering-Transactions of the Asme* 128(3): 467-480.
- RAULINE, D., LE BLEVEC, J. M., BOUSQUET, J. & TANGUY, P. A. 2000. A comparative assessment of the performance of the Kenics and SMX static mixers. *Chemical Engineering Research & Design*, 78, 389-396.
- RAULINE, D., TANGUY, P. A., LE BLÉVEC, J.-M. & BOUSQUET, J. 1998. Numerical investigation of the performance of several static mixers. *The Canadian Journal of Chemical Engineering*, 76, 527-535.
- SAATDJIAN, E., RODRIGO, A. J. S. & MOTA, J. P. B. 2012. A study of mixing by chaotic advection in two three-dimensional open flows. *Chemical Engineering Science*, 81, 179-190.
- SCHLUTT, M. G., HEGNA, C. C., SOVINEC, C. R., KNOWLTON, S. F. & HEBERT, J. D. 2012. Numerical simulation of current evolution in the Compact Toroidal Hybrid. *Nuclear Fusion*, 52, 103023.
- SHAH, N. F. & KALE, D. D. 1991. Pressure drop for laminar flow of non-Newtonian fluids in static mixers. *Chemical Engineering Science*, 46, 2159-2161.
- SIMMONS, M., ZHU, H., BUJALSKI, W., HEWITT, C. & NIENOW, A. 2007. Mixing in a model bioreactor using agitators with a high solididity ratio and deep blades. *Chemical Engineering Research and Design*, 85, 551-559.

- SMX PLUS Sulzer static mixer brochure. <http://www.sulzer.com/en/Products-and-Services/Agitators-Mixers-and-Dispensers/Static-Mixers/General-Purpose-Mixers/SMX-plus>.
- SPENCER, R. S. AND R. M. WILEY (1951). "The mixing of very viscous liquids." *Journal of Colloid Science* 6(2): 133-145.
- SRIDHAR, T., TIRTAATMADJA, V., NGUYEN, D. A. & GUPTA, R. K. 1991. Measurement of extensional viscosity of polymer solutions. *Journal of Non-Newtonian Fluid Mechanics*, 40, 271-280.
- SZALAI, E., ARRATIA, P., JOHNSON, K. & MUZZIO, F. 2004. Mixing analysis in a tank stirred with Ekato Intermig[®] impellers. *Chemical Engineering Science*, 59, 3793-3805.
- TALANSIER, E., DELLAVALLE, D., LOISEL, C., DESRUMAUX, A. & LEGRAND, J. 2013. Elaboration of Controlled Structure Foams with the SMX Static Mixer. *Aiche Journal*, 59, 132-145.
- TECANTE, A. & CHOPLIN, L. 1993. GAS-LIQUID MASS-TRANSFER IN NON-NEWTONIAN FLUIDS IN A TANK STIRRED WITH A HELICAL RIBBON SCREW IMPELLER. *Canadian Journal of Chemical Engineering*, 71, 859-865.
- THAKUR, R. K., VIAL, C., NIGAM, K. D. P., NAUMAN, E. B. & DJELVEH, G. 2003. Static Mixers in the Process Industries—A Review. *Chemical Engineering Research and Design*, 81, 787-826.
- THERON, F. & SAUZE, N. L. 2011. Comparison between three static mixers for emulsification in turbulent flow. *International Journal of Multiphase Flow*, 37, 488-500.
- TODD D B, Mixing of highly viscous fluids, polymers and pastes. In: Paul EL, Atiemo-Obeng VA, Kresta SM. *Handbook of industrial mixing: science and practice*. New Jersey: John Wiley & Sons Inc., 2004:987-1025.
- TOZZI, E. J., MCCARTHY, K. L., BACCA, L. A., HARTT, W. H. & MCCARTHY, M. J. 2012. Quantifying mixing using magnetic resonance imaging. *Journal of visualized experiments : JoVE*, e3493.
- TROOLIN, D. R. & LONGMIRE, E. K. 2010. Volumetric velocity measurements of vortex rings from inclined exits. *Experiments in Fluids*, 48, 409-420.
- VANDERMEER, T. H. & HOOGENDOORN, C. J. 1978. HEAT-TRANSFER COEFFICIENTS FOR VISCOUS FLUIDS IN A STATIC MIXER. *Chemical Engineering Science*, 33, 1277-1282.
- VENTRESCA, A. L., CAO, Q. & PRASAD, A. K. 2002. The Influence of Viscosity Ratio on Mixing Effectiveness in a Two-fluid Laminar Motionless Mixer. *The Canadian Journal of Chemical Engineering*, 80, 614-621.
- VISSER, J. E., ROZENDAL, P. F., HOOGSTRATEN, H. W. & BEENACKERS, A. A. C. M. 1999. Three-dimensional numerical simulation of flow and heat transfer in the Sulzer SMX static mixer. *Chemical Engineering Science*, 54, 2491-2500.
- WADLEY, R. & DAWSON, M. K. 2005. LIF measurements of blending in static mixers in the turbulent and transitional flow regimes. *Chemical Engineering Science*, 60, 2469-2478.
- YAO, M. W., S. H. SPIEGELBERG, ET AL. (2000). "Dynamics of weakly strain-hardening fluids in filament stretching devices." *Journal of Non-Newtonian Fluid Mechanics* 89(1-2): 1-43.
- ZALC, J., ALVAREZ, M., MUZZIO, F. & ARIK, B. 2001. Extensive validation of computed laminar flow in a stirred tank with three Rushton turbines. *AIChE Journal*, 47, 2144-2154.

- ZALC, J., SZALAI, E., ALVAREZ, M. & MUZZIO, F. 2002a. Using CFD to understand chaotic mixing in laminar stirred tanks. *AIChE Journal*, 48, 2124-2134.
- ZALC, J. M., SZALAI, E. S., MUZZIO, F. J. & JAFFER, S. 2002b. Characterization of flow and mixing in an SMX static mixer. *Aiche Journal*, 48, 427-436.